



Schweizerische Eidgenossenschaft  
Confédération suisse  
Confederazione Svizzera  
Confederaziun svizra

Eidgenössisches Departement für Umwelt, Verkehr, Energie und Kommunikation UVEK  
Département fédéral de l'environnement, des transports, de l'énergie et de la communication DETEC  
Dipartimento federale dell'ambiente, dei trasporti, dell'energia e delle comunicazioni DATEC

**Bundesamt für Strassen**  
**Office fédéral des routes**  
**Ufficio federale delle Strade**

# **On the variability of squeezing behaviour in tunnelling**

**Zur Variabilität des Gebirgsverhaltens beim Tunnelbau im  
druckhaften Gebirge**

**Sur la variabilité du comportement des roches poussantes  
pendant l'excavation de tunnels**

**ETH Zürich, Institut für Geotechnik, Professur für Untertagbau  
Florence Mezger  
Prof. Dr. Georg Anagnostou**

**Forschungsprojekt AGT 2014/003 auf Antrag der Arbeitsgruppe  
Tunnelforschung (AGT)**

**November 2019**

**1664**

Der Inhalt dieses Berichtes verpflichtet nur den (die) vom Bundesamt für Strassen unterstützten Autor(en). Dies gilt nicht für das Formular 3 "Projektabschluss", welches die Meinung der Begleitkommission darstellt und deshalb nur diese verpflichtet.

Bezug: Schweizerischer Verband der Strassen- und Verkehrsfachleute (VSS)

Le contenu de ce rapport n'engage que les auteurs ayant obtenu l'appui de l'Office fédéral des routes. Cela ne s'applique pas au formulaire 3 « Clôture du projet », qui représente l'avis de la commission de suivi et qui n'engage que cette dernière.

Diffusion : Association suisse des professionnels de la route et des transports (VSS)

La responsabilità per il contenuto di questo rapporto spetta unicamente agli autori sostenuti dall'Ufficio federale delle strade. Tale indicazione non si applica al modulo 3 "conclusione del progetto", che esprime l'opinione della commissione d'accompagnamento e di cui risponde solo quest'ultima.

Ordinazione: Associazione svizzera dei professionisti della strada e dei trasporti (VSS)

The content of this report engages only the author(s) supported by the Federal Roads Office. This does not apply to Form 3 'Project Conclusion' which presents the view of the monitoring committee.

Distribution: Swiss Association of Road and Transportation Experts (VSS)



# **On the variability of squeezing behaviour in tunnelling**

**Zur Variabilität des Gebirgsverhaltens beim Tunnelbau im  
druckhaften Gebirge**

**Sur la variabilité du comportement des roches poussantes  
pendant l'excavation de tunnels**

**ETH Zürich, Institut für Geotechnik, Professur für Untertagbau  
Florence Mezger  
Prof. Dr. Georg Anagnostou**

**Forschungsprojekt AGT 2014/003 auf Antrag der Arbeitsgruppe  
Tunnelforschung (AGT)**

**November 2019**

**1664**

# Impressum

## **Forschungsstelle und Projektteam**

### **Projektleitung**

Prof. Dr. Georg Anagnostou

### **Mitglieder**

Florence Mezger

## **Begleitkommission**

### **Präsident**

Dr. Marco Ramoni

### **Mitglieder**

Christian Gammeter

Dr. Alex Schneider

Dr. Linard Cantieni

Konrad Elmar Blank

## **Antragsteller**

Arbeitsgruppe Tunnelforschung (AGT)

## **Bezugsquelle**

Das Dokument kann kostenlos von <http://www.mobilityplatform.ch> heruntergeladen werden.

# Table of contents

<b>Impressum</b> .....	<b>4</b>
<b>Zusammenfassung</b> .....	<b>7</b>
<b>Résumé</b> .....	<b>15</b>
<b>Summary</b> .....	<b>19</b>
<b>1 Introduction</b> .....	<b>23</b>
1.1 Context and objectives of the research project .....	23
1.2 Outline of the investigations .....	24
1.3 Remarks .....	27
1.4 Acknowledgements .....	27
<b>2 Analysis of case histories</b> .....	<b>31</b>
2.1 Sedrun Section of the Gotthard Base Tunnel .....	31
2.1.1 Introduction .....	31
2.1.2 Geology .....	32
2.1.3 Construction Method .....	34
2.1.4 Rock response to tunnelling .....	36
2.1.5 Data Analysis .....	38
2.1.6 Predictive capacity of the empirical equation .....	45
2.1.7 Conclusions .....	46
2.2 Giumello Gneiss Section of the Ceneri Base Tunnel .....	47
2.2.1 Introduction .....	47
2.2.2 Geology .....	47
2.2.3 Construction method .....	48
2.2.4 Rock response to tunnelling .....	49
2.2.5 Data analysis .....	49
2.2.6 Conclusions .....	50
2.3 Carbon Section of the Lötschberg Base Tunnel .....	50
2.3.1 Introduction .....	50
2.3.2 Geology .....	53
2.3.3 Construction Method .....	54
2.3.4 Rock response to tunnelling .....	56
2.3.5 Analysis of the short-term behaviour of the rock .....	57
2.3.6 Analysis of the long-term behaviour of the rock .....	60
2.3.7 Conclusions .....	64
<b>3 Tunnelling perpendicularly to alternating weak and competent rock layers</b> .....	<b>65</b>
3.1 Introduction .....	65
3.2 Closed-form solution for the ground response curve in tunnelling perpendicularly to thinly alternating weak and competent rocks .....	66
3.2.1 Introduction .....	66
3.2.2 Formulation of the GRC .....	66
3.2.3 Relevance of hard interlayers .....	67
3.2.4 Remarks concerning the adequacy of the homogenised model .....	68
3.2.5 Conclusions .....	69
3.3 Determination of equivalent parameters for a rock mass consisting of thinly alternating weak and competent rocks .....	69
3.3.1 Introduction .....	69
3.3.2 Determination of the parameters of the equivalent isotropic medium .....	70
3.3.3 Relationships between the material constants of the equivalent isotropic medium and those of the transversely isotropic medium .....	71
3.3.4 Accuracy of the proposed simplified model .....	74
3.3.5 Application examples .....	75
3.3.6 Closing remarks .....	76
3.4 Influence of the heterogeneity scale on the squeezing variability along the tunnel .....	77

3.4.1	Introduction .....	77
3.4.2	Longitudinal distribution of the displacements .....	77
3.4.3	A simple equation for the displacements in a weak zone considering a wall-effect .....	79
3.4.4	Conclusions .....	82
<b>4</b>	<b>Tunnelling parallel to alternating weak and competent rock layers .....</b>	<b>83</b>
4.1	Introduction .....	83
4.2	Response of a thinly stratified rock mass, striking parallel to tunnel axis .....	84
4.2.1	Introduction .....	84
4.2.2	Constitutive model .....	84
4.2.3	Basic aspects of the bedded rock response to excavation .....	88
4.2.4	Development of nomograms .....	94
4.2.5	Parameters of an equivalent isotropic material .....	95
4.2.6	Conclusions .....	98
4.3	Influence of the heterogeneity scale on the distribution of the ground displacements in the profile .....	98
4.3.1	Introduction .....	98
4.3.2	Adequacy of the homogenised model .....	99
4.3.3	Tunnelling parallel to the interface between a weak and a competent formation .....	105
4.3.4	Alternating weak and competent layers of medium thickness .....	107
4.3.5	Conclusions .....	107
4.4	Response of a schistous rock mass striking parallel to the tunnel axis .....	108
4.4.1	Introduction .....	108
4.4.2	Constitutive model .....	110
4.4.3	Basic aspects of the schistous rock response to excavation .....	112
4.4.4	Development of nomograms .....	116
4.4.5	Parameters of an equivalent isotropic material .....	118
4.4.6	Conclusions .....	119
<b>5</b>	<b>Tunnelling with an arbitrary angle to the schistosity or bedding planes .....</b>	<b>121</b>
5.1	Influence of the orientation of the anisotropy planes on the squeezing deformations .....	121
5.1.1	Introduction .....	121
5.1.2	Tunnelling in schistous rock, perpendicular to the strike direction .....	122
5.1.3	Tunnelling in thinly stratified rock, perpendicular to the strike direction .....	128
5.1.4	Arbitrary strike .....	132
5.1.5	Conclusions .....	133
5.2	Variability of squeezing deformations in folded rocks .....	134
5.2.1	Introduction .....	134
5.2.2	Problem definition .....	135
5.2.3	Schistous rocks .....	137
5.2.4	Stratified rocks .....	143
5.2.5	Case history of the Sedrun section of the Gotthard Base Tunnel .....	146
5.2.6	Conclusions .....	148
<b>6</b>	<b>Concluding remarks .....</b>	<b>149</b>
	<b>Appendices .....</b>	<b>153</b>
	<b>Notation .....</b>	<b>171</b>
	<b>References .....</b>	<b>175</b>
	<b>Projektabschluss .....</b>	<b>180</b>
	<b>Verzeichnis der Berichte der Forschung im Strassenwesen .....</b>	<b>183</b>

## Zusammenfassung

Unter "druckhaftem Gebirge" versteht man das Phänomen von grossen und oft zeitabhängigen Verformungen, die beim Vortrieb durch Gebirge kleiner Steifigkeit und Festigkeit entstehen. Die Intensität der Gebirgsverformung in einer druckhaften Strecke ist in der Regel stark veränderlich. Trotz gleichbleibender Ausbruchsicherung, Überlagerungshöhe und lithologischer Zusammensetzung lassen sich häufig auf kurzer Distanz beträchtliche Änderungen der Konvergenzen feststellen. So lange die Gründe für diese Variabilität nicht bekannt sind, sind zuverlässige Voraussagen des Gebirgsverhaltens beim Vortrieb schwierig. Letztere sind aber wichtig, um die Sicherungsmittel und den Ausbruchsquerschnitt zu bestimmen und damit kostspielige und aufwändige Nachprofilierungsarbeiten zu vermeiden. Die Variabilität der Druckhaftigkeit ist eine der Hauptursachen für Rückschläge, die selbst hochqualifizierte Ingenieure in einigen Fällen erfahren können.

Für eine gegebene Überlagerung und Ausbruchmethode ist bekannt, dass die Gebirgsverformungen von den mechanischen Eigenschaften des Gebirges, von der Raumstellung der Schichtung oder Schieferung, vom Primärspannungszustand und vom Porenwasserdruck abhängen. Es liegt daher auf der Hand, dass die Gründe für die Wechselhaftigkeit der Druckhaftigkeit beim Vortrieb in der Wechselhaftigkeit dieser Einflussfaktoren entlang des Tunnels liegen müssen. Trotz der intensiven Forschung der letzten Jahre zum Thema "druckhaften Gebirge" ist nach wie vor nicht bekannt, inwieweit diese Faktoren das Gebirgsverhalten nach dem Tunnelausbruch beeinflussen und wie sie bei der Planung berücksichtigt werden können, insbesondere dann, wenn sie entlang des Tunnels stark veränderlich sind. Dies ist zum Beispiel der Fall bei einem Vortrieb durch eine Wechsellagerung von starken und schwachen Schichten oder durch gefaltetes Gebirge.

Ziel des vorliegenden Forschungsberichtes ist es daher, die Sicherheit und die Wirtschaftlichkeit des Tunnelbaus in druckhaftem Gebirge zu erhöhen, das Verständnis der Variabilität der Druckhaftigkeit zu verbessern und die damit verbundenen Erfahrungen aus dem AlpTransit-Projekt der Ingenieurgemeinschaft zugänglich zu machen. Um dieses Ziel zu erreichen, ist es erforderlich, (i), die Faktoren, die für die Variabilität der Druckhaftigkeit verantwortlich sind, zu identifizieren und, (ii), den Einfluss dieser Faktoren zu quantifizieren, um sie während des Tunnelbaus für die rechtzeitige Identifizierung und Vorhersage des Gebirgsverhaltens zu verwenden.

Um diese Ziele zu erreichen, werden die Daten aus dem Gotthard-, Ceneri- und Lötschberg-Basistunnel qualitativ und empirisch untersucht, numerische Berechnungen zur quantitativen Untersuchung des Einflusses der Faktoren durchgeführt und Entscheidungshilfen für die Planung, Bemessung und den Bau von Tunnels entwickelt. Besonderes Augenmerk wird auf Faktoren gelegt, die die Konvergenzen sensitiv beeinflussen, d.h. deren Schwankungen – auch wenn sie relativ klein sind – eine signifikante Wechselhaftigkeit des makroskopisch beobachteten Verhaltens verursachen können. Daher konzentriert sich dieses Forschungsprojekt auf die Variabilität der Druckhaftigkeit infolge der Heterogenität des Baugrunds in Bezug auf seine mechanischen Eigenschaften (in verschiedenen Massstäben) sowie die Variation der Raumstellung der Anisotropieebenen (Schichtung, Schieferung). In diesem Forschungsprojekt wird die zeitliche Abhängigkeit des Gebirgsverhaltens (durch Konsolidierung) nicht berücksichtigt. Darüber hinaus ist bekannt, dass der Primärspannungszustand die Intensität der Druckhaftigkeit beeinflussen kann: Wenn der primäre Spannungszustand entlang des Tunnels variiert, wie es bei intensiv gefalteten Gesteinen oder in Störungszonen der Fall sein kann, kann die Intensität der Druckhaftigkeit variabel sein. Der Effekt der Variabilität der *in-situ* Spannungen wird in diesem Forschungsprojekt nicht untersucht.

Kapitel 2 analysiert die Beobachtungen beim Bau der drei AlpTransit-Basistunnels. Konkret gibt dieses Kapitel einen knappen Überblick über die verfügbaren Daten zur Geologie, zum Ausbruch und zur Sicherung sowie zum Gebirgsverhalten nach dem Vortrieb von verschiedenen Abschnitten des Gotthard- (Abschnitt 2.1), Ceneri- (Abschnitt 2.2) und

Lötschberg-Basistunnel (Abschnitt 2.3) und identifiziert die Faktoren, die für die Intensität und Variabilität der Druckhaftigkeit verantwortlich waren. Der Einfluss dieser Faktoren wird diskutiert und es werden empirische Korrelationen bestimmt, die es ermöglichen, die Vorhersagen der durch den Tunnelbau entstandenen Verformungen zu verbessern.

Die Fallbeispiele der Gotthard-, Ceneri und Lötschberg-Basistunnels (Kapitel 2) konnten zeigen, dass die Gebirgsverformungen hauptsächlich von der Lithologie, von der Orientierung der Schieferung und den Einfluss von benachbarten schwächeren oder stärkeren Zonen beeinflusst wurden. Diese – wenn auch relativ kleine – Schwankungen können daher zu einer signifikanten Variabilität der Intensität der Druckhaftigkeit entlang des Tunnels führen, die zusätzlich mit einer ausgeprägten Ungleichmässigkeit der Verformungen im Tunnelprofil einhergehen kann. Abschnitt 2.1 konnte zeigen, dass der Einfluss der Raumstellung der Schieferung auf die Tunnelkonvergenzen durch eine einfache, empirisch nachgewiesene (und später – im Kapitel 5 – auch theoretisch begründete) Gleichung bestimmt werden kann, die in Kombination mit Vorauserkundungen eine zuverlässige Vorhersage der Konvergenzen ermöglicht. Daher wurde in den nächsten Kapiteln dieses Forschungsberichts der Einfluss der oben genannten Faktoren ermittelt, um sie als Indikatoren während der Bauzeit für die rechtzeitige Identifizierung und Vorhersage des Gebirgsverhaltens zu nutzen. Darüber hinaus zeigte die Karbon Zone des Lötschberg-Basistunnel, dass erhebliche Langzeitverformungen aufgetreten sind, die unter anderem auf das Kriechen zurückzuführen sind. Auffällig war, dass bei grösseren (kurzfristigen) Verformungen (definiert als die Verformungen, die innerhalb von ca. 50 m hinter der Ortsbrust auftreten) grössere langfristige Verformungen durch das Kriechen auftraten. Daher beeinflusst das Kriechen die Intensität der Druckhaftigkeit entlang des Tunnels.

Der theoretische Hintergrund dieser Beobachtungen ist in den Kapiteln 3 bis 5 des Berichtes enthalten, welche die Intensität der Druckhaftigkeit im Tunnelbau durch eine Wechsellagerung von schwachen und stärkeren Gesteinen oder durch gefaltete Gesteine mittels analytischer Methoden oder numerischer Berechnungen untersuchen. Für die Analyse des Tunnelvortriebs durch eine Wechsellagerung von schwachen und stärkeren Schichten werden drei Fälle hinsichtlich der Orientierung der Schichten (zur Tunnelachse) unterschieden: (a) senkrecht, (b) parallel oder (c) mit einer beliebigen Ausrichtung zur Tunnelachse. Im ersten Fall kann die Intensität der Druckhaftigkeit in Abhängigkeit der Schichtdicke zum Tunnelradius – d.h. in Abhängigkeit der mechanischen Heterogenität des Baugrunds – sehr unterschiedlich sein. Im zweiten Fall ist die Intensität der Druckhaftigkeit entlang der Tunnelachse konstant, aber die Verformungen sind nicht gleichmässig entlang des Tunnelprofils verteilt. Wie beim Bau des Gotthard- und des Ceneri-Basistunnel beobachtet wurde, können diese beiden geotechnischen Situationen in der Realität effektiv auftreten und sind daher von besonderer praktischer Bedeutung. Natürlich kann eine solche Abfolge von harten und schwachen Schichten in Wirklichkeit durch Übergangszonen gekennzeichnet sein. Dennoch konzentriert sich dieses Forschungsprojekt aus Gründen der Einfachheit auf eine Wechsellagerung von nur einem starken und einem schwachen Material.

Die Kapitel 3 und 4 betreffen die Gebirgsverformungen in Querschnitten weit hinter der Ortsbrust. Diese sind grösser als die Konvergenzen des ausgebrochenen Profils, da sie die vor der Ortsbrust auftretenden Verformungen (sogenannte "Vorverformungen") beinhalten. Wie in den Kapiteln 3 und 4 dargestellt, können die Vorverformungen (und damit auch die Konvergenzen des ausgebrochenen Tunnelprofils) mit den bekannten Verfahren für isotrope, elasto-plastische Materialien berechnet werden.

Kapitel 3 untersucht die durch den Tunnelausbruch verursachten Verformungen beim Tunnelbau senkrecht zu den Schichten. Ist die Wechsellagerung in Bezug zum Tunneldurchmesser dick, so kann die Druckhaftigkeit sehr wechselhaft längs des Tunnels sein, wie dies beispielsweise beim Teilabschnitt Sedrun des Gotthard-Basistunnels beobachtet wurde. Besteht die Formation jedoch aus sehr dünnen, abwechselnden schwachen und stärkeren Gesteinsschichten, ist die Verformungsverteilung entlang der Tunnelachse praktisch gleichmässig. Das bedeutet, dass anstatt ein heterogenes Modell zu betrachten und somit die einzelnen Schichten numerisch zu modellieren – was in Bezug auf räumliche Diskretisierung und Rechenzeit anspruchsvoll wäre – das Gebirge als ein

homogenes, transversal isotropes Modell betrachtet werden kann. Für diesen Sonderfall präsentiert der Abschnitt 3.2 eine analytische Lösung für die Gebirgskennlinie (GKL; d.h. die Beziehung zwischen der radialen Verschiebung am Ausbruchsrund und dem Ausbauwiderstand) unter Verwendung der Homogenisierungstechnik und unter der Annahme von Rotationssymmetrie, ebenem Verformungszustand, ideal plastischem Verhalten für die schwachen Schichten und entweder ideal plastischem oder sprödem Verhalten (mit Entfestigung) für die harten Schichten. Die Herleitung dieser Gebirgskennlinie ist mathematisch anspruchsvoll, da eine Vielzahl von Fällen hinsichtlich des Versagenszustands des Gesteins berücksichtigt werden müssen (plastisches und/oder elastisches Verhalten der schwachen und/oder harten Schichten unter Berücksichtigung eines plastischen Fließens im Tunnelquerschnitt oder auch senkrecht dazu). Diese analytische Lösung ist aus praktischen Gründen besonders wichtig, da die numerische Modellierung einer engen Abfolge von harten und schwachen Gesteinen sehr zeitaufwändig ist. Numerische Berechnungen in Abschnitt 3.4, die die Schichten diskret betrachten, zeigen, dass die zuvor genannte analytisch abgeleitete Lösung für praktische Zwecke ausreichend genau ist, wenn die Dicke der harten Schichten weniger als etwa 5% des Tunnelradius beträgt.

Das Verhalten des betrachteten, homogenisierten Materials nach dem Tunnelausbruch ist isotrop (da der Ausbruchrand eine gleichmässige radiale Verschiebung aufweist). Dies deutet darauf hin, dass es möglich sein könnte, das Gebirge als isotropes und homogenes Material mit mechanischen Parametern zu betrachten, die von den Parametern und den Anteilen der schwachen und harten Schichten abhängen. Der Abschnitt 3.3 geht dieser Idee auf den Grund und bestimmt die äquivalenten Parameter (Elastizitätsmodul  $E_{eq}$ , Poissonzahl  $\nu_{eq}$ , Reibungswinkel  $\varphi_{eq}$ , Kohäsion  $c_{eq}$  und Dilatanzwinkel  $\psi_{eq}$ ) eines isotropen homogenen Gebirges in Abhängigkeit der Eigenschaften und Anteile der schwachen und der harten Schichten. Die Parameter eines mechanisch äquivalenten homogenen, isotropen und elasto-plastischen Materials werden bestimmt und in Abschnitt 3.3 dargestellt. Dies ist für Bemessungszwecke sehr nützlich, da es den Einsatz gängiger Berechnungsmethoden und -programmen zur Lösung von Problemen ermöglicht, die nicht den Bedingungen der Rotationssymmetrie oder dem ebenen Verformungszustand entsprechen, und dies auch für dünnbankiges Gebirge. Damit kann man beispielsweise mit den ermittelten äquivalenten Parametern einfach die Wirksamkeit eines Ausbausystems im Tunnelbau mittels Tunnelbohrmaschine bestimmen.

Die Ergebnisse der Abschnitte 3.2 und 3.3 gelten für eine Wechsellagerung aus schwachen und stärkeren Schichten, die (bezogen auf den Tunnelradius) so dünn sind, dass das Gebirge im Massstab des Tunnelquerschnitts als homogen angesehen werden kann. Andernfalls, wenn die Schichten dicker sind und damit die Annahme eines homogenisierten Modells nicht gerechtfertigt ist, müssen nach dem derzeitigen Stand der Forschung numerische Berechnungen durchgeführt werden, bei denen die schwachen und die stärkeren Schichten diskret modelliert werden müssen. Der Abschnitt 3.4 zeigt jedoch, dass die Verformungen in den schwachen Zonen mit Hilfe einer einfachen Gleichung abgeschätzt werden können, die den stabilisierenden Einfluss der benachbarten harten Schichten berücksichtigt. Die Gleichung aus Abschnitt 3.4 ermöglicht es die Intensität der Druckhaftigkeit für alle Schichtdicken schnell und einfach zu bestimmen, ohne dass eine numerische Modellierung erforderlich ist (zumindest nicht im Rahmen eines Vorprojekts). Durch eine umfassende Parameterstudie konnte gezeigt werden, dass diese Gleichung für praktische Zwecke ausreichend genau ist.

In Kapitel 4 werden die vortriebsbedingten Tunnelverformungen in geschichteten Baugrund untersucht, die aus einer Wechsellagerung aus schwachen und stärkeren Schichten bestehen, die parallel zur Tunnelachse orientiert sind. Wenn die Schichten sehr dick sind und ihre Grenzfläche in grossen Abstand zum Tunnel liegt, dann sind die Verformungen des Tunnelprofils natürlich praktisch gleichmässig und die Heterogenität des Baugrunds kann vernachlässigt werden. Andernfalls sind die Gebirgsverformungen entlang des Tunnelprofils nicht gleichmässig verteilt, auch wenn die Schichten sehr dünn sind.

Der Vortrieb durch dünne, alternierende schwache und harte Schichten, die parallel zur Tunnelachse auftreten, kann unter Berücksichtigung eines homogenen und transversal isotropen Mediums analog zu Abschnitt 3.2 analysiert werden (Abschnitt 4.2). Im

Gegensatz aber zu Abschnitt 3.2 sind die Bedingungen der Rotationssymmetrie jedoch nicht mehr erfüllt und daher muss dieses Randwertproblem numerisch gelöst werden. Daher wurde das Materialmodell von Abschnitt 4.2 für allgemeine 3D-Spannungs- und Dehnungszustände (mittels Homogenisierungstechnik) formuliert und in Abaqus implementiert. Die elasto-plastischen Parameter dieses homogenen und transversal isotropen Mediums hängen von den Anteilen sowie den Festigkeits- und Steifigkeitseigenschaften der Schichten der Wechsellagerung ab. Damit kann das Gebirgsverhalten beim Tunnelbau durch dünne, alternierende schwache und stärkere Schichten rechnerisch untersucht werden (unter der Annahme vom ebenen Verformungszustand).

Mit Hilfe dieses Modells wurde eine umfassende parametrische Studie durchgeführt, die ein breites Spektrum geotechnischer Parameter abdeckt. Da die homogenisierte Lösung aus praktischen Gründen besonders wichtig ist (die numerische Modellierung einer engen Abfolge von schwachen und stärkeren Gesteinen ist sehr zeitaufwändig), wird die Abschätzung der Verschiebungen entlang des Tunnelprofils für gegebene geotechnische Bedingungen durch dimensionslose Diagramme – dargestellt in Abschnitt 4.2 – erleichtert, die ein wertvolles Werkzeug für die Ingenieurpraxis darstellen, da sie es ermöglichen, die Maximal- und Minimalverschiebungen im Tunnelprofil für ein breites Spektrum geotechnischer Bedingungen zu bestimmen. Auch wenn das Verhalten des Gebirges in diesem Fall anisotrop ist, ermöglichen diese Diagramme analog zu Abschnitt 3.3 die Bestimmung der Parameter für ein isotropes homogenes Material, welches dem eigentlich anisotropen Gebirge in dem Sinne entspricht, dass seine durch den Tunnelbau induzierte Verschiebungen entweder dem Maximum oder dem Minimum der Verschiebungen des anisotropen Gebirges entsprechen. Wie in Abschnitt 4.2.5 gezeigt, ermöglicht die Verwendung dieses äquivalenten isotropen Modells das Auffinden einer oberen und einer unteren Grenze der Verschiebungen bei komplexeren Problemen (die nicht die Bedingung des ebenen Verformungszustands erfüllen).

Schliesslich untersucht Abschnitt 4.3 die Angemessenheit und die Grenzen der Homogenisierung eines geschichteten Gebirges und den Einfluss der Schichtdicke: Die numerischen Berechnungen, die den Einfluss der Schichtdicke durch diskrete Betrachtung der einzelnen Schichten analysieren, konnten zeigen, dass das zuvor genannte homogenisierte Modell für die Praxis hinreichend genau ist, wenn die Dicke der harten Schichten weniger als etwa 5% des Tunnelradius beträgt. Da dieses Kriterium auch für eine Folge von alternierenden Schichten gilt, die senkrecht zur Tunnelachse liegen, gilt dieses Kriterium für eine beliebige Orientierung der Schichten zur Tunnelachse. Darüber hinaus konnte Abschnitt 4.3 zeigen, dass bei sehr dicken Formationen die Ungleichmässigkeit der Verformungen im Profil nahezu verschwindet, wenn die schwache und die härtere Formation in einem Abstand von mindestens dem Fünffachen des Tunnelradius zur Tunnelachse liegt, so dass die schwache oder die harte Formation bei der Bemessung vernachlässigt werden kann. Daher müssen keine numerischen Berechnungen durchgeführt werden (zumindest nicht im Rahmen eines Vorprojekts).

Abschnitt 4.4 beschäftigt sich mit dem Fall eines Vortriebs durch geschiefertes Gebirge, wobei die Schieferungsflächen parallel zur Tunnelachse verlaufen. Der Grund für die Berücksichtigung der Schieferung in Kapitel 4 (welches sich eigentlich mit geschichteten Gebirgsmassen befasst) ist, dass das Verhalten des geschieferten Gesteins nach dem Tunnelausbruch gewisse Ähnlichkeiten mit der eines geschichteten Gebirges aufweist: Ein geschiefertes Gestein kann aus kontinuumsmechanischer Sicht als Grenzfall eines dünnbankigen Gebirges betrachtet werden. Die Schieferung spielt keine Rolle für einen Tunnelvortrieb senkrecht hierzu, hat aber einen ausgeprägten Einfluss auf die Verformungen, wenn sie parallel zur Tunnelachse verläuft.

Da das implementierte Materialmodell für (dünn) geschichtete Gesteine rechnerisch ineffizient ist für den Grenzfall der Schieferung, wurde in Abschnitt 4.4, ein Materialmodell speziell für geschieferte Gesteine formuliert und implementiert. Damit konnten in Abschnitt 4.4 numerische Berechnungen (unter der Annahme vom ebenen Verformungszustand) durchgeführt werden, die zeigten, dass die Schieferung die Gesteinsverformungen negativ beeinflussen kann, insbesondere wenn ihre Kohäsion und ihr Reibungswinkel klein sind. Ist zudem die einachsige Druckfestigkeit der Matrix gering, können die

Gebirgsverformungen wesentlich höher sein als bei nicht-geschieferten Gesteinen. Um den Einfluss der Schieferung besser abschätzen zu können, wurden in Abschnitt 4.4 dimensionslose Diagramme entwickelt und dargestellt, die es ermöglichen, die maximalen und minimalen Verformungen im Tunnelprofil bei gegebenen geotechnischen Bedingungen einfach abzuschätzen.

Das Kapitel 5 betrachtet den Tunnelbau durch dünn geschichtete oder geschieferte Gesteine mit einer beliebigen Ausrichtung der Anisotropieebenen in Bezug zur Tunnelachse. Zunächst wird in Abschnitt 5.1 der relativ einfache Fall einer konstanten Ausrichtung der Anisotropieebenen entlang des Tunnels betrachtet, wobei besonderes Augenmerk auf die Wirkung des Fallwinkels und der Streichrichtung der Anisotropieebenen relativ zur Tunnelachse auf die Vorverformungen und damit auf die Verformungen des Tunnelausbruchprofils ("Konvergenzen") gelegt wird. Da die unter der Annahme vom ebenen Verformungszustand (wie in den Kapiteln 3 und 4) ermittelten Verformungen die vor der Ortsbrust auftretenden Verformungen (sogenannte "Vorverformungen") beinhalten und damit wesentlich grösser sind als die Konvergenzen des ausgebrochenen Tunnelprofils, wird in Abschnitt 5.1 der Einfluss der Anisotropieebenen auf die Konvergenzen mit Hilfe von räumlichen Berechnungsmodellen mit beliebiger Orientierung der Anisotropieebenen zur Tunnelachse untersucht. Dieser Abschnitt konnte zum einen zeigen, dass es relevante Unterschiede zum bekannten Fall eines isotropen Gebirges gibt und zum anderen, dass die numerischen Berechnungen den empirisch ermittelten Zusammenhang zwischen Konvergenz und Raumstellung der Schieferung unter Berücksichtigung des sogenannten "Einflussfaktors der Schieferung" (der den Fallwinkel und die Streichrichtung der Anisotropieebenen zur Tunnelachse kombiniert) – welcher auf der Grundlage der Daten aus dem Gotthard- Basistunnel entwickelt wurde – gut reproduziert (vgl. Abschnitt 2.1). Basierend auf dieser Beziehung wurde eine einfache Gleichung entwickelt, die für die meisten Tunnelbauprobleme ausreichend genau ist und es ermöglicht, die Konvergenz für eine beliebige Raumstellung der Anisotropieebenen zur Tunnelachse unter Berücksichtigung des Einflussfaktors der Schieferung zu berechnen. Mit dieser Gleichung müssen für einen Tunnelvortrieb durch geschieferte oder geschichtete Gebirgsmassen keine aufwändigen räumlich-numerischen Analysen zur Abschätzung der Tunnelkonvergenzen durchgeführt werden (zumindest nicht in den Vorphasen eines Tunnelprojektes).

Anschliessend analysiert der Abschnitt 5.2 den Fall eines Vortriebs durch gefaltete Gebirgsformationen, bei denen die Orientierung der Anisotropieebenen und damit die Intensität der Druckhaftigkeit entlang der Tunnelachse variieren. Eine vereinfachte, gefaltete Gebirgsstruktur mit einer sinusförmigen Form der Anisotropieebenen wird dabei numerisch berücksichtigt. Die Faltung wird direkt im Materialmodell numerisch berücksichtigt, indem berücksichtigt wird, dass der Normalenvektor der Anisotropieebene positionsabhängig ist. Die numerischen Ergebnisse zeigen, dass die Variation der Ausrichtung der Anisotropieebenen in der Tat ein wichtiger Faktor für die Variabilität der Druckhaftigkeit ist und dies beim Tunnelbau durch geschieferte sowie geschichtete Gesteine. Die Ergebnisse der numerischen Untersuchungen zeigen, dass es eine gegenseitige Beeinflussung der wechselnden Bereiche der günstigen und ungünstigen Neigung der Anisotropieebenen entlang des Tunnels gibt. Trotz dieser gegenseitigen Beeinflussung führt die Faltung jedoch zu einer erheblichen Variabilität der Gesteinsverformungen entlang des Tunnels.

Schliesslich wird im Abschnitt 5.2.5 das Fallbeispiel des Teilabschnitts Sedrun des Gotthard Basistunnels nochmals aufgegriffen und der theoretische Hintergrund für den in Abschnitt 2.1 vorgestellten Einflussfaktor der Schieferung dargestellt. In diesem Abschnitt konnte gezeigt werden, dass (i) die im Teilabschnitt Sedrun des Gotthard-Basistunnels beobachtete Variabilität der Druckhaftigkeit mit Hilfe numerischer Berechnungen unter Berücksichtigung der Orientierung der Schieferung zur Tunnelachse gut nachvollzogen werden kann und (ii) dass der Einflussfaktor der Schieferung als zuverlässiger Indikator für die Abschätzung der Intensität der Druckhaftigkeit während dem Vortrieb in Kombination mit Vorauserkundungen verwendet werden kann.

In diesem Forschungsprojekt wurde die zeitliche Abhängigkeit des Gebirgsverhaltens infolge Konsolidation nicht berücksichtigt. Das Vorhandensein von Grundwasser oder

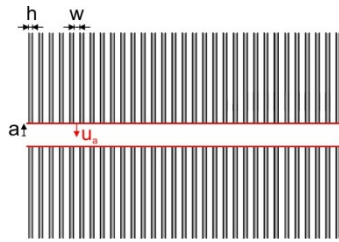
hohem Porenwasserdruck begünstigt die Entwicklung von Gesteinsverformungen. In einem gesättigten Gestein bestimmt die Durchlässigkeit des Baugrunds die Geschwindigkeit der Verformungen, die mit dem Abbau von übermässigen Porenwasserdrücken verbunden sind. Schwankungen der Durchlässigkeiten können daher zu variablen Intensitäten der Druckhaftigkeit führen. Insbesondere dünne, durchlässige Zwischenschichten können eine erhebliche Beschleunigung der Verformungen bewirken, da sie zu einer Verkürzung der Entwässerungswege führen. Diese Hypothese wurde bisher nicht quantitativ untersucht. Daher sollte der Einfluss der Heterogenitäten des Baugrunds in Bezug auf seine hydraulischen Eigenschaften auf die Variabilität der Druckhaftigkeit weiter untersucht werden.

Die Tabelle 1 gibt einen Überblick über die Bemessungshilfen, die im Rahmen dieses Forschungsprojektes entwickelt wurden.

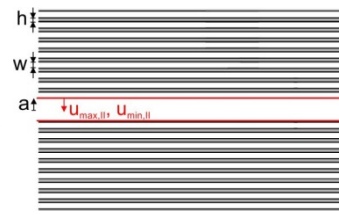
Einige Teile der Kapitel wurden bereits durch wissenschaftliche Publikationen für die Ingenieurgesellschaft zugänglich gemacht. Der Abschnitt 2.1 wurde in Mezger *et al.* [5] veröffentlicht und in Mezger *et al.* [6] präsentiert; Abschnitt 2.2 wurde in Mezger and Anagnostou [7] präsentiert.

**Tabelle 1. Übersicht über die Bemessungshilfen.**

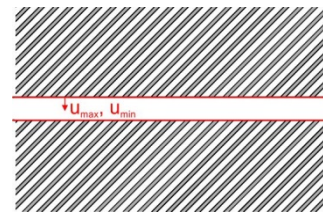
**Vortrieb durch dünnbankiges Gebirge (Schichtdicke  $h < 5\%$  des Tunnelradius  $a$ ):**



Die Radialverschiebung  $u_a$  ist gleichmässig über den Umfang des Tunnelprofils verteilt und kann mit der analytischen Lösung aus Abschnitt 3.2 bestimmt werden; Zudem wurde eine Methode zur Bestimmung von äquivalenten Parametern vorgeschlagen, mit welcher Probleme analysiert werden können, die nicht Rotationssymmetrie erfüllen (Abschnitt 3.3).

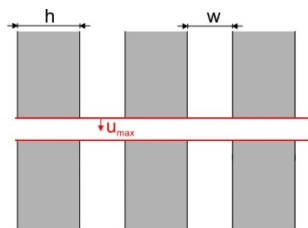


Die Radialverschiebung ist ungleichmässig über den Umfang des Tunnelprofils verteilt. Für die minimalen und maximalen Verformungen wurden dimensionslose Diagramme erstellt (Abschnitt 4.2.4); Zudem wird eine Methode zur Bestimmung von äquivalenten Parametern vorgeschlagen, mit welcher das Gebirgsverhalten unter beliebigen Bedingungen eingegrenzt werden kann (Abschnitt 4.2.5).

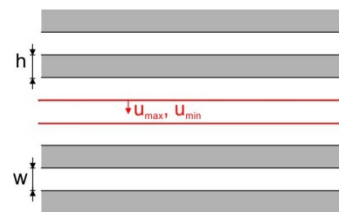


Die Radialverschiebung ist ungleichmässig über den Umfang des Tunnelprofils verteilt. Die kleinste und grösste Verschiebung kann mit den Gleichungen 5.1 und 5.4 (Abschnitt 5.1) abgeschätzt werden.

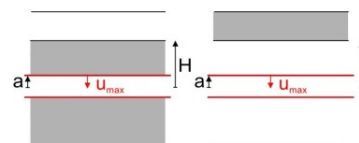
**Vortrieb durch eine Wechsellagerung von Gesteinen unterschiedlicher Festigkeit:**



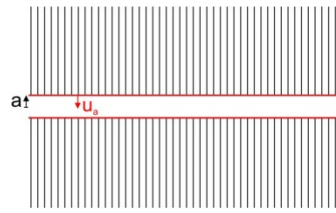
Die grösste Verformung  $u_{max}$  tritt in der Mitte der schwachen Zone auf. Sie kann durch eine in Abschnitt 3.4 entwickelte Gleichung abgeschätzt werden.



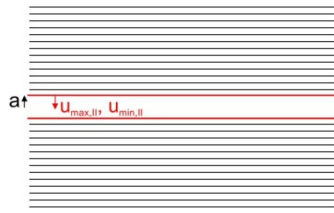
Im Allgemeinen ist die Radialverschiebung ungleichmässig über den Umfang des Profils verteilt. Die maximale Verformung kann näherungsweise basierend auf Abschnitt 4.3 bestimmt werden. Wenn jedoch  $H/a > 5$  (siehe Abbildung unten), dann ist die Radialverschiebung etwa gleichmässig über den Umfang des Profils verteilt und die üblichen Gleichungen für die GKL können unter Berücksichtigung der schwachen Gesteinsparameter angewendet werden.



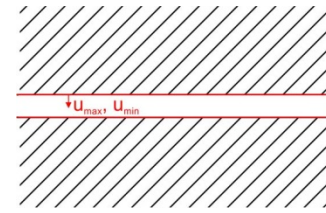
(Fortsetzung der Tabelle auf der nächsten Seite)

**Tabelle 1 (Forts.). Übersicht über die Bemessungshilfen.****Vortrieb durch ungefaltetes geschiefertes Gebirge (konstante Raumstellung der Schieferung):**

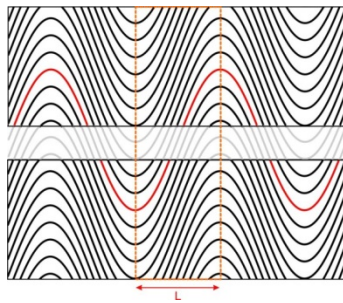
Die Radialverschiebung  $u_a$  ist gleichmässig über den Umfang des Tunnelprofils verteilt und kann mit den gängigen GKL-Gleichungen unter Berücksichtigung der Parameter der Gesteinsmatrix bestimmt werden.



Die Radialverschiebung ist ungleichmässig über den Umfang des Tunnelprofils verteilt. Für die grösste und kleinste Verformung wurden dimensionslose Diagramme erstellt (Abschnitt 4.4.4.4); Zudem wird eine Methode zur Bestimmung von äquivalenten Parametern vorgeschlagen, mit welcher das Gebirgsverhalten unter beliebigen Bedingungen eingegrenzt werden kann (Abschnitt 4.5.5).



Die Radialverschiebung ist ungleichmässig über den Umfang des Tunnelprofils verteilt. Die minimalen und maximalen Verformungen können mit den Gleichungen 5.1 und 5.4 (Abschnitt 5.1) abgeschätzt werden.

**Vortrieb durch gefaltetes geschiefertes Gebirge:**

Die Verformung ist ungleichmässig über den Umfang des Tunnelprofils und längs des Tunnels verteilt. Die grössten und kleinsten Verformungen treten dort, wo die Schieferung horizontal bzw. am steilsten ist, auf und unterscheiden sich im Allgemeinen von den Verformungen, die im ungefalteten Gebirge auftreten würden. Der Einfluss der Faltung ist vernachlässigbar (und die o.g. Verfahren für ungefaltetes Gebirge können angewendet werden), wenn die Periode  $2L$  der Faltung gross ist:

$$2L > \frac{8}{1 - \frac{2}{\pi} \arccos \frac{\tan 10^\circ}{\tan \omega_{s,max}}} a$$

## Résumé

Les "roches poussantes" désignent le phénomène de grandes déformations souvent dépendantes du temps qui se développent lors du creusement de tunnels à travers des roches faibles. L'intensité des déformations pendant l'excavation de tunnels dans des roches poussantes est habituellement très variable, même lorsqu'il n'y a pas de changement évident dans la méthode de construction, dans la profondeur de la couverture, dans la lithologie ou dans la structure de la roche. Tant que les raisons de cette variabilité ne sont pas connues, les convergences induites par l'excavation des tunnels ne peuvent pas être prédites avec une fiabilité suffisante. Cependant, des prédictions fiables sont importantes pour déterminer le soutènement ou le diamètre de l'excavation et ainsi éviter des travaux de reprofilage coûteux et fastidieux.

Pour une profondeur de couverture et une méthode de construction données, il est admis que les déformations de la roche dépendent des propriétés mécaniques de la roche, de l'orientation spatiale de la stratification ou de la schistosité, de l'état de contrainte initial et de la pression d'eau interstitielle. Il est donc évident que les raisons de la variabilité des roches poussantes pendant l'excavation de tunnels doivent être la variabilité de ces facteurs d'influence le long du tunnel. Malgré les recherches intensives menées ces dernières années sur le problème des roches poussantes, on ignore dans quelle mesure ces facteurs influencent le comportement de la roche et comment ils peuvent être pris en compte dans la conception des tunnels, notamment s'ils changent sur de courtes distances le long du tunnel. C'est par exemple le cas lors du creusement de tunnels à travers des couches faibles et compétentes alternantes ou à travers des roches plissées.

Les objectifs de ce projet de recherche sont donc d'améliorer la sécurité et l'économie de la construction de tunnels dans des roches poussantes, d'améliorer la compréhension de la variabilité des roches poussantes et de mettre les expériences du projet AlpTransit à la disposition de la communauté des ingénieurs. Les principaux objectifs sont les suivants : (i) l'identification des facteurs responsables de la variabilité des roches poussantes, et (ii) la quantification de l'influence de ces facteurs, afin de les utiliser comme indicateurs pendant la construction pour l'identification et la prévision en temps du comportement des roches poussantes. Pour atteindre ces objectifs, les données des tunnels de base du Saint-Gothard, du Ceneri et du Lötschberg sont analysées qualitativement – empiriquement, des calculs numériques sont effectués pour étudier quantitativement l'influence des facteurs et des outils décisionnels pour la planification, la conception et la construction des tunnels sont élaborées. Une attention particulière est accordée aux facteurs qui influencent les convergences de manière sensible, c'est-à-dire dont les variations – même si elles sont relativement petites – peuvent entraîner une variabilité significative du comportement macroscopique. Par conséquent, ce projet de recherche se concentre sur la variabilité des roches poussantes due à l'hétérogénéité du sol par rapport à ses caractéristiques mécaniques à différentes échelles ainsi qu'à la variation de l'orientation des plans d'anisotropie (stratification, schistosité). Dans ce projet de recherche, la dépendance temporelle du comportement de la roche (due à la consolidation) ne sera pas prise en compte. De plus, il est connu que l'état de contrainte initial peut influencer l'intensité des déformations des roches poussantes : Si l'état de contrainte initial varie le long du tunnel, comme ce peut être le cas dans des roches plissées de façon intensive ou dans des zones de faille, l'intensité des déformations des roches poussantes peut être variable. L'effet des variations des contraintes *in situ* ne sera pas étudié dans ce projet de recherche.

Le chapitre 2 analyse les observations liées à la construction des trois tunnels de base de l'AlpTransit. Ce chapitre donne en particulier un aperçu concis de données disponibles concernant la géologie, l'excavation, le soutènement et la réponse des roches au creusement de tunnels dans différentes sections du Saint-Gothard (section 2.1) du Ceneri (section 2.2) et du Lötschberg (section 2.3), en précisant les facteurs qui sont responsables pour l'intensité et la variabilité des roches poussantes. De plus, l'influence de ces facteurs est discutée et des corrélations empiriques sont établies qui permettent d'améliorer les prévisions de convergences induites par les tunnels. Les observations de la construction

des tunnels de l'AlpTransit ont montré que la variabilité des roches poussantes peut être attribuée à des variations de la structure du sol, comme la variation des propriétés mécaniques de la roche (par exemple lors du creusement de tunnels à travers des roches faibles et compétentes alternantes) ou la variation de l'orientation de la schistosité à l'axe du tunnel due au plissement des roches.

Le contexte théorique de ces observations est fourni dans les chapitres 3 à 5 du rapport, qui étudient l'intensité des roches poussantes dans le creusement de tunnels à travers des roches faibles et compétentes alternantes ou à travers des roches plissées, en utilisant des moyens de méthodes analytiques ou de calculs numériques. Pour l'analyse du creusement de tunnels à travers des couches faibles et compétentes alternantes, il faut distinguer trois cas concernant l'orientation des couches : une séquence de roches faibles et compétentes alternantes, se trouvant (a) perpendiculairement, (b) parallèlement ou (c) avec une orientation arbitraire par rapport à l'axe du tunnel. Dans le premier cas, l'intensité des roches poussantes peut être très variable selon l'épaisseur des couches par rapport au diamètre du tunnel, c'est-à-dire à l'échelle de l'hétérogénéité mécanique du sol. Dans le second cas, l'intensité des roches poussantes est constante le long de l'axe du tunnel, mais les déformations ne sont pas uniformes le long du profil du tunnel. Comme cela a été observé lors de la construction des tunnels de base du Saint-Gothard et du Ceneri, ces deux situations géotechniques peuvent effectivement se produire dans la réalité et revêtent donc une importance pratique particulière. Bien sûr, en réalité, une telle séquence de couches faibles et compétentes alternantes peut être caractérisée par des zones de transition. Néanmoins, pour des raisons de simplicité, ce projet de recherche se concentre sur un avancement à travers une séquence d'un seul matériau faible et d'un matériau compétent.

Les chapitres 3 et 4 se concentrent sur les déformations du sol en sections transversales loin derrière le front de taille. Celles-ci sont plus grandes que les convergences du profil excavé parce qu'elles incluent les déformations qui se produisent en avant du front de taille (dites "pré-déformations"). Comme indiqué aux chapitres 3 et 4, les pré-déformations (et donc aussi les convergences du profil excavé) peuvent être obtenues avec les méthodes connues pour les matériaux élasto-plastiques isotropes.

Le chapitre 3 étudie les déformations induites par l'excavation dans les tunnels perpendiculaires aux couches. Si les zones alternantes sont épaisses par rapport au diamètre du tunnel, la réponse de ces formations au creusement du tunnel peut présenter une grande variabilité, comme cela a été observé par exemple dans le tronçon de Sedrun du tunnel de base du Saint-Gothard. Toutefois, si la formation est constituée de couches faibles et compétentes très minces, la répartition des déformations le long de l'axe du tunnel sera pratiquement uniforme. Cela signifie qu'au lieu de considérer un modèle hétérogène et de modéliser numériquement les couches individuelles, ce qui serait exigeant en termes de discrétisation spatiale et de temps de calcul, la structure rocheuse peut être prise en compte en considérant un modèle homogène, mais néanmoins transversalement isotrope. Pour ce cas particulier, la section 3.2, présente une solution analytique pour la courbe de convergence (CV; c'est-à-dire la relation entre les déformations du tunnel en fonction de la pression de soutènement), en utilisant la technique d'homogénéisation et en assumant une symétrie de rotation, de conditions de déformation plane, un comportement parfaitement plastique pour les couches faibles et un comportement parfaitement plastique ou cassant (avec une diminution de la résistance après la rupture) pour les couches compétentes.

La réponse du matériau homogénéisé considéré au creusement de tunnels est isotrope (puisque la paroi du tunnel subit une déformation radiale uniforme). Ceci suggère qu'il est possible de considérer la masse rocheuse comme un matériau isotrope et homogène avec des paramètres mécaniques, qui dépendent des paramètres et des fractions des couches faibles et compétentes. Une telle approche serait utile en pratique parce qu'elle permettrait d'utiliser des méthodes de calcul et des programmes communs pour résoudre des problèmes qui ne répondent pas aux conditions de symétrie de rotation ou de déformation plane et cela, même pour des roches finement stratifiées. La section 3.3 approfondit cette idée et détermine des paramètres équivalents (module d'Young  $E_{eq}$ , coefficient de Poisson  $\nu_{eq}$ , angle de frottement  $\varphi_{eq}$ , cohésion  $c_{eq}$  et angle de dilatation  $\psi_{eq}$ ) d'une masse rocheuse

isotrope homogène en fonction des propriétés et fractions des couches faibles et compétentes.

Les résultats des sections 3.2 et 3.3 s'appliquent à des couches faibles et compétentes alternantes qui sont si minces (par rapport au diamètre du tunnel) que la masse rocheuse peut être considérée comme homogène à l'échelle de la section transversale du tunnel. Dans le cas contraire, si les couches sont plus épaisses et que l'hypothèse d'un modèle homogénéisé n'est donc pas valable, des calculs numériques doivent être effectués dans l'état actuel de la recherche, où les couches faibles et compétentes doivent être modélisées discrètement. Cependant, la section 3.4 montre que les déformations dans les zones faibles peuvent être estimées au moyen d'une équation simple qui prend en compte l'influence stabilisatrice des couches dures adjacentes.

Le chapitre 4 étudie les déformations du tunnel induites par l'excavation dans la masse rocheuse stratifiée, constituée de couches faibles et compétentes orientées parallèlement à l'axe du tunnel. Évidemment, si les couches sont très épaisses et que leur interface se trouve à une grande distance du tunnel, alors les déformations du profil du tunnel seront pratiquement uniformes et l'hétérogénéité du sol pourra être négligée. Sinon, les déformations des roches poussantes le long du profil du tunnel ne seront pas uniformes et cela, même si les couches sont très minces.

Le creusement de tunnels à travers des couches faibles et compétentes alternantes, étant très minces et qui sont orientées parallèlement à l'axe du tunnel, peut être analysé en considérant, comme en section 3.2, un médium homogène et transversalement isotrope. Cependant, contrairement à la section 3.2, les conditions de symétrie de rotation ne sont plus satisfaites et, par conséquent, ce problème de valeur limite doit être résolu numériquement. Par conséquent, le modèle constitutif de la section 4.2 a été formulé pour les états de contrainte et de déformation 3D généraux et implémenté dans Abaqus. Les constantes du matériau de ce modèle homogène équivalent sont constituées des fractions d'épaisseur et de paramètres mécaniques de couches alternantes. À l'aide de ce modèle, une étude paramétrique complète a été réalisée couvrant une large variété de paramètres géotechniques. Les résultats sont présentés sous forme de diagrammes de conception sans dimension qui permettent une estimation rapide des déformations maximum et minimum du profil du tunnel. Même si la réponse du sol est anisotrope dans ce cas, ces diagrammes peuvent également être utilisés, par analogie avec la section 3.3, pour déterminer les paramètres d'une masse rocheuse isotrope homogène, qui est équivalente à la masse rocheuse isotrope en ce sens que ses déformations induites par le tunnel sont égales soit aux déformations maximum ou minimum du modèle anisotrope. Comme le montre la section 4.2.5, l'utilisation de ce modèle isotrope équivalent permet de trouver une limite supérieure et une limite inférieure des déformations dans des problèmes plus complexes (qui ne satisfont pas la condition de déformation plane).

Finalement, la section 4.3 examine l'adéquation et les limites de l'homogénéisation d'une masse rocheuse stratifiée et l'influence de l'épaisseur des couches. La section 4.4 traite du cas du creusement de tunnels à travers des roches schisteuses orientées parallèlement à l'axe du tunnel. La raison pour laquelle on considère la schistosité au chapitre 4 (qui traite en fait des masses rocheuses stratifiées) est que la réponse d'une masse rocheuse schisteuse présente certaines similitudes avec celle d'une masse rocheuse stratifiée : Une masse rocheuse schisteuse peut être conçue, du point de vue mécanique, comme un cas limite d'une masse rocheuse finement stratifiée. La schistosité est sans importance pour le creusement de tunnels perpendiculaires aux couches, mais a une influence prononcée sur les déformations si les plans de schistosité sont orientés parallèlement à l'axe du tunnel. Puisque le modèle constitutif qui a été implémenté pour les roches finement stratifiées en section 4.2 est inefficace sur le plan informatique dans le cas limite de la schistosité, la section 4.4 commence par la formulation d'un modèle constitutif optimisé spécifiquement pour la roche schisteuse, continue avec l'étude des effets de la schistosité sur les déformations et se termine avec l'élaboration des diagrammes de conception qui permettent une estimation rapide des déformations dans des tunnels traversant des roches schisteuses (en assumant à nouveau des conditions de déformation plane) pour une large variété de paramètres.

Le chapitre 5 traite du creusement de tunnels à travers des masses de roches schisteuses ou à stratification mince avec une orientation arbitraire des plans d'anisotropie par rapport à l'axe du tunnel. Premièrement, dans la section 5.1, le cas relativement simple de l'orientation constante des plans d'anisotropie le long du tunnel est examiné, tout en prêtant attention à l'effet de l'inclinaison ainsi qu'à la direction des plans d'anisotropie par rapport à l'axe du tunnel sur les pré-déformations et donc sur les déformations du profil du tunnel excavé ("convergences"). Les pré-déformations dépendent essentiellement de l'orientation des plans d'anisotropie et, comme le montre la section 5.1.2.2, peuvent être considérablement plus élevées que celles estimées avec les méthodes connues qui ont été développées pour les matériaux isotropes. La section 5.1 présente une méthode simplifiée d'estimation des convergences des tunnels. Par la suite, la section 5.2 analyse numériquement le cas du creusement de tunnels à travers des formations rocheuses plissées, où l'orientation des plans d'anisotropie et par conséquent l'intensité des roches poussantes varient le long de l'axe du tunnel. Une structure de roche plissée simplifiée est considérée avec une forme sinusoïdale de la stratification ou de la schistosité. Le plissage est pris en compte numériquement dans les modèles constitutifs en considérant que le vecteur normal à la surface d'anisotropie est dépendant de la position. Les résultats numériques montrent que la variabilité des convergences dépend essentiellement de l'amplitude et de la période des plans d'anisotropie. Finalement, la section 5.2.5 revient sur le cas du tronçon de Sedrun du tunnel de base du Saint-Gothard et présente le contexte théorique du facteur de schistosité présenté dans la section 2.1.

## Summary

Squeezing refers to the phenomenon of large and often time-dependent deformations that develop when tunnelling through weak rocks. The magnitude of squeezing deformations in tunnelling often varies over short distances even where there is no obvious change in the construction method, in the depth of cover, in the lithology or rock structure. As long as the reasons for the variability are not known, the tunnelling-induced convergences cannot be predicted with sufficient reliability. Reliable predictions, however, are important for determining the temporary support or the excavation diameter. Otherwise, large-scale tunnel repairs may be necessary, which can cause delay and additional costs due to remedial actions as well as due to the enforced interruption of other operations in progress at the same time. The variability of squeezing intensity is one main cause of setbacks that even highly qualified engineers may experience in some cases.

For a given overburden and construction method, it is known that the rock deformations depend on the mechanical properties of the rock, on the spatial orientation of the stratification or schistosity, on the initial stress state and on the pore water pressure. It is therefore obvious that the reasons for the squeezing variability during advance must be the variability of these influencing factors along the tunnel. In spite of the intensive research of the last years on the problem of squeezing ground, it is not known to what extent these factors influence the rock behaviour and how they can be taken into account during design, particularly if they change within short distances along the tunnel. This is for example the case when tunnelling through alternating weak and competent layers or through folded rocks.

The goals of the present research project are thus to improve safety and economy of tunnel construction in squeezing ground, to improve the understanding of squeezing variability and to make the related experiences from the AlpTransit project available to the engineering community. The main objectives serving these goals are: (i) the identification of those factors, which are responsible for the squeezing variability, and (ii) the quantification of the influence of these factors, in order to use them as indicators during construction for the timely identification and prediction of the squeezing behaviour. To achieve these objectives, the data from the Gotthard, Ceneri and Lötschberg Base Tunnels are analysed qualitatively – empirically, numerical calculations are performed to investigate quantitatively the influence of the factors and decision aids for the planning, design and construction of tunnels are developed. Particular attention is paid to factors that influence convergences sensitively, *i.e.*, whose variations – even if relatively small – may cause a significant variability in the macroscopic behaviour. Therefore, this research project focuses on the squeezing variability due to the heterogeneity of the ground with respect to its mechanical characteristics at different scales as well as the variation of the orientation of the anisotropy planes (bedding, schistosity). In this research project, the time-dependence of the rock behaviour (due to consolidation) will not be considered. Furthermore, it is known that the initial stress state may influence the squeezing intensity: If the initial stress state varies along the tunnel, as it may be the case in intensively folded rocks or in fault zones, squeezing intensity may be variable. The effect of *in situ* stress variations will not be studied in this research project.

Chapter 2 analyses the observations of the construction of the three AlpTransit Base Tunnels. Specifically, this chapter gives a concise overview of the available data concerning the geology, the excavation and support and the rock response to tunnelling of different sections of the Gotthard (Section 2.1), Ceneri (Section 2.2) and Lötschberg Base Tunnel (Section 2.3) and identifies the factors that are responsible for the squeezing intensity and variability. Furthermore, the influence of these factors is discussed and empirical correlations are established that allow to improve the predictions of the tunnelling-induced convergences. The observations of the construction of the AlpTransit tunnels could show that the squeezing variability can be traced back to variations of the structure of the ground, as the variation of the mechanical properties of the rock (for example when

tunnelling through alternating weak and competent rocks) or the variation of the orientation of the schistosity to the tunnel axis due to folding.

The theoretical background of these observations is provided in Chapters 3 to 5 of the report, which investigate the squeezing intensity in tunnelling through alternating weak and competent rocks or through folded rocks by means of analytical methods or numerical computations. For the analysis of tunnelling through alternating weak and competent layers, three cases are distinguished with respect to the orientation of the layers: a sequence of alternating weak and hard rocks lying (a) perpendicular, (b) parallel or (c) with an arbitrary orientation to the tunnel axis. In the first case, the squeezing intensity may be very variable depending on the thickness of the layers with respect to the tunnel radius, *i.e.*, on the scale of the mechanical heterogeneity of the ground. In the second case, the squeezing intensity is constant along the tunnel axis, but the deformations are not uniform along the tunnel profile. As was observed during the construction of the Gotthard and the Ceneri Base Tunnels, these two geotechnical situations can effectively occur in reality and are thus of particular practical importance. Of course, in reality, such a sequence of hard and weak layers may be characterised by transition zones. Nevertheless, for simplicity reasons, this research project focuses on an advance through a sequence of only one hard and one weak material.

Chapters 3 and 4 focus on the displacements of the ground in cross-sections far behind the tunnel face. These are greater than the convergences of the excavated profile because they include the deformations that occur ahead of the face (so-called “pre-deformations”). As shown in Chapters 3 and 4, the pre-deformations (and thus also the convergences of the excavated profile) can be obtained with the known methods for isotropic elasto-plastic materials.

Chapter 3 investigates the excavation-induced displacements in tunnelling perpendicular to the layers. If the alternating zones are thick relatively to the tunnel diameter, the response of such formations to the tunnel excavation may exhibit a great variability, as was observed for instance in the Sedrun Section of the Gotthard Base Tunnel. If, however, the formation consists of very thin alternating weak and competent rock layers, the deformation distribution along the tunnel axis will be practically uniform. This means that rather than considering a heterogeneous model and modelling the individual layers numerically, which would be demanding in terms of spatial discretisation and computation time, the rock structure can be taken into account by considering a homogeneous, but nevertheless transversely isotropic model. For this special case, Section 3.2 presents a closed-form solution for the ground response curve (GRC; *i.e.*, the relationship between the radial displacement at the tunnel boundary and the support pressure), using the homogenisation technique and assuming rotational symmetry, plane strain conditions, perfectly plastic behaviour for the weak layers and either perfectly plastic or brittle behaviour (with post-failure decrease in strength) for the hard layers. The response of the considered homogenised material to tunnelling is isotropic (since the excavation boundary experiences a uniform radial displacement). This suggests that it may be possible to consider the rock mass as an isotropic and homogeneous material with mechanical parameters, which depend on the parameters and fractions of the weak and hard layers. Such an approach would be useful in practice because it would allow using common calculation methods and programs to solve problems that do not meet the conditions of rotational symmetry or plane strain and this even for thinly stratified rocks. Section 3.3 investigates into more depth this idea and determines the equivalent parameters (Young’s modulus  $E_{eq}$ , Poisson’s ratio  $\nu_{eq}$ , friction angle  $\varphi_{eq}$ , cohesion  $c_{eq}$  and dilatancy angle  $\psi_{eq}$ ) of an isotropic homogeneous rock mass as a function of the properties and fractions of the weak and the hard layers. The results of Sections 3.2 and 3.3 apply to alternating weak and hard layers that are so thin (relative to the tunnel radius) that the rock mass can be considered as homogeneous at the scale of the tunnel cross-section. Otherwise, if the layers are thicker and thus the assumption of a homogenised model is not valid, at the current state of research numerical calculations have to be performed, where the weak and the hard layers have to be modelled discretely. However, Section 3.4 shows that the displacements in weak zones can be estimated by means of a simple equation which takes into account the stabilising influence of the adjacent hard layers.

Chapter 4 investigates the excavation-induced tunnel displacements in stratified rock mass, consisting of alternating weak and hard layers that are oriented parallel to the tunnel axis. Obviously, if the layers are very thick and their interface lies at a great distance to the tunnel, then the displacements of the tunnel profile will be practically uniform and thus the heterogeneity of the ground can be neglected. Otherwise, the squeezing deformations along the tunnel profile will not be uniform and this even if the layers are very thin. Tunnelling through thinly alternating weak and hard layers that strike parallel to the tunnel axis can be analysed by considering, analogously to Section 3.2, a homogeneous and transversely isotropic medium. However, in contrast to Section 3.2, the conditions of rotational symmetry are not fulfilled anymore and, consequently, this boundary value problem has to be solved numerically. Therefore, the constitutive model of Section 4.2 was formulated for general 3D stress- and strain-states and implemented in Abaqus. The material constants of this equivalent homogeneous model consist of the thickness fractions and mechanical parameters of the alternating layers. Using this model, a comprehensive parametric study was carried out covering a wide range of geotechnical parameters. The results are presented in the form of dimensionless design diagrams that allow for a quick estimation of the maximum and minimum displacements of the tunnel profile. Even if the response of the ground is anisotropic in this case, these diagrams can also be used, analogously to Section 3.3, to determine the parameters for an isotropic homogeneous rock mass, which is equivalent to the isotropic rock mass in the sense that its tunnelling-induced displacements are equal either to the maximum or to the minimum displacements of the anisotropic model. As shown in Section 4.2.5, using this equivalent isotropic model makes it possible to find an upper and a lower bound of the displacements in more complex problems (that do not meet the condition of plane strain). Finally, Section 4.3 examines the adequacy and limits of the homogenisation of a stratified rock mass and the influence of the layer thickness. Section 4.4 concerns the case of tunnelling through *schistous* rocks striking parallel to the tunnel axis. The reason for considering schistosity in Chapter 4 (which actually deals with *stratified* rock masses) is that the response of a schistous rock mass exhibits certain similarities to that of a stratified rock mass: A schistous rock mass can be conceived, from the mechanical point of view, as a borderline case of a thinly stratified rock mass. Schistosity is irrelevant for tunnelling perpendicular to the layers, but has a pronounced influence on the displacements if the schistosity plane strikes parallel to the tunnel axis. Since the constitutive model that was implemented for thinly stratified rocks in Section 4.2 is computationally inefficient for the borderline case of schistosity, Section 4.4 starts with the formulation of an optimised constitutive model specifically for schistous rock, continues with the investigation into the effect of schistosity on the displacements and closes with working out design diagrams that allow a quick estimation of the tunnel displacements in schistous rocks (assuming again plane strain conditions) for a wide parameter range.

Chapter 5 considers tunnelling through thinly stratified or schistous rock masses with an arbitrary orientation of the anisotropy planes with respect to the tunnel axis. First, in Section 5.1, the relatively simple case of constant orientation of the anisotropy planes along the tunnel is considered, while paying attention to the effect of the dip angle and strike of the anisotropy planes relative to the tunnel axis on the pre-deformations and thus on the deformations of the excavated tunnel profile ("convergences"). The pre-deformations depend essentially on the orientation of the anisotropy planes and, as shown in Section 5.1.2.2, may be considerably higher than those estimated with the known methods which were developed for isotropic materials. Section 5.1 shows a simplified method for estimating the tunnel convergences. Subsequently, Section 5.2 analyses numerically the case of tunnelling through folded rock formations, where the orientation of the anisotropy planes and consequently the squeezing intensity vary along the tunnel axis. A simplified folded rock structure is considered with a sinusoidal form of the bedding or schistosity surface. Folding is taken into account numerically in the constitutive models by considering that the normal vector to the anisotropy surface is position-dependent. The numerical results show that the variability of the convergences depends essentially on the amplitude and period of the anisotropy surface. Finally, Section 5.2.5 revisits the case history of the Sedrun section of the Gotthard Base Tunnel, providing the theoretical background of the schistosity factor introduced in Section 2.1.



# 1 Introduction

## 1.1 Context and objectives of the research project

Squeezing refers to the phenomenon of large and often time-dependent deformations that develop when tunnelling through weak rocks. The magnitude of squeezing deformations in tunnelling often varies over short distances even where there is no obvious change in the construction method, in the depth of cover, in the lithology or rock structure. As long as the reasons for the variability are not known, the tunnelling-induced convergences cannot be predicted with sufficient reliability. Reliable predictions, however, are important for determining the temporary support or the excavation diameter. Otherwise, large-scale tunnel repairs may be necessary, which can cause delay and additional costs due to remedial actions as well as due to the enforced interruption of other operations in progress at the same time. The variability of squeezing intensity is one main cause of setbacks that even highly qualified engineers may experience in some cases [1].

For a given overburden and construction method, it is known that the rock deformations depend on the mechanical properties of the rock, on the spatial orientation of the stratification or schistosity, on the initial stress state and on the pore water pressure. It is therefore obvious that the reasons for the squeezing variability during advance must be the variability of these influencing factors along the tunnel. In spite of the intensive research of the last years on the problem of squeezing ground, it is not known to what extent these factors influence the rock behaviour and how they can be taken into account during design, particularly if they change within short distances along the tunnel. This is for example the case when tunnelling through alternating weak and competent layers (Fig. 1.1a) or through folded rocks (Fig. 1.1b).

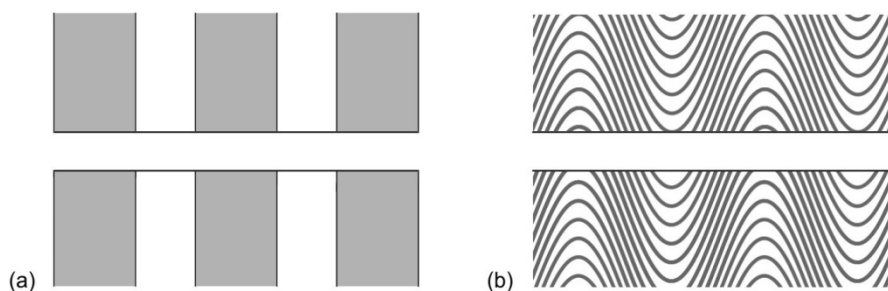


**Figure 1.1.** Tunnel drive through, (a), alternating weak and hard layers, (b), through folded rocks.

The goals of the present research project are thus to improve safety and economy of tunnel construction in squeezing ground, to improve the understanding of squeezing variability and to make the related experiences from the AlpTransit project available to the engineering community. The main objectives serving these goals are: (i) the identification of those factors, which are responsible for the squeezing variability, and (ii) the quantification of the influence of these factors, in order to use them as indicators during construction for the timely identification and prediction of the squeezing behaviour. To achieve these objectives, the data from the Gotthard, Ceneri and Lötschberg Base Tunnels are analysed qualitatively – empirically, numerical calculations are performed to investigate quantitatively the influence of the factors and decision aids for the planning, design and construction of tunnels are developed. Particular attention is paid to factors that influence convergences sensitively, *i.e.*, whose variations – even if relatively small – may cause a significant variability in the macroscopic behaviour. Therefore, this research project focuses on the squeezing variability due to the heterogeneity of the ground with respect to its mechanical characteristics at different scales as well as the variation of the orientation of the anisotropy planes (bedding, schistosity). In this research project, the time-dependence of the rock behaviour (due to consolidation) will not be considered. Furthermore, it is known that the initial stress state may influence the squeezing intensity: If the initial stress state

varies along the tunnel, as it may be the case in intensively folded rocks or in fault zones, squeezing intensity may be variable. The effect of *in situ* stress variations will not be studied in this research project.

## 1.2 Outline of the investigations

This research report consists of four parts (Chapters 2 to 5):

Chapter 2 analyses the observations of the construction of the three AlpTransit Base Tunnels. Specifically, this chapter gives a concise overview of the available data concerning the geology, the excavation and support and the rock response to tunnelling of different sections of the Gotthard (Section 2.1), Ceneri (Section 2.2) and Lötschberg Base Tunnel (Section 2.3) and identifies the factors that are responsible for the squeezing intensity and variability. Furthermore, the influence of these factors is discussed and empirical correlations are established that allow to improve the predictions of the tunnelling-induced convergences. The observations of the construction of the AlpTransit tunnels could show that the squeezing variability can be traced back to variations of the structure of the ground, as the variation of the mechanical properties of the rock (for example when tunnelling through alternating weak and competent rocks) or the variation of the orientation of the schistosity to the tunnel axis due to folding.

The theoretical background of these observations is provided in Chapters 3 to 5 of the report, which investigate the squeezing intensity in tunnelling through alternating weak and competent rocks (Fig. 1.1a) or through folded rocks (Fig. 1.1b) by means of analytical methods or numerical computations. For the analysis of tunnelling through alternating weak and competent layers, three cases are distinguished with respect to the orientation of the layers (*cf.* Fig. 1.2): a sequence of alternating weak and hard rocks lying (a) perpendicular, (b) parallel or (c) with an arbitrary orientation to the tunnel axis. In the first case, the squeezing intensity may be very variable depending on the thickness of the layers with respect to the tunnel radius, *i.e.*, on the scale of the mechanical heterogeneity of the ground. In the second case (*cf.* Fig. 1.2b), the squeezing intensity is constant along the tunnel axis, but the deformations are not uniform along the tunnel profile. As was observed during the construction of the Gotthard and the Ceneri Base Tunnels, these two geotechnical situations can effectively occur in reality and are thus of particular practical importance. Of course, in reality, such a sequence of hard and weak layers may be characterised by transition zones. Nevertheless, for simplicity reasons, this research project focuses on an advance through a sequence of only one hard and one weak material.



**Figure 1.2.** Investigated orientations of the layers to the tunnel axis for a sequence of alternating weak and hard rocks.

Chapters 3 and 4 focus on the displacements of the ground in cross-sections far behind the tunnel face. These are greater than the convergences of the excavated profile because they include the deformations that occur ahead of the face (so-called “pre-deformations”). As shown in Chapters 3 and 4, the pre-deformations (and thus also the convergences of the excavated profile) can be obtained with the known methods for isotropic elasto-plastic materials.

Chapter 3 investigates the excavation-induced displacements in tunnelling perpendicular to the layers (*cf.* Fig. 1.2a). If the alternating zones are thick relatively to the tunnel diameter

(diagram 1.a in Fig. 1.3), the response of such formations to the tunnel excavation may exhibit a great variability, as was observed for instance in the Sedrun Section of the Gotthard Base Tunnel. If, however, the formation consists of very thin alternating weak and competent rock layers, the deformation distribution along the tunnel axis will be practically uniform (diagram 1.c in Fig. 1.3). This means that rather than considering a heterogeneous model and modelling the individual layers numerically, which would be demanding in terms of spatial discretisation and computation time, the rock structure can be taken into account by considering a homogeneous, but nevertheless transversely isotropic model (diagram 1.i in Fig. 1.3). For this special case, Section 3.2 presents a closed-form solution for the ground response curve (GRC; *i.e.*, the relationship between the radial displacement at the tunnel boundary and the support pressure; [2]), using the homogenisation technique (see, *e.g.*, [3]) and assuming rotational symmetry, plane strain conditions, perfectly plastic behaviour for the weak layers and either perfectly plastic or brittle behaviour (with post-failure decrease in strength) for the hard layers.

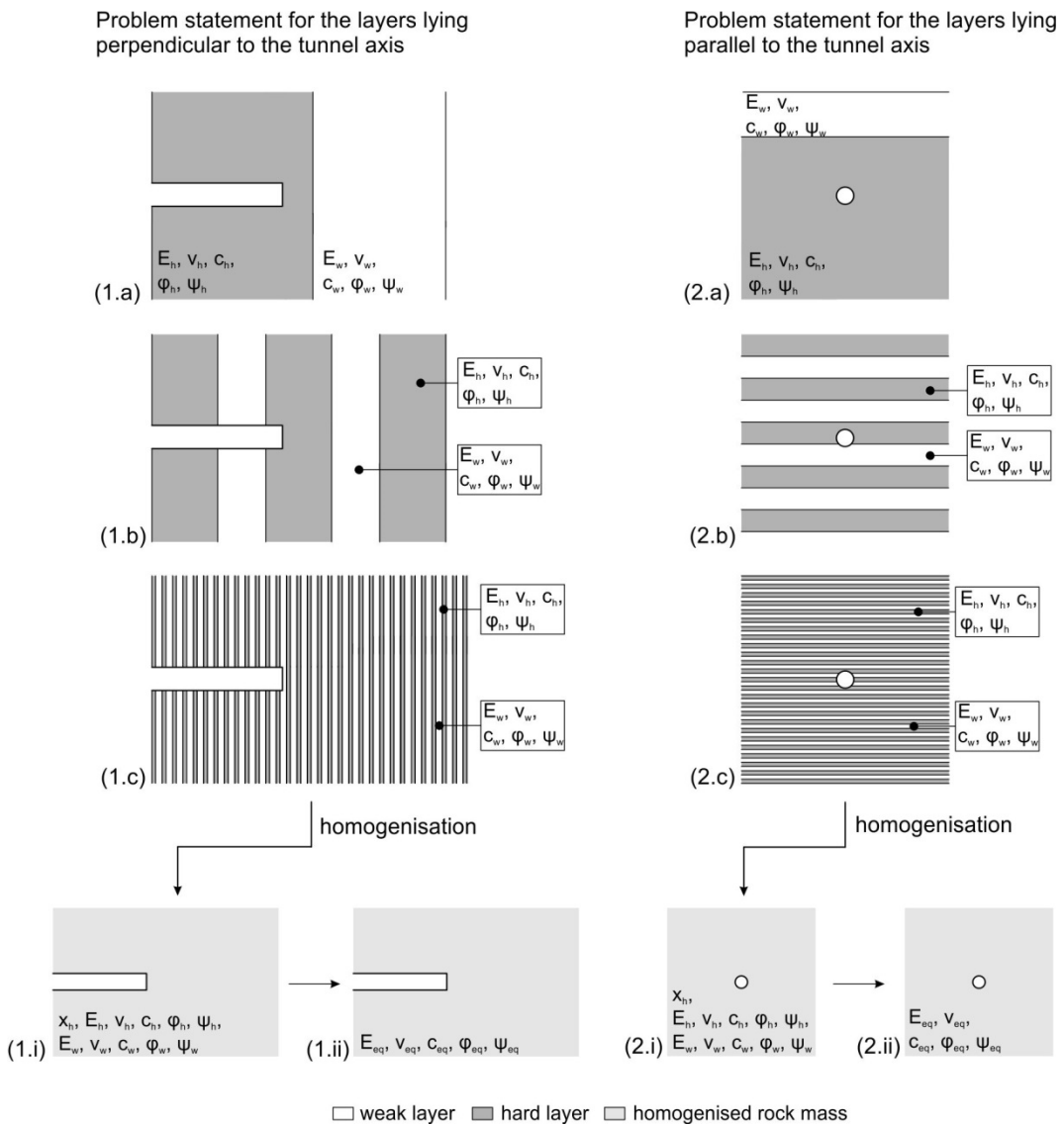


**Figure 1.3.** Left: Problem statement for alternating weak and hard layers lying perpendicular to the tunnel axis. Right: Problem statement for alternating weak and hard layers lying parallel to the tunnel axis.

The response of the considered homogenised material to tunnelling is isotropic (since the excavation boundary experiences a uniform radial displacement). This suggests that it may be possible to consider the rock mass as an isotropic and homogeneous material (diagram 1.ii in Fig. 1.3) with mechanical parameters, which depend on the parameters and fractions

of the weak and hard layers. Such an approach would be useful in practice because it would allow using common calculation methods and programs to solve problems that do not meet the conditions of rotational symmetry or plane strain and this even for thinly stratified rocks. Section 3.3 investigates into more depth this idea and determines the equivalent parameters (Young's modulus  $E_{eq}$ , Poisson's ratio  $\nu_{eq}$ , friction angle  $\varphi_{eq}$ , cohesion  $c_{eq}$  and dilatancy angle  $\psi_{eq}$ , diagram 1.ii in Fig. 1.3) of an isotropic homogeneous rock mass as a function of the properties and fractions of the weak and the hard layers.

The results of Sections 3.2 and 3.3 apply to alternating weak and hard layers that are so thin (relative to the tunnel radius) that the rock mass can be considered as homogeneous at the scale of the tunnel cross-section. Otherwise, if the layers are thicker and thus the assumption of a homogenised model is not valid, at the current state of research numerical calculations have to be performed, where the weak and the hard layers have to be modelled discretely. However, Section 3.4 shows that the displacements in weak zones can be estimated by means of a simple equation which takes into account the stabilising influence of the adjacent hard layers.

Chapter 4 investigates the excavation-induced tunnel displacements in stratified rock mass, consisting of alternating weak and hard layers that are oriented parallel to the tunnel axis (Fig. 1.2b). Obviously, if the layers are very thick and their interface lies at a great distance to the tunnel (diagram 2.a in Fig. 1.3), then the displacements of the tunnel profile will be practically uniform and thus the heterogeneity of the ground can be neglected. Otherwise (diagram 2.b in Fig. 1.3), the squeezing deformations along the tunnel profile will not be uniform and this even if the layers are very thin (diagram 2.c in Fig. 1.3).

Tunnelling through thinly alternating weak and hard layers that strike parallel to the tunnel axis can be analysed by considering, analogously to Section 3.2, a homogeneous and transversely isotropic medium (diagram 2.i in Fig. 1.3; Section 4.2). However, in contrast to Section 3.2, the conditions of rotational symmetry are not fulfilled anymore and, consequently, this boundary value problem has to be solved numerically. Therefore, the constitutive model of Section 4.2 was formulated for general 3D stress- and strain-states (using the homogenisation technique of [4]) and implemented in Abaqus. The material constants of this equivalent homogeneous model consist of the thickness fractions and mechanical parameters of the alternating layers. Using this model, a comprehensive parametric study was carried out covering a wide range of geotechnical parameters. The results are presented in the form of dimensionless design diagrams that allow for a quick estimation of the maximum and minimum displacements of the tunnel profile. Even if the response of the ground is anisotropic in this case, these diagrams can also be used, analogously to Section 3.3, to determine the parameters for an isotropic homogeneous rock mass (diagram 2.ii in Fig. 1.3), which is equivalent to the isotropic rock mass in the sense that its tunnelling-induced displacements are equal either to the maximum or to the minimum displacements of the anisotropic model. As shown in Section 4.2.5, using this equivalent isotropic model makes it possible to find an upper and a lower bound of the displacements in more complex problems (that do not meet the condition of plane strain).

Finally, Section 4.3 examines the adequacy and limits of the homogenisation of a stratified rock mass and the influence of the layer thickness.

Section 4.4 concerns the case of tunnelling through *schistous* rocks striking parallel to the tunnel axis. The reason for considering schistosity in Chapter 4 (which actually deals with *stratified* rock masses) is that the response of a schistous rock mass exhibits certain similarities to that of a stratified rock mass: A schistous rock mass can be conceived, from the mechanical point of view, as a borderline case of a thinly stratified rock mass. Schistosity is irrelevant for tunnelling perpendicular to the layers (diagram 1.c in Fig. 1.3), but has a pronounced influence on the displacements if the schistosity plane strikes parallel to the tunnel axis.

Since the constitutive model that was implemented for thinly stratified rocks in Section 4.2 is computationally inefficient for the borderline case of schistosity, Section 4.4 starts with the formulation of an optimised constitutive model specifically for schistous rock, continues with the investigation into the effect of schistosity on the displacements and closes with

working out design diagrams that allow a quick estimation of the tunnel displacements in schistous rocks (assuming again plane strain conditions) for a wide parameter range.

Chapter 5 considers tunnelling through thinly stratified or schistous rock masses with an arbitrary orientation of the anisotropy planes with respect to the tunnel axis (*cf.* Fig. 1.2c). First, in Section 5.1, the relatively simple case of constant orientation of the anisotropy planes along the tunnel is considered, while paying attention to the effect of the dip angle and strike of the anisotropy planes relative to the tunnel axis on the pre-deformations and thus on the deformations of the excavated tunnel profile (“convergences”). The pre-deformations depend essentially on the orientation of the anisotropy planes and, as shown in Section 5.1.2.2, may be considerably higher than those estimated with the known methods which were developed for isotropic materials. Section 5.1 shows a simplified method for estimating the tunnel convergences.

Subsequently, Section 5.2 analyses numerically the case of tunnelling through folded rock formations (Fig. 1.1b), where the orientation of the anisotropy planes and consequently the squeezing intensity vary along the tunnel axis. A simplified folded rock structure is considered with a sinusoidal form of the bedding or schistosity surface. Folding is taken into account numerically in the constitutive models by considering that the normal vector to the anisotropy surface is position-dependent. The numerical results show that the variability of the convergences depends essentially on the amplitude and period of the anisotropy surface. Finally, Section 5.2.5 revisits the case history of the Sedrun section of the Gotthard Base Tunnel, providing the theoretical background of the schistosity factor introduced in Section 2.1.

Table 1.1 gives an overview of the design aids, which were developed in the context of this research project and which will be presented in the following chapters.

### 1.3 Remarks

In this research project, as usual in geotechnics, compression will be taken as positive for the stresses and the strains.

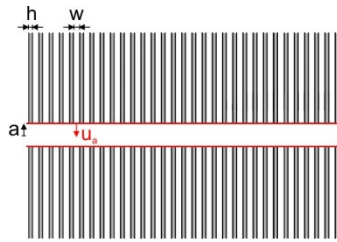
### 1.4 Acknowledgements

The authors wish to thank:

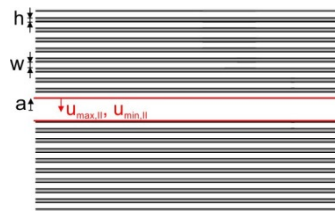
- the AlpTransit Gotthard AG, Switzerland, for the permission to use data from the construction of the Gotthard and the Ceneri Base Tunnel;
- the ITC ITECSA-TOSCANO, particularly Stefano Morandi (Pini Swiss Engineers), for allowing access to the documents needed as well as for the discussions about the Ceneri Base Tunnel;
- the BLS Netz AG – Alptransit, Switzerland, in particular Dr. Stefan Irmgartinger and Peter Teuscher, for the permission to use data from the construction of the Lötschberg Base Tunnel;
- Reto Wagner (Kellerhals + Haefeli AG) and Hans-Ulrich Riesen (ristag Ingenieure AG), for facilitating access to the Lötschberg documents and monitoring data;
- Stephan Gimmel, who participated to the analysis of the Lötschberg data within the framework of his Master thesis under the lead and close support of the authors; and
- the members of the accompanying commission for their constructive critique.

**Table 1.1. Overview of the design aids.**

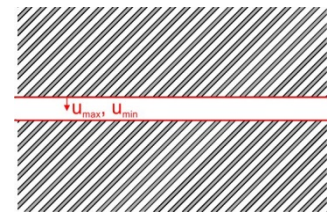
**Tunnelling through thinly stratified rocks (layer thickness  $h < 5\%$  tunnel radius  $a$ ):**



The radial displacement  $u_a$  is uniformly distributed over the circumference of the profile and can be determined using the closed-form solution of Section 3.2; Furthermore, a method for determining equivalent parameters is proposed, which can be used to analyse problems not obeying rotational symmetry (Section 3.3).

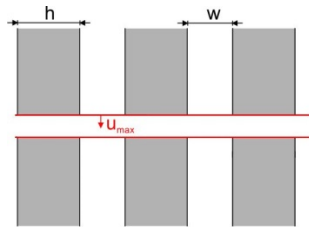


The radial displacement is non-uniformly distributed over the circumference of the profile. Dimensionless diagrams are provided for the minimum and maximum displacement (Section 4.2.4); Furthermore, a method for determining equivalent parameters is proposed, which can be used to bound the ground response under arbitrary conditions (Section 4.2.5).

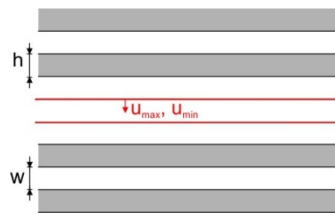


The radial displacement is non-uniformly distributed over the circumference of the profile. The minimum and maximum displacement can be estimated approximately using Eqs. 5.1 and 5.4 (Section 5.1).

**Tunnelling through alternating weak and competent rocks:**



The maximum displacement  $u_{max}$  occurs in the middle of the weak zone. It can be determined approximately by an equation proposed in Section 3.4.



In general, the radial displacement is non-uniformly distributed over the circumference of the profile. The maximum displacement can be determined approximately based upon Section 4.3. However, if  $H/a > 5$  (see figure below), then the radial displacement is approximately uniformly distributed over the circumference of the profile and the common GRC equations can be applied considering the weak rock parameters.

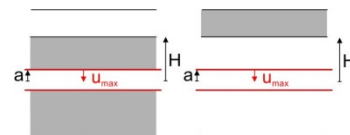
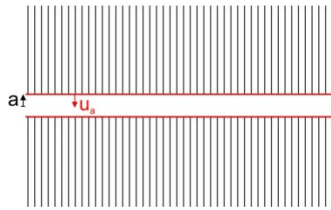


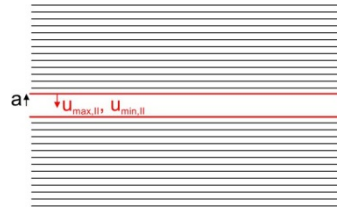
(Table continues on the next page)

**Table 1.1 (cont.). Overview of the design aids.**

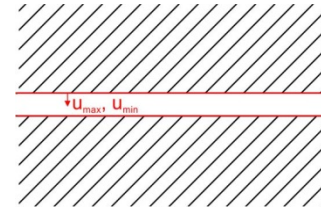
**Tunnelling through unfolded schistous rocks (constant schistosity plane orientation):**



The radial displacement  $u_0$  is uniformly distributed over the circumference of the profile and can be determined using the common GRC equations considering the parameters of the rock matrix.

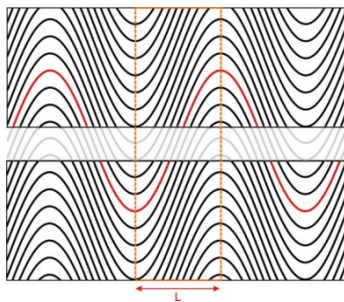


The radial displacement is non-uniformly distributed over the circumference of the profile. Dimensionless diagrams are provided for the maximum and minimum displacement (Section 4.4.4); Furthermore, a method for determining equivalent parameters is proposed, which can be used to bound the ground response under arbitrary conditions (Section 4.5.5).



The radial displacement is non-uniformly distributed over the circumference of the profile. The minimum and maximum displacements can be estimated approximately using Eqs. 5.1 and 5.4 (Section 5.1).

**Tunnelling through folded schistous rocks:**



The displacement is non-uniformly distributed over the circumference of the profile and along the tunnel. The maximum and the minimum displacements occur at the locations with horizontal and steepest schistosity planes, respectively, and are in general different from the displacements that would occur in the case of unfolded rock. The influence of folding is negligible (and the above-mentioned methods for unfolded rocks can be applied) if the folding period

$$2L > \frac{8}{1 - \frac{2}{\pi} \arccos \frac{\tan 10^\circ}{\tan \omega_{s,max}}} a$$



## 2 Analysis of case histories

### 2.1 Sedrun Section of the Gotthard Base Tunnel<sup>1</sup>

#### 2.1.1 Introduction

The magnitude of squeezing deformations occurring in tunnelling often varies over short distances even where there is no obvious change in the excavation method, depth of the cover and lithology. The variability of the ground response to excavation is one of the causes of the setbacks observed sometimes in tunnelling through squeezing rock [1]. As long as the reasons for the variability are not identified and understood, the tunnelling-induced convergences cannot be predicted with sufficient reliability. Reliable predictions, however, are important for determining the temporary support or the excavation diameter. Otherwise, large-scale tunnel repairs may be necessary, which can cause, as may be seen for example in the southern section of the Gotthard Base Tunnel [8], delay and extra costs due to remedial actions as well as due to the enforced interruption of other operations in progress at the same time. For reviews on the problem and the mechanics of squeezing in tunnelling see Kovári [1] and Barla [9].

The 57 km long Gotthard Base Tunnel is the core of the AlpTransit project [10]. The project offers the possibility of moving the majority of the goods traffic crossing the Alps from road to rail and guarantees the connection of Switzerland to the European high-speed railway network for passenger traffic. The tunnel crosses the Aare massif, the Tavetsch-Massif, the Gotthard massif and the penninic gneiss zone (*cf.* [11]) from north to south. These tectonic units consist predominantly of granites, gneisses and schists [10]. The present section focuses on the Clavaniev Zone (abbreviated to CZ, *cf.* [11]) and on the Intermediate Tavetsch-Massif (abbreviated to TZM, *cf.* [11]), where heavily squeezing conditions were expected in the planning phase and also encountered during construction.

The aim of this chapter is to identify factors that have a significant influence on the convergences and might be used as indicators during construction for the timely identification of squeezing conditions. The chapter starts with a concise overview of the available data concerning the geology, the excavation and support and the rock response to tunnelling (Sections 2.1.2 to 2.1.4) and then seeks for empirical correlations between the deformations observed during construction and the lithological and structural features of the rock mass (Section 2.1.5). The analysed tunnel section crosses the northern TZM and the Clavaniev Zone, hereafter referred to as “Sedrun North” (*cf.* [11]), and includes both the northwestern and northeastern tubes. The two tubes are separated by a centreline distance of 50 to 70 m. Section 2.1.5 demonstrates that the observed convergence correlates reasonably well with the degree of shearing and the schistosity orientation of the rock. In addition, Section 2.1.5 discusses the effect of nearby zones of more or less competent rock ([12], [13]) as well as the usefulness of the displacement vector orientation for predictions [14]. Finally, Section 2.1.6 checks the predictive capability of the empirical correlations obtained in Section 2.1.5 by calibrating them, based on the observations in a part of the tunnel, applying them to the remaining stretch of tunnel and comparing the empirical predictions with the measured deformations. Section 2.1.6 shows that the comparison is satisfactory and concludes that the empirical relationships in combination with advance probing are in fact very useful for estimating the squeezing intensity ahead of the tunnel face.

The present chapter is closely related to the work of Cantieni *et al.* [15], which examined the possibility of predicting ground response to tunnelling on the basis of the axial extrusion of the core ahead of the face. Cantieni *et al.* [15] also analysed the monitoring data from

<sup>1</sup> This chapter has been published in: Mezger, F., Anagnostou, G., Ziegler, H. J. (2013). The excavation-induced convergences in the Sedrun section of the Gotthard Base Tunnel. *Tunnelling and Underground Space Technology*, Vol. 38: 447-463.

the construction of the western tube of the Gotthard Base Tunnel. However, Cantieni *et al.* [15] could not find a clear correlation that would allow them to predict convergences with sufficient reliability on the basis of extrusion monitoring alone and proposed evaluating extrusion data in combination with other information, such as advance probing.

## 2.1.2 Geology

The Gotthard Base Tunnel crosses the Clavaniev Zone and the northern TZM over a length of 285 m and 793 m, respectively. The depth of cover is about 800 m. The tectonic units consist of different rock types: Gneisses alternate with steeply inclined layers composed of soft phyllites and schists, which have a thickness in the range of decimetres to decametres [10]. The major part of these units consists of so-called kakiritic rocks, *i.e.* rocks that are systematically interspersed with shear planes filled with rock fragments (fault breccia) or more finely ground material (fault gouge). In general, the term “kakirite” denotes “a broken or intensively sheared rock, which has lost a large part of its original strength” [16]. Vogelhuber [17] and Anagnostou *et al.* [18] performed a total of 112 consolidated drained and undrained triaxial tests to obtain the strength parameters of the kakiritic rocks in the Sedrun section. Depending on the development of the failure surface, a distinction is made between anisotropic and isotropic failure to evaluate the strength parameters. Anisotropic failure occurs when the failure surface develops through the existing discontinuity, *e.g.* through a plane of schistosity. Figure 2.1 shows the strength parameters determined from triaxial tests. The friction angles are between 25 and 30° and the cohesion-values between 200 and 600 kPa. Figure 2.1 considers only samples with isotropic failure. In the case of anisotropic failure, the friction angle was about 25° and the cohesion-values were mostly below 200 kPa.

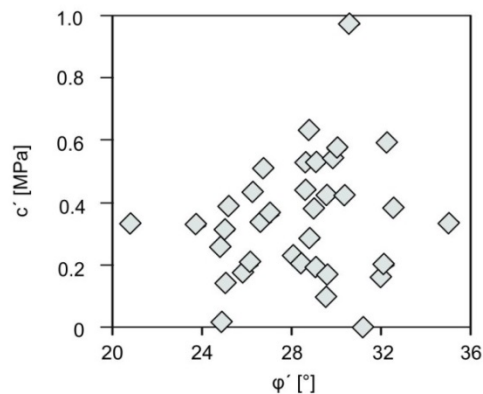


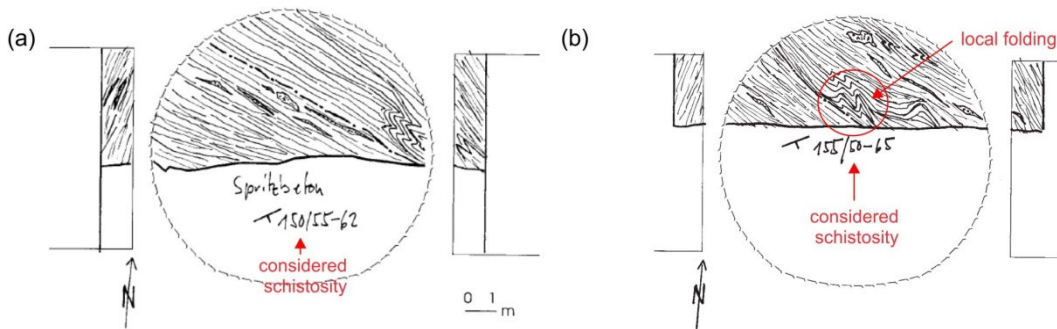
**Figure 2.1.** Cohesion  $c$  and angle of internal friction  $\phi$  of samples with isotropic failure (after [18]).

The Clavaniev Zone is located at the southern boundary of the Aare massif and was intensively sheared and strongly deformed tectonically during the alpine orogeny [16]. The degree of kakiritization is variable. About 67% of the rocks in the northern TZM and over 95% of the rocks in the Clavaniev Zone may be designated as kakirites. The rest of the gneisses and slates are at least interspersed with irregular hairline cracks. The weak, kakiritic rocks in the encountered section of the tunnel are saturated but have a very low permeability ( $k = 10^{-8}$  m/s to  $10^{-10}$  m/s according to [17]).

The following section provides an overview of the available information on the encountered geology based on the data in the integrated web platform of the Gotthard Base Tunnel project [19] and the synthesis report by Guntli and Weber [20]. Some lithologic and structural characteristics of the rock (lithological type, degree of shearing and schistosity), which were deemed to be important for its response to tunnelling, have been codified using project-specific classifications, which are presented in Figures 4 to 8 of [5] and are discussed below.

**Table 2.1.** Rock mass classification on the basis of the degree of shearing  $F$  (after [20]).

Degree of shearing $F$	Description
1	Competent
2	Sporadic shear fractures, slickensides
3	Schistous and laminated rocks, mylonites, phyllites
4	Sheared, fractured rocks (portion of rock flour <10%, disturbed over <25% of the tunnel face surface)
5	Sheared, crumbly, friable rocks (portion of rock flour 10-30%, disturbed over >25% of the tunnel face surface)
6	Rocks with a portion of rock flour >30% and plastic consistency. It can be deformed by hand and disturbed over the majority of the tunnel face surface.

**Figure 2.2.** Geological mappings of the tunnel face with traces of the schistosity planes. (a) NW tube, chainage 1535 m; (b) NE tube, chainage 1202 m (after [20]).

During advance, the ground was classified into rock types based upon both the lithology and the degree of shearing  $F$ , which was introduced as a project-specific measure of the tectonic disturbance of the rock mass. Six classes for the degree of shearing were defined (Table 2.1) according to the fraction of rock powder, resulting from the failure of the rocks during their tectonic oversteering in the geologic past. The lithological types  $T$  are presented in Table 2.2. The quality of the intact rock (on the scale of a specimen) decreases from lithological type 1 (which includes the strongest units, such as amphibolites or quartzites) to lithological type 9 (completely kakiritized, fine grained material). The last two types in Table 2.2 do not represent lithological types in the narrow sense, but have been included because heavily sheared rocks on account of their nature (almost engineering soil) can be seen as another lithological type.

The discontinuities of the rock were recorded during tunnel advance both with respect to the surfaces of schistosity and to the jointing. During advance it became evident that the degree of shearing  $F$  and the lithological type  $T$  are somehow connected with one other: in general, the higher the rock quality on the specimen scale, the smaller the degree of shearing.

The alpine schistosity is clearly recognizable over major portions of Sedrun North and this even in strongly kakiritic reaches [20]. In general, the strata dip steeply towards the north but are strongly disturbed by more recent shearing deformations. In fault zones, the intensive shearing (kakiritization) governs the behaviour of the rock mass.

However, since this shearing did not lead to a complete homogenization of the rock mass, the older rock structure between these shear zones has been preserved [20]. Thus, schistosity is still an important structural feature of the rock in the present case (Fig. 2.2). The so-called “schistosity influence factor” presented in Figures 4c to 8c in [5] is introduced in Section 2.1.5.2. It accounts for the orientation of the schistosity planes and combines their dip angle and dip direction in a single number.

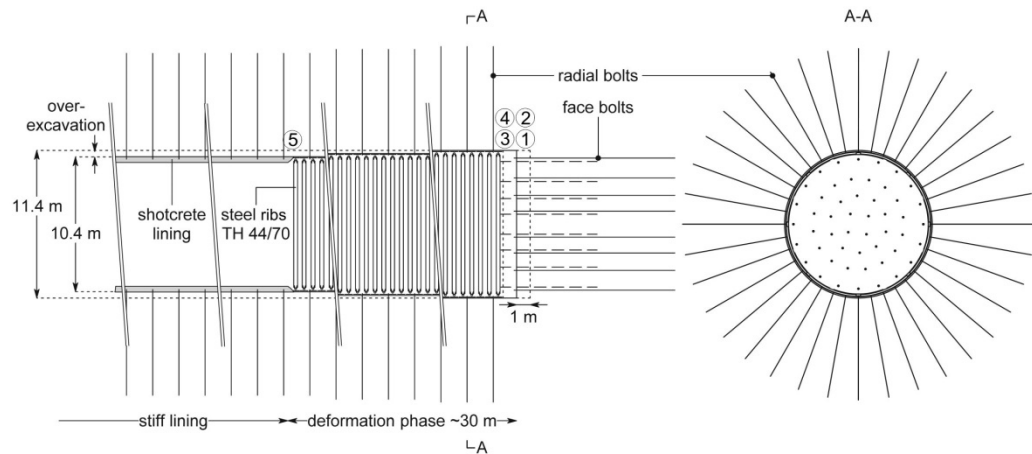


**Figure 2.3.** Longitudinal section and cross section of the yielding support system (after [21]) and sequence of applying the support: 1: Excavation, 2: Sealing of the working area, 3: Installation of the steel ribs, 4: Installation of the radial bolts, 5: Application of the shotcrete ring.

Depending on the thickness of the beds, which were developed as a result of the schistosity, the rock mass was classified into classes from “schistous to phyllitic” (thickness < 0.5 cm) to “not bedded” (thickness > 100 cm). Over 40% to 50% of the tunnel in the northern TZM and the Clavaniev Zone was assigned to the class “schistous to phyllitic” [20].

As a consequence of the kakiritization of the rock and of the schistosity, the development of jointing was small. Only in the weakly kakiritized rock were small joints or hairline cracks present. The jointing in the TZM and the Clavaniev Zone was described as small for more than 72% of the tunnel length [20].

**Table 2.2.** Rock mass classification on the basis of the lithology (after [20]).

Lithological type <i>T</i>	Description
1	Pegmatites, amphibolites, quartzites
2	Quartz- and feldspar-rich gneisses, migmatites
3	Striped gneisses
4	Gneisses with a high content of mica, dolomites
5	Gneisses with a high content of schists
6	Schists
7	Phyllites
8	Kakirites (fault gouge)
9	Kakirites with high plasticity and high percentage of fines

### 2.1.3 Construction Method

Due to the known presence and poor mechanical characteristics of kakiritic rocks, heavily squeezing conditions were expected for Sedrun North. Therefore, a circular tunnel cross-section in combination with full-face excavation and yielding support was chosen (Figs. 2.3 and 2.4a). The basic idea behind this concept has been explained by Kovári [1]: Full-face excavation makes it possible to have a statically favourable profile right from the start. The yielding support, which consists of sliding steel ribs connected by friction loops (Fig. 2.4b), reduces the rock pressure to a manageable level [22]. With this method, deformations could occur, while providing continuous support of the rock. An over-excavation of 0.1 to 0.7 m (in radius) was foreseen in order to accommodate the convergences without impairing the necessary clearance profile. The steel ribs used were TH 44/70. In heavily squeezing rock, the steel ribs were spaced at 0.33 – 0.66 m, which leads to a steel quantity of up to 9.4

tons per linear metre [10]. Additionally, fully grouted bolts with a length of 8 to 12 m were installed (Fig. 2.3).

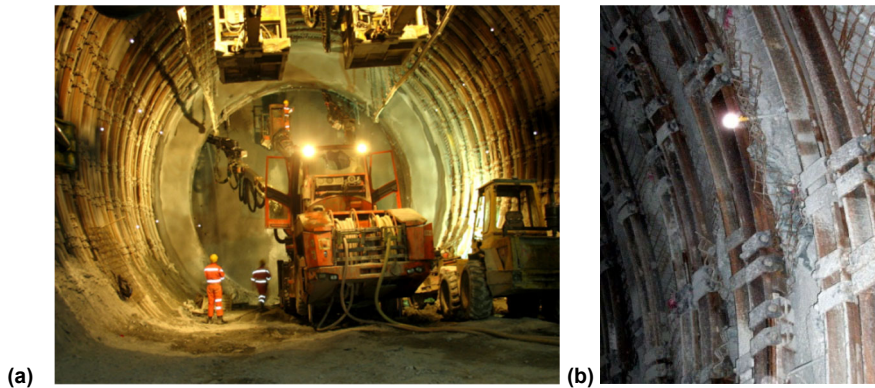


**Figure 2.4.** (a) Tunnelling works at chainage 2155.5 m (from [19]); (b) Support detail with steel ribs and friction loops (from [19]).

After the rate of convergence slowed down a 0.3 to 0.6 m thick shotcrete ring was applied. This was usually at a distance of about 30 m behind the tunnel face (approximately 1 month after excavation). In less squeezing ground, a stiff support was installed right from the start according to the so-called resistance principle [1].

To ensure stability of the tunnel face the ground ahead of the tunnel face was reinforced using 40 to 60 12 m-long steel bolts and steel fibre-reinforced shotcrete was applied to the face immediately after each excavation step. Additionally, systematic forepoling was used to prevent rock loosening and rock fall.

**Table 2.3.** Definition of the support classes applied in Sedrun North (after [20]).

Support class	SA 2.3	SA 4.1	SA 4.1+	SA 4.2	SA 4.2+
Excavated radius [m]	4.70	5.14	5.69	5.69	6.24
Over-excavation [cm]	10	30	50	50	70
Length of round [m]	1-2	1-1.5	1-1.34	1.34	1
Type of steel ribs [-]	TH 29/70		TH 44/70		
Sliding resistance [kN]	4 friction loops x 100 kN = 400 kN per connection				
Spacing of steel ribs [m]	1.0 – 2.0	1-1.5	0.67-1.34	0.67	0.33/0.67 – 1.0
Radial bolts, type [-]	Ø 25 mm, 320 kN, S500				
Radial bolts, length [m]	6	6-8	8	8-12	8-12
Radial bolts, quantity [-]	13-14	17-28	17-28	11-25	28
Face bolts, length [m]	12	12	12-18	12	12-18
Face bolts, quantity [-]	40	40	50	50	60
Forepoling, length [m]	8	6	6-8	6	6
Forepoling, quantity [-]	0-25	25-30	0-51	If required	If required
Thickness of the shotcrete ring [cm]	20-25	25-30	25-30	25-30	25-60
Thickness of the concrete lining [cm]	30	30	30	60	60

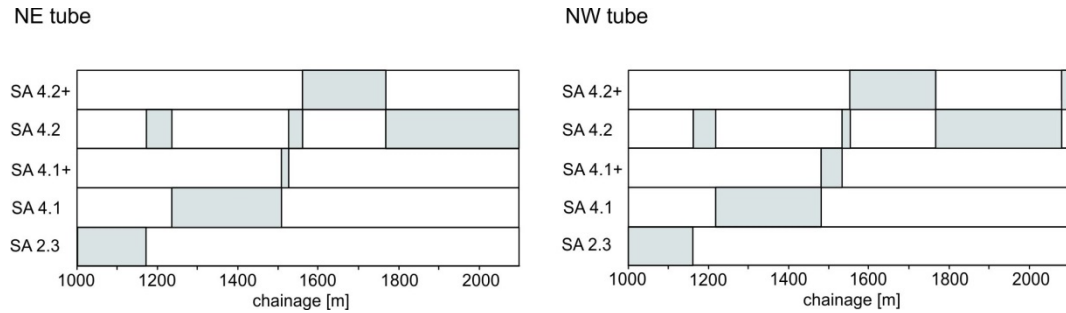


**Figure 2.5.** Distribution of the applied support classes along the tunnel (after [20]).

Table 2.3 and Figure 2.5 show the definition of the applied support classes, their distribution along the tunnel as well as the sequence of applying the support. The determination of the temporary support and of the excavation diameter during construction was based on the results of design calculations, the experience gained with the rock and support behaviour from the already excavated tunnel section and the findings from advance core borings. More specifically, 28 horizontal advance core borings of lengths between 31 m to 196 m were carried out during tunnel construction in order to explore the prevailing rock conditions ahead of the tunnel face and to obtain rock samples for triaxial testing [18]. Figure 2.6 shows, for example, the estimated degree of kakiritization based on the obtained core (bottom of Fig. 2.6) as well as the encountered degree of shearing  $F$  after excavation (top of Fig. 2.6). Figure 2.6 shows that the shearing degree can be estimated on the basis of advance core drilling but is still subject to some uncertainty.

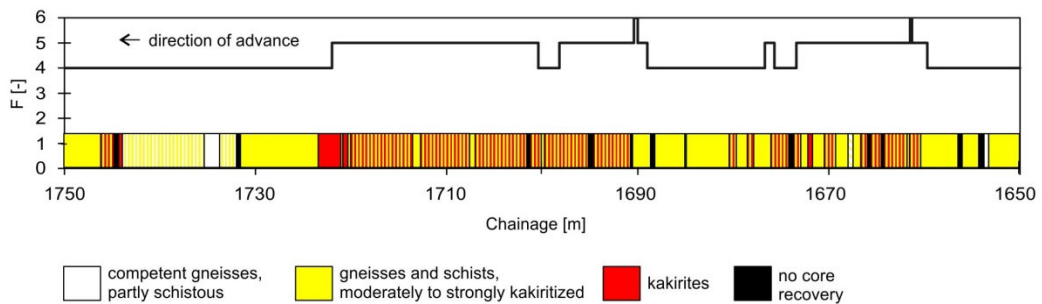


**Figure 2.6.** Comparison of the borehole findings (degree of kakiritization) with the encountered geology (degree of shearing  $F$ ) of the chainage 1650 m to 1750 m of the NW tube (evaluation based upon the data from [19] and [20]).

### 2.1.4 Rock response to tunnelling

In order to observe the behaviour of the rock and check the effectiveness of the tunnel support, a monitoring system with 3D optical measurements, radial extensometers, reverse-head-extensometers (RH-extensometers, [23]) and measuring anchors was implemented.

- The convergences of the tunnel boundary during tunnel advance were monitored optically at monitoring stations spaced every 5 m to 20 m. Each monitoring station had 5 or 7 measuring points (Fig. 2.7). The displacements were measured at 165 monitoring stations in the NE tube and in 163 monitoring stations in the NW tube.
- 5 monitoring stations were instrumented with up to 5 radial extensometers of length 4 – 25 m to determine the extent of the rock zone around the tunnel affected by the excavation and thus the underlying rock deformation mechanism of the observed convergences. In some cases the measuring head was destroyed due to the large rock deformations so that no measurements were possible.
- To determine the load on the radial anchors, 4 m long measuring anchors were installed in 2 monitoring stations.

- The RH-extensometers served to observe the extrusion of the tunnel face as well as the axial deformation of the core ahead of the face.

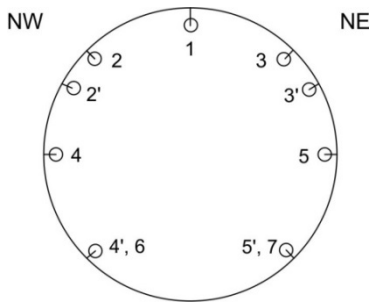


**Figure 2.7.** Monitoring station with 5 (numbers with apostrophes) or 7 measuring points (numbers without apostrophes).

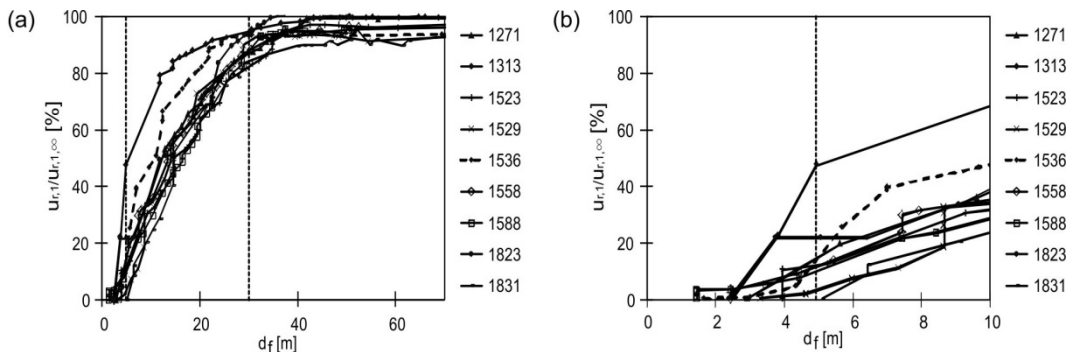
The optical measurements were the most important means of observing the behaviour of the tunnel since they were installed frequently and systematically in contrast to the other measurements. For this reason, the present chapter analyses only the optical measurements (Sections 2.1.5 and 2.1.6). The results of the RH-extensometers have already been discussed by Cantieni *et al.* [15].

Figure 2.8a illustrates the typical development of the convergence. The diagram shows the vertical displacement  $u_{r,1}$  of the crown (normalized by its value  $u_{r,1,\infty}$  far behind the face) as a function of the distance to the tunnel face  $d_f$ . Each curve of the diagram corresponds to a different monitoring station. It is readily seen that the biggest portion of the convergence took place within two tunnel diameters behind the face and that significant long-term deformations (which were initially feared) did not occur [24]. The figure also shows that the shotcrete ring (which was applied at a distance of about 30 m behind the face) almost stopped the displacements.

Water inflows occurred only in the gneiss and weakly kakiritized sections of the formations, where hairline cracks allowed some water circulation. In the core boreholes small water quantities between  $<0.1$  l/s (dripping water) and 0.3 l/s were measured [20].

The main phenomenon observed in Sedrun North was squeezing [20]. Rock falls, which could also occur due to the presence of schistosity and kakiritization, hardly occurred at all.

During tunnel advance of the Sedrun section no mutual influence between the two tubes regarding deformations could be detected [20]. The reason seems to be that the two tubes were excavated almost simultaneously.



**Figure 2.8.** Vertical displacement  $u_{r,1}$  of the crown (measuring point 1 of Fig. 2.7) normalized by its value  $u_{r,1,\infty}$  far behind the face as a function of the distance to the face  $d_f$  for different monitoring stations of the NE tube, (a), large scale, (b), detail of the first 10 m of  $d_f$ .

## 2.1.5 Data Analysis

### 2.1.5.1 Convergences

Following Cantieni *et al.* [15], the present analysis of the monitoring data always takes into account the same portion of the measured displacement at each monitoring station: In order to ensure comparability among the monitoring stations, only the displacement that develops as the face moves from a distance of 5 m to a distance of 30 m ahead of the monitoring station, is considered. Cantieni *et al.* [15] decided to consider this interval because the zero readings of the monitoring stations were made at various locations, but latest 5 m behind the face (see Fig. 2.8b), while the shotcrete ring (which practically stops deformations) was applied at a distance of about 30 m from the face. Due to the choice of this interval, a certain fraction of each displacement cannot be considered for evaluation, especially in the first 5 m ahead of the monitoring station.

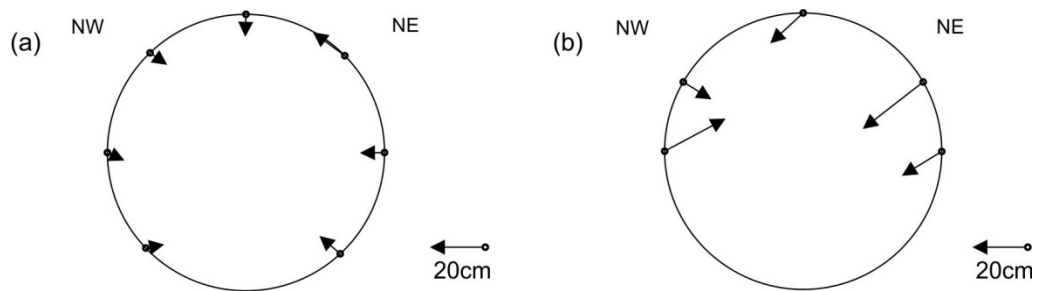


**Figure 2.9.** Distribution of the displacements over the cross-section, (a), for the NW tube, chainage 1535 m and, (b), for the NE tube, chainage 1202 m (based upon the data from [19] and [20]).

It should be noted that in general the displacements were not distributed uniformly over the cross-section (see examples of Fig. 2.9). The non-uniformity is partially due to the overall anisotropy of the rock mass (*cf.* [25]) which is based on local structural rock features such as quartz inclusions or local schistosity orientation changes.

In order to reduce these effects, the following analysis of the monitoring data considers the average values of the measuring points of each monitoring station rather than the magnitude of single displacement vectors. Hereafter an overscore (*e.g.*,  $\bar{u}$ ) is used to denote the average value of  $u$  over all the measuring points of a monitoring station.

Figure 2.10 shows the distribution along the tunnel of the magnitude of the displacement vector  $\bar{u}$ , the magnitude of the projection  $\bar{u}_c$  of the displacement vector in the cross-sectional plane of the tunnel as well as of the radial displacement  $\bar{u}_r$  (averaged over each monitoring station as mentioned above). The difference between all these displacement values is small, which indicates that the main component of the displacement vector is the radial one. In the following analysis only the average magnitude of the displacement vector in the cross-sectional plane of the tunnel  $\bar{u}_c$ , which is referred to hereafter as “the average displacement”, is considered.

For dimensional reasons, the displacements of a structure increase linearly with its size, all other parameters being constant. In the present case the excavated cross-sectional area varies from 69.4 m<sup>2</sup> to 122.3 m<sup>2</sup>. In order to eliminate the effect of opening size in the evaluation of the monitoring data, the displacements will be normalized by the radius of the relevant monitoring station (4.7 to 6.24 m).

To determine the factors influencing the convergences, only factors that are variable over the length of the examined section of the tunnel can be analysed. The monitoring stations were located mostly in tunnel sections with support classes 4.1, 4.2 and variations thereof (marked with a “+” in Table 2.3 and Fig. 2.5).

Support differences can be neglected in the evaluation of the convergences for the following reason: The deformations occur practically only during the yielding phase of the

support, *i.e.* up to the application of the shotcrete lining. The support pressure during the yielding phase is provided by the frictional resistance of the sliding connections and is very low (in relation to the initial stress) for all support classes in this section of the Gotthard Base Tunnel. Thus the differences between the support classes are small during the yielding phase. Closely spaced steel ribs, however, provide a higher safety against rock loosening. The support classes are also different with respect to the over-excavation. This difference can easily be taken into account by normalizing the displacements.

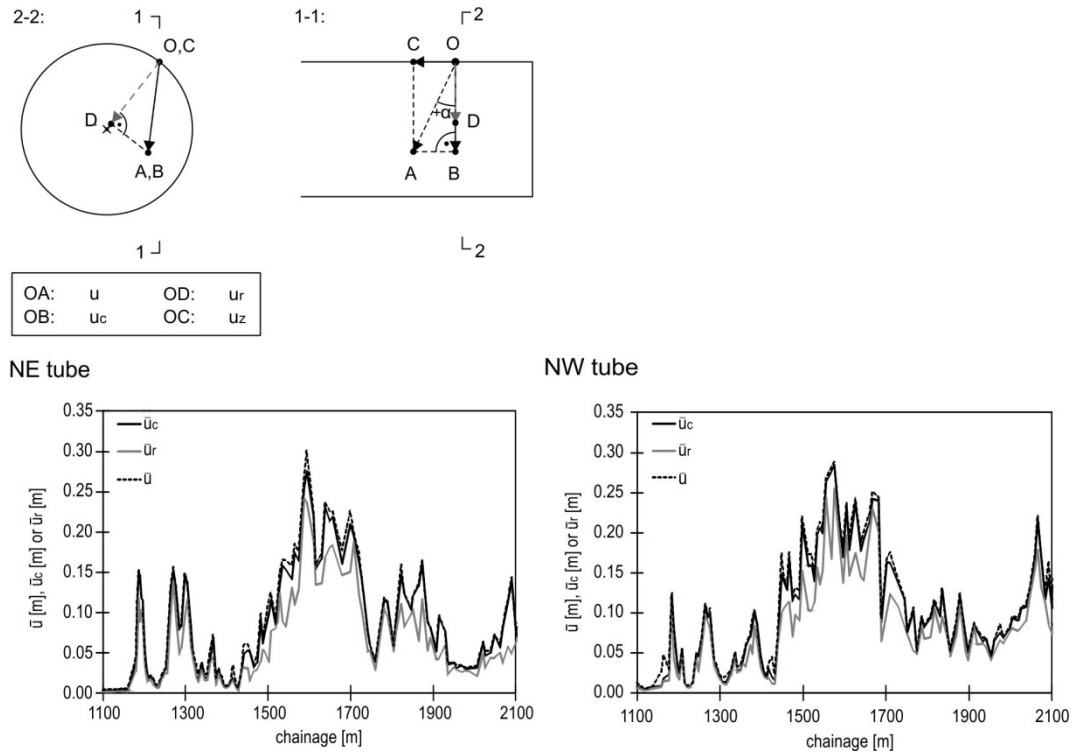


**Figure 2.10.** Definition of the displacement components and the magnitude of the displacement vector, of its projection in the cross-sectional plane and of the radial displacement along the tunnel (values averaged over every monitoring station).

As mentioned above, the tectonic units in Sedrun North consist of alternating layers of different permeability. The hard rock is often fractured and has a higher permeability than the weak rock, which was sheared and therefore consists largely of rock powder. In a saturated rock the permeability governs the rate of the deformations associated with the dissipation of excess pore pressures. Permeability variations may therefore lead to variable squeezing intensities [15]. However, the effect of pore water pressure was not considered in the data evaluation because it was not possible to measure the pore pressure in situ (the permeability of the ground was very low) and the macroscopic observations did not indicate the existence of significant differences along the considered tunnel section with respect to water.

During construction in Sedrun North it was observed that both the degree of shearing of the rock and the schistosity orientation had a strong effect on the convergences. Due to the kakiritization, the jointing and the thickness of the beds are only of secondary importance for the development of the convergences. As the degree of shearing and the lithological type are related, only the degree of shearing is used for the evaluation of the data. The following two sections therefore deal with the effects of schistosity orientation and degree of shearing.

### 2.1.5.2 Schistosity orientation

The effect of schistosity orientation on convergences is well known from the literature (e.g., [25], [26], [27]). Planes of weakness may affect rock behaviour adversely, particularly if their strike direction forms a small angle with (or is parallel to) the tunnel axis (Fig. 2.11, cases B, C and D). The anisotropy due to bedding or schistosity may also cause asymmetric deformations of the profile. The anisotropy is irrelevant if the tunnel crosses the schistosity or bedding planes perpendicularly (Fig. 2.11, case A). The orientation of the schistosity, *i.e.* its angle  $\theta_s$  to the tunnel axis as well as its dip angle  $\omega_s$  are thus potentially important factors for the deformations.

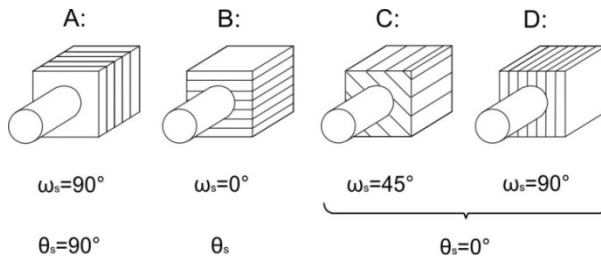


**Figure 2.11.** Typical cases of schistosity dip angle  $\omega_s$  and the angle  $\theta_s$  between strike direction and tunnel axis.

In the present case, the angles  $\theta_s$  and  $\omega_s$  have been determined at all monitoring stations based upon the geological mappings (e.g., Fig. 2.2a) of Guntli and Weber [20]. Local folding, as in Figure 2.2b, was not taken into account. Figure 2.12 shows the average displacements as a function of the dip  $\omega_s$  and of the orientation of the schistosity to the tunnel axis  $\theta_s$ . In order to eliminate the effects of other factors (lithology, degree of shearing, etc.), Figure 2.12 includes only the data from monitoring stations in rock with a degree of shearing  $F$  of 4. Figure 2.12 illustrates clearly that a small dip angle or a small angle between the schistosity strike direction and the tunnel axis is associated with larger deformations (*cf.* cases B to D in Fig. 2.11), while a large dip angle and a large angle between the strike direction and the tunnel axis leads to smaller deformations (*cf.* case A in Fig. 2.11).

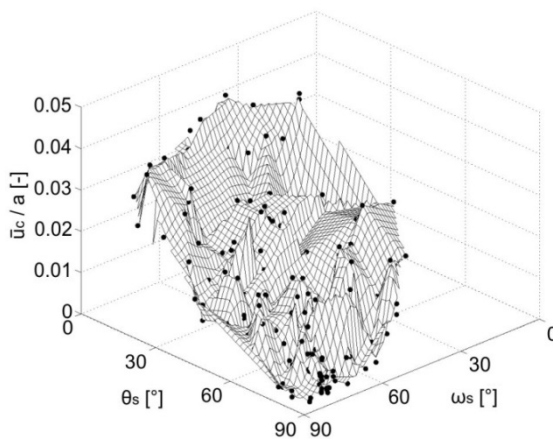


**Figure 2.12.** Average normalized displacement  $\bar{u}_c/a$  as a function of the dip angle  $\omega_s$  and the angle  $\theta_s$  between the schistosity strike direction and tunnel axis.

These two angles, which determine schistosity orientation, are important for the convergences. They can be combined to obtain a “schistosity influence factor  $S$ ”, that is defined as follows:

$$S = 1 - \frac{\omega_s}{90} \frac{\theta_s}{90} \in [0,1] . \quad (2.1)$$

The idea behind this definition is that the influence factor  $S$  is zero, if the schistosity influence disappears (*i.e.* when the schistosity planes are perpendicular to the tunnel axis), and is 1, if the schistosity influence is maximum (*i.e.* when the schistosity planes are horizontal or strike parallel to the tunnel axis). The 3D diagram in Figure 2.13 shows the schistosity influence factor  $S$  as a function of the two angles. A similarity can be recognized between the  $S$  versus  $(\theta_s, \omega_s)$  diagram (Fig. 2.13) and the measured displacement versus  $(\theta_s, \omega_s)$  diagram (Fig. 2.12).

The diagrams (c) in Figures 4 to 8 of [5] show the schistosity influence factor determined in this way along the tunnel. The diagrams also include the average displacements for the purpose of comparison. In general, the larger the schistosity influence factor  $S$ , the larger the displacements. This is particularly evident from Figure 7 of [5] (diagrams for NE tube) for a tunnel reach with a constant degree of shearing: The large variability of the convergences in this case is solely due to the change of the schistosity orientation, which is adequately expressed by the schistosity influence factor  $S$ .

The notion of the schistosity influence factor will be revisited in Section 5.1, where its theoretical background will be shown, and in Section 5.2.5, which investigates if the measured displacements can also be reproduced by means of numerical calculations.

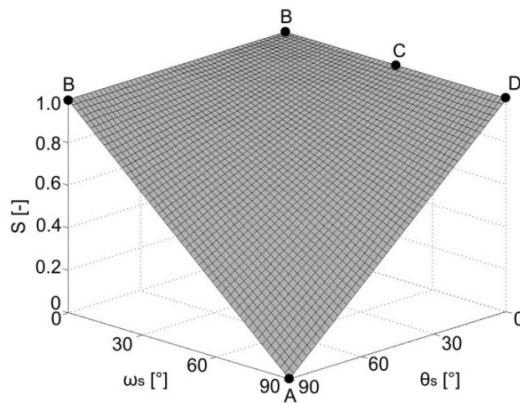


**Figure 2.13.** Schistosity influence factor  $S$  as a function of the schistosity dip angle  $\omega_s$  and the angle  $\theta_s$  between strike direction and tunnel axis (points marked by A, B, C and D: see Fig. 2.11).

### 2.1.5.3 Combined effect of schistosity orientation and shearing degree

Figures 4 to 8 of [5] indicate that besides an unfavourable orientation of the schistosity (characterized by high values of the factor  $S$ ) a higher degree of shearing also leads in general to larger displacements. The combined effect of rock shearing and schistosity orientation can be expressed by the product of the schistosity orientation factor  $S$  with the degree of shearing  $F$  (normalized by the maximum degree of shearing  $F$  of 6 in order to obtain a factor between 0 and 1):

$$I_R = S \frac{F}{6} \in [0,1]. \quad (2.2)$$

This product will hereafter be referred to as “influence factor of the rock”. Figure 2.14 shows the average displacements as a function of this factor for all monitoring stations. A linear regression model was fitted using the least squares approach with the aim of quantifying the quality of the relationship between the rock influence factor  $I_R$  and the normalized average displacements and, in the case of a satisfactory relationship, to fit an empirical equation that could be used to predict convergence. According to the regression analysis,

$$\frac{\bar{u}_c}{a} = \beta I_R, \quad (2.3)$$

in which the proportionality constant  $\beta = 0.052$ , while the R-squared coefficient of determination is 0.75 indicating an acceptable fit of the regression.

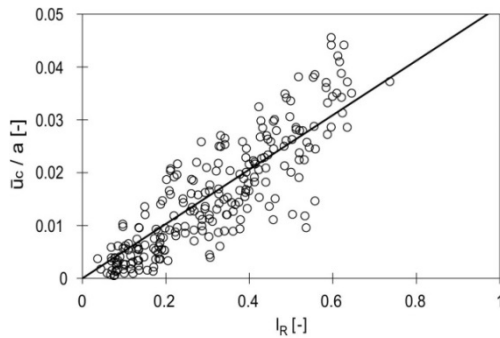


**Figure 2.14.** Normalized displacement  $\bar{u}_c/a$  as a function of the influence factor of the rock  $I_R$ .

Figure 2.15 shows the measured average displacements (dashed lines) as well as the calculated average displacements according to Equation (2.3) over the entire length of the two tubes. The average difference between measured and calculated average displacements amounts to only 2.4 cm and the standard deviation to 2.0 cm. Thus the agreement between observed and fitted data is satisfactory.

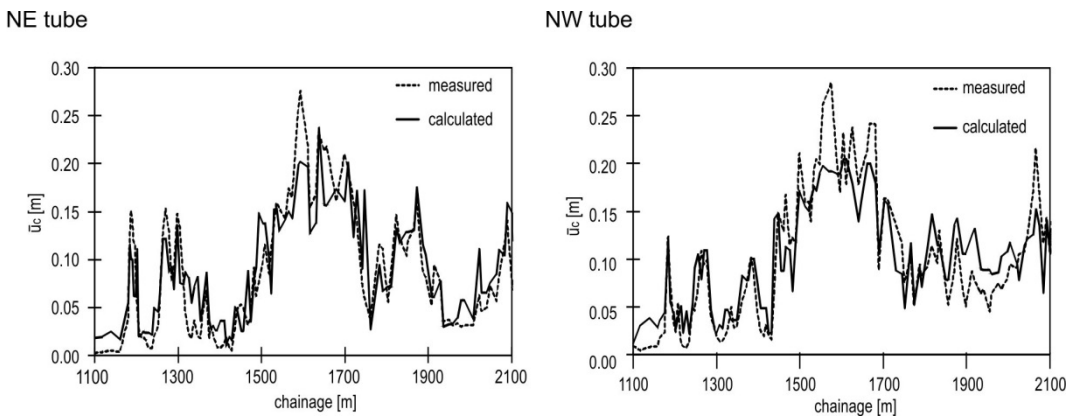


**Figure 2.15.** Calculated and measured displacement  $\bar{u}_c$  along the tunnel.

#### 2.1.5.4 Influence of adjacent weaker or stronger zones

The Sedrun North formations consist predominately of rock zones that have a degree of shearing  $F$  of 4 and are interrupted by shorter zones with more or less competent rock. Based on theoretical considerations, the deformations when tunnelling through heterogeneous ground depend not only on the quality of the ground at each specific location, but also on the quality of the ground in its vicinity [12]. More specifically, a longitudinal arching effect develops, which is favourable for the weak zones, but leads to an additional loading of the competent rock layers and therefore to higher displacements [13].

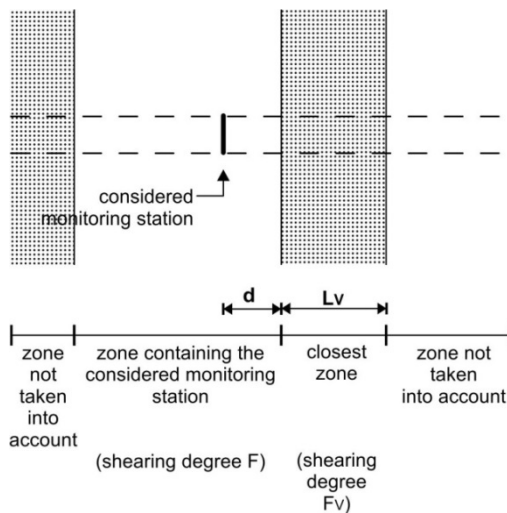
In order to check the validity of these theoretical considerations, the following “vicinity influence factor  $I_V$ ” is introduced as a measure of the effect of adjacent weaker or stronger zones:

$$I_V = \frac{F_v - F}{F} \frac{L_v}{d}, \tag{2.4}$$

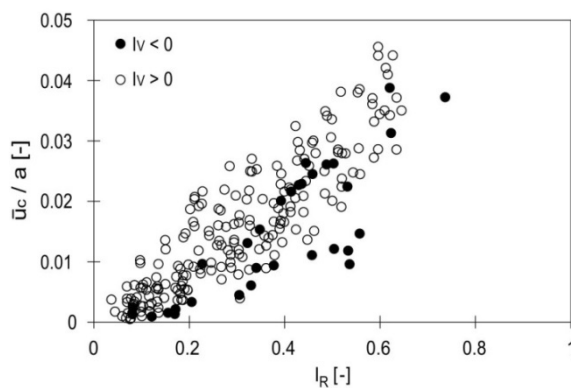
in which  $F_v$ ,  $L_v$  and  $d$  denote the degree of shearing, the thickness and the distance of the closest zone to the considered monitoring station (Fig. 2.16), while  $F$  is the degree of

shearing at the considered monitoring station. This definition assumes that only the closest zone has an influence (Fig. 2.16). The structure of Equation (2.4) is based on plausibility considerations: The thicker this nearby zone and the closer it is to the considered monitoring station, the higher is the absolute value of the vicinity influence factor. The quotient  $(F_v - F)/F$  represents a measure of the relative difference of the rock quality between the considered monitoring station and the nearby zone. If the nearby zone exhibits a higher degree of shearing, this quotient (and consequently also the vicinity influence factor  $l_v$ ) will be positive, otherwise they will be negative. In the first case (positive  $l_v$ ), one would expect that the convergences would be higher than without the nearby zone. In the second case (negative  $l_v$ ), one would expect that the nearby more competent zone would have a stabilizing effect (reduction of the convergence in the monitoring station).

Figure 2.17 shows the normalized displacements as a function of the influence factor of the rock  $l_R$  for negative and positive values of the vicinity influence factor  $l_v$ . The black circles apply to  $l_v < 0$ , i.e. to monitoring stations that are placed close to more competent rock zones. The black circles are located mainly at the lower part of the cluster of points, which means that the convergences at these monitoring stations are in general lower than average.



**Figure 2.16.** Longitudinal section with parameters considered in the definition of the vicinity influence factor.



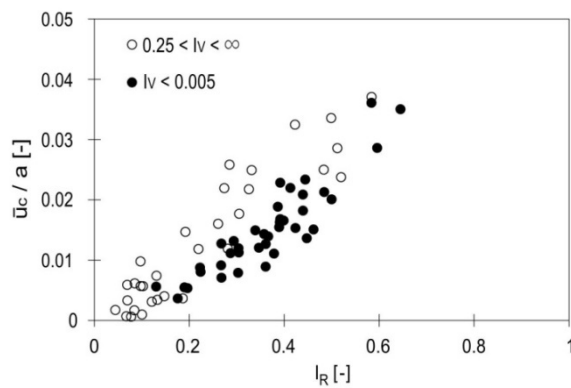
**Figure 2.17.** Normalized displacement  $\bar{u}_c/a$  as a function of the influence factor of the rock  $l_R$  for negative and positive vicinity influence factors  $l_v$ .

Figure 2.18 considers only the monitoring stations with positive vicinity influence factors, i.e. monitoring stations which are close to weaker zones. As mentioned above, one would expect in this case that the nearby weak zone has an unfavourable effect, i.e. it leads to higher convergences; the higher the vicinity influence factor, the more pronounced this

effect should be. In fact, the data shows just this tendency: The white circles, which correspond to higher vicinity factors, are located in the upper region of the cluster of points.

In conclusion, Figures 2.17 and 2.18 support qualitatively the hypothesis that weaker or stronger zones in the vicinity have a significant effect on convergence at a specific monitoring station. Nevertheless, the large scatter does not allow one to formulate a reasonable quantitative relationship. A consideration of the schistosity in the closest zone might lead to better results, but was not considered in this chapter due to the difficulty of defining the zone boundaries when considering the schistosity. For these reasons, the empirical equation (2.3) was not developed further. As can be seen from Figure 2.15, Equation (2.3), which considers the degree of shearing and the orientation of the schistosity at each specific location, still provides a reasonably good approximation of the convergences.

A point that should be borne in mind, when evaluating the monitoring results, concerns the spatial resolution of the measured displacements. According to the theoretical results of Cantieni and Anagnostou [13], the convergences may vary significantly even over very short distances (on the order of the spacing of the monitoring stations), if the geology consists of alternating layers of weak and hard rock. As a result of this variability the displacements may not be completely monitored when the distance between the monitoring stations is large; the displacements at a monitoring station may be representative only for the close vicinity of the monitoring station.



**Figure 2.18.** Normalized displacement  $\bar{u}_c/a$  as a function of the influence factor of the rock  $I_R$  for low and high positive vicinity influence factors  $I_v$ .

### 2.1.5.5 The longitudinal component of displacement

According to Steindorfer [14], the direction of the longitudinal component of the displacement vector, *i.e.* the sign of the angle  $\alpha$  (see top of Figure 2.10) changes when the tunnel face approaches a weaker or a stronger rock zone. More specifically, when the excavation approaches a “stiffer” zone the displacement vectors tend to point in the direction of excavation ( $\alpha < 0$ ). Shortly after the excavation enters the “stiffer” rock, the vector orientation shows the opposite tendency ( $\alpha > 0$ ), *i.e.* an increasing trend against the direction of excavation [14]. These observations suggest that one might be able to predict the rock behaviour ahead of the tunnel face by evaluating the changes of the displacement vector orientation.

The data from Sedrun North supports, to some extent and under certain conditions, Steindorfer’s hypothesis. Figure 2.19 shows the angle  $\alpha$  of the crown displacement (*i.e.*, measuring point 1 in Fig. 2.7) and the degree of shearing  $F$  along two reaches. Only the displacements were considered that developed as the distance between the tunnel face and monitoring station increased from 5 m to 10 m (*i.e.*, one tunnel diameter). In the first reach, the displacement orientation changes correlate with the actual rock mass quality changes. In the second reach, however, the displacement vector orientation varies although the degree of shearing of the rock mass is constant. The reason for this behaviour

seems to be the schistosity orientation, which is almost constant in the first case (*cf.* Fig. 4 of [5]), but varies considerably in the second case (Figs. 7 and 8 of [5]) and influences the orientation of the displacement vectors. Therefore, longitudinal displacements alone do not permit a reliable prediction of the conditions ahead of the face.

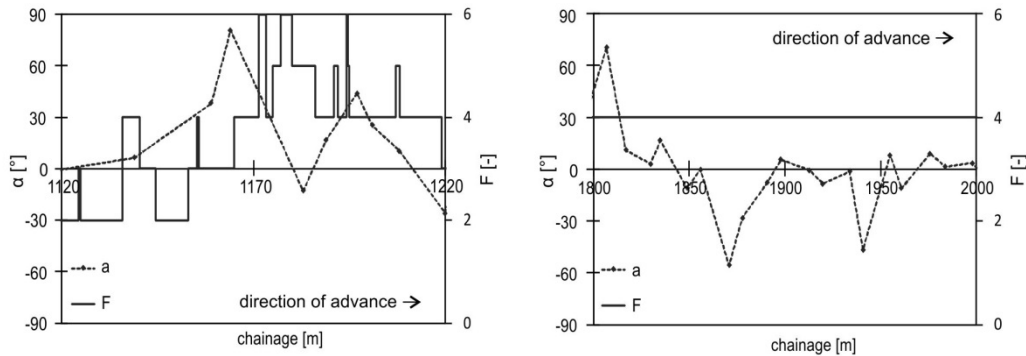


**Figure 2.19.** Angle  $\alpha$  and degree of shearing  $F$  along two reaches of the NW tube.

### 2.1.6 Predictive capacity of the empirical equation

This section investigates whether the empirical equation (2.3) derived in the last section could be used to predict the convergences. As mentioned above, Eq. (2.3) accounts for the degree of shearing and the schistosity orientation. It is clear that this equation can be used for predictions only if all other possible influence factors, which were not considered for developing this equation, are identical.

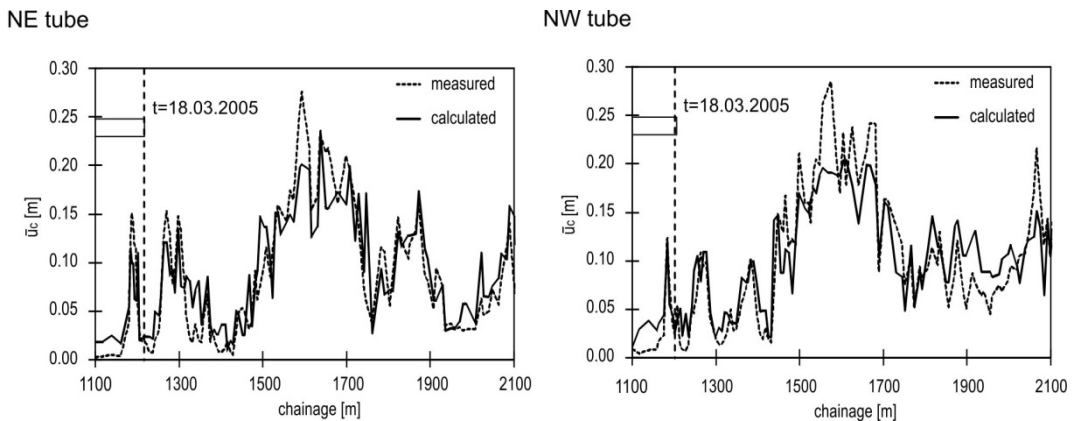


**Figure 2.20.** Displacement prediction for Sedrun North by means of the empirical equation (2.3), calibrated based upon the monitoring data from the first 100 tunnel metres.

Furthermore, the use of Equation (2.3) presupposes that the input parameters (degree of shearing and the schistosity orientation) can be identified in advance. This information can be obtained by means of advance probing. In fact, during the construction of the Gotthard Base Tunnel the degree of kikirization was estimated by means of the optical inspection of the cores (*cf.*, *e.g.*, Figure 2.6). An optical borehole scanner can be used to detect the structures at the borehole walls. Thereby the dip angle and the orientation of the schistosity relative to the tunnel axis can be determined with an accuracy of about half a degree. The only difficulty could be the estimation of the orientation of the schistosity in the case of an intense orientation variation in the cross-section. The optical borehole scanner can only be used if the borehole is sufficiently stable. Otherwise, the determination of the orientation of the schistosity is obtained from borehole findings and the orientation of the drill axis of the boring connected with a reorientation during excavation.

Finally, the use of Equation (2.3) presupposes calibration of this equation on the basis of project-specific information. For this purpose two tests were carried out.

In the first test, Equation (2.3) was calibrated based on the observations made up to the 18th of March 2005, *i.e.* during the first 100 m of advance in Sedrun North, and used the calibrated equation in order to predict the deformations in the remaining part of Sedrun North. The calibration over the first 100 m gave a correlation factor  $\beta$  of 0.051, which is almost equal to the correlation factor for the entire data set (0.052, see Section 2.1.5.3). As a result, the predicted convergence agrees well with the measured values (Fig. 2.20), which means that such an empirical approach would be useful in the present case. The agreement between predicted and actual convergence would probably be poorer in reality due to the uncertainties that exist with respect to the estimation of the input values (degree of shearing, schistosity orientation) on the basis of advance core drilling.

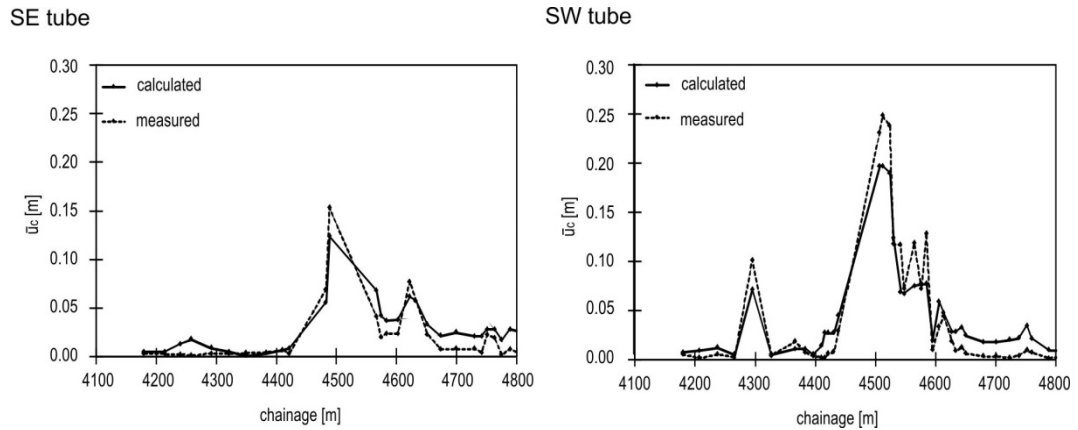


**Figure 2.21.** Displacement prediction for Sedrun South by means of the empirical equation (2.3), calibrated based upon the monitoring data from Sedrun North.

In the second test, the convergences in Sedrun South (Fig. 2.12) are predicted by using Equation (2.3). The only difference between Sedrun North and South is the overburden, which is about twice as large in Sedrun South (1650 m compared to about 800 m in Sedrun North). For the prediction of the displacements in Sedrun South Equation (2.3) was calibrated based upon the data from Sedrun North and applied the calibrated equation to predict the convergences in Sedrun South (Fig. 2.12). The difference in overburden is not taken into account. Figure 2.21 shows the predicted and the actual displacement. Their average and maximum difference amount to 1.5 cm and 5 cm, respectively. The comparison with Figure 2.21 shows that the empirical equation from Sedrun North slightly underestimates the convergence, particularly in the weaker zones around chainage 4300 and 4500 m (perhaps due to the higher overburden). However, the equation is still reliable for estimating the order of magnitude of the convergences.

## 2.1.7 Conclusions

The case history of the Gotthard Base Tunnel shows that the frequently observed phenomenon of squeezing variability can be traced back to different degrees of shearing, different schistosity orientations and the effect of nearby weaker or stronger zones. A simple empirical equation can map the effect of shearing and schistosity reasonably well and provides, in combination with advance core drilling, reliable indications of the squeezing intensity. The longitudinal displacement of the tunnel boundary [14] or the extrusion of the core ahead of the tunnel face [15] may provide additional indications under certain conditions (constant orientation of the schistosity, no significant creep, respectively).

## 2.2 Giumello Gneiss Section of the Ceneri Base Tunnel<sup>2</sup>

### 2.2.1 Introduction

In Section 2.1, the reasons for the variability of rock deformations observed during construction in the Sedrun section of the Gotthard Base Tunnel, where heavy squeezing conditions were encountered, were investigated. It was shown that the variability of the squeezing intensity along the tunnel could be traced back to a variable degree of tectonic shearing, variable schistosity orientation with respect to the tunnel axis and the effect of nearby weaker or stronger zones.

The present section analyses data from the construction of the Ceneri Base Tunnel (a 15.4 km long twin tunnel, which also belongs to the Swiss AlpTransit project) in the Giumello Gneiss formation (hereafter referred to as “GGium”), which was crossed over a length of 1000 m in the eastern tube and 600 m in the western tube. Due to the poor rock quality and the high depth of cover (about 650 m), squeezing was expected from the planning phase. The deformations in the GGium were, however, higher than those predicted at the project stage, resulting in localised damage in the shotcrete shell ([28], [29]). After a brief overview of the available data on the geology (Section 2.2.2), excavation and support (Section 2.2.3) and rock response to the tunnelling (Section 2.2.4), an attempt is made to find empirical correlations between rock structure and observed deformations (Section 2.2.5). In contrast to the Sedrun section of the Gotthard Base Tunnel, where the alignment crossed the tectonic units almost perpendicularly, in the GGium formation the schistosity and fault zones lay parallel to the tunnel axis (a so-called “parallelismo zone”). Squeezing phenomena were therefore less variable along the tunnel. Nevertheless, squeezing was characterised by a very non-uniform deformation of the tunnel cross-section. As rock anisotropy is known to lead to non-uniformly distributed deformations of the profile (*cf.*, *e.g.*, [26], [25], [30], [27] and Chapter 4 of the present research project), particular attention is paid here to the examination of the influence of schistosity on the convergences.

### 2.2.2 Geology

The Ceneri Base Tunnel is situated in the crystalline bedrock of the Southern Alps [29]. The GGium is heterogeneous, consisting of different geological rock layers [28]. Although the rock formations have retained their original pre-alpine structure, they were affected by the orogeny, thus forming disturbed areas of cataclastic and kakiritic fault zones [31]. The GGium consists of gneisses with a high content of mesocratic schist (comprising 40 to 60% biotite). The rocks also contain quartz veins a few centimetres thick and calcium silicates on a scale of decimetres [32]. During advance, the rock was classified lithologically as follows: Gneisses (with a high content of schist) with medium grains; gneisses (with a high content of schist) with medium to fine grains; mica-schists with medium grains; and mica-schists with medium to fine grains (with the rock quality decreasing from the first to the last-mentioned lithological type, [32]).

Discontinuities in the rock were recorded with respect to schistosity, jointing and fault zones (Fig. 2.22). The fault zones were 5 to 100 cm thick and ran subparallel to the direction of excavation [29]. The fault gouge generally exhibited a low cohesion [32]. The fault zones were classified according to their degree of shearing into the following project-specific classes: a degree of shearing  $Z$  of 1 denotes a superficial, slight shear zone; 2 mylonites; 3 a cataclastic fault zone; 4 a cataclastic-kakiritic fault zone; and 5 a kakiritic fault zone. Kakirites are intensively sheared rocks.

The main element in the anisotropy of the rock mass was the schistosity. Due to the direction of advance (ca.  $194^\circ$ ), the schistosity planes (oriented in E-ESE) lay parallel to

<sup>2</sup> This chapter has been published in: Mezger, F., Anagnostou, G. (2015). On the non-uniformity of squeezing deformations in the Ceneri Base Tunnel. Schubert, W. & Kluckner, A. (Eds.), ISRM Regional Symposium EUROCK 2015 & 64th Geomechanics Colloquium, Salzburg, Oesterreich, pp. 113-118.

the tunnel axis with variable dip ([32], Fig. 2.22). The schistosity was apparent even in the fault zones, but tended to be locally distorted in the vicinity. The major part of the GGium was classified with respect to the thickness of the schist beds as “laminated” (0.5 – 5 cm) or “thinly bedded” (5 – 15 cm, [32]). Due to the small thickness of the beds compared to the tunnel size, bed thickness had no observable influence on the convergences. The rock mass was only weakly jointed. Consequently, the jointing is deemed to be of only minor importance compared to the fault zones and the schistosity. No water inflows occurred [32].

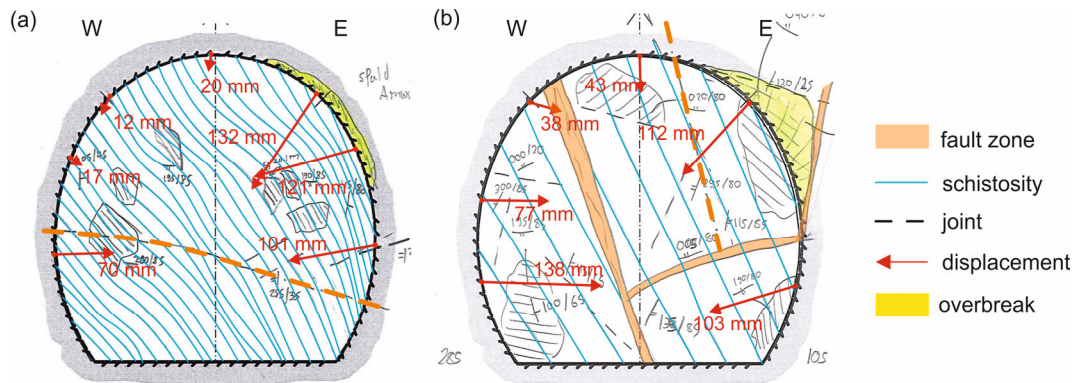


**Figure 2.22.** Examples of geological mappings of the tunnel face showing traces of the schistosity planes and fault zones and measured displacements (see Section 2.2.5, after [32]): (a), NE tube, chainage 668; (b), NE tube, chainage 614.

### 2.2.3 Construction method

For the excavation of the Ceneri Base Tunnel, a total of ten support classes (abbreviated to SPV) were developed. In the GGium only SPVs 3 to 6 were applied. SPV 3 and 4 consist of radial bolts and fibre-reinforced shotcrete and have no invert arch; SPV 5 and 6 have an invert arch, radial and face bolts, mesh or fibre-reinforced shotcrete and steel sets (Fig. 2.23, [29]). SPV 3 and SPV 5 differ from SPV 4 and SPV 6, respectively, only in the bolt length and spacing [32]. SPV 3 contains 4 m long bolts spaced at 1 m x 1.5 m; SPV 4 also has longer bolts (up to 6 m) spaced at 1.2 m x 1.2 m ([32], [33]).

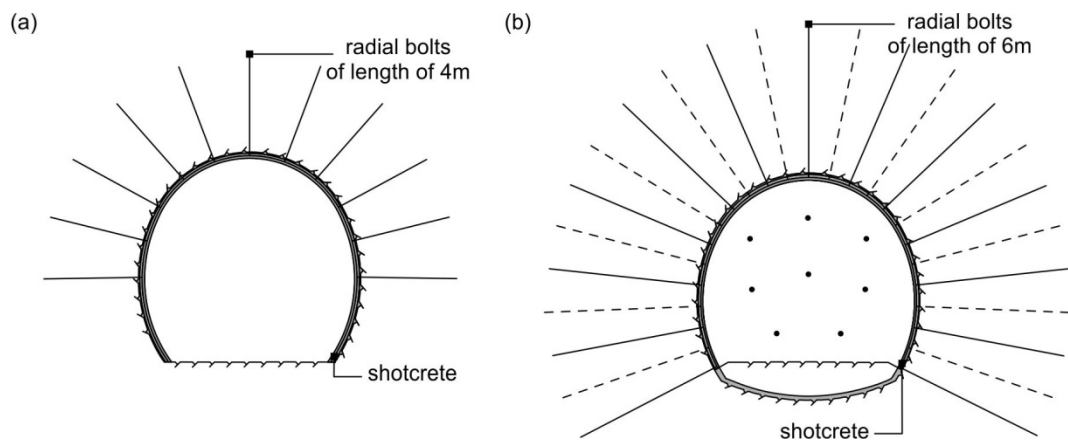


**Figure 2.23.** Cross-section and longitudinal section of the support classes (after [32]): (a), SPV 3; (b), SPV 6.

The centreline distance of the two tubes is equal to 40 m. The tubes were excavated asynchronously. The NW tube was excavated first. No mutual influence was observed between the two tubes [32].

## 2.2.4 Rock response to tunnelling

The behaviour of the rock mass and the tunnel support was monitored by 3D optical measurements [32]. In the GGium, 46 monitoring stations were installed, spaced at 2 - 110 m and each containing up to 7 measuring points (*i.e.* about 240 measuring points in total). The deformations reached values of up to 40 cm. During excavation through the GGium, the rock response was found to be clearly affected by the faults and shear zones and by the schistosity, so that the displacements were distributed non-uniformly over the cross-section (Fig. 2.22, [29]). Due to the discontinuities, loosening and rock falls also occurred, mostly in the eastern part of the tunnel roof (overbreak in Fig. 2.22) immediately after blasting above the unsupported span.

## 2.2.5 Data analysis

In the following, the magnitude of the projection of the displacement vector is considered in the cross-sectional plane of the tunnel at every measuring point (and hereafter referred to as “the displacement”). Measuring points lying in the intersection of the tunnel and the cross-passages are not taken into account as they are influenced by the complex geometry of the excavation. In order to ensure comparability between the measuring points, the same portion of the displacement measured at each measurement point (more specifically, the difference between the final displacement and the displacement that develops when the face is located 5 m ahead of the measuring point) is considered. For dimensional reasons, the displacements in a structure increase linearly with its size, all other parameters being constant. In this section of the Ceneri Base tunnel, the excavated width  $b$  of the tunnel is 9.06 - 9.36 m. In order to eliminate this effect, the displacements are normalised by  $b/2$ .

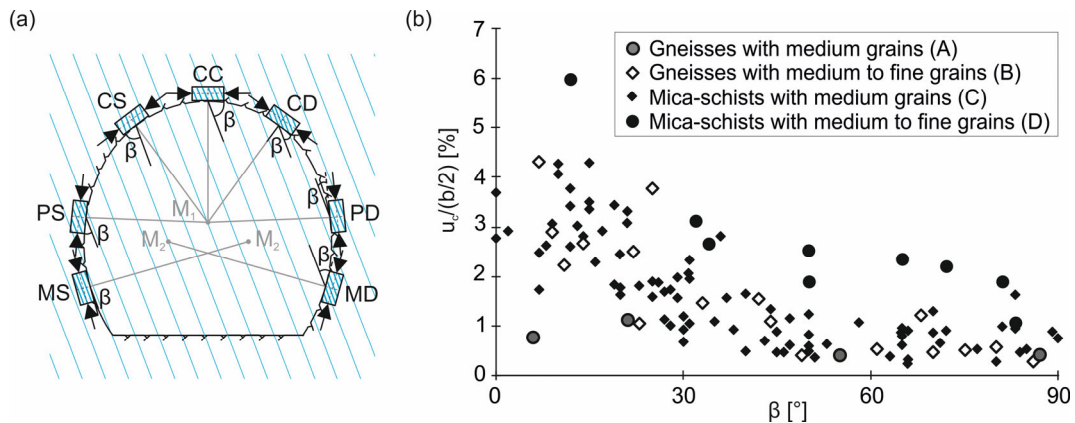


**Figure 2.24.** (a) Typical cases of the schistosity angle  $\beta$  in the cross-sectional plane of the tunnel; (b), normalised displacement  $u_c/(b/2)$  as a function of the schistosity angle  $\beta$  (data only from the support classes SPV 3 and 4 and measuring points not lying inside a fault zone).

In order to investigate the effect of schistosity orientation, the angle  $\beta$  is considered between the direction of the maximum principal stress (*i.e.* the tangential stress at the excavation boundary) and the schistosity planes (hereafter referred to as “the schistosity angle”, Fig. 2.24a). Figure 2.24b shows the normalised displacement as a function of the schistosity angle  $\beta$  for different lithological types. In order to eliminate the effects of other factors (support class and fault zones), Figure 2.24b includes only the data from measuring stations with support classes SPV 3 and 4 (no invert arch) and measuring points that do not lie inside a fault zone. A distinction between SPV 3 and 4 is not necessary because the difference in support pressures is small in relation to the initial stress.

The Figure 2.24b shows that the smaller the schistosity angle  $\beta$ , the higher are the displacements (for a given lithological type). The biggest displacements occur at locations where the schistosity is almost parallel to the excavation boundary, *i.e.* to the direction of the maximum principal stress. The schistosity is consequently at least partly responsible for the non-uniformity of the deformations in the cross-section.

Nevertheless, in addition to schistosity, the lithology also has a remarkable influence on deformation (compare the lithological types A and D in Fig. 2.24b).

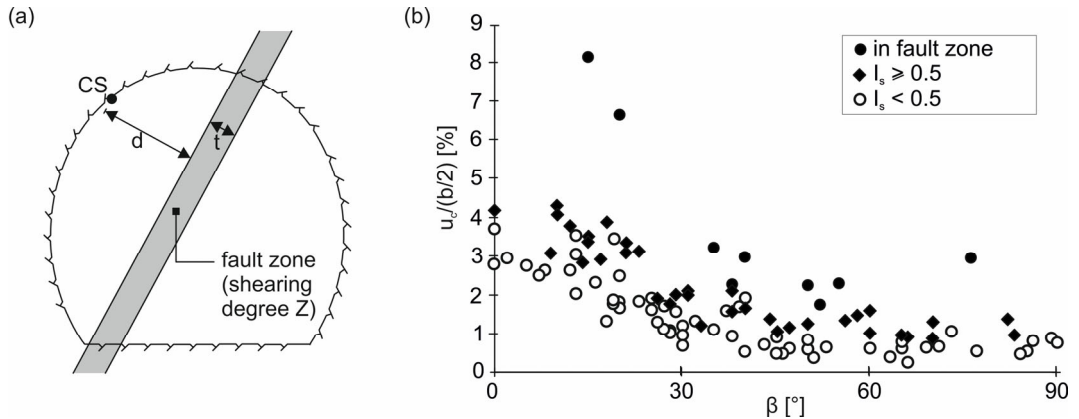


**Figure 2.25.** (a) Cross-section of the tunnel with the parameters considered for defining the influence of the fault zone; (b), normalized displacement  $u_c/(b/2)$  as a function of the schistosity angle  $\beta$  for measuring points lying in the fault zone and for measuring points with low and high factors of the fault zone  $I_s$  (data only from the support classes SPV 3 and 4 and rock consisting of Mica-schists with medium grains).

Another potential influence is associated with the heterogeneity of the rock mass. As shown in Section 2.1 based upon monitoring results from the Sedrun section of the Gotthard Base Tunnel, the excavation-induced deformations in heterogeneous ground depend not only on the quality of the ground at each specific location, but also on the quality of the ground in the vicinity of the measuring points. The closer a measuring point is to a weak zone and the weaker and thicker this zone is, the greater will be the displacement. This hypothesis can be checked empirically by considering the following factor as a measure of the effect of adjacent fault zones:

$$I_s = \frac{Z \cdot t}{d}, \quad (2.5)$$

where  $Z$ ,  $t$  and  $d$  denote the degree of shearing in the fault zone (see Section 2.2.2), the thickness of the fault zone and the distance from the measuring point to the fault zone (see Fig. 2.25a), respectively (see Section 2.1).

Figure 2.25b shows the normalised displacements as a function of the schistosity angle  $\beta$ , grouped according to the  $I_s$  factor (measuring points lying inside fault zones are marked separately). If several fault zones lie in the vicinity of a measuring point, the fault zone with the highest influence factor  $I_s$  was considered for the data evaluation. In order to eliminate other effects, only cross-sections with the same lithology (mica-schists with medium grains) and support types SPV 3 or 4 were considered. The black circles, which correspond to displacements measured at points inside fault zone, are located in the upper region of the cluster. The white circles, which correspond to small  $I_s$  factors, are located in the lower region. Higher influence factors  $I_s$  correlate with higher convergences.

## 2.2.6 Conclusions

The case history of the Ceneri Base Tunnel shows that schistosity has a considerable influence on deformation and is the main reason for the observed non-uniformity in the profile deformations. In addition to schistosity, the lithological variations and the fault zones also contributed to the non-uniformity in the deformations.

## 2.3 Carbon Section of the Lötschberg Base Tunnel

### 2.3.1 Introduction

From the viewpoint of the geology, the case histories of the Sections 2.1 and 2.2 were completely different: In contrast to the Sedrun section of the Gotthard Base Tunnel, where the alignment crossed the tectonic units almost perpendicularly, in the GGium, the schistosity and the fault zones were oriented parallel to the tunnel axis. In the Sedrun section, squeezing intensity varied remarkably along the alignment, while in the GGium, squeezing was characterised by a very non-uniform deformation of the tunnel cross-section. Nevertheless, both case histories showed that the squeezing deformations were mainly affected by the lithology, the schistosity and the effect of nearby weaker or stronger zones.

The goal of this chapter is to confirm these findings based on a third case history: the autochthon and the carbon sections of the Lötschberg Base Tunnel (LBT, Fig. 2.26), a 34.5 km long twin tunnel (whereupon the western tube only serves as rescue tunnel) of the Swiss AlpTransit project.

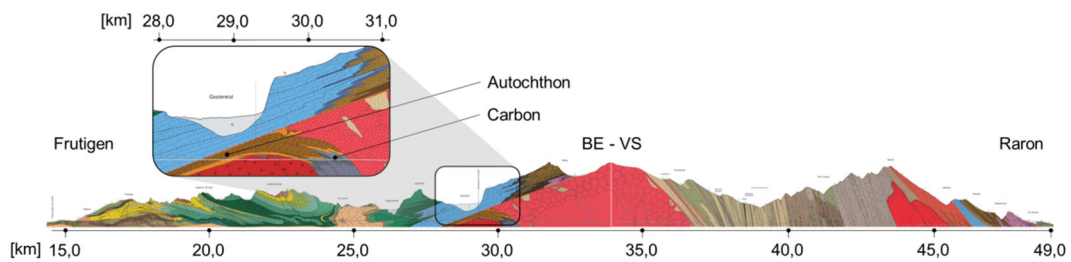


**Figure 2.26.** Longitudinal geological profile of the Lötschberg Base tunnel.

After the squeezing section of the autochthon (at about km 28'500 to km 29'150) was crossed (advance from Frutigen, see Fig. 2.26), the engineers assumed that all constructional difficulties had been overcome and that the remaining tunnel advance in the Aar massif (at a depth of cover of ca. 1400 m) would take place predominately in granite. However, in the western tube at about km 29'850, again sedimentary rocks (of the autochthon and the carbon) were encountered, which had finally a length of about 700 m. Over a length of 200 m, the schistous carbon rocks turned out to be heavily squeezing, leading to convergences of up to 70 cm. They were distributed non-uniformly over the tunnel cross-section, varied strongly along the tunnel, have led to damage to the support and necessitated considerable tunnel repairs [34]. Even after a considerable distance to the tunnel face, large long-term (time-dependent) deformations occurred. As long-term deformations could also be observed in other tunnel constructions, as for example in the Lyon-Turin Base Tunnel (*cf.* [35]), investigating the reasons for these long-term deformations is indispensable. Therefore, this chapter further examines the influence of lithology and schistosity on the long-term deformations.

The main phenomenon, which was observed during tunnel construction, was squeezing. However, it turned out that in some sections of the tunnel also swelling phenomena were noticeable. Figure 2.27 shows, on the one hand, the horizontal convergences  $\Delta u$ , which occurred in the construction phase (*i.e.*, directly after excavation until 2005) and, on the other hand, the floor deformations  $u_F$ , which were measured during the monitoring phase (*i.e.*, after the construction phase in 2006 until 2017).

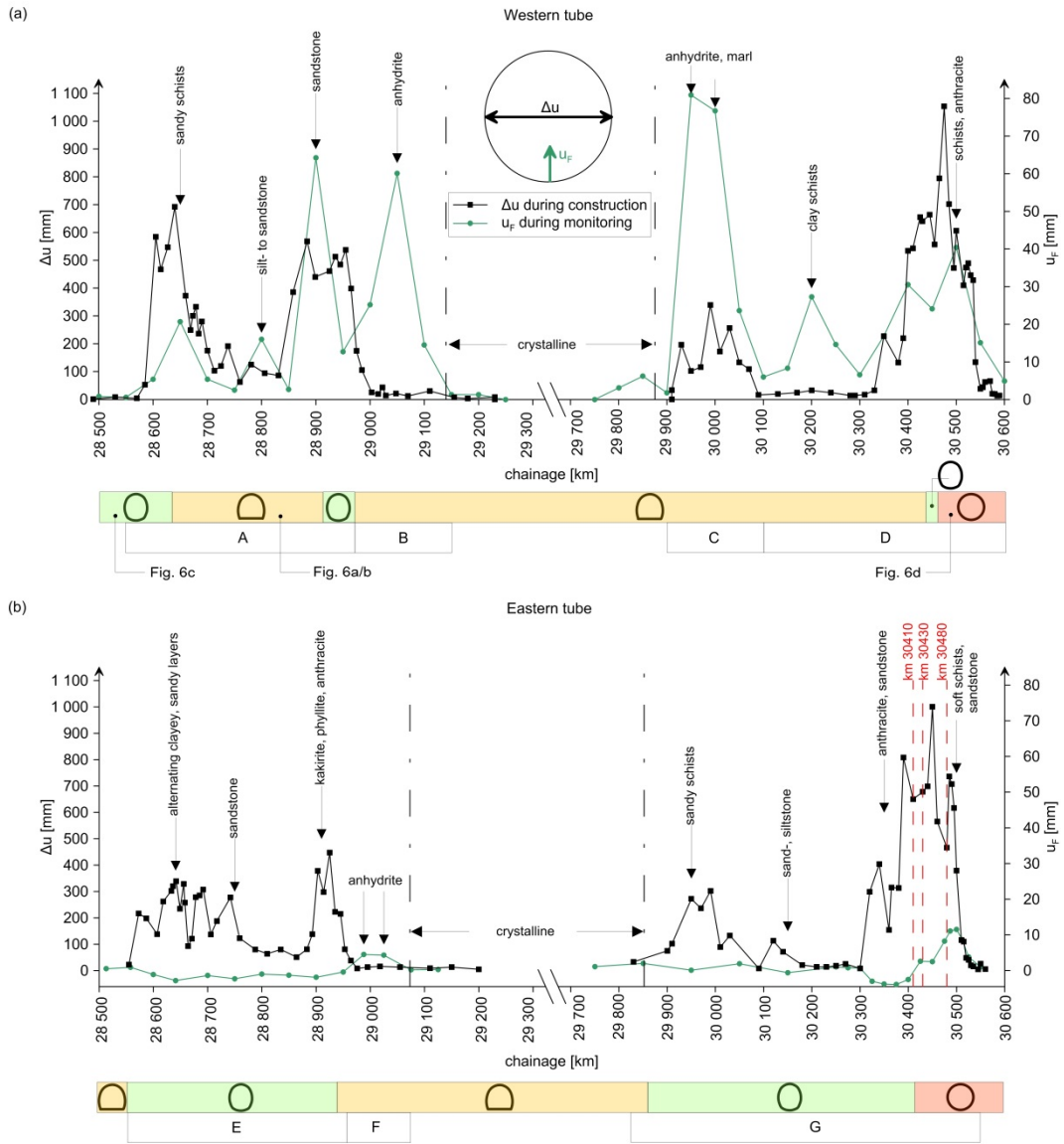


**Figure 2.27.** Horizontal convergences  $\Delta u$  (measured during tunnel construction) and floor deformations  $u_F$  (measured during monitoring phase) along the tunnel, (a), in the western tube and, (b), in the eastern tube.

In order to determine if the deformations can be traced back to squeezing or swelling phenomena, the lithology as well as the development and the location of the occurred deformations over time have to be analysed. Therefore, in Figure 2.27, besides the deformations, the lithology is also specified, as swelling phenomena may only occur in anhydritic clay stones. Furthermore, the development of the occurred deformations over time in swelling and squeezing rocks differs fundamentally (cf. Fig. 2.28): while the swelling mechanism needs time to develop over time (and may not subside even after a long time period), the squeezing deformations occur immediately after tunnelling, while their velocity decreases with time. Furthermore, in an unsealed tunnel, swelling deformations are only recognisable in the floor, while squeezing deformations occur along the whole tunnel boundary.

Figure 2.27 summarises the tunnel sections, where swelling phenomena occur (sections B, C, F): The areas closest to the crystalline formation (monitoring stations at km29'050, km29'950 and km30'000 in the western tube as well as km28'988, km29'025 in the eastern tube) show a pronounced swelling behaviour. This is particularly evident in Figure 2.27a (e.g., km29'950 in the western tube), as large portion of deformations occurs in the floor (in the tunnel reaches lying in the anhydritic clay stones; cf. Fig. 2.27a) and does not take

place immediately after tunnel construction (but needs time to develop; *cf.* Fig. 2.28). Furthermore, Figure 2.27 shows that the floor deformations in the eastern tube are rather small even in the areas closest to the crystalline formation (compared to those of the western tube), as an inner lining made of concrete was installed.

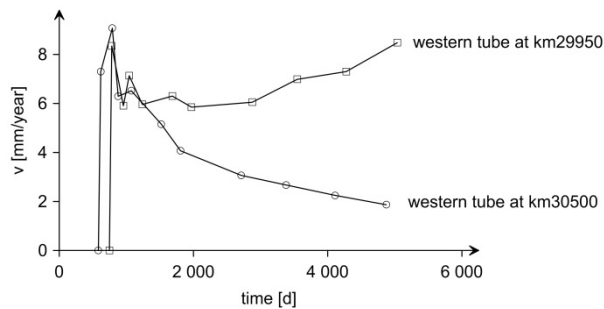


**Figure 2.28.** Floor deformation velocity for two selected monitoring stations (measured during monitoring phase).

In all the other tunnel sections, squeezing phenomena occurred (*cf.* Fig. 2.27 sections A, D, E, G). This research project will only focus on these squeezing tunnel sections. The largest deformations developed in the carbon section of the LBT between km30'350 to km30'590 in the western tube (see Fig. 2.27a) and between km30'320 to km30'545 in the eastern tube (see Fig. 2.27b).

After a brief overview of the available data on the geological units, the excavation and support method as well as rock response to tunnelling (Sections 2.3.2 to 2.3.4), an attempt is made to identify the decisive factors, which are responsible for the squeezing variability, considering, on the one hand, the short-term behaviour in Section 2.3.5 and, on the other hand, the long-term behaviour (due to creep) in Section 2.3.6.

## 2.3.2 Geology

As expected, after having crossed the autochthon section (at about km 28'500 to km 29'150), the tunnel encountered the granites belonging to the crystalline formation (at about km 29'150; *cf.* Fig. 2.27). After more than 800 m of granite were crossed, the tunnel encountered unexpectedly sedimentary rocks, which consist of the autochthon and the carbon rocks [34].

The autochthon rocks can be assigned on the one hand to the Triassic and, on the other hand, to the Dogger. The Triassic rocks consist of alternating recrystallized anhydrite and dolomite layers, which can appear in combination with schists and quartz sandstones [36]. The Dogger rocks consist of foliated and sometimes strongly graphitic sandy schists, which alternate with silt- and sandstones [36].

The carbon rocks (encountered at km 30'200 to km 30'500; *cf.* Fig. 2.27) consist of a sequence of alternating layers of sandstones, siltstones, clay slates and layers of anthracite ([34], [37], [38]). One third of the carbon rocks contains thick-bedded sand- and siltstones, while the remaining two thirds mainly consist of schistous rocks with up to 1 m thick anthracite layers ([34], [37]). The carbon rocks dip at about 30° in direction of advance [34]. The quartz sandstones (containing 40 – 60% of quartz) are hard, have medium to coarse grains and form banks of a few centimetres to metres [38]. In some parts of the tunnel, the siltstones can hardly be distinguished from the sandstones and the schists [38]. The schists consist of foliated and graphitic clay slates with organic compounds and with smoothly polished schistosity planes ([38], [39]). The up to 1 m thick anthracite layers have high clay contents and are always associated with the schists ([36], [38]). In the present chapter, the schistous rocks with high anthracite content will be referred to anthracite schists (see also [36]).

In the autochthon and the carbon sections, the schistosity dips mainly to SE (thus lying subparallel to the tunnel axis and leading to an angle  $\theta_s$  between the strike direction and the tunnel axis of ca.  $90^\circ$ , see Fig. 2.29), but can be folded locally ([36], [38]).

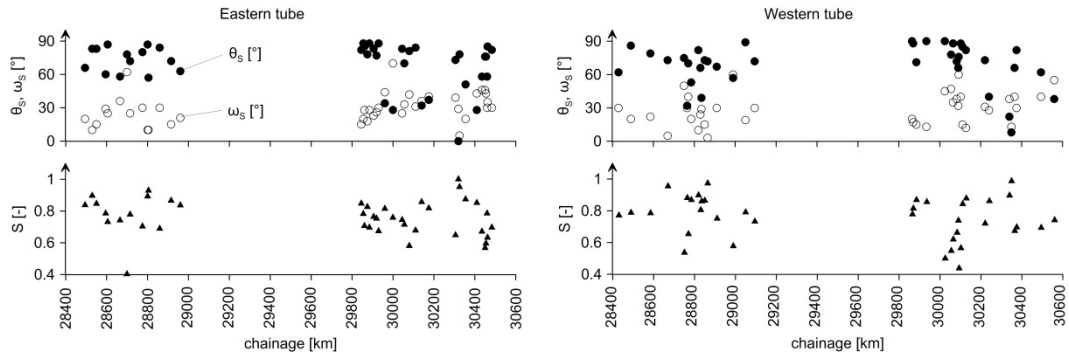


**Figure 2.29.** Distribution of dip angle  $\omega_s$  and the angle  $\theta_s$  between the strike direction of the schistosity planes and the tunnel axis, and the resulting influence factor of the schistosity  $S$  along the tunnel in the eastern and western tube, respectively.

During tunnel advance, the lithology, the schistosity and the jointing of the tunnel face were recorded (see Fig. 2.30) and then summarised in a longitudinal map (with less detailed information). As the tunnel section was already excavated in 2004 and the storing of a huge amount of data is expensive, some of the geological mappings of the tunnel face are missing. This makes the analysis of the tunnel difficult, given that the exact location of the anthracite layers or the orientation change of the schistosity are unknown in some specific measuring points.

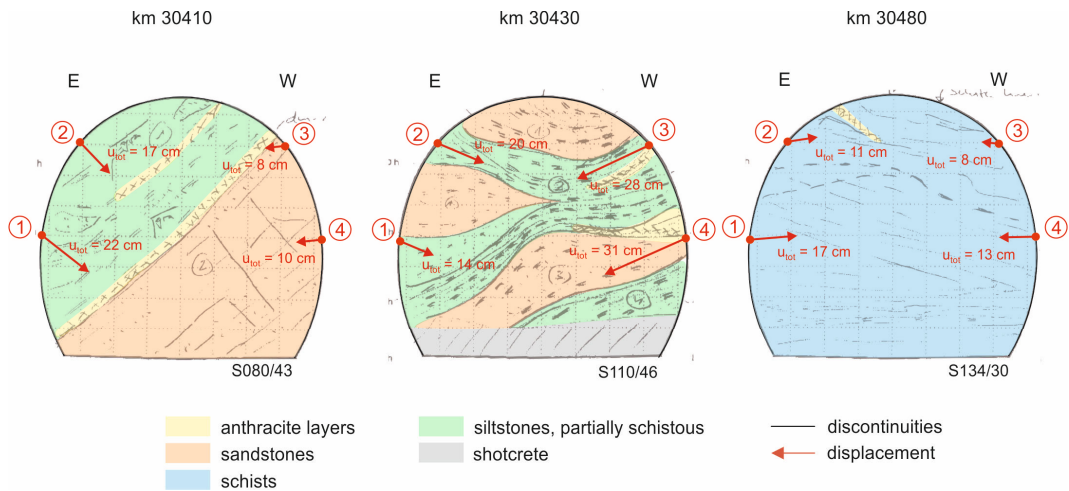


**Figure 2.30.** Examples of geological mappings of the tunnel face of the eastern tube showing the lithology, the traces of the discontinuities and measured displacements  $u_{tot}$  (after [37]).

Apart from occasional small water inflows, in the whole autochthon and carbon sections, the drive was dry ([38], [39]).

### 2.3.3 Construction Method

Squeezing conditions were anticipated for the autochthon section of the Lötschberg Base Tunnel (at about km 28'500 to km 29'150; cf. Fig. 2.27) – the design documents included an appropriate support class foreseeing an invert arch in combination with a full-face excavation and a yielding support (support class ES6A in Figs. 2.31 and 2.32). The yielding

support, which consists of sliding steel ribs and 6 longitudinal joints in the shotcrete shell, reduces the rock pressure to a manageable level [38]. With these joints, convergences of up to 1 m could be theoretically accommodated without damage to the shotcrete shell [34].

In the non-squeezing sandstones, the support class ES3 (Fig. 2.31) was installed, which was then also applied when excavating the autochthon rocks (at about km 29'850 to km 30'200; cf. Fig. 2.27). Only after the occurrence of larger convergences in the carbon section, which required tunnel repairs, the support class ES6A was again installed (from km 30'390).

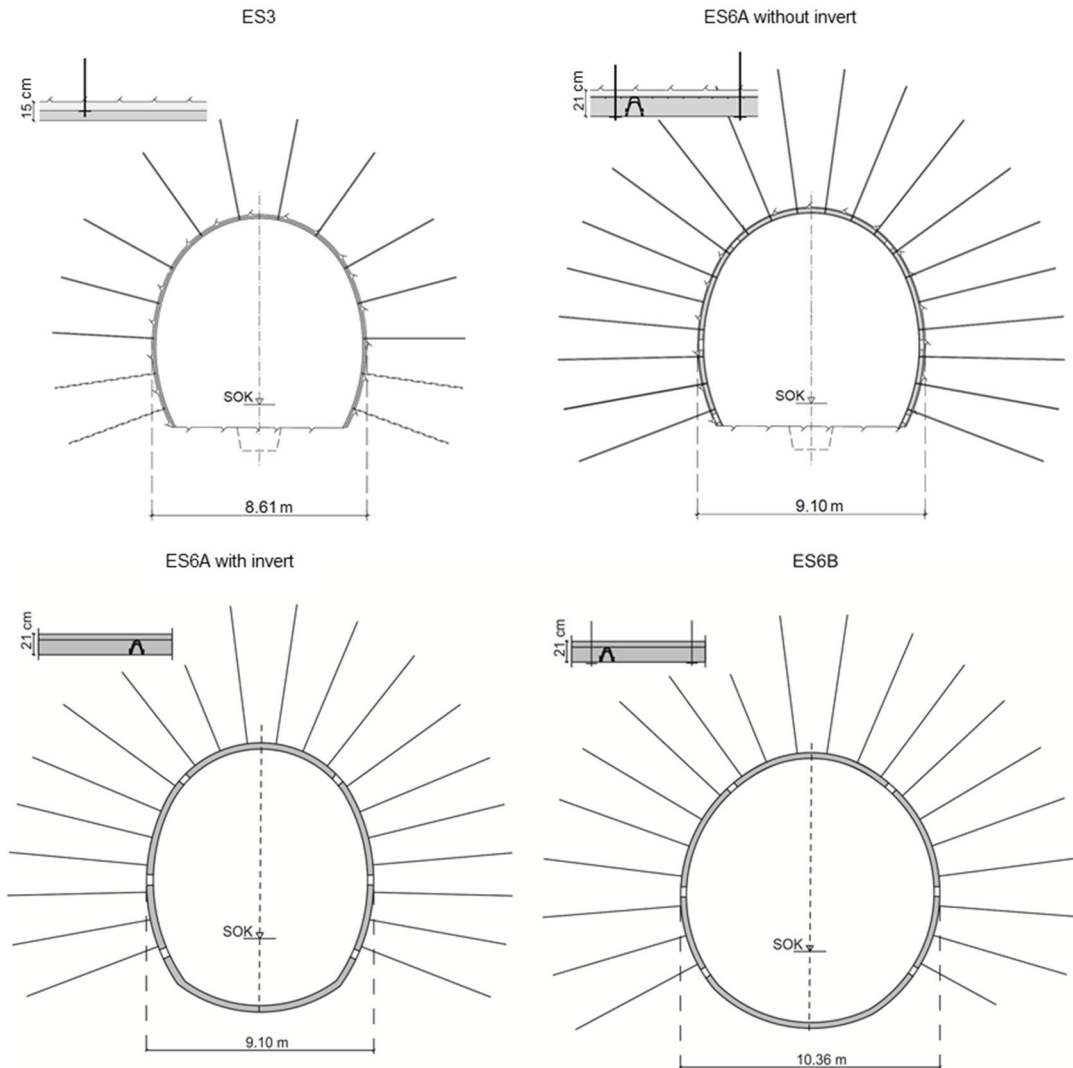


**Figure 2.31.** Support classes for squeezing conditions [34].

In the carbon section from km 30'390 to km 30'470, the support class ES6A was applied in both tubes. However, several months after excavation, the support was already damaged, so that considerable tunnel repairs became necessary [34]. As an initial measure, additional radial bolts with a length of 12 m were installed. However, this measure failed to reduce the deformation rate [34]. Therefore, a part of the carbon section had to be repaired, using the support class ES6B [34] with a nearly circular tunnel cross-section (Fig. 2.31). Furthermore, the support resistance was increased by installing compressible elements in the longitudinal joints in the shotcrete shell. In the eastern tube the so-called hiDCon elements [40] were applied, in the western tube the LSC elements [41]. During the repair works, the support pressure was reduced temporarily, leading thus to an acceleration of the convergences (see, e.g., increase in convergences  $u_{tot}$  at distance  $d_f = 53$  m of the tunnel face in Fig. 2.34c, [34]). After these tunnel repairs, the deformations stopped temporarily (during ca. 6 months), but continued to increase again in the same way, leading

once again to damage and tunnel repairs. More specifically, the ribs of the tunnel roof had to be set in a higher position, in order to guarantee the necessary clearance profile [34].

Based on these experiences, the engineers decided to apply the support class ES6B right from the start in the carbon sections from about km 30'470 to km 30'550. Class ES6B offers a 50 – 100% higher support pressure [34]. However, damage was observed in some parts of the tunnel after several months, so that tunnel repairs had to be performed again [34].

Unfortunately, the compressible elements installed in the joints did not behave as expected in some parts of the tunnel: Due to the heterogeneous rock structure, the deformations were distributed non-uniformly over the tunnel cross-section, so that some elements already reached their deformation capacity, while other elements were still uncompressed [34]. Particularly, the use of the LSC elements was not successful, as the steel cylinders tipped over and did not buckle [34].



**Figure 2.32.** Left: Support class ES6A of the Lötschberg Base Tunnel (eastern tube at km 28'759; [36]); right: buckled steel ribs (eastern tube at km 30'421; [37]).

The centreline distance of the two tubes is equal to 40 m. The tubes were excavated asynchronously, whereas the western tube was excavated first. No mutual influence was observed between the two tubes (as no increase of the convergences was observed in the western tube due to the excavation of the eastern tube, see, e.g., Fig. 2.34d).

After excavation was completed, the inner lining was installed in the eastern tube while the western tube remained in the unfinished state. In order to ensure long-term stability, tunnel repairs had to be carried out, e.g., the convergence slots were closed and additional shotcrete along the tunnel boundary was applied in the western tube.

### 2.3.4 Rock response to tunnelling

The behaviour of the rock mass and the tunnel support was monitored by 3D optical measurements and extensometers. In the investigated sections only one monitoring station was instrumented with radial extensometers [36]. However, as this monitoring station was installed at a distance of about 60 m behind the tunnel face, the extensometer data cannot be used for the purpose of this research project. The displacements of the tunnel boundary during tunnel advance were monitored optically at stations spaced at about 10 m, each usually containing 4 measuring points (cf. Fig. 2.33). The convergences reached locally about 70 cm. The displacements were clearly affected by the lithology (cf. Fig. 2.33) and the discontinuities (*i.e.*, schistosity planes), so that the displacements varied strongly both over the cross-section and along the tunnel [38]. One could clearly observe that large deformations correlated with high anthracite contents of the schists [38].

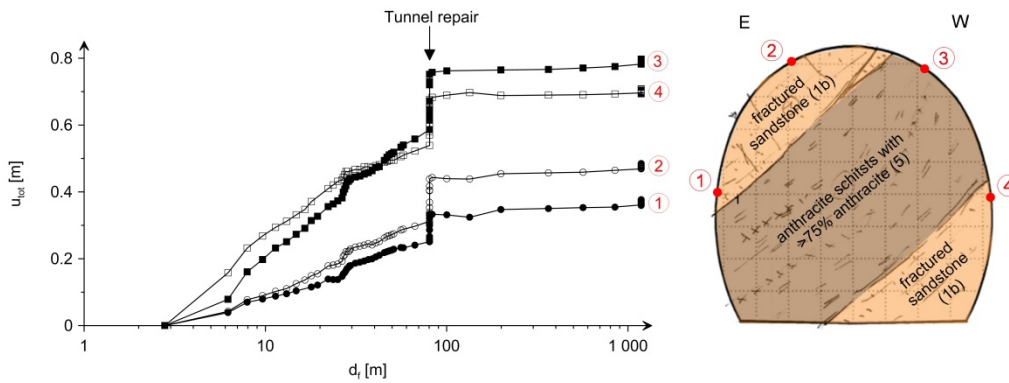


**Figure 2.33.** Measured displacements  $u_{tot}$  as a function of the distance to the face  $d_f$ , western tube at km 30'465.

According to Figure 2.33, significant long-term deformations occur, which are recognisable as the deformations continue to increase at a large distance to the tunnel face (*i.e.*, in a distance of more than 80 m), even if, in such a distance to the face, excavation has no significant influence on the deformations. Long-term deformations can either be traced back to consolidation [42] or creep processes [43]. As no water was present in the carbon section, the long-term deformations can be assigned to creep. Creep is defined as the progressive deformation of a material under a constant load, whereby creep deformations particularly occur when tunnelling through squeezing rocks (*cf.* [9]). As creep essentially occurs in tunnel sections, where the limiting shear stress is exceeded (*cf.* [9]), the major portion of creep deformations occurs behind the tunnel face. Of course, small portion of creep deformations may also occur in proximity of the tunnel face. In the following, however, for reasons of simplicity, we will speak about short-term deformations, when the creep deformations can be neglected for data analysis (as the deformations are mainly influenced by tunnel excavation), and about long-term deformations, when we consider the deformations which are additionally influenced by creep.

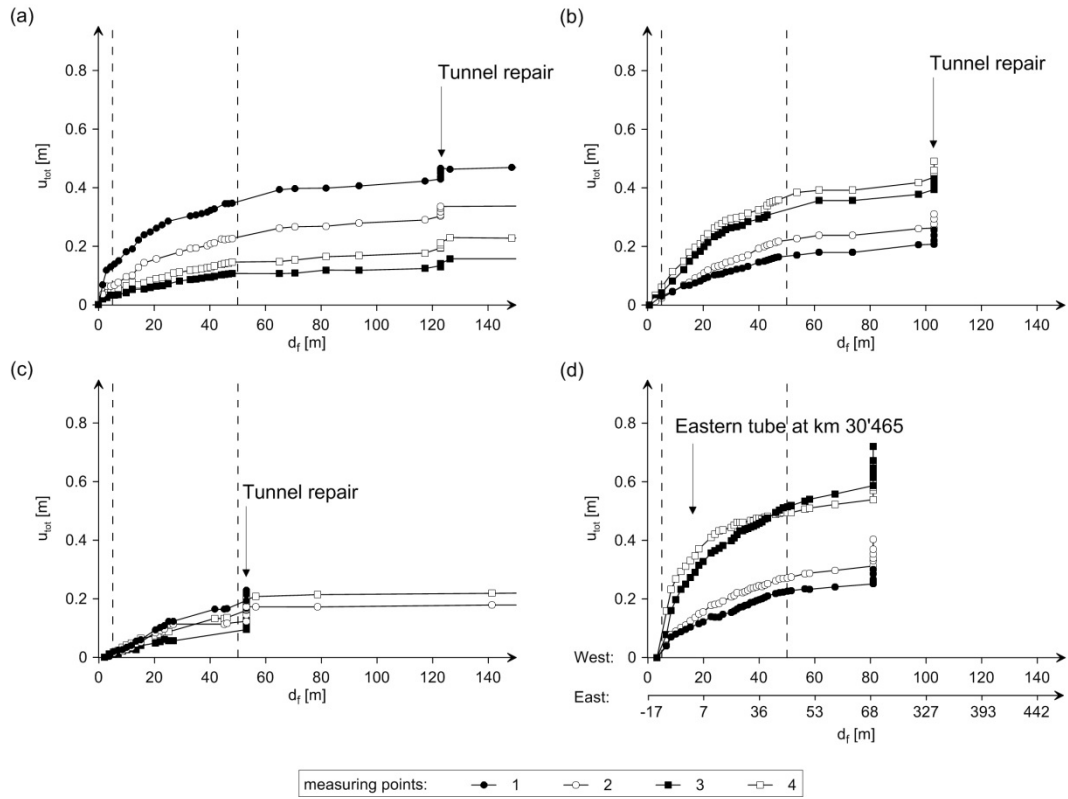
Due to the discontinuities and the anthracite layers, loosening also occurred in the tunnel roof (particularly in the unsupported span), however, the main phenomenon observed in the carbon and autochthon sections was squeezing.

### 2.3.5 Analysis of the short-term behaviour of the rock

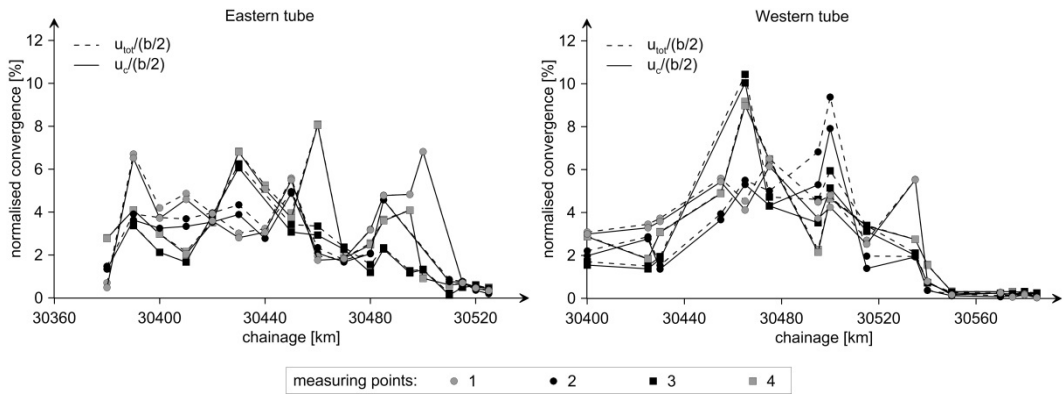
Contrary to the Sedrun Section of the Gotthard Base Tunnel (Section 2.1) and the GGium of the Ceneri Base Tunnel (Section 2.2), the zero readings of many monitoring stations were taken only 20 m behind the tunnel face. These displacement measurements could of course not be considered for the data analysis, as a big fraction of the displacement is missing: Only monitoring stations with zero readings within 6 m from the tunnel face were considered for the data analysis.

In order to ensure comparability between the measuring points, a fixed interval of the monitoring period is considered. More specifically, we consider only the displacement that develops as the face moves from a distance of 5 m to a distance of 50 m ahead of the monitoring station. We decided to consider this interval because the zero readings of the useable measuring points were usually made at maximum 5 m behind the face (see Fig. 2.34), while the tunnel repair works took place at about a distance of minimum 50 m from the face.

For dimensional reasons, the displacements in a structure increase linearly with its size, while all other parameters remain constant. In this section of the Lötschberg Base tunnel, the excavated width  $b$  of the tunnel varies from 9.10 to 10.36 m. In order to eliminate this effect, all the displacements are normalised by  $b/2$ .



**Figure 2.34.** Magnitude  $u_{tot}$  of the displacement vector as a function of the distance to the face  $d_f$  (for the positions of the measuring points in the profile: see Fig. 2.30): (a) eastern tube at km 30'410; (b) eastern tube at km 30'430; (c) eastern tube at km 30'480; (d) western tube at km 30'465.



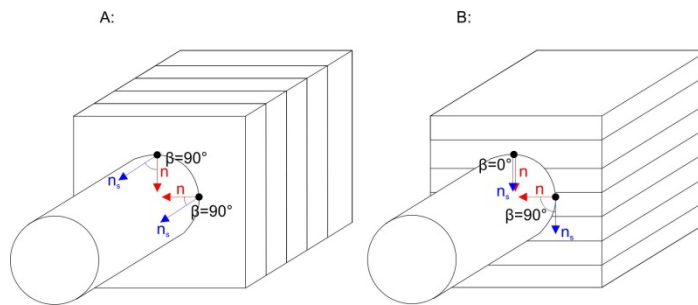
**Figure 2.35.** Normalised magnitude of the displacement vector  $u_{tot}$  and of its projection in the cross-sectional plane  $u_c$  along the tunnel.

Figure 2.35 shows the longitudinal distribution of the magnitude of the displacement vector  $u_{tot}$  and of the magnitude of the projection of the displacement vector in the cross-sectional plane of the tunnel  $u_c$  (that develops as the face moves from a distance of 5 m to a distance of 50 m ahead of the monitoring station) for the measuring points of the different monitoring stations (for the definition, see Section 2.1). The difference between these values is small (the dashed lines almost coincide with the solid lines), which means that the longitudinal displacement component is small compared to the radial and the tangential ones. Subsequently only the magnitude of the displacement vector  $u_{tot}$  will be considered.

As the tunnel does not cross the tectonic units perpendicularly, the measuring points of every monitoring station lie partially in different lithological units. In order to investigate the effect of the schistosity orientation, analogously to Section 2.2, a schistosity angle  $\beta$  is

introduced, which is defined as the angle between the normal vector of the schistosity planes and the radial direction of the tunnel (angle between  $n_s$  and  $n$  in Fig. 2.36; the normal vector of the schistosity planes for a given dip and dip direction can be determined, e.g., after [44]).

From the literature (cf. [25], [45]), it is principally known that the largest displacements occur at locations where the schistosity is almost parallel to the excavation boundary (i.e.,  $\beta \approx 0^\circ$ ; cf. Fig. 2.36), the smallest displacement where the schistosity is almost perpendicular to the excavation boundary (i.e.,  $\beta \approx 90^\circ$ ; cf. Fig. 2.36). Therefore, the smaller the schistosity angle, the higher the displacement should be (for a given lithological type and support class).



**Figure 2.36.** Schistosity angle  $\beta$  at different points of the tunnel boundary: angle between the normal vector of the schistosity planes  $n_s$  and the radial direction  $n$ .

Figure 2.37 shows the normalised displacement as a function of the schistosity angle  $\beta$  for the various lithological units and for the four support classes. An influence of the schistosity angle can be observed only for the anthracite schists for the support class ES6A with invert (Fig. 2.37). For the sand- and siltstones this influence is less pronounced. This is presumably because the sand- and siltstones are solely partly schistous [36].

Furthermore, it must be noted that the schistosity mainly dips towards SE and does not vary strongly along the alignment. As the displacements are always measured at the same location of the cross-section (see Fig. 2.30), the range of the analysed schistosity angles is limited (i.e., mainly between  $60$  and  $90^\circ$ ). Therefore, the influence of the schistosity is less visible than, e.g., in the GGium (Section 2.2). Furthermore, local schistosity changes, which might also affect the deformations, were not recorded and could not be considered in the evaluation of the data. In addition, it can be seen in Section 5.1 that, besides the schistosity angle, the dip angle of the schistosity influences the deformations, which was not taken into account in the data analysis.

The effect of the lithology on the deformations is remarkable (compare, e.g., the lithological types 1a with 5 in Fig. 2.37):

The schists (lithological type 3) and the partly schistous siltstones (lithological type 2) seem to have similar mechanical properties, given that the displacements of these two lithologies are nearly the same. However, the range of the displacements of these two lithologies is large, which results probably from the spacing and the persistence of the schistosity that were not recorded during tunnel advance. An additional source of interpretation uncertainty is that the siltstones could hardly be distinguished from the sandstones and the schists during tunnel construction (see Section 2.3.2).

The anthracite content of the schists seems to affect the convergences significantly (i.e., compare the lithological types 4 and 5). Unfortunately, the anthracite content was not recorded systematically. A more detailed data analysis is therefore not possible.

According to the Geological Group of the Löttschberg Base Tunnel [36], the lithologies in the different tunnel sections were not distinguishable. Therefore, a reduction of the convergences in the different tunnel sections can be traced back to some small extent to

the installation of the heavier support class ES6B (particularly visible for the sandstones in Fig. 2.37).

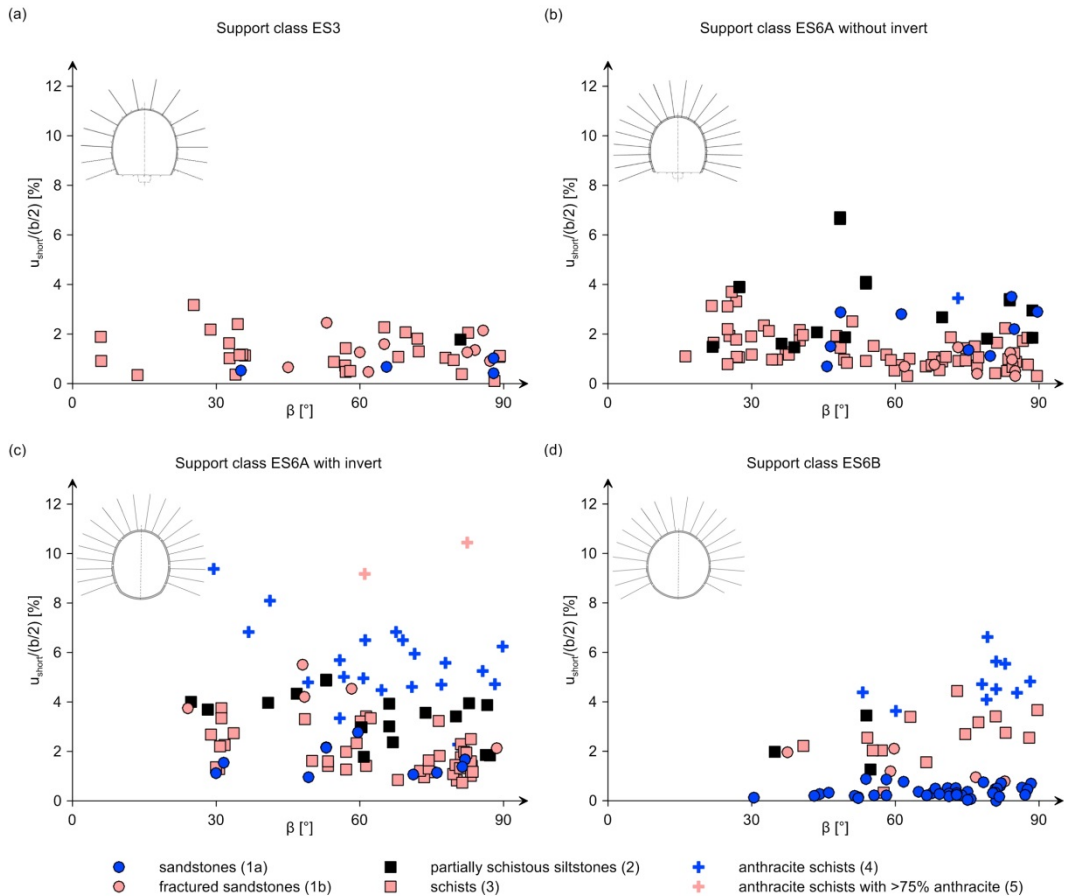


**Figure 2.37.** Normalised displacement  $u_{\text{year}}/(b/2)$  as a function of the schistosity angle  $\beta$ .

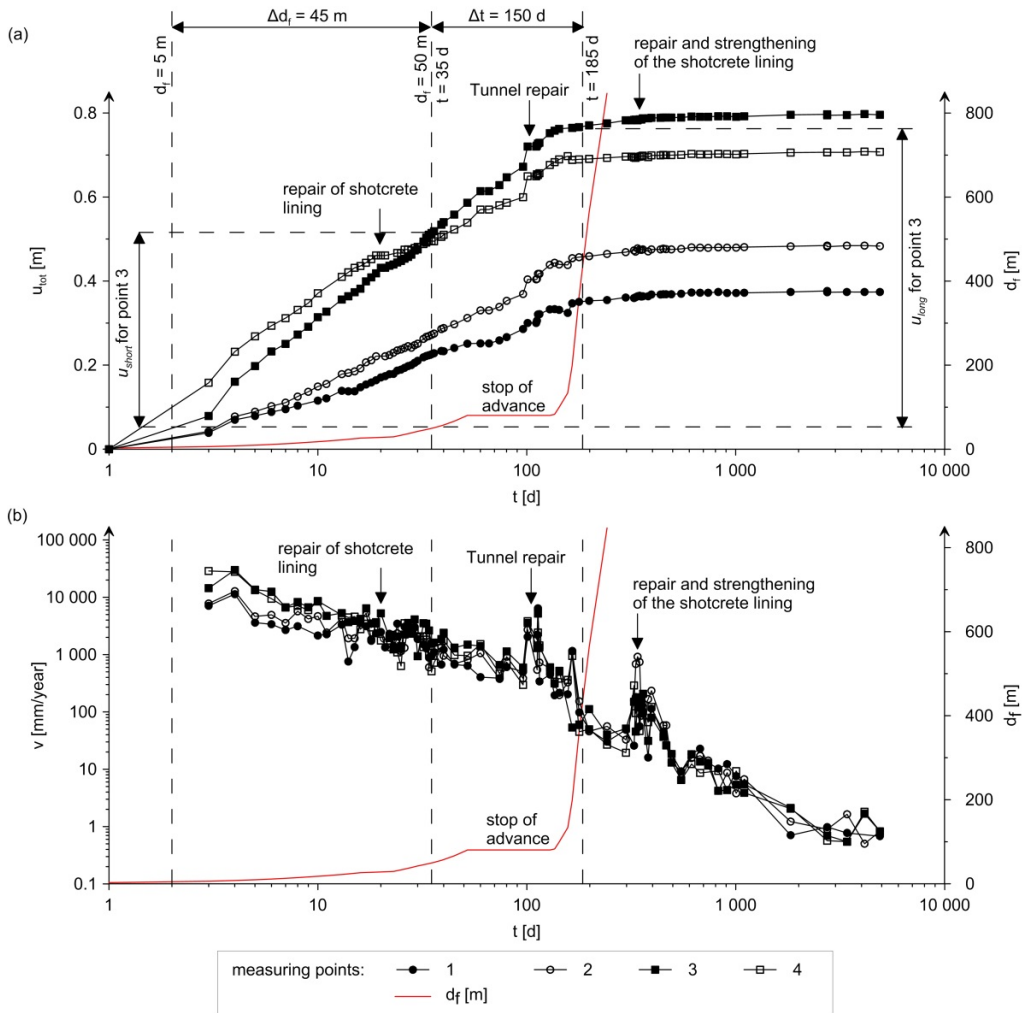
### 2.3.6 Analysis of the long-term behaviour of the rock

Figure 2.38a illustrates the typical development of the tunnel convergences in function of time. Each curve of the diagram corresponds to a different measuring point at a specific monitoring station. It is readily recognisable that large long-term deformations occur: Even a year after tunnel excavation, the convergences increased by 5 cm/year. Besides creep, also the tunnel repairs influenced the long-term squeezing deformations considerably as they led to a sudden increase in deformations (*cf.* Fig. 2.38a). Due to these tunnel repairs, new monitoring stations had to be installed, so that some portions of the displacements could not be measured; the effectively occurred deformations are thus larger than the measured deformations.

Figure 2.38b shows the development of the velocity of the displacement over time. One can readily recognise that, due to the tunnel repairs, the displacements accelerate temporarily, but then decelerate either as a result of the strengthening of the shotcrete shell or due to the occurred deformations caused by the tunnel repair itself. However, even after 13 years, the velocity of the displacements still amounts to 1 mm/year. We assume that this value can be traced back, on the one hand, due to the creep of the shotcrete shell and, on the other hand, due to measurement inaccuracies, which are in an order of magnitude of several millimetres.

In order to analyse the long-term deformations, we have to distinguish between the short- and the long-term deformations. The short-term deformations are mainly influenced by the tunnel excavation, which is not true for the long-term deformations. For the data analysis, we assume that the short-term deformations take place after tunnel excavation until a

distance of 50 m behind the face, as after this distance, the deformations increase constantly over time even though the advance stops (meaning that the excavation has no influence on the deformations). In order to ensure comparability between the monitoring stations (*cf.* Section 2.3.5), the short-term displacement  $U_{short}$  is defined as the displacement that develops as the face moves from a distance of 5 m to a distance of 50 m ahead of the monitoring station.



**Figure 2.38.** (a) Magnitude  $u_{tot}$  of the displacement vector and, (b), deformation velocity  $v$  as a function of time (for the position of the measuring points in the profile: see Fig. 2.30).

After a distance of 50 m behind the face, the deformations increase due to creep: The major portion of deformations takes place within 150 days after reaching a distance to the face of 50 m. Therefore, in the following, the long-term displacement  $U_{long}$  is defined as the difference between the displacement that develops within these 150 days (after reaching a distance to the face of 50 m) and the displacement that develops after reaching a face distance of 5 m to the monitoring station (for the definition: see Fig. 2.38a).

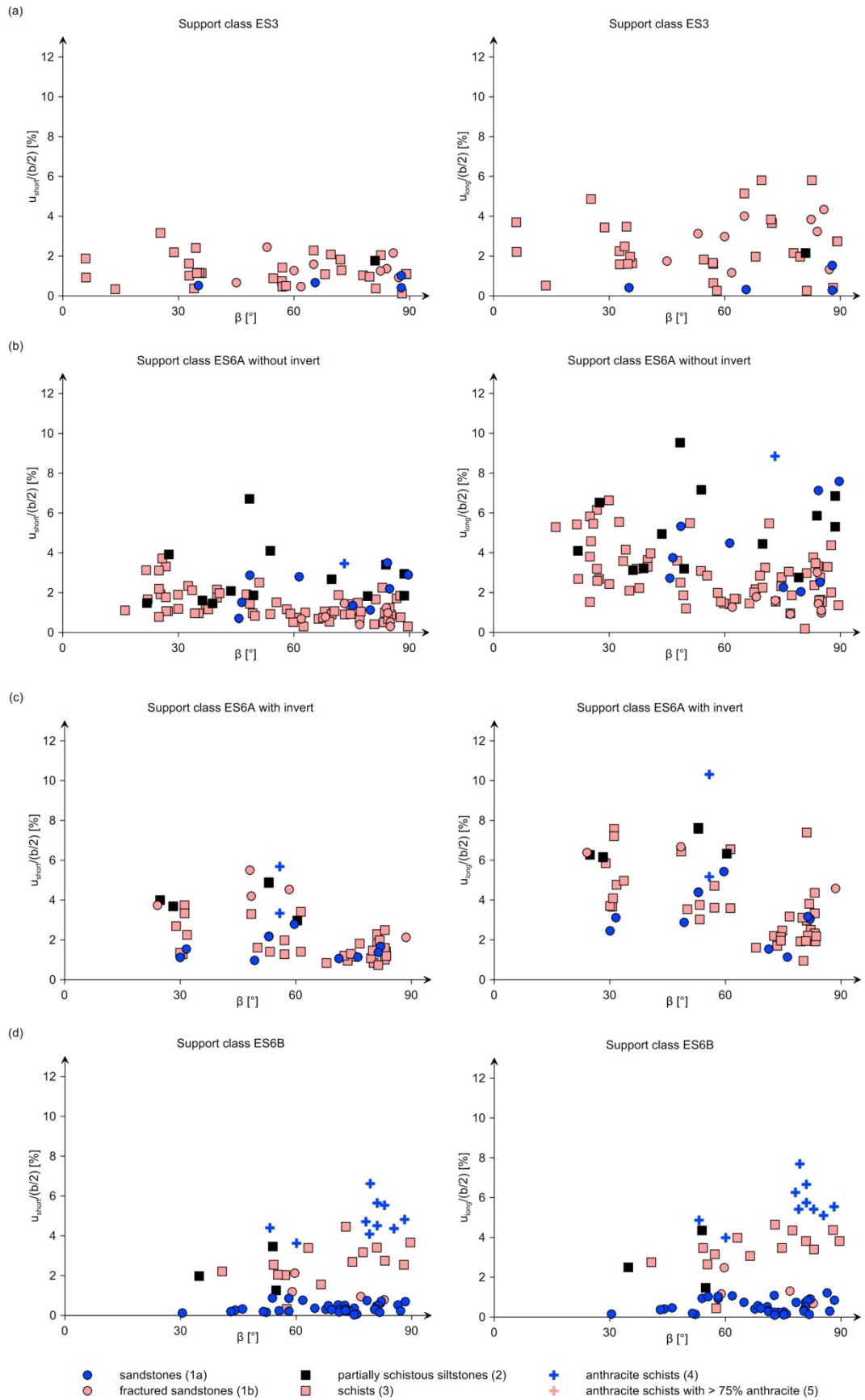


**Figure 2.39.** Normalised displacement as a function of the schistosity angle  $\beta$  for the short-term behaviour (l.h.s. diagrams) and for the long-term behaviour (r.h.s. diagrams) for the different tunnel support classes.

The l.h.s. diagrams of Figure 2.39 show the short-term deformations, while the r.h.s. diagrams show the long-term deformations as a function of the schistosity angle  $\beta$  for the four different support classes (Fig. 2.39, cf. Section 2.3.5). In order to ensure comparability between the measurements, the Figure 2.39 contains only the measuring points of the monitoring stations, which were not affected by support class changes due to tunnel repairs (*i.e.*, change of the support class ES6A to ES6B; cf. Section 2.3.3). Therefore, the l.h.s. diagrams of Figure 2.39 contain less data than the Figure 2.37.

The largest increase in deformations due to creep (difference between the l.h.s. and the r.h.s. diagrams) can be observed in the anthracites (4) and in the schists (3), while this increase is less recognisable in the partially schistous siltstones (2) and the sandstones (1a, 1b). Therefore, the lithology, which influenced the short-term deformations (see Section 2.3.5), also influences the creep deformations considerably. In fact, measuring points with larger short-term deformations also exhibit larger long-term deformations, leading thus to larger differences in deformations along the tunnel with time.

As could already be observed in Section 2.3.5 for the short-term deformations, the influence of the schistosity on the long-term deformations is not evident from Figure 2.39. Also, an influence of the support class is, contrarily to Section 2.3.5, not clearly recognisable in Figure 2.39.

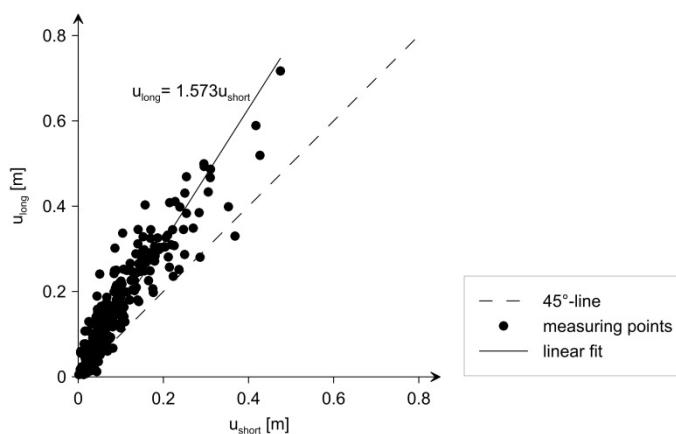


**Figure 2.40.** Long-term deformations in function of the short-term deformations.

Some of the monitoring stations were located in the vicinity of the tunnel sections, where repair works had to be carried out. Due to this, the considered long-term deformations may be influenced by the adjacent tunnel repair works, so that a certain amount of the long-term deformations may be caused by a longitudinal arching effect and not by creep.

The Figure 2.39 showed that the squeezing intensities along the tunnel are influenced by creep. This can also be confirmed with Figure 2.40, which shows the long-term deformations in function of the short-term deformations. If the measured deformations would lie on the dashed line (*i.e.*, the 45°-line), the long-term deformations would amount to the short-term deformations and thus no creep deformations would occur. As the measuring points are lying above the dashed line, the deformations are considerably influenced by creep. According to Figure 2.40, the measuring points are lying on a linear regression line (with the R-squared coefficient of determination amounting to 0.935 indicating an acceptable fit of the regression). This means that larger short-term deformation may be an indicator for the timely identification of larger long-term deformation during tunnel construction.

In conclusion, larger differences in deformations along the tunnel occur due to creep.

### **2.3.7 Conclusions**

As for the case histories of the GGium and the Sedrun section, the squeezing deformations in the carbon section were mainly affected by the lithology and partly by the schistosity. However, the correlations found in this chapter are much weaker than for the other two case histories, which is to some extent due to the quantity and quality of the data.

The long-term deformations, which are due to creep, depend linearly on the short-term deformations: Larger short-term deformations lead to larger long-term deformations. Therefore, the differences in deformations along the tunnel increase considerably in time due to creep.

### 3 Tunnelling perpendicularly to alternating weak and competent rock layers

#### 3.1 Introduction

Rock mass heterogeneity may lead – depending on the heterogeneity scale [46] – to significant variations in the squeezing intensity during tunnelling. A specific case of heterogeneous rock mass is that of frequently alternating weak and competent zones (Fig. 3.1). Theoretical considerations ([12], [13]) and field observations (*cf.* Chapter 2) show that there is a mutual influence between the weaker and the stronger rock mass components. The latter reduce the deformations of the adjacent weak rock (via shear stresses that develop along the zone interfaces), but may – due to the influence of the weak interlayers – become overstressed. The rock mass response to tunnelling depends thus on thickness, strength and deformability both of the hard and the weak zones and obviously also on their orientation relatively to the tunnel axis.

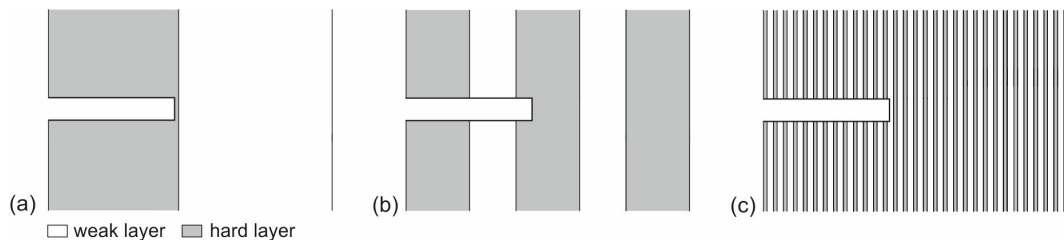


**Figure 3.1.** Tunnelling through a sequence of, (a), very thick weak and competent rock zones, (b), alternating weak and competent layers of medium thickness, (c), thinly alternating weak and competent layers.

Chapter 3 investigates the squeezing behaviour during tunnelling perpendicular to a sequence of alternating weak and hard rock layers (Fig. 3.1). Depending on the heterogeneity scale, the following three cases can be distinguished:

- If a weak formation is very thick relatively to the tunnel diameter (Fig. 3.1a), then the stabilising effect of adjacent competent rock is limited to the zone close to the formation interface and can be neglected in design.
- If, on the other hand, the alternating weak and competent rock layers are very thin relatively to the tunnel radius (Fig. 3.1c), then the deformation distribution along the tunnel axis will be practically uniform. This means that rather than modelling the individual layers, which would be demanding in terms of spatial discretisation and computation time, rock mass can be conceived as a homogeneous, but, in view of the rock structure transversely isotropic material, the mechanical behaviour of which depends on the behaviour of the individual layers and on the ratio of their thicknesses. For this special case, a closed-form solution (assuming rotational symmetry and plane strain conditions) is presented and the adequacy of a homogeneous model is investigated in Section 3.2.
- In a medium thickness weak zone (Fig. 3.1b), the excavation-induced displacements vary frequently along the tunnel. The stabilising effect of the hard interlayers can be taken into account computationally by numerical methods, whereby, due to the non-uniformity of squeezing intensity along the tunnel, the alternating weak and competent zones have to be modelled discretely ([12], [13]).

The response of the considered homogenised material to tunnelling is isotropic. This suggests that the rock mass could be considered as an isotropic and homogeneous elastoplastic material, with mechanical parameters that depend on those of the weak and hard components and on the fractions of the latter. Section 3.3 shows how the parameters of

the equivalent homogeneous and isotropic material can be determined. This is very valuable for design practice, as it makes it possible to analyse problems, which do not fulfil the conditions of rotational symmetry or plane strain, also for the case of tunnelling perpendicular to thinly alternating weak and hard layers.

Section 3.4 investigates how the heterogeneity scale (represented by the thickness of the weak layers normalised by the tunnel radius) affects the longitudinal distribution of the displacements in tunnelling perpendicularly to a sequence of weak and hard layers of finite thickness. Furthermore, this section introduces a simple equation which allows estimating the displacements in weak zones (considering the stabilising effect of the hard layers) analytically, rendering numerical modelling unnecessary at least in the preliminary design stage.

## 3.2 Closed-form solution for the ground response curve in tunnelling perpendicularly to thinly alternating weak and competent rocks

### 3.2.1 Introduction

For the formulation of appropriate constitutive models accounting for the thickness fractions and mechanical properties of the rock layers, homogenisation techniques have been proposed in the literature (e.g., [47]), initially only focussing on the linearly elastic response of the stratified rock mass (cf., e.g., [3], [48]) and later on also investigating some aspects of failure of a stratified rock mass (e.g., [49], [50], [51], [52], [53]).

Closed-form solutions exist for estimating the displacements and the stresses of tunnels excavated in transversely isotropic rocks, considering either elastic or elasto-plastic behaviour (e.g., [54], [55], [56], [57]), whereby these methods do not account explicitly for the mechanical parameters of the individual layers. At the current state of research, there is no closed-form solution that allows determining the response of a homogenised rock mass consisting of alternating weak and hard layers due to tunnelling. Such a solution would, however, be of great importance, as numerical modelling of thinly alternating rock structures is very demanding in terms of spatial discretisation and computation time.

Consequently, Mezger [11] derived analytically the ground response curve (GRC) for tunnelling perpendicularly to thinly alternating weak and hard layers, considering the rock mass as homogeneous, transversely isotropic material, assuming perfectly plastic behaviour for both rock constituents and considering additionally a brittle behaviour of the hard layers with a sudden post-failure decrease in strength (Park and Kim [58] considered only a *isotropic* elastic, brittle-plastic rock mass) and out-of-plane plastic flow of the individual layers, respectively. This solution is particularly important for practical reasons, as the numerical modelling of a narrow sequence of hard and weak rocks is very time-consuming.

The closed-form solution will be presented shortly in Section 3.2.2 (while the entire derivation can be found in [11]). However, in the Sections 3.2.3 and 3.2.4, the practical relevance of the developed closed-form solution will be discussed. Particularly, guidelines are provided, which describe:

- under which conditions it is indispensable to consider both the weak and hard layers (or, in contrary, one can disregard the hard interlayers); and
- under which conditions it is adequate to consider the stratified rock mass as a homogeneous material.

### 3.2.2 Formulation of the GRC

For the formulation of the closed-form solution, a deep, cylindrical tunnel excavated in the homogenised rock mass (the mechanical behaviour of which depends on the behaviour of

the hard and the weak layers and on the ratio of their thickness fraction  $x_h/x_w$ , where  $x_h + x_w = 1$ ) was considered. The constitutive model for the homogenised rock mass was formulated by extending the procedure of Salamon [3] for elasto-plastic behaviour of the individual layers, disregarding relative displacements at the layer interfaces. The alternating weak and hard layers are considered as linearly elastic – perfectly plastic materials obeying Mohr-Coulomb failure criterion with a non-associated flow rule. The closed-form solution enables to determine the rock deformations and stresses caused by the excavation of the tunnel at a large distance to the tunnel face, where the tunnel is supported by a uniform and radial pressure  $\sigma_a$  (see Fig. 3.2), and thus makes it possible to derive the GRC for a thinly stratified rock mass. The latter can be found in Mezger [11]. The derivation of this analytical solution was mathematically demanding, as a variety of cases regarding the failure state of the rock had to be considered (plastic and/or elastic behaviour of the weak and/or the hard layers considering a plastic flow either only in the tunnel cross-section plane or also perpendicular to it). As the assessment of the ground response of Mezger [11] is an arduous task, a Matlab-code [59] is provided as electronic supplementary material<sup>3</sup>, which makes it possible to estimate easily the GRC for given properties and thickness fractions of the weak and the hard layers:

$$u_a = \frac{\sigma_0 \cdot a}{E_w} \cdot f_{TI} \left( \frac{\sigma_a}{\sigma_0}, \frac{x_h}{x_w}, \frac{E_h}{E_w}, \frac{\sigma_{d,h}}{\sigma_{d,w}}, \frac{\sigma_{d,w}}{\sigma_0}, \nu_h, \varphi_h, \psi_h, \nu_w, \varphi_w, \psi_w \right). \quad (3.1)$$

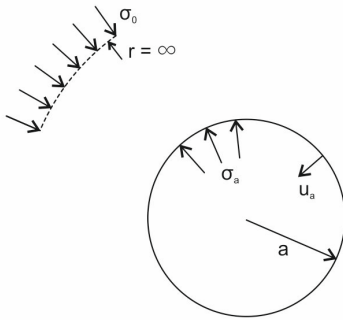


**Figure 3.2.** Problem statement for the determination of the GRC.

### 3.2.3 Relevance of hard interlayers

This section investigates under which conditions the stabilising effect of the hard layers can be disregarded. As a measure for the stabilising effect, the ratio  $u_a/u_{w,2D}$  will be considered, which can be expressed as follows:

$$\frac{u_a}{u_{w,2D}} = f \left( \frac{\sigma_a}{\sigma_0}, \frac{x_h}{x_w}, \frac{\sigma_{d,h}}{\sigma_{d,w}}, \frac{E_h}{E_w}, \frac{\sigma_{d,w}}{\sigma_0}, \nu_h, \varphi_h, \psi_h, \nu_w, \varphi_w, \psi_w \right), \quad (3.2)$$

where  $u_{w,2D}$  is the displacement that would occur in the absence of the hard layers (*i.e.*, for  $x_w = 1$ ) and can be computed using known equations (*e.g.*, those of [60]) and  $u_a$  is the displacement of the transversely isotropic material according to Equation (3.1).

Figure 3.3 shows this ratio as a function of the thickness fraction of the hard layers for an unsupported opening, for a bigger and a smaller contrast in the mechanical parameters of the layers as well as for a high and a low *in situ* stress.

The latter is considered as a borderline case where all the layers behave elastically and the reduction factor is given by the following simple equation:

<sup>3</sup> The Matlab-code can be downloaded from [www.tunnel.ethz.ch](http://www.tunnel.ethz.ch).

$$\frac{u_a}{u_{w,2D}} = \frac{\mu_w}{\mu^*} = \frac{1}{x_h \left( \frac{\mu_h}{\mu_w} - 1 \right) + 1}, \quad (3.3)$$

where  $\mu^*$  is the shear modulus of the composite material (see Eq. A-6 of [11]). One can recognise from Figure 3.3 that the hard layers have a significant stabilising effect even if their thickness fraction is as low as a few percent. For example, in the presence of 10% hard layers, the displacements decrease by a factor of 1.4 - 4 depending on the contrast in the mechanical parameters and on the *in situ* stress. In general, the higher the contrast in the mechanical parameters (see also Eq. 3.3) and the higher the *in situ* stress (and thus the squeezing potential), the more pronounced the stabilising effect will be for a given thickness fraction of the hard layers.

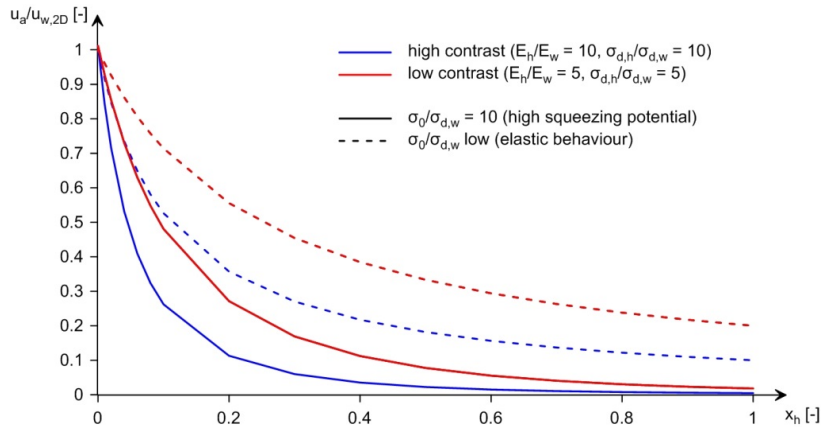


**Figure 3.3.** Ratio  $u_a/u_{w,2D}$  as a function of the thickness fraction of the hard layers (unsupported tunnel,  $\nu_h = \nu_w = 0.3$ ,  $\varphi_h = \varphi_w = 20^\circ$ ,  $\psi_h = \psi_w = 1^\circ$ ).

### 3.2.4 Remarks concerning the adequacy of the homogenised model

The displacements that occur in the case of a stratified rock mass with finite layer thicknesses  $w/a$  and  $h/a$  converge to the closed-form solution for  $w/a \rightarrow 0$  (numerical calculations and details can be found in Section 3.4). The purpose of the present section is to analyse whether the homogenisation is adequate or not for a stratified rock mass with given normalised layer thickness  $w/a$ . This depends mainly on the contrast in the mechanical parameters of the hard and weak layers:

If the mechanical parameters of the weak and of the hard layers are not very different, then the rock mass can obviously be considered as homogeneous even for very large values of the normalised thicknesses  $w/a$ . Conversely, in the case of a big contrast in the mechanical parameters, homogenisation would be adequate only for a very thinly stratified rock mass. This will be illustrated by means of additional computational results (see Fig. 3.4), which were obtained assuming a high parameter contrast.

The diagrams of Figure 3.4 show the error of the homogenised model as a function of the normalised layer thickness  $w/a$  (upper diagrams) and  $h/a$  (lower diagrams) for a series of thickness ratios  $h/w$  and for two values of the initial stress (at the lower stress of 0.75 MPa both the hard and the weak layers behave elastically for the assumed strength parameters). The error is defined as  $(u_a - u_{max})/u_{max}$ , where  $u_{max}$  is the displacement at the vertical symmetry plane of the weak layer (see inset in Fig. 3.12) and  $u_a$  denotes the displacement of the homogeneous, transversely isotropic material, which is strictly correct only for  $w/a \rightarrow 0$  or  $h/a \rightarrow 0$ , respectively. Considering an underestimation of the displacements by maximally 20% as acceptable from the practical viewpoint, the homogenised model would be adequate solely if the hard layers would be up to 0.05 – 0.125 $a$  thick (see lower diagrams of Fig. 3.4), depending on the thickness ratio  $h/w$  and on the initial stress. The error is bigger in the case of the lower initial stress (r.h.s.

diagrams), where the behaviour is elastic, but this is irrelevant because the displacements in the elastic range are anyway small.

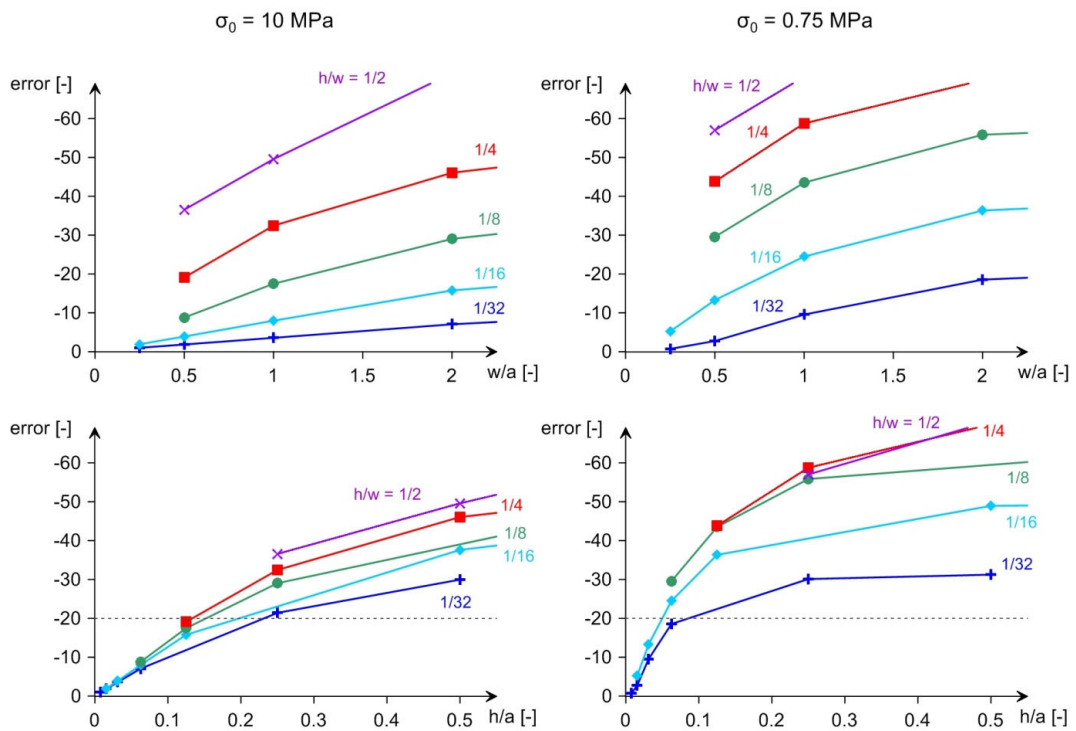


**Figure 3.4.** Error of the homogenised model as a function of the normalised thickness of the weak layers  $w/a$  (upper diagrams) and of the hard layers  $h/a$  (lower diagrams; unsupported tunnel,  $a = 4$  m,  $E_h = 10$  GPa,  $c_h = 5$  MPa,  $E_w = 0.5$  GPa,  $c_w = 0.5$  MPa,  $\nu_h = \nu_w = 0.3$ ,  $\varphi_h = \varphi_w = 25^\circ$ ,  $\psi_h = \psi_w = 5^\circ$ ).

### 3.2.5 Conclusions

In this chapter, an analytical solution (which was developed under the assumptions of rotational symmetry and plane strain conditions in [11]) for determining the displacements and the stresses of tunnels excavated in a sequence of thinly alternating weak and competent layers, assuming an equivalent homogeneous, transversely isotropic rock mass, was shortly presented. This solution is particularly important for practical reasons, as the numerical modelling of thinly alternating hard and weak rocks is very time-consuming.

Even if the hard rock layers make a small fraction of the composite (a few percent), in most tunnel problems they cannot be neglected during design. They have a considerable stabilising effect, which can be easily considered by using the developed analytical solution.

## 3.3 Determination of equivalent parameters for a rock mass consisting of thinly alternating weak and competent rocks

### 3.3.1 Introduction

The closed-form solution developed by Mezger [11] considers the thinly stratified rock mass as a homogeneous, transversely isotropic material, the parameters of which consist of those of the hard and weak layers and their thickness fractions. As the response of the homogenised rock mass to tunnel excavation is isotropic in the plane of the tunnel cross-section, it was investigated whether (and was found out that) it is possible to model the stratified rock mass as usually in design practice, *i.e.*, by considering a homogeneous and

isotropic (rather than transversely isotropic) linearly elastic – perfectly plastic material obeying Mohr-Coulomb failure criterion with a non-associated flow rule.

This approach makes it possible to analyse problems that do not meet the conditions of rotational symmetry or plane strain, applying known and commonly used methods (e.g., those of [61] and of [62] for yielding supports and TBM tunnelling, respectively, under squeezing conditions) also for the case of tunnelling perpendicularly to thinly stratified rocks.

Section 3.3.2 presents a method for the determination of the parameters of the equivalent isotropic material, which makes use of the closed-form solution for the GRC [11] and considers the parameters of the transversely isotropic material, *i.e.*, the thickness fractions and mechanical parameters of the weak and the hard layers. By analysing the results of a parametric study, which was performed with the method of Section 3.3.2, it is possible to express mathematically the parameters of the equivalent isotropic material as functions of the parameters of the transversely isotropic material; this is done in Section 3.3.3 using the closed-form solution of Mezger [11], disregarding out-of-plane plastic flow. Sections 3.3.4 and 3.3.5 discuss the accuracy and illustrate by means of examples the usefulness of the proposed method.

### 3.3.2 Determination of the parameters of the equivalent isotropic medium

The Young's modulus  $E_{eq}$  and the Poisson's ratio  $\nu_{eq}$  of the equivalent isotropic material will be taken such that the latter reproduces exactly the elastic response of the transversely isotropic material:

$$E_{eq} = \frac{3\mu_{eq} \cdot (\lambda_{eq} + 2\mu_{eq} / 3)}{(\lambda_{eq} + \mu_{eq})}, \quad (3.4)$$

$$\nu_{eq} = \frac{\lambda_{eq}}{2 \cdot (\lambda_{eq} + \mu_{eq})}, \quad (3.5)$$

where  $\lambda_{eq}$  and  $\mu_{eq}$  are taken equal to the Lamé constants of the REV:

$$\mu_{eq} = x_h \mu_h + x_w \mu_w, \quad (3.6)$$

$$\lambda_{eq} = \frac{x_w^2 \lambda_w (\lambda_h + 2\mu_h) + x_h^2 \lambda_h (\lambda_w + 2\mu_w) + 2x_h x_w (\lambda_h (\lambda_w + \mu_h) + \lambda_w \mu_w)}{x_w (\lambda_h + 2\mu_h) + x_h (\lambda_w + 2\mu_w)}, \quad (3.7)$$

where  $\mu_h$  and  $\lambda_h$  as well as  $\mu_w$  and  $\lambda_w$  denote the Lamé constants of the hard and the weak layers, respectively<sup>4</sup>.

The three plasticity parameters ( $\sigma_{d,eq}$ ,  $\varphi_{eq}$  and  $\psi_{eq}$ ) of the equivalent isotropic medium will be determined such that the GRC of the latter, which in general can be expressed as:

$$u_a = \frac{\sigma_0 \cdot a}{E_{eq}} \cdot f_l \left( \frac{\sigma_a}{\sigma_0}, \frac{\sigma_{d,eq}}{\sigma_0}, \nu_{eq}, \varphi_{eq}, \psi_{eq} \right), \quad (3.8)$$

<sup>4</sup> The Lamé constants are interconnected with the Young's modulus  $E$  and the Poisson's ratio  $\nu$  by the following equations:

$$\lambda = \frac{E \cdot \nu}{(1+\nu) \cdot (1-2\nu)}, \quad \mu = \frac{E}{2 \cdot (1+\nu)}, \quad E = \frac{3\mu \cdot (\lambda + 2 \cdot \mu / 3)}{(\lambda + \mu)} \quad \text{and} \quad \nu = \frac{\lambda}{2 \cdot (\lambda + \mu)}.$$

(cf. [60]) coincides at three selected values of the support pressure with the GRC of the transversely isotropic material:

$$u_a = \frac{\sigma_0 \cdot a}{E_w} \cdot f_{\pi} \left( \frac{\sigma_a}{\sigma_0}, \frac{x_h}{x_w}, \frac{E_h}{E_w}, \frac{\sigma_{d,h}}{\sigma_{d,w}}, \frac{\sigma_{d,w}}{\sigma_0}, \nu_h, \varphi_h, \psi_h, \nu_w, \varphi_w, \psi_w \right), \quad (3.9)$$

i.e.,

$$\frac{E_{eq}}{E_w} f_{\pi} \left( \frac{\sigma_{ak}}{\sigma_0}, \frac{x_h}{x_w}, \frac{E_h}{E_w}, \frac{\sigma_{d,h}}{\sigma_{d,w}}, \frac{\sigma_{d,w}}{\sigma_0}, \nu_h, \varphi_h, \psi_h, \nu_w, \varphi_w, \psi_w \right) = f_l \left( \frac{\sigma_{ak}}{\sigma_0}, \frac{\sigma_{d,eq}}{\sigma_0}, \nu_{eq}, \varphi_{eq}, \psi_{eq} \right) \quad (3.10)$$

(for  $k = 1, 2, 3$ ),

or, considering (on account of Eqs. 3.4 to 3.7) that:

$$\frac{E_{eq}}{E_w}, \nu_{eq} = f_0 \left( \frac{x_h}{x_w}, \frac{E_h}{E_w}, \nu_h, \nu_w \right), \quad (3.11)$$

$$f \left( \frac{\sigma_{d,eq}}{\sigma_0}, \varphi_{eq}, \psi_{eq}, \frac{\sigma_{ak}}{\sigma_0}, \frac{x_h}{x_w}, \frac{E_h}{E_w}, \frac{\sigma_{d,h}}{\sigma_{d,w}}, \frac{\sigma_{d,w}}{\sigma_0}, \nu_h, \varphi_h, \psi_h, \nu_w, \varphi_w, \psi_w \right) = 0 \quad (\text{for } k = 1, 2, 3). \quad (3.12)$$

Equation (3.12) represents a system of three nonlinear equations, the solution of which provides the normalised strength  $\sigma_{d,eq}/\sigma_0$ , the friction angle  $\varphi_{eq}$  and the dilatancy angle  $\psi_{eq}$  of the equivalent isotropic material for given thickness fraction  $x_h$  and material constants of the hard and weak layers:

$$\frac{\sigma_{d,eq}}{\sigma_0}, \varphi_{eq}, \psi_{eq} = f \left( \frac{x_h}{x_w}, \frac{E_h}{E_w}, \frac{\sigma_{d,h}}{\sigma_{d,w}}, \frac{\sigma_{d,w}}{\sigma_0}, \nu_h, \varphi_h, \psi_h, \nu_w, \varphi_w, \psi_w \right). \quad (3.13)$$

In this way the parameters of an isotropic material can be determined, the response curve of which is close to the one of the rigorously defined transversely isotropic material. Specifically, the GRC of the equivalent material has the same elastic part as the GRC of the transversely isotropic material and intersects the latter at the three selected values of the support pressure. The latter can be taken equal to  $0, 0.1\sigma_0$  and  $0.2\sigma_0$  in order to capture the practically important portion of the GRC.

### 3.3.3 Relationships between the material constants of the equivalent isotropic medium and those of the transversely isotropic medium

The material constants of the equivalent isotropic medium will be expressed as functions of the material constants of the transversely isotropic medium. This is possible by post-processing the results of a parametric study, which was carried out by applying the method of Section 3.3.2 to a large number of parameter sets ( $x_h/x_w, E_h/E_w, \sigma_{d,h}/\sigma_{d,w}, \sigma_{d,w}/\sigma_0, \nu_h, \varphi_h, \psi_h, \nu_w, \varphi_w, \psi_w$ ). The parametric study was carried out with the closed-form solution of Mezger [11] disregarding an out-of-plane plastic flow. The considered parameter sets cover a range that is sufficiently wide for practical purposes. For the sake of economy, the Poisson's ratios were kept fixed to 0.3 and the dilatancy angles were taken equal to  $\max(\varphi - 20^\circ; 1^\circ)$ . In addition, use will be made of the fact that weaker materials are generally also softer, exhibiting a Young's modulus in the order of 500 - 1000 times the uniaxial strength, i.e.,  $E_h = \alpha_h \sigma_{d,h}$  and  $E_w = \alpha_w \sigma_{d,w}$  (where  $500 \leq \alpha_{h,w} \leq 1000$ ), which means that the moduli ratio amounts to  $E_h/E_w = \alpha \sigma_{d,h}/\sigma_{d,w}$ , where  $0.5 \leq \alpha \leq 2$ . In this way, the number of parameters to be considered decreases from ten (Eq. 3.13) to six:

$$\frac{\sigma_{d,eq}}{\sigma_0}, \varphi_{eq}, \psi_{eq} = f \left( \frac{\sigma_{d,w}}{\sigma_0}, \frac{x_h}{x_w}, \alpha, \frac{\sigma_{d,h}}{\sigma_{d,w}}, \varphi_h, \varphi_w \right). \quad (3.14)$$

The computational results (obtained with the parameters of Table 3.1) were post-processed by representing graphically the parameters  $\sigma_{d,eq}/\sigma_0$ ,  $\varphi_{eq}$  and  $\psi_{eq}$  of the isotropic medium as functions of the normalised strength  $\sigma_{d,w}/\sigma_0$  of the weak layers for each set of the last five parameters of Equation (3.14). Figure 3.5 shows an example of these diagrams for a specific parameter set; the computational results are represented by the black circular markers. By analysing these graphs, mathematical relationships were found between the parameters of the isotropic material and those of the transversely isotropic model (red curves in Fig. 3.5).

As can be seen in the example of Figure 3.5, the relationships between the parameters of the isotropic model and the normalised strength  $\sigma_{d,w}/\sigma_0$  consist of three parts, delimited by the characteristic values  $(\sigma_{d,w}/\sigma_0)_{crit}$  and  $(\sigma_{d,w}/\sigma_0)_{cor}$ .

**Table 3.1.** Overview of the considered parameter ranges for determining the equivalent parameters.

$x_h/x_w$	1/8, 1/4, 1/2, 1, 2
$\sigma_{d,h}/\sigma_{d,w}$	2, 6, 10
$\alpha$	0.5, 1, 1.5, 2
$\varphi_h$	20°, 25°, 30°
$\varphi_w$	$\varphi_h - (0^\circ, 5^\circ, 10^\circ)$

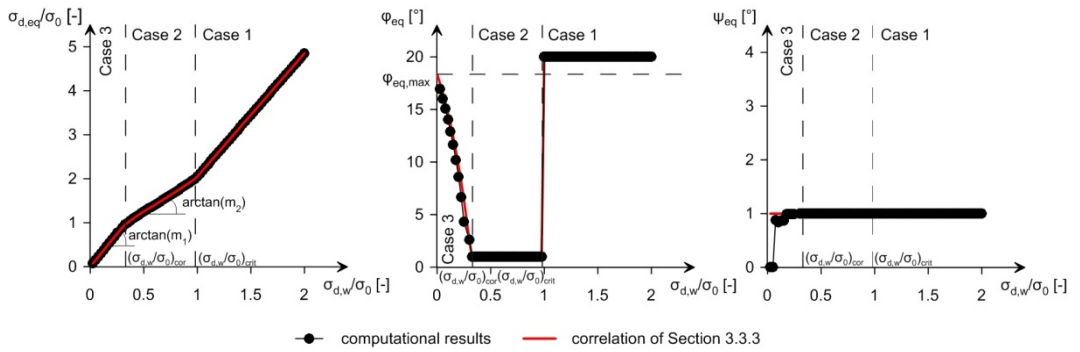


**Figure 3.5.** Parameters of the simplified isotropic model as functions of the normalised strength of the weak layers ( $x_h/x_w=1/4$ ,  $\alpha = 1$ ,  $\sigma_{d,h}/\sigma_{d,w} = 10$ ,  $\varphi_h = \varphi_w = 20^\circ$ ).

The first characteristic value is the strength, for which neither the weak nor the hard layers reach failure (even if  $\sigma_w/\sigma_0 = 0$ ), and can be determined analytically based upon the equations that were derived for the transversely isotropic medium (cf. [11]):

$$\left(\frac{\sigma_{d,w}}{\sigma_0}\right)_{crit} = \max \left( \frac{-\mu_{eq} \cdot (-1 + m_w) + (1 + m_w) \cdot \mu_w}{\mu_{eq}}, \frac{-\mu_{eq} \cdot (-1 + m_h) + (1 + m_h) \cdot \mu_h}{\mu_{eq} \cdot \frac{\sigma_{d,h}}{\sigma_{d,w}} \cdot \frac{\sigma_{d,w}}{\sigma_0}} \right). \quad (3.15)$$

If the second r.h.s. term of this equation is greater than the first r.h.s. term, then the hard layers reach failure earlier than the weak layers. This is usually the case due to the higher stiffness of the hard layers (cf. [11]).

The second characteristic value,  $(\sigma_{d,w}/\sigma_0)_{cor}$ , has no physical meaning. By trial-and-error, the following relationship could be found:

$$\left(\frac{\sigma_{d,w}}{\sigma_0}\right)_{cor} = \left( -0.055 \cdot \frac{\sigma_{d,h}}{\sigma_{d,w}} \cdot \frac{m_h}{m_w} + 1.45 \right) \cdot \frac{E_w}{E_{eq}}. \quad (3.16)$$

The relationships between plasticity parameters of the isotropic model and the ground parameters can be approximated as follows.

If  $\sigma_{d,w}/\sigma_0 \geq (\sigma_{d,w}/\sigma_0)_{crit}$  (Case 1 of Fig. 3.5), the plasticity parameters are taken such, that the minimum support pressure  $\sigma_\rho$  for which the rock remains elastic is the same for the isotropic and for the transversely isotropic material:

$$\frac{\sigma_{d,eq}}{\sigma_0} = 2 - \frac{\sigma_\rho}{\sigma_0} \frac{2}{1 - \sin \varphi_{eq}}, \quad (3.17)$$

where

$$\frac{\sigma_\rho}{\sigma_0} = \max \left( 1 - \frac{\mu_{eq}}{\mu_w} \frac{m_w - 1 + \frac{\sigma_{d,w}}{\sigma_0}}{1 + m_w}, 1 - \frac{\mu_{eq}}{\mu_h} \frac{m_h - 1 + \frac{\sigma_{d,h}}{\sigma_0} \cdot \frac{\sigma_{d,w}}{\sigma_0}}{1 + m_h} \right), \quad (3.18)$$

$$\varphi_{eq} = X_h \cdot \varphi_h + X_w \cdot \varphi_w, \quad (3.19)$$

$$\psi_{eq} = X_h \cdot \psi_h + X_w \cdot \psi_w. \quad (3.20)$$

If  $(\sigma_{d,w}/\sigma_0)_{cor} \leq \sigma_{d,w}/\sigma_0 \leq (\sigma_{d,w}/\sigma_0)_{crit}$  (Case 2 of Fig. 3.5), then

$$\frac{\sigma_{d,eq}}{\sigma_0} = (m_1 - m_2) \left( \frac{\sigma_{d,w}}{\sigma_0} \right)_{cor} + m_2 \cdot \frac{\sigma_{d,w}}{\sigma_0}, \quad (3.21)$$

$$\varphi_{eq} = 1^\circ, \quad (3.22)$$

and

$$\psi_{eq} = X_h \cdot \psi_h + X_w \cdot \psi_w, \quad (3.23)$$

where

$$m_1 = \frac{0.94}{\cos(\varphi_h)} + X_h \left( \frac{\sigma_{d,h}}{\sigma_{d,w}} - 1 \right) \cdot \left( 0.96 \cos(\varphi_h) + 0.088 m_h \frac{\sigma_{d,w}}{\sigma_{d,h}} \frac{E_h}{E_w} \right), \quad (3.24)$$

$$m_2 = \max \left( \frac{2 - m_1 \cdot \left( \frac{\sigma_{d,w}}{\sigma_0} \right)_{cor}}{\left( \frac{\sigma_{d,w}}{\sigma_0} \right)_{crit} - \left( \frac{\sigma_{d,w}}{\sigma_0} \right)_{cor}}; 0 \right). \quad (3.25)$$

If  $\sigma_{d,w}/\sigma_0 \leq (\sigma_{d,w}/\sigma_0)_{cor}$  (Case 3 of Fig. 3.5) then

$$\frac{\sigma_{d,eq}}{\sigma_0} = m_1 \cdot \frac{\sigma_{d,w}}{\sigma_0}, \quad (3.26)$$

$$\varphi_{eq} = \frac{\left( 1 - e^{-3.5 \cdot \sigma_s \left( \frac{\sigma_{d,w}}{\sigma_0} \right)_{cor} \left\{ \left( \frac{\sigma_{d,w}}{\sigma_0} \right)_{cor} - \frac{\sigma_{d,w}}{\sigma_0} \right\}} \right)}{\left( 1 - e^{-3.5 \cdot \sigma_s \left( \frac{\sigma_{d,w}}{\sigma_0} \right)_{cor}^2} \right)} \cdot \left( 1 - 0.6 \cdot \frac{m_h}{m_w} \cdot e^{-(12 \cdot x_h + 3) \cdot E_w / E_{eq}} \right) \cdot (x_h \cdot \varphi_h + x_w \cdot \varphi_w), \quad (3.27)$$

$$\psi_{eq} = x_h \cdot \psi_h + x_w \cdot \psi_w, \quad (3.28)$$

where

$$\sigma_s = \left( x_h \cdot \frac{\sigma_{d,h}}{\sigma_{d,w}} + x_w \right). \quad (3.29)$$

### 3.3.4 Accuracy of the proposed simplified model

Note, that in certain cases, particularly if  $E_h/E_w$  and  $\sigma_{d,w}/\sigma_{d,h}$  are high and  $\sigma_{d,w}/\sigma_0$  small, the middle section of the GRC cannot be captured perfectly (error up to 20%) by using the isotropic model, no matter how well its parameters are chosen (compare green line with black markers in the l.h.s. diagram of Fig. 3.6).

However, the proposed equations for  $\sigma_{d,eq}/\sigma_0$ ,  $\varphi_{eq}$  and  $\psi_{eq}$  reproduce well the computational results (compare red lines with black markers in Fig. 3.5). Generally, for  $\varphi_h = \varphi_w$ , the error is less than 10%.

The equations of Section 3.3.3 provide in general satisfactory results also for  $\varphi_w < \varphi_h$ , but may result (particularly the equations for  $\varphi_{eq}$  and  $\psi_{eq}$ ; Eqs. 3.21 to 3.29) in an overestimation of the displacements (by maximum 50%) in the range of  $\sigma_a/\sigma_0 = 0.1 - 0.2$ , especially if  $E_h/E_w$  and  $\sigma_{d,h}/\sigma_{d,w}$  are high and  $\sigma_{d,w}/\sigma_0$  small (compare red line with black markers in the r.h.s. diagram of Fig. 3.6).

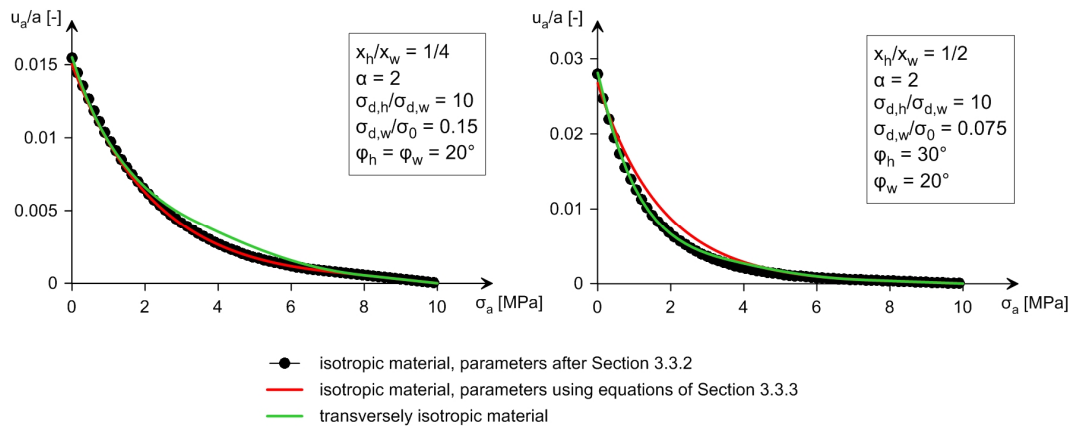


**Figure 3.6.** Ground response curves for  $\sigma_0 = 10$  MPa and  $E_w = 1$  MPa (all other rock parameters: see labels inside the diagrams).

Given  $\varphi_{eq}$  and  $\psi_{eq}$  according to Equations (3.22), (3.23), (3.27) and (3.28), the value of  $\sigma_{d,eq}/\sigma_0$  that results from Equations (3.21) and (3.26) deviates by maximum 20% from the value that would reproduce the correct displacement at  $\sigma_a/\sigma_0 = 0$  (compare red line with black markers in Fig. 3.7). Curve fitting by the proposed equations is significantly better at higher  $\varphi_h$  values (compare detail in Fig. 3.7a with detail in Fig. 3.7b). The maximum error occurs again for high  $E_h/E_w$  and  $\sigma_{d,w}/\sigma_{d,h}$  values in combination with low  $\sigma_{d,w}/\sigma_0$  values. This is particularly problematic, as especially under a high initial stress  $\sigma_0$ , a small error in  $\sigma_{d,eq}$  can produce a considerable error in the displacements. However, considering the usual

uncertainties with respect to the rock parameters, a threshold error of 20% (Fig. 3.7b) can be considered as acceptable.

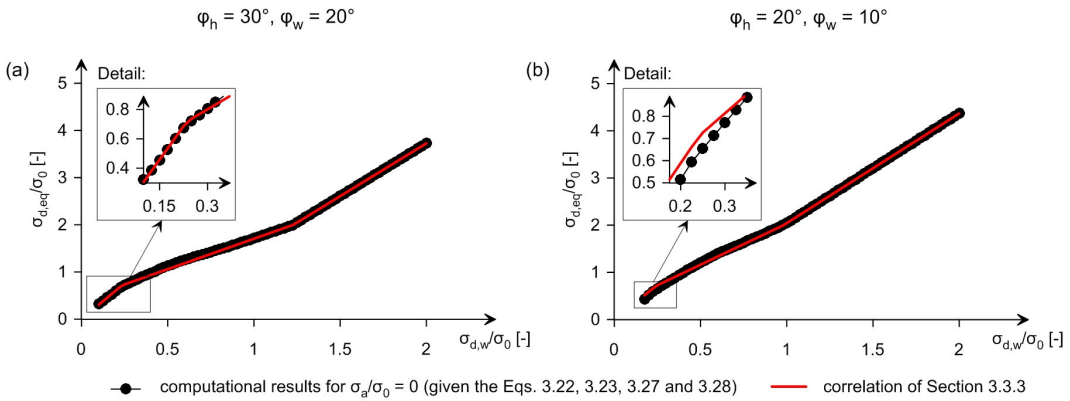


**Figure 3.7.** Equivalent parameters  $\sigma_{d,eq}/\sigma_0$  ( $x_h/x_w = 1/4$ ,  $\alpha = 1$ ,  $\sigma_{d,h}/\sigma_{d,w} = 10$ ).

### 3.3.5 Application examples

The usefulness and accuracy of the proposed simplified equivalent isotropic model will be illustrated by means of four tunnelling problems (considering an initial hydrostatic stress field of 10 MPa): (1) The ground response curve of a cylindrical tunnel (shown for evaluating the accuracy of the equivalent parameters; Fig. 3.8); (2) The longitudinal displacement profile of an unsupported tunnel (Fig. 3.9); (3) The boundary displacements of an unsupported tunnel with a horseshoe profile assuming plane strain conditions (Fig. 3.10); (4) The ground pressure  $p$  developing upon the shield and the lining in shielded TBM tunnelling (Fig. 3.11).

The exact solutions were obtained either analytically (for problem 1) or numerically (for the problems 2 to 4) using the Abaqus finite element code, where the transversely isotropic material model was implemented (see Section 4.2). All the numerical details for problem 2 can be found in Section 5.1; Fig. 3.9). Problem 4 was solved by modelling tunnel excavation and support installation step-by-step; further numerical details can be found in [63], Fig. 3.11). Table 3.2 shows the assumed parameters of the weak and of the hard layers as well as the parameters of the equivalent isotropic material (calculated after Section 3.3.3).

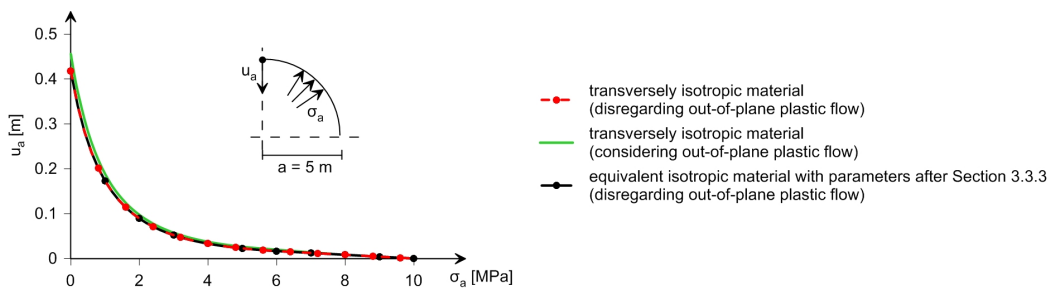


**Figure 3.8.** GRC of a cylindrical tunnel.

The comparative computations show that the simplified isotropic model with the parameters after Section 3.3.3 is sufficiently accurate even for problems that do not meet rotational symmetry and plane strain conditions. The error amounts to less than 10% and is due to the out-of-plane plastic flow, which was not considered in the determination of the parameters of the equivalent isotropic material. (The out-of-plane is negligible in this case, as  $\varphi_h = \varphi_w$ ; see [11]).

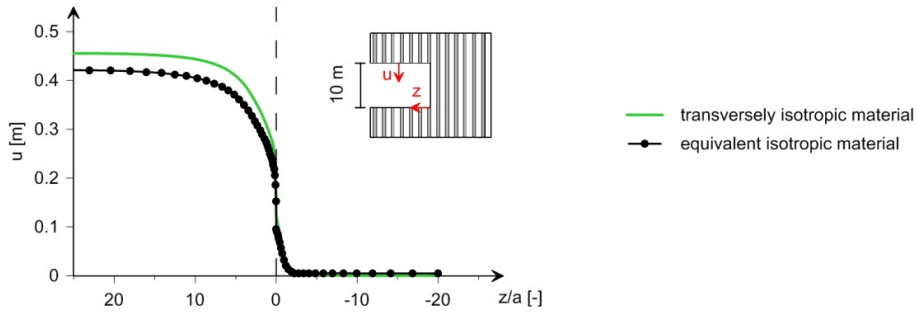


Figure 3.9. Longitudinal displacement profile of an unsupported tunnel.

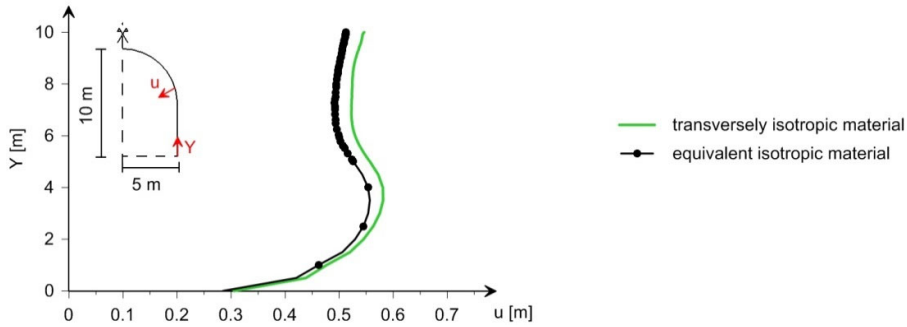


Figure 3.10. Magnitude of the displacement vector along the unsupported tunnel boundary of a horseshoe profile.

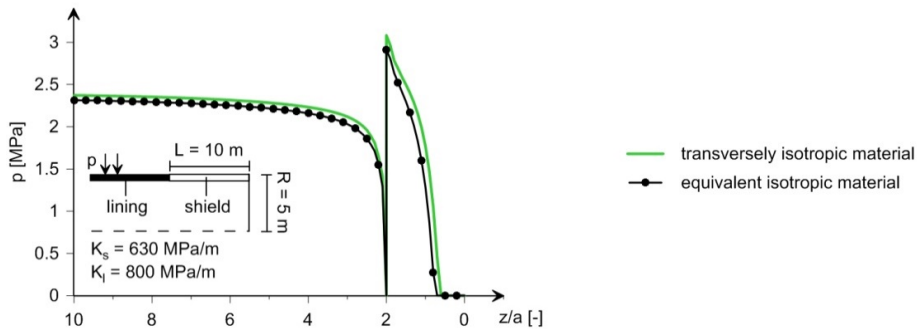


Figure 3.11. Ground pressure  $p$  acting upon the shield and the lining in TBM-tunnelling.

Table 3.2. Rock parameters and equivalent parameters.

$x_h/x_w$ [-]	$E_h$ [GPa]	$\nu_h$ [-]	$\varphi_h$ [°]	$c_h$ [MPa]	$\psi_h$ [°]	$E_w$ [GPa]	$\nu_w$ [-]	$\varphi_w$ [°]	$c_w$ [MPa]	$\psi_w$ [°]
1/8	6	0.3	20	2.6258	1	1	0.3	20	0.4376	1

$E_{eq}$ [GPa]	$\nu_{eq}$ [-]	$\varphi_{eq}$ [°]	$c_{eq}$ [MPa]	$\psi_{eq}$ [°]
1.536	0.28	18.6	0.719	1

### 3.3.6 Closing remarks

Section 3.3.2 explained how the analytical solutions of Mezger [11] for the ground response curve can be used in order to determine the parameters of an equivalent homogeneous, isotropic and elasto-plastic material for given parameters of the weak and the hard layers of a thinly stratified rock mass. This is very useful for design purposes since it allows the

use of common calculation methods and programs to solve problems that do not meet the conditions of rotational symmetry or plane strain.

Using the method of Section 3.3.2, relationships between the parameters of the equivalent isotropic model and those of the rigorous transversely isotropic model were developed in Section 3.3.3. These equations were found by applying the closed-form solution of Mezger [11] disregarding an out-of-plane plastic flow. Therefore, they may lead to an underestimation of the rock displacements and pressures. In most cases the effect of out-of-plane plastic flow is negligible. However, if  $\varphi_h$  is considerably higher than  $\varphi_w$  and the strength  $\sigma_{d,w}/\sigma_0$  of the weak layers very low, neglecting the out-of-plane plastic flow may lead to inaccurate results (see [11]). The effect of the out-of-plane plastic flow can be assessed for given parameters of the hard and of the weak layers using the closed-form solutions of Mezger [11]. If this effect is significant, then the parameters of the simplified equivalent isotropic material can be determined with the procedure shown in Section 3.3.2.

## 3.4 Influence of the heterogeneity scale on the squeezing variability along the tunnel

### 3.4.1 Introduction

Rock mass heterogeneity may lead – depending on the heterogeneity scale [46] – to significant variations in the squeezing intensity during tunnelling (see Section 3.1). Section 3.4.2 investigates how the heterogeneity scale (represented here by the normalised thickness  $w/a$  of the weak layers) affects the longitudinal distribution of the displacements in tunnelling perpendicularly to a sequence of weak and hard layers of finite thickness. With the exception of extremely wide weak zones (for which known closed-form solutions can be used) or thinly stratified rocks consisting of weak and hard interlayers (for which the analytical solution of [11] applies), the displacements can be determined only by means of numerical computations. However, as shown in Section 3.4.3, one can obtain a reasonably accurate estimation of the displacements in weak zones also analytically, by means of a simple equation.

### 3.4.2 Longitudinal distribution of the displacements

Figure 3.12 shows the maximum  $u_{max}$  and the minimum displacements  $u_{min}$  (occurring in the middle of the weak and of the hard layer, respectively) as a function of the layer thicknesses  $w/a$  for various thickness ratios  $h/w$ , which were obtained by axisymmetric numerical calculations which were carried out with the FE-program Abaqus [64]. Specifically, an unsupported, cylindrical tunnel that crosses alternating hard and weak layers of a finite thickness of  $h$  and  $w$ , respectively, will be studied (cf. [13]). The rock layers were modelled discretely as isotropic, linearly elastic and perfectly plastic material with the Mohr-Coulomb yield criterion (considering the subroutine of [65]). Figure 3.13 shows the longitudinal displacement distribution for a fixed thickness ratio  $h/w = 0.5$  and various  $w/a$ -values.

The computational results allow drawing the following conclusions:

- There is clearly an interaction between the hard and the weak layers, since the displacement in the cross-section in the middle of a weak layer ( $u_{max}$ ) or of a hard layer ( $u_{min}$ ) may be bigger or smaller depending on the distance between these cross-sections and the layer interface (*i.e.* depending on  $w/a$  and  $h/a$ , respectively). The hard layers have a stabilising effect on the weak layers and, vice versa, the latter have a destabilising effect on the hard layers.
- The interaction between the layers is maximum for  $w/a \rightarrow 0$  (and arbitrary  $h/w$ ), *i.e.*, when the layers are very thin in relation to the tunnel radius. In this case, the displacements are practically uniformly distributed and can be obtained by means of the closed-form solution of Mezger [11].
- With increasing layer thicknesses (*i.e.*, for increasing  $w/a$ - and arbitrary  $h/w$ -values), the interaction between the layers (the stabilising effect of the hard layers and the

destabilising effect of the weak layers) becomes less and less pronounced. The displacement  $u_{max}$  in the middle of the weak layer increases, while the displacement  $u_{min}$  in the middle of the hard layer decreases (see also Fig. 3.13). The squeezing intensity varies along the tunnel within a scale of a few metres (*cf.* [13]).

- For  $w/a \rightarrow \infty$  (which practically means for  $w/a > 16$  in the example of Fig. 3.12), the displacements in the middle of the weak and of the hard layer approach the displacements  $u_{w,2D}$  and  $u_{h,2D}$ , respectively, obtained assuming plane strain conditions with the parameters of the weak and of the hard layers, respectively; the interaction between the layers is limited to the vicinity of their interface (Fig. 3.13).

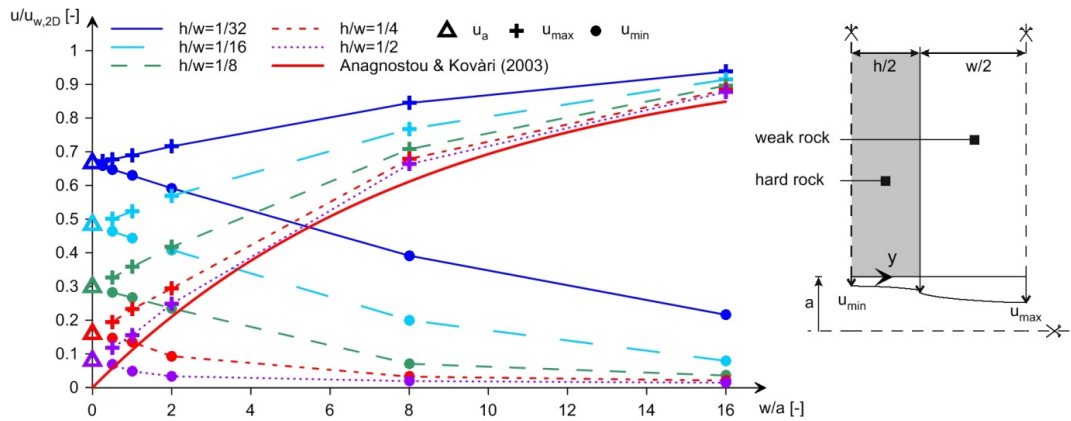


**Figure 3.12.** Normalised displacement in the middle of the weak layer ( $u_{max}$ ) and of the hard layer ( $u_{min}$ ); unsupported tunnel,  $a = 4$  m,  $\sigma_0 = 10$  MPa,  $E_h = 10$  GPa,  $c_h = 5$  MPa,  $E_w = 1$  GPa,  $c_w = 0.5$  MPa,  $\nu_h = \nu_w = 0.3$ ,  $\varphi_h = \varphi_w = 25^\circ$ ,  $\psi_h = \psi_w = 5^\circ$ .

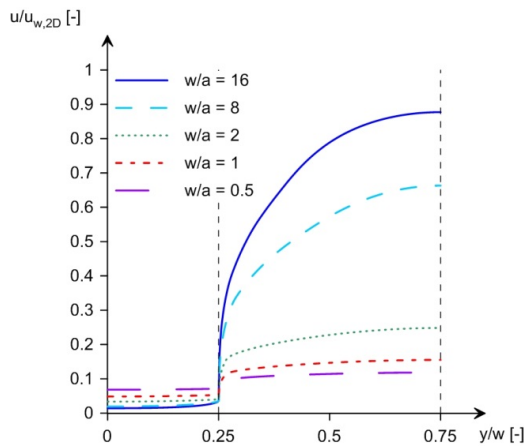


**Figure 3.13.** Longitudinal displacement distribution for  $h/w = 1/2$  (unsupported tunnel,  $a = 4$  m,  $\sigma_0 = 10$  MPa,  $E_h = 10$  GPa,  $c_h = 5$  MPa,  $E_w = 1$  GPa,  $c_w = 0.5$  MPa,  $\nu_h = \nu_w = 0.3$ ,  $\varphi_h = \varphi_w = 25^\circ$ ,  $\psi_h = \psi_w = 5^\circ$ ).

Similar remarks apply to the case of hard layers that exhibit brittle behaviour, the only difference being that the stabilising effect of the hard layers is smaller if they become overstressed and experience brittle failure. Figure 3.14 compares the results obtained by numerical computations under the assumption of brittle behaviour of the hard layers (red lines) with those obtained assuming perfectly plastic behaviour (black lines). For the former, the numerical calculations were performed with the program FLAC [66]: The hard layers were modelled with the so-called “softening model”, which considers the cohesion as a function of the deviatoric plastic strain. The effect of brittle behaviour is evident. It results in larger displacements (both in the hard and in the weak layers) particularly for small ratios  $w/a$  and  $h/w$ , where the hard layers are heavily loaded (*cf.* [13]).

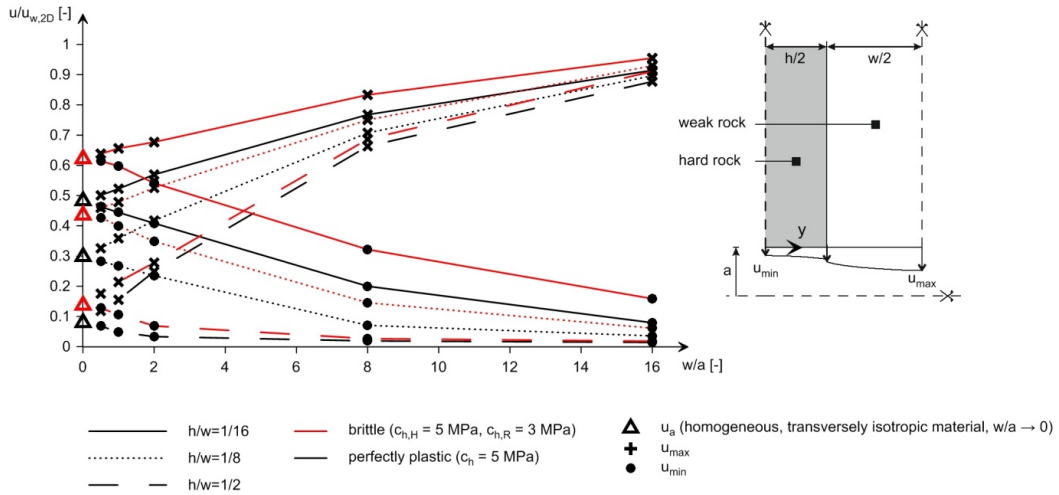


**Figure 3.14.** Normalised displacements in the weak ( $u_{max}$ ) and in the hard ( $u_{min}$ ) layers as a function of the normalised thickness  $w/a$  for perfectly plastic or brittle behaviour of the hard layers (unsupported tunnel,  $a = 4$  m,  $\sigma_0 = 10$  MPa,  $E_h = 10$  GPa,  $E_w = 1$  GPa,  $c_w = 0.5$  MPa,  $\nu_h = \nu_w = 0.3$ ,  $\varphi_h = \varphi_w = 25^\circ$ ,  $\psi_h = \psi_w = 5^\circ$ ).

### 3.4.3 A simple equation for the displacements in a weak zone considering a wall-effect

Anagnostou and Kovári [67] proposed the following equation for estimating the displacements  $u_{max}$  in a weak zone of limited length  $w$  bounded by competent rock:

$$u_{max} = \delta u_{w,2D}, \quad (3.30)$$

where  $u_{w,2D}$  denotes the displacement that would occur in an infinitely long weak zone while  $\delta$  represents a reduction factor ( $0 < \delta < 1$ ) that accounts for the stabilising effect of the adjacent competent rock:

$$\delta = 1 - e^{-0.4w/\rho_{w,2D}}, \quad (3.31)$$

where  $\rho_{w,2D}$  denotes the radius of the plastic zone in the case of an infinitely long weak zone. As both  $u_{w,2D}$  and  $\rho_{w,2D}$  can be computed applying the commonly used closed-form GRC solution, the equations above allow a quick estimation of the wall-effect without performing numerical analyses.

The equation for the reduction factor  $\delta$  was found by analysing the results of a parametric study, which was carried out assuming that the competent rock is rigid. Due to this assumption, the equation of Anagnostou and Kovári [67], in general, overestimates the wall-effect and underestimates the displacements in the weak zone, particularly if the latter is bounded by relatively thin layers of competent rock. In the numerical example of Figure 3.12, the equation of Anagnostou and Kovári [67] (red solid line) underestimates the displacements considerably if  $h/w < 0.5$ .

In the present research project, it was investigated whether the equation of Anagnostou and Kovári [67] can be modified, so that it includes the effects of deformation and failure of the competent rock. Intuitively, by studying numerical results as those of Figure 3.12 and by considering some important conditions (given below), the following simple equation was constructed:

$$\frac{u_{max}}{u_{w,2D}} = \delta \cdot \left( 1 - \frac{u_a}{u_{w,2D}} \right) + \frac{u_a}{u_{w,2D}}, \quad (3.32)$$

where  $u_a$  is the displacement that would occur in the case of a thinly stratified rock mass (*i.e.*, for  $w/a \rightarrow 0$  and arbitrary  $h/w$ ) and can be computed analytically after Mezger [11]. The modified equation fulfils the following three conditions:

- $U_{max} \rightarrow u_a$  for  $w/a \rightarrow 0$  (note that  $\delta \rightarrow 0$  in this case; Eq. 3.31);
- $U_{max} \rightarrow U_{w,2D}$  for  $w/a \rightarrow \infty$  (note that  $\delta \rightarrow 1$  in this case; Eq. 3.31);
- $U_{max} = \delta \cdot u_{w,2D}$  (*i.e.*, equation of [67]) if the competent rock is rigid (note that  $u_a = 0$  in this case).

Figure 3.15 plots the displacements after Equation (3.32) and the exact ones obtained from the numerical calculations as a function of  $w/a$ . For this specific parameter set, the equation is reasonably accurate.

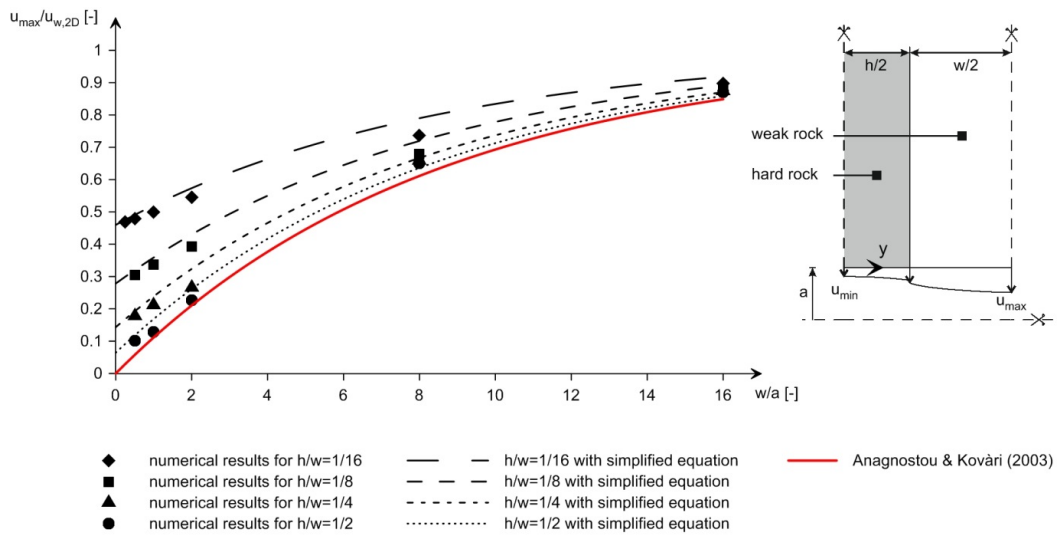


**Figure 3.15.** Accuracy of the simplified Equation (3.32) for perfectly plastic behaviour of the hard layers: Normalised displacement  $u_{max}$  as a function of the normalised weak layer thickness (unsupported tunnel,  $a = 4 \text{ m}$ ,  $\sigma_0 = 10 \text{ MPa}$ ,  $E_h = 10 \text{ GPa}$ ,  $c_h = 5 \text{ MPa}$ ,  $E_w = 1 \text{ GPa}$ ,  $c_w = 0.5 \text{ MPa}$ ,  $\nu_h = \nu_w = 0.3$ ,  $\varphi_h = \varphi_w = 25^\circ$ ,  $\psi_h = \psi_w = 5^\circ$ ).

The accuracy of the proposed equation was further checked by means of a comprehensive parametric study considering the significant parameters of the problem (disregarding brittle behaviour of the hard layers):

$$\frac{u_{max}}{a} = f\left(\frac{h}{w}, \frac{w}{a}, \frac{\sigma_a}{\sigma_0}, \frac{\sigma_{d,w}}{\sigma_0}, \frac{\sigma_{d,h}}{\sigma_{d,w}}, \frac{E_h}{E_w}, \nu_h, \varphi_h, \psi_h, \nu_w, \varphi_w, \psi_w\right), \quad (3.33)$$

with the values after Table 3.3. Figure 3.16 plots the displacements after Equation (3.32) as a function of the exact ones and shows that the equation is reasonably accurate.

Equation (3.32) was not checked comprehensively for the case of brittle behaviour of the hard layers, but holds probably also for this case, as indicated by the computational example of Figure 3.17.

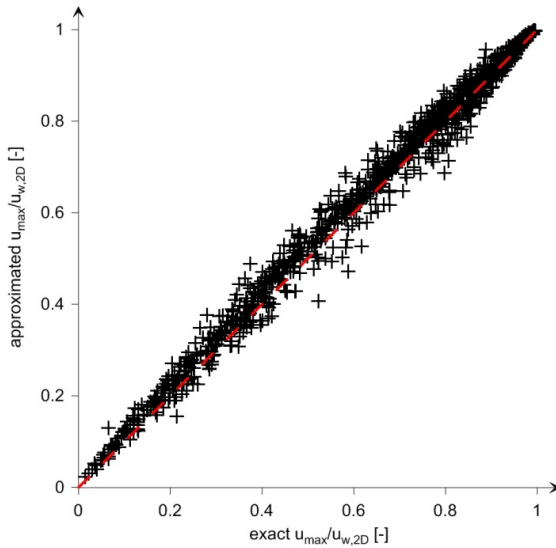


**Figure 3.16.** Accuracy of the simplified Equation (3.32): Normalised (approximated) displacement after Equation (3.32) versus exact normalised displacement.

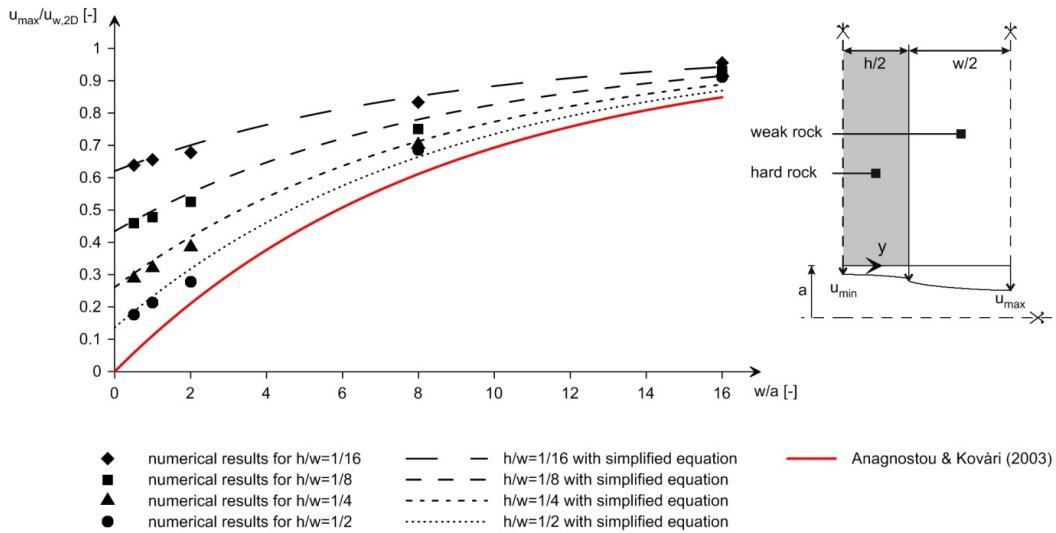


**Figure 3.17.** Accuracy of the simplified Equation (3.32) for brittle behaviour of the hard layers: Normalised displacement  $u_{max}$  as a function of the normalised weak layer thickness (unsupported tunnel,  $a = 4 \text{ m}$ ,  $\sigma_0 = 10 \text{ MPa}$ ,  $E_h = 10 \text{ GPa}$ ,  $c_{h,H} = 5 \text{ MPa}$ ,  $c_{h,R} = 3 \text{ MPa}$ ,  $E_w = 1 \text{ GPa}$ ,  $c_w = 0.5 \text{ MPa}$ ,  $\nu_h = \nu_w = 0.3$ ,  $\varphi_h = \varphi_w = 25^\circ$ ,  $\psi_h = \psi_w = 5^\circ$ ).

Disregarding the wall-effect introduces an error on the safe side (it overestimates the deformations in the weak zone), which however is small if the weak zone is sufficiently long in relation to tunnel radius. Expressing the error as  $(u_{w,2D} - u_{max})/u_{max}$ , taking  $u_{max}$  after Equation (3.32) and denoting the acceptable error by  $\epsilon_{tol}$ , the wall-effect can be neglected if the weak zone thickness is:

$$w > 2.5 \rho_{w,2D} \ln \left( \frac{\epsilon_{tol} + 1}{\epsilon_{tol}} \left( 1 - \frac{u_a}{u_{w,2D}} \right) \right), \quad (3.34)$$

where the plastic radius  $\rho_{w,2D}$  and the radial displacement  $u_{w,2D}$  depend on the *in situ* stress  $\sigma_0$  and on the mechanical parameters of the weak zone and can be computed using the common GRC equations, while the radial displacement  $u_a$  depends on the *in situ* stress  $\sigma_0$ , on the thickness ratio  $h/w$  and on the mechanical parameters of both layers and can be determined using the closed-form solution of Mezger [11]. Figure 3.18 represents graphically Equation (3.34).

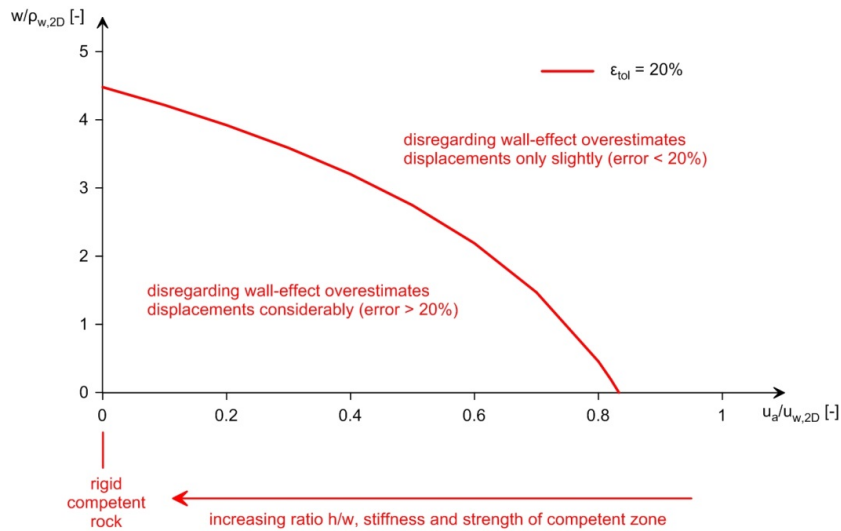


**Figure 3.18.** Normalised weak zone length for which disregarding wall-effect overestimates displacements by 20%.

**Table 3.3.** Parameter range considered for checking accuracy of Equation (3.32).

$h/w$ [-]	$\frac{1}{2}; 1/8; 1/32$
$w/a$ [-]	0.5; 1; 2; 8; 16
$\sigma_a/\sigma_0$ [-]	0
$\sigma_{d,w}/\sigma_0$ [-]	0.15; 0.3; 0.45
$\sigma_{d,h}/\sigma_{d,w}$ [-]	2
$E_h/E_w$ [-]	1; 4
$\nu_h = \nu_w$ [-]	0.3
$\varphi_h$ [°]	20; 30
$\varphi_w$ [°]	$\varphi_h - (5^\circ, 10^\circ)$
$\psi_{h,w}$ [°]	$1^\circ$ for $\varphi_{h,w} \leq 20^\circ$ $\varphi_{h,w} - 20^\circ$ for $\varphi_{h,w} > 20^\circ$ (according to [68])

### 3.4.4 Conclusions

At the current state of research, the displacements in tunnelling perpendicularly to a sequence of weak and hard layers of finite thickness can be determined only by means of numerical computations. For this, in this chapter, a simple analytical equation was developed based on the solution of Anagnostou and Kovári [67], which makes it possible to estimate the displacements in a weak zone considering the wall-effect of the hard layers and which is accurate enough for practical purposes. This equation seems also to hold for the case of brittle behaviour of the hard layers, where the stabilising effect is less pronounced.

## 4 Tunnelling parallel to alternating weak and competent rock layers

### 4.1 Introduction

When tunnelling parallel to alternating hard and weak layers, the tunnel profile may experience non-uniform deformations, but the displacements do not vary along the tunnel axis. Although there is no squeezing variability in tunnelling parallel to the bedding, this case is analysed in this research project because it represents a borderline case for the general case of an arbitrary orientation of the anisotropy plane, which is studied in Chapter 5.

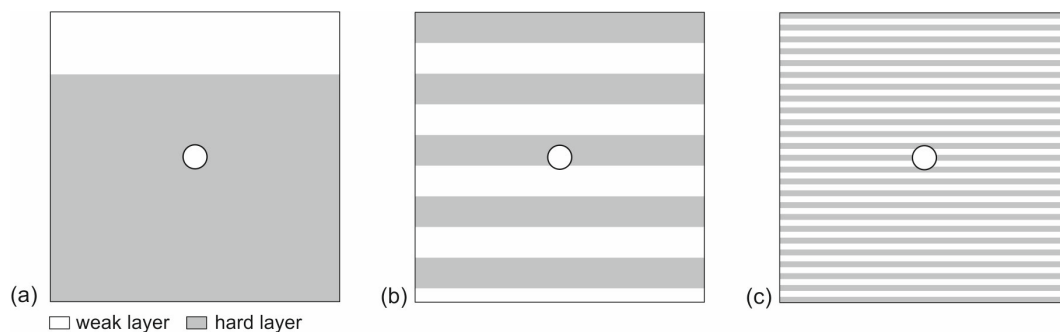


**Figure 4.1.** Tunnelling through a sequence of, (a), very thick weak and competent rock formations, (b), alternating weak and competent layers of medium thickness, (c), thinly alternating weak and competent layers.

Depending on the heterogeneity scale, the following three cases can be distinguished (cf. Fig. 4.1):

- If the weak (or the hard) layers are very thick and their interface lies far away from the tunnel (Fig. 4.1a), their unfavourable (or stabilising) effect will not be noticeable in the convergence distribution.
- If the alternating weak and hard rock layers are very thin relatively to the tunnel radius (Fig. 4.1c), then the rock mass can be conceived as a homogeneous, but, in view of the rock structure, transversely isotropic material.
- Otherwise (Fig. 4.1b), the heterogeneity of the rock mass has to be considered explicitly in the numerical modelling.

The present chapter of the research report is structured as follows:

Section 4.2 deals with the special case of a very thinly stratified rock mass (Fig. 4.1c). The constitutive model of Section 3.2 is formulated in 3D and implemented in Abaqus. This model serves to investigate the tunnelling-induced displacements under plane strain conditions and to develop design diagrams that allow to estimate quickly the ground response for a wide range of conditions in terms of the mechanical parameters and the thickness fractions of the weak and hard layers.

Section 4.3 analyses the effect of the rock structure on squeezing deformations paying attention to the various heterogeneity scales of Figure 4.1. Specifically, numerical (plane strain) calculations are performed, where the individual layers are modelled discretely. The ratio of the thickness of the layers to the tunnel radius is considered as a measure of the heterogeneity scale. The numerical results indicate, (i), under which conditions it is adequate to consider the homogenised model rather than the individual layers (Section 4.3.2), (ii), in which cases the heterogeneity of the ground can be neglected in the design (Section 4.3.3), (iii), or must be considered explicitly in numerical modelling (Section 4.3.4).

Section 4.4 deals with schistous rocks, as they represent, from the mechanical point of view, a special case (and their behaviour exhibits similarities to that) of a stratified rock mass. The excavation-induced displacements are investigated using a constitutive model, which was formulated (using the homogenisation technique) and implemented in Abaqus. For this purpose, design diagrams were also worked out that allow assessing quickly the effect of schistosity on the squeezing deformations.

## 4.2 Response of a thinly stratified rock mass, striking parallel to tunnel axis

### 4.2.1 Introduction

The squeezing behaviour in tunnelling parallel to a sequence of thinly alternating weak and hard rocks has not been analysed so far. This will be done in the present section based upon a homogeneous, transversely isotropic material model. An overview about stratified rock mass and homogenisation techniques can be found in Section 3.2. Contrarily to Section 3.2, however, a closed-form solution cannot be formulated for the GRC, because the problem is not rotationally symmetric. Therefore, the problem will be solved numerically. To this end, a constitutive model was formulated and implemented into the FE-program Abaqus ([64]; Section 4.2.2). Section 4.2.3 discusses the tunnelling-induced displacements and stresses by means of computational examples considering a circular tunnel cross-section under plane strain conditions, which corresponds to the situation that prevails in deep tunnels far behind the face. Subsequently, based upon a comprehensive parametric study, dimensionless diagrams are worked out in Section 4.2.4 that allow depicting the tunnelling-induced displacements for practically arbitrary conditions. These dimensionless diagrams can be used to determine the mechanical parameters of an isotropic homogeneous elasto-plastic material that can be characterised as "equivalent" to the transversely isotropic material in the sense that it experiences the same maximum or minimum displacements (Section 4.2.5). By using this equivalent isotropic material in combination with existing computational methods or design nomograms (e.g., those of [62]) one can estimate the range of rock pressures or deformations developing when tunnelling parallel to thinly stratified rocks.

### 4.2.2 Constitutive model

#### 4.2.2.1 Formulation

For the formulation of appropriate constitutive equations (accounting for the thickness fractions and mechanical properties of the individual rock layers), homogenisation techniques for a sequence of alternating weak and hard layers have been proposed in the literature, initially considering linearly elastic behaviour (*cf.*, e.g., [3], [48]) and later on extended for elasto-plastic behaviour of the layers ([4]; [69]; [70]) and shear failure along their interfaces [71].

The representative elementary volume (REV), which consists of hard and weak layers lying perpendicular to the  $y$ -axis, considered for the formulation of the constitutive model is presented in Figure 4.2. The constitutive model of the REV is equivalent to the one used in Section 3.2, but is formulated for the general 3D case (and not solely for plane strain conditions). An arbitrary bedding orientation can be considered by appropriate coordinate transformations: the stresses and the strains are transformed from the global into the local coordinate system (in which the  $y$ -axis is perpendicular to the layers) and, after having performed all the computations in the local coordinate system, the resulting stresses are back-calculated into the global coordinate system. The only input needed for the coordinate transformation is the normal vector of the layers.

The model – whose elasto-plastic parameters depend on thickness fraction, strength and stiffness properties of the alternating layers – was formulated and implemented in the finite element code Abaqus [64] based upon the general homogenisation procedure of Lourenço [4], the only difference being that Lourenço [4] used the von Mises rather than the Mohr-

Coulomb yield criterion. Therefore, as usual in design practice, the individual layers are modelled as linearly elastic – perfectly plastic materials obeying Mohr-Coulomb failure criterion with a non-associated flow rule (no tension cut-off, no brittle behaviour), using the stress return algorithm after Clausen [65], which, of course, considers an out-of-plane plastic flow.

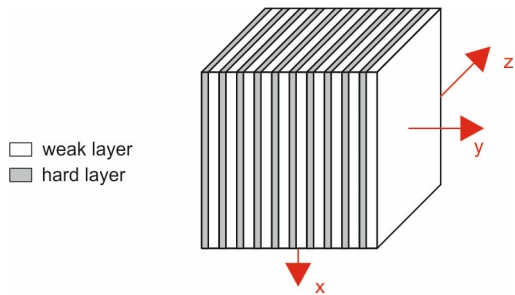


**Figure 4.2.** REV consisting of a sequence of hard and weak layers.

More details concerning the formulation and validation of the constitutive model can be found in Mezger [11].

#### 4.2.2.2 Rock element behaviour

In order to illustrate some basic aspects of the material behaviour, simple displacement-controlled element tests (considering a single quadratic element, 1 m x 1 m big, under plane strain conditions) were performed computationally. A uniform displacement  $u$  is applied either perpendicularly or parallel to the layers (see insets of Fig. 4.3). For simplicity, the thickness fractions of the hard and weak layers were taken equal to 50%.

The l.h.s. diagrams of Figure 4.3 show the results for the case of a displacement applied in the  $y$ -direction, *i.e.* perpendicularly to the layers. The stresses in  $y$ -direction are the same in the hard and in the weak layers and thus also in the REV (*i.e.*,  $\sigma_{yy,h} = \sigma_{yy,w} = \sigma_{yy}$ ). The weak layers experience, due to their lower stiffness, a bigger compressive strain in  $y$ -direction than the hard layers and, in the absence of the hard layers, would expand also more laterally (in  $x$ -direction). As they are retained by the hard layers in  $x$ -direction, compressive stresses develop in the weak layers (*i.e.*,  $\sigma_{xx,w} = \sigma_{max,w} > 0$ ) and tensile stresses in the hard layers (*i.e.*,  $\sigma_{xx,h} = \sigma_{max,h} < 0$ , as  $\sigma_{xx} = x_h \sigma_{xx,h} + x_w \sigma_{xx,w}$ ). The development of tensile stress in the harder layers was already described by Bourne [72]. It results in a tensile failure (at  $\epsilon_{yy} \approx 0.0037$  in the present example) and so in a slight decrease in the stiffness. Subsequently, also the weak layers fail (at  $\epsilon_{yy} \approx 0.004$ ) and the stress remains subsequently constant.

The r.h.s. diagrams of Figure 4.3 show the results for a displacement applied in the  $x$ -direction, *i.e.* parallel to the layers. The hard and the weak layers experience the same stresses in  $y$ -direction but different stresses in the  $x$ -direction. Expectedly, the stress in the REV corresponds to the volumetric averages of the stresses in the different layers (*i.e.*,  $\sigma_{xx} = x_h \sigma_{xx,h} + x_w \sigma_{xx,w}$ ). The hard layers are by a factor 10 stiffer than the weak layers and experience, therefore, in the elastic state, a 10 times higher stress in the  $x$ -direction. As the uniaxial compressive strength of the hard layers was taken 10 times higher than the one of the weak layers, the weak and the hard layers fail at the same time.

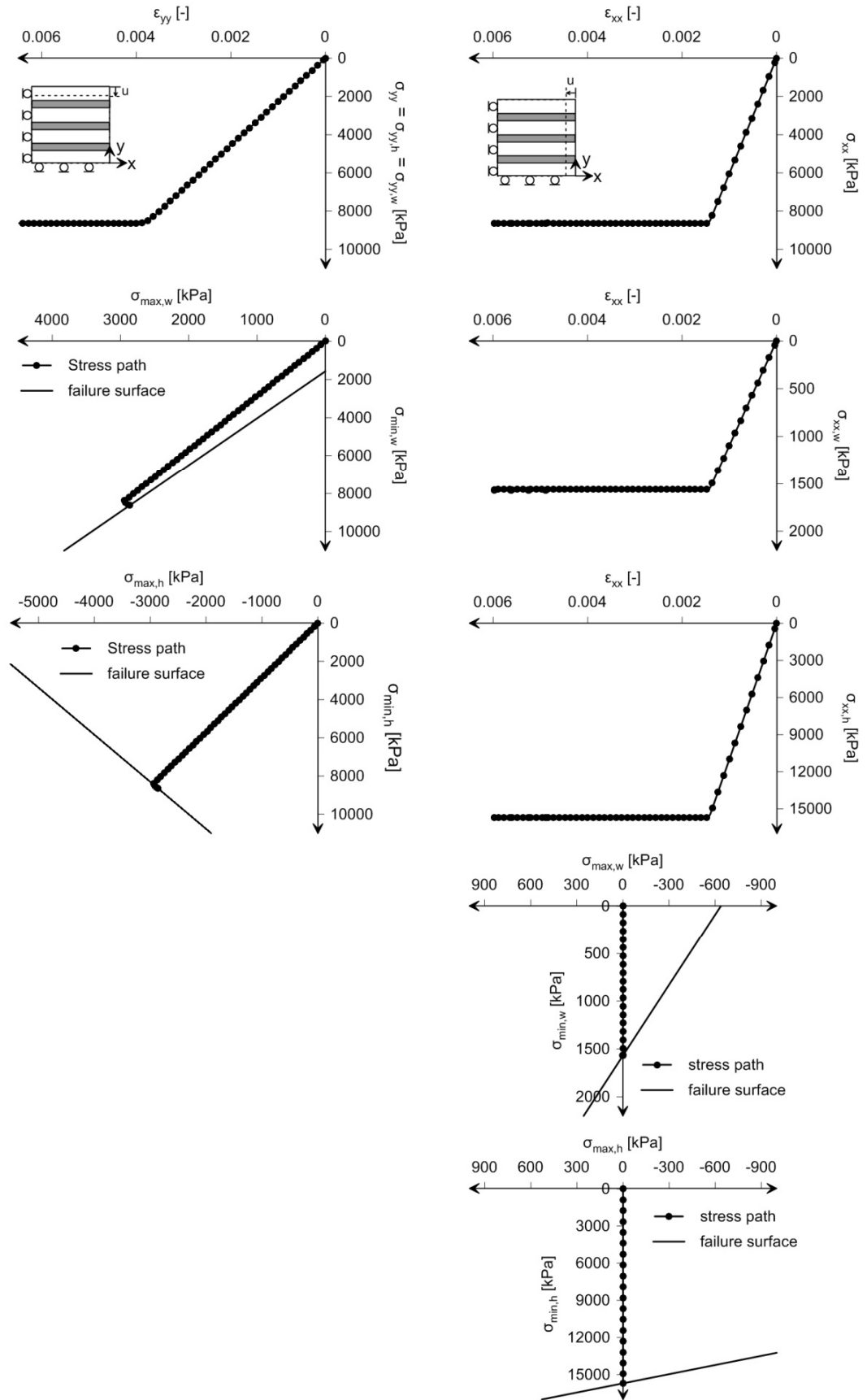


**Figure 4.3.** Results of the single element tests for displacement application perpendicularly (l.h.s.) or parallel (r.h.s) to the layers ( $x_h = x_w = 0.5$ ,  $E_h = 10$  GPa,  $c_h = 5$  MPa,  $E_w = 1$  GPa,  $c_w = 0.5$  MPa,  $\nu_h = \nu_w = 0.3$ ,  $\varphi_h = \varphi_w = 25^\circ$ ,  $\psi_h = \psi_w = 5^\circ$ ).

Furthermore, the composite behaves expectedly considerably softer when it is loaded perpendicularly to the layers (compare r.h.s with l.h.s curves) and the stiffnesses agree to the analytical predictions. Specifically, Hooke's law for the composite reads as follows [3]:

$$\begin{pmatrix} \varepsilon_{xx} \\ \varepsilon_{yy} \\ \varepsilon_{zz} \\ \gamma_{xy} \end{pmatrix} = \begin{pmatrix} \frac{1}{E_1} & -\frac{\nu_2}{E_1} & -\frac{\nu_1}{E_1} & 0 \\ -\frac{\nu_2}{E_1} & \frac{1}{E_2} & -\frac{\nu_2}{E_1} & 0 \\ -\frac{\nu_1}{E_1} & -\frac{\nu_2}{E_1} & \frac{1}{E_1} & 0 \\ 0 & 0 & 0 & \frac{1}{G_2} \end{pmatrix} \cdot \begin{pmatrix} \sigma_{xx} \\ \sigma_{yy} \\ \sigma_{zz} \\ \tau_{xy} \end{pmatrix} = \begin{pmatrix} S_{11} & S_{12} & S_{13} & 0 \\ S_{12} & S_{22} & S_{12} & 0 \\ S_{12} & S_{12} & S_{33} & 0 \\ 0 & 0 & 0 & S_{44} \end{pmatrix} \cdot \begin{pmatrix} \sigma_{xx} \\ \sigma_{yy} \\ \sigma_{zz} \\ \tau_{xy} \end{pmatrix}, \quad (4.1)$$

where

$$\nu_1 = \frac{E_h \nu_h (-1 + \nu_w^2) (-1 + x_w) - E_w (-1 + \nu_h^2) \nu_w x_w}{E_h (-1 + \nu_w^2) (-1 + x_w) - E_w (-1 + \nu_h^2) x_w}, \quad (4.2)$$

$$\nu_2 = \frac{(-E_h (1 + \nu_w) (-1 + x_w) + E_w (1 + \nu_h) x_w) (-\nu_w x_w + \nu_h (-1 + \nu_w + x_w))}{-E_h (-1 + \nu_w^2) (-1 + x_w) + E_w (-1 + \nu_h^2) x_w}, \quad (4.3)$$

$$E_1 = -\frac{E_h^2 (-1 + \nu_w^2) (-1 + x_w)^2 - 2E_h E_w (-1 + \nu_h \nu_w) (-1 + x_w) x_w + E_w^2 (-1 + \nu_h^2) x_w^2}{E_h (-1 + \nu_w^2) (-1 + x_w) - E_w (-1 + \nu_h^2) x_w}, \quad (4.4)$$

$$E_2 = \frac{E_h E_w (E_h (-1 + \nu_w) (-1 + x_w) - E_w (-1 + \nu_h) x_w)}{Z}, \quad (4.5)$$

$$Z = E_w^2 (-1 + \nu_h + 2\nu_h^2) (-1 + x_w) x_w + E_h^2 (-1 + \nu_w + 2\nu_w^2) (-1 + x_w) x_w - E_h E_w (-1 + 2x_w + (-2 + \nu_h) x_w^2 + \nu_w (-1 + x_w) (-1 + x_w + 4\nu_h x_w)), \quad (4.6)$$

$$G_2 = \frac{E_h E_w}{2(-E_w (1 + \nu_h) (-1 + x_w) + E_h (1 + \nu_w) x_w)}, \quad (4.7)$$

assuming plane strain conditions (i.e.,  $\varepsilon_{zz} = 0$ ),

$$\begin{pmatrix} \varepsilon_{xx} \\ \varepsilon_{yy} \\ \gamma_{xy} \end{pmatrix} = \begin{pmatrix} S_{11} - \frac{S_{13}^2}{S_{11}} & S_{12} - \frac{S_{13} S_{12}}{S_{11}} & 0 \\ S_{12} - \frac{S_{13} S_{12}}{S_{11}} & S_{22} - \frac{S_{12}^2}{S_{11}} & 0 \\ 0 & 0 & S_{44} \end{pmatrix} \cdot \begin{pmatrix} \sigma_{xx} \\ \sigma_{yy} \\ \tau_{xy} \end{pmatrix} = \begin{pmatrix} S_{11} & S_{12} & 0 \\ S_{21} & S_{22} & 0 \\ 0 & 0 & S_{33} \end{pmatrix} \cdot \begin{pmatrix} \sigma_{xx} \\ \sigma_{yy} \\ \tau_{xy} \end{pmatrix}. \quad (4.8)$$

The two upper diagonal terms represent the stiffness of the composite perpendicular and parallel to the layers and are equal to 2278 MPa and 6044 MPa, respectively, which agrees with those obtained from the numerical calculations.

Furthermore, the uniaxial compressive strength of the stratified is equal to 8633 kPa (*i.e.*,  $\sigma_d = x_h \sigma_{d,h} + x_w \sigma_{d,w}$ ) and is the same, when loaded perpendicular or parallel to the layers (*cf.* [49]).

The failure of the stratified rock mass, accounting for the thickness fractions and mechanical properties of the rock layers, was investigated by various authors (*e.g.*, [49], [52], [53]). The uniaxial compressive strength of the stratified rock mass depends on the direction of loading (*cf.* Fig. 4.4). The lowest uniaxial compressive strength occurs at an angle  $\delta = 45^\circ - \varphi_w/2$  between the layers and the loading direction. Hence, at this orientation, the composite behaves as though it was provided with the strength properties ( $c_w, \varphi_w$ ) of the weakest layers (*cf.* [49]). The largest uniaxial compressive strengths occur at an angle of  $\delta = 0^\circ$  and  $90^\circ$  (*cf.* Fig. 4.4).

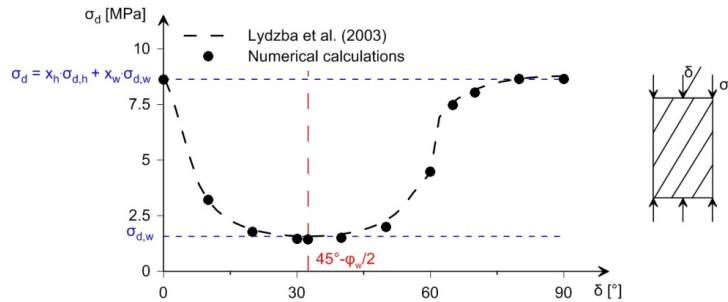


**Figure 4.4.** Uniaxial compressive strength  $\sigma_d$  of the stratified rock mass as a function the angle between loading direction and bedding ( $x_h = x_w = 0.5$ ,  $E_h = 10$  GPa,  $c_h = 5$  MPa,  $E_w = 1$  GPa,  $c_w = 0.5$  MPa,  $\nu_h = \nu_w = 0.3$ ,  $\varphi_h = \varphi_w = 25^\circ$ ,  $\psi_h = \psi_w = 5^\circ$ ).

### 4.2.3 Basic aspects of the bedded rock response to excavation

The ground response to tunnel excavation parallel to the layers is analysed by plane strain numerical computations (as in Section 4.3) for a series of layer thicknesses considering, due to symmetry, only a quarter of the system (Fig. 4.5).

According to Figure 4.6, which presents the displacement as a function of the support pressure for two points (Fig. 4.6a) as well as the displacement distribution along an unsupported excavation boundary (Fig. 4.6b), respectively, the results of the discrete models converge to those of the homogenised model with decreasing layer thickness, thus validating the formulation and numerical implementation of the homogenisation procedure.

Additional evidence is provided by Figure 4.7, which presents the principal stress orientation as well as the stress field beside and above the crown, and by Figure 4.8, which presents the evolution of the plastic zone and of the deformation field during the reduction of the support pressure according to the homogenised model and to a discrete model of very thin alternating layers.

The computational results of Figures 4.6 to 4.8, besides validating the implementation of the homogenised model, provide valuable insight in the response of a thinly stratified rock to tunnel excavation.

According to Figure 4.6, the crown displacement  $u_y$  is larger than the wall displacement  $u_x$ . The reason for this ovalisation of the tunnel cross-section is that the layers beside the tunnel experience a larger tangential strain than the layers above the crown. This is such because the composite stiffness perpendicular (*i.e.*,  $E_{yy} = E_2$ ) to the layers is higher than parallel thereto (*i.e.*,  $E_{xx} = E_1$ , *cf.* Section 4.4.2).

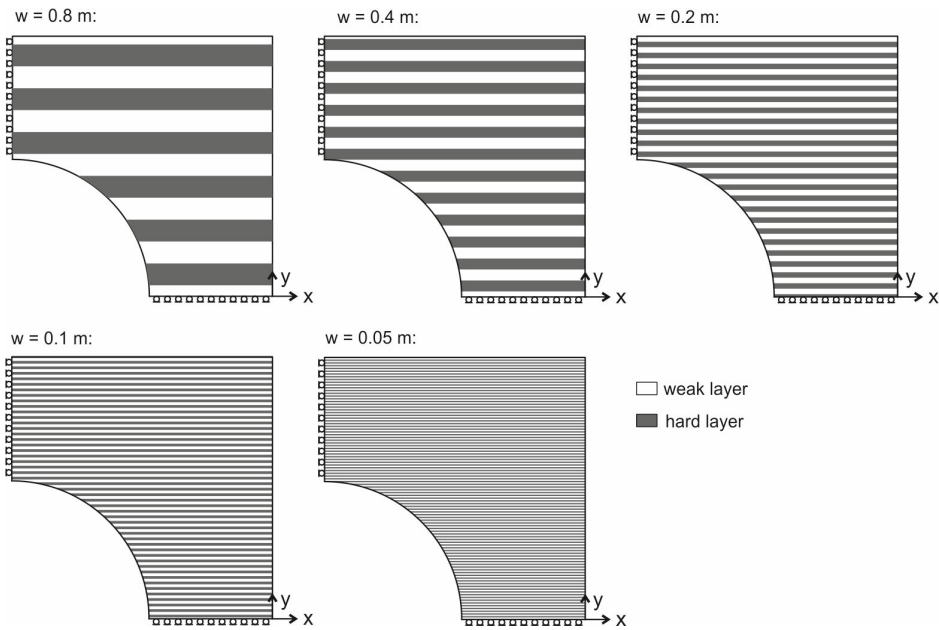


**Figure 4.5.** Discrete models for a rock mass consisting of alternating, 0.05 to 0.8 m thick competent and weak layers.

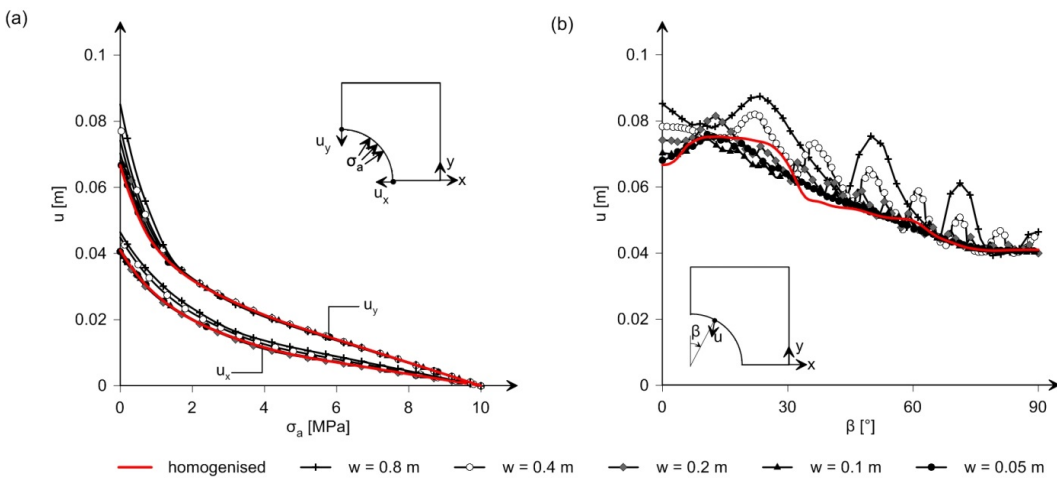


**Figure 4.6.** (a) Horizontal wall displacement and vertical crown displacement as a function of the support pressure, (b), magnitude of the displacement vector along an unsupported tunnel boundary according to the homogenised model (red line) as well as according to the discrete models of Figure 4.5 ( $a = 5 \text{ m}$ ,  $\sigma_0 = 10 \text{ MPa}$ ,  $x_h = x_w = 0.5$ ,  $E_h = 10 \text{ GPa}$ ,  $c_h = 5 \text{ MPa}$ ,  $E_w = 1 \text{ GPa}$ ,  $c_w = 0.5 \text{ MPa}$ ,  $\nu_h = \nu_w = 0.3$ ,  $\phi_h = \phi_w = 25^\circ$ ,  $\psi_h = \psi_w = 5^\circ$ ).

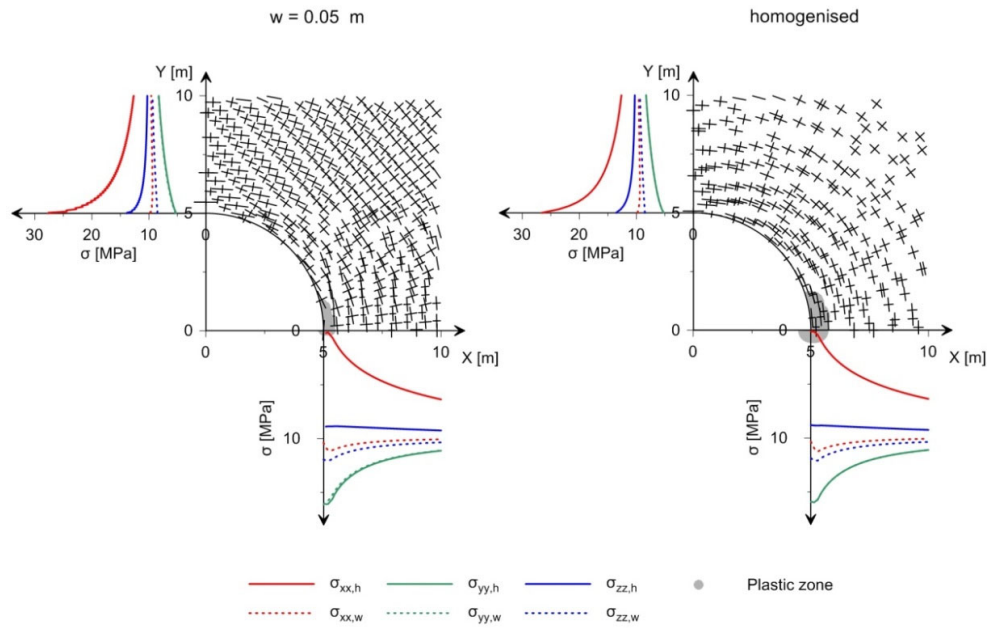


**Figure 4.7.** Principal stress orientation as well as stress field beside the tunnel and above the crown according to the homogenised model (r.h.s.) and to the discrete model of 0.05 m thick alternating layers (l.h.s.) for  $\sigma_a = 5.2$  MPa ( $a = 5$  m,  $\sigma_0 = 10$  MPa,  $x_h = x_w = 0.5$ ,  $E_h = 10$  GPa,  $c_h = 5$  MPa,  $E_w = 1$  GPa,  $c_w = 0.5$  MPa,  $\nu_h = \nu_w = 0.3$ ,  $\varphi_h = \varphi_w = 25^\circ$ ,  $\psi_h = \psi_w = 5^\circ$ ).

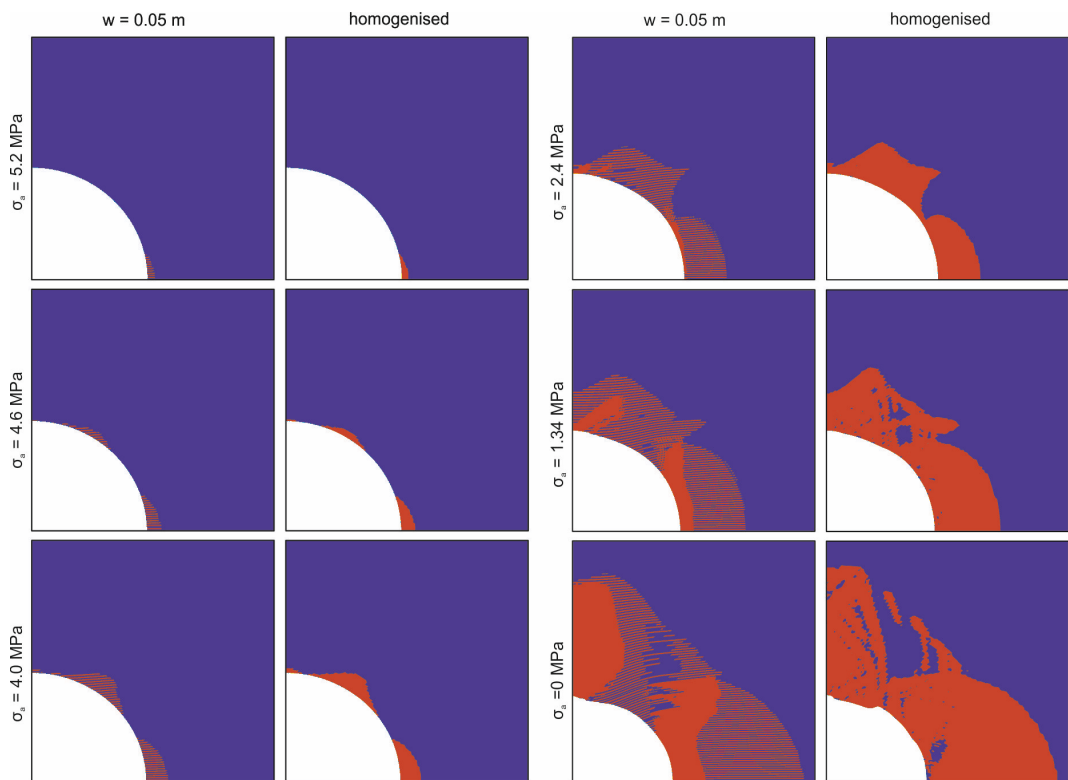


**Figure 4.8.** Plastic zone and deformed mesh (magnified by factor 20) at different support pressures  $\sigma_a$  according to the homogenised model as well as to a discrete model of 0.05 m thick layers (red: plastic points; blue: elastic points;  $a = 5$  m,  $\sigma_0 = 10$  MPa,  $x_h = x_w = 0.5$ ,  $E_h = 10$  GPa,  $c_h = 5$  MPa,  $E_w = 1$  GPa,  $c_w = 0.5$  MPa,  $\nu_h = \nu_w = 0.3$ ,  $\varphi_h = \varphi_w = 25^\circ$ ,  $\psi_h = \psi_w = 5^\circ$ ).

The ovalisation is recognisable already in the elastic range (*i.e.*, for  $\sigma_a > \text{ca. } 5.8 \text{ MPa}$  in the present example), where the radial  $u_{a,r}$  and the tangential displacement  $u_{a,t}$  as well as the tangential stress  $\sigma_t$  along the tunnel boundary (*i.e.*, as a function of  $\theta = 90^\circ - \beta$ , with  $\beta$  after Fig. 4.6b) can be calculated after Hefny and Lo [54]:

$$\sigma_t = \frac{2 + 2(\gamma_1 + \gamma_2)^2 - 2\gamma_1^2\gamma_2^2 - 4(\gamma_1 + \gamma_2)\cos(2\theta)}{(1 + \gamma_1^2 - 2\gamma_1\cos(2\theta))(1 + \gamma_2^2 - 2\gamma_2\cos(2\theta))}(\sigma_0 - \sigma_a) + \sigma_a, \quad (4.9)$$

$$u_{a,r} = \frac{a(\sigma_0 - \sigma_a)}{2(\gamma_1 - \gamma_2)}((\gamma_1\rho_2 - \gamma_2\rho_2) + (\gamma_1\delta_2 - \gamma_2\delta_1)\cos(2\theta)), \quad (4.10)$$

and

$$u_{a,t} = \frac{a(\sigma_0 - \sigma_a)}{2(\gamma_1 - \gamma_2)}(\gamma_2\delta_1 - \gamma_1\delta_2)\cos(2\theta), \quad (4.11)$$

with

$$\gamma_1 = \frac{\alpha_1 - 1}{\alpha_1 + 1}, \quad |\gamma_1| < 1, \quad \gamma_2 = \frac{\alpha_2 - 1}{\alpha_2 + 1}, \quad |\gamma_2| < 1, \quad (4.12)$$

$$\alpha_1^2\alpha_2^2 = \frac{S_{11}}{S_{22}}, \quad \alpha_1^2 + \alpha_2^2 = \frac{2S_{12} + S_{33}}{S_{22}}, \quad (4.13)$$

$$\delta_1 = (1 + \gamma_1)\beta_2 - (1 - \gamma_1)\beta_1, \quad \delta_2 = (1 + \gamma_2)\beta_1 - (1 - \gamma_2)\beta_2, \quad (4.14)$$

$$\rho_1 = (1 + \gamma_1)\beta_2 + (1 - \gamma_1)\beta_1, \quad \rho_2 = (1 + \gamma_2)\beta_1 + (1 - \gamma_2)\beta_2, \quad (4.15)$$

$$\beta_1 = S_{12} - S_{22}\alpha_1^2, \quad \beta_2 = S_{12} - S_{22}\alpha_2^2, \quad (4.16)$$

and  $S_{12}$ ,  $S_{22}$ ,  $S_{21}$  and  $S_{33}$  after Section 4.4.2. (Note that the displacement and the tangential stress along the tunnel boundary for a given support pressure, which originates from Hefny and Lo [54], was corrected in this chapter. The tangential stress obtained with the original formula of Hefny and Lo [54] amounts to zero and the displacements are unequal to zero for  $\sigma_a = \sigma_0$ , which is obviously wrong.) According to Equation (4.9), the tangential stress is slightly higher in the crown than in the side wall (*cf.* Fig. 4.7), while the lowest tangential stress occurs at about  $\beta \approx 40^\circ$ .

With decreasing support pressure, yielding occurs first at the side wall and this in the hard rather than in the weak layers (see results for  $\sigma_a = 5.2 \text{ MPa}$  in Fig. 4.8). This result is somehow surprising at the first glance because the hard layers are subjected to the same tangential stress as the weak layers ( $\sigma_{yy,w} = \sigma_{yy,h} \approx 16.0 \text{ MPa}$ ; Fig. 4.7) and the latter exhibit a lower strength. The hard layers fail first because of the constraint they impose to the lateral (horizontal) extension of the weak layers, which results to a very low radial stress ( $\sigma_{xx,h} \approx 0$ ) in the hard layers (*cf.* Section 4.4.2). It should be noted that, at  $\sigma_a = 5.2 \text{ MPa}$ , the hard layers are subjected to even higher tangential stresses than at the side wall ( $\sigma_{xx,h} \approx 26.6 \text{ MPa}$ , *cf.* Fig. 4.7), but remain elastic; this is such because of the high minimum principal stress (the radial stress at the crown corresponds to the support pressure, *i.e.*  $\sigma_{yy,h} = 5.2 \text{ MPa}$  both in the hard and in the weak layers; Fig. 4.7).

A further decrease in the support pressure  $\sigma_a$  results in yielding of the weak layers within a second plastic zone that starts developing at  $\beta \approx 45^\circ - \varphi_w/2 = 32.5^\circ$  (see results for  $\sigma_a = 4.6 \text{ MPa}$  in Fig. 4.8). At this angle (which corresponds to the angle between the maximum principal stress and the planes of anisotropy), the composite exhibits the lowest

uniaxial compressive strength (Section 4.4.2). Therefore, one might expect that failure, due to the decrease in support pressure, would first occur at this angle  $\beta$  and not at the side wall of the tunnel. However, due to the different stiffness in horizontal and vertical direction ( $E_1 \gg E_2$ ), the tangential stresses in this area (at  $\beta \approx 40^\circ$ ) are reduced, leading thus to a later failure.

As the support pressure  $\sigma_a$  decreases further, the hard layers reach failure also at the tunnel crown (see results for  $\sigma_a = 4.0$  MPa in Fig. 4.8) and afterwards the three plastic zones increase in size. Due to the direction-dependent strength of the composite (*cf.* Fig. 4.4), the second plastic zone does not increase uniformly and symmetrically. As soon as in certain areas both the weak and the hard layers reach their failure criterion, the deformations increase significantly in these areas. This is for example the case, when the second plastic zone meets the third plastic zone (at  $\sigma_a = 2.4$  MPa in Fig. 4.8), thus leading to high deformations in the area of the crown (see  $u$  at  $\beta \approx 10 - 25^\circ$  in Fig. 4.6b).

Further insight into the model behaviour and into the effect of the parameters of the hard layers provide the computational results of Figure 4.9. Specifically, the figure shows for the same parameter set as Figures 4.6 to 4.8 as well as for four additional parameter sets ( $x_h$ ,  $E_h$ ,  $c_h$ ,  $\varphi_h$ ; given in the leftmost column):

- the GRC at the crown and the side wall, including for comparison the GRC in the absence of the hard layers (dashed line; l.h.s diagrams);
- the magnitude of the displacement vector along the tunnel boundary for  $\sigma_a = 0$  (middle diagrams); and
- the plastic zones at support pressures of 0 to 5.2 MPa (r.h.s. diagrams).

The following conclusions can be drawn:

- The hard layers have a considerable stabilising effect (compare dashed with solid lines in the l.h.s. diagrams).
- A decrease in the thickness fraction of the hard layers (from  $x_h/x_w = 1$  to 0.25) results in a less pronounced but still remarkable stabilising effect. Particularly, the first and the third plastic zones (developing at the side wall and the crown of the tunnel, respectively), in which the hard layers reach failure, increase considerably, as the latter are more loaded (compare, *e.g.*, results for  $\sigma_a = 5.2$  MPa in Figs. 4.9a and 4.9b).
- A decrease in the stiffness of the hard layers from  $E_h = 10$  to 2 GPa results to an overall lower stiffness and larger displacements. As the contrast in  $E$  of the weak and the hard layers is smaller than before, the stiffness in horizontal direction (parallel to bedding) is only slightly higher than the one in vertical direction (perpendicular to bedding) and, therefore, the displacement distribution in the elastic range is nearly uniform along the tunnel boundary. Therefore, the weak layers reach failure first (at  $\beta \approx 45^\circ - \varphi_w/2 = 32.5^\circ$ ; see results for  $\sigma_a = 5.2$  MPa in Fig. 4.9c). With a further decrease in the support pressure, the non-uniformity of the displacements in the tunnel profile increases (compare  $u_y$  and  $u_x$  in l.h.s. diagram of Fig. 4.9c), due to the considerable direction-dependent strength of the composite (*cf.* Section 4.4.2).
- A decrease in the cohesion of the hard layers to  $c_h = 3$  MPa leads to a more extended plastification of the composite and thus to considerably larger displacements (Fig. 4.9d). Particularly, the plastic zones, in which the hard layers reach failure, increase considerably.
- An increase in the friction angle of the hard layers (from  $\varphi_h = 25^\circ$  to  $35^\circ$ ) results expectedly in smaller displacements (Fig. 4.9e). However, the effect of the friction angle of the hard layers is rather small compared to the other factors discussed above.

In conclusion, due to the strength and stiffness anisotropy of a stratified rock, a tunnel drive parallel to the bedding is characterised by a very non-uniform deformation of the profile. Principally, the largest deformations occur at locations where the layers are almost (but not exactly) parallel to the excavation boundary (*i.e.*, in the crown for a horizontal stratification).

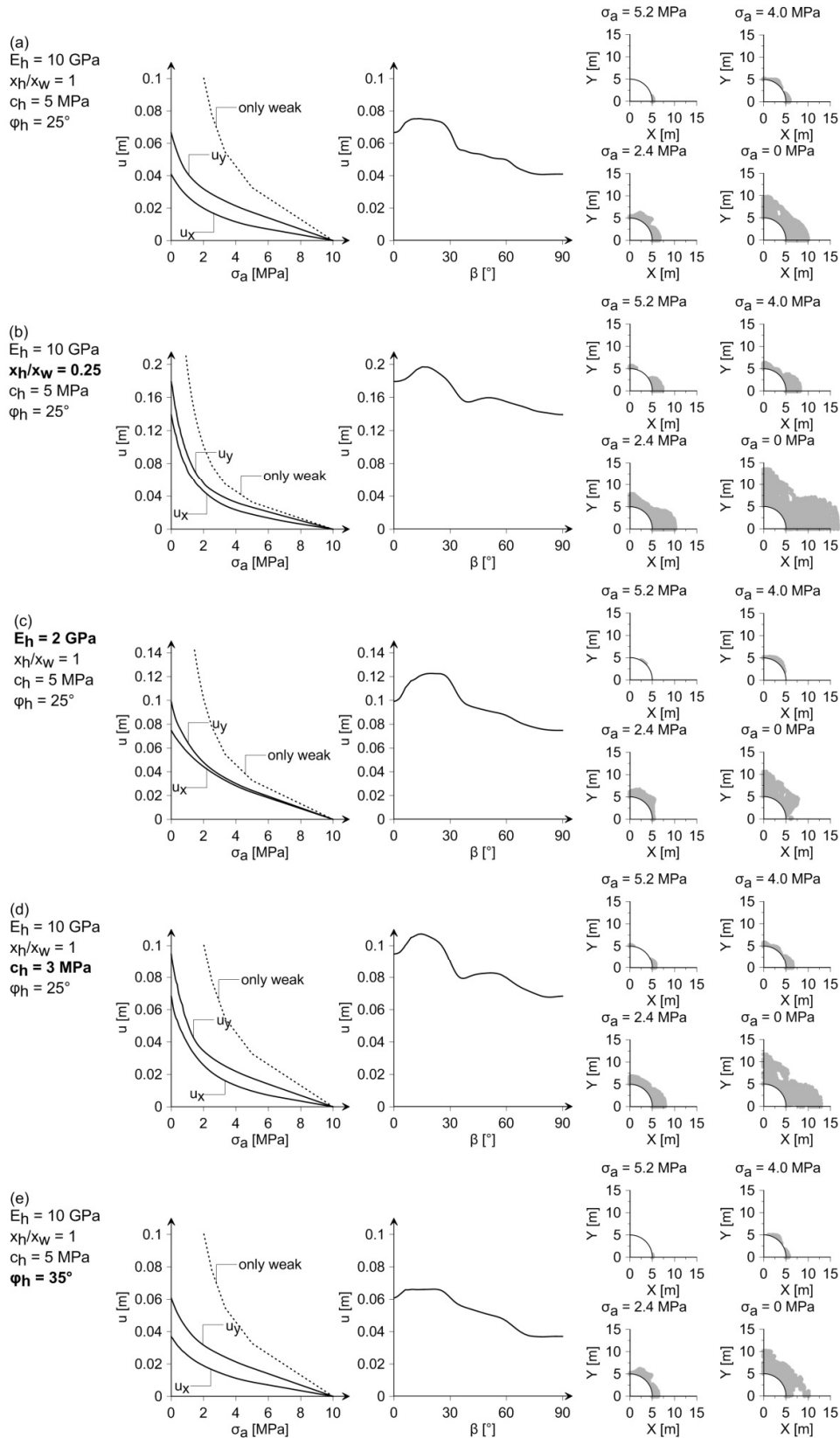


**Figure 4.9.** GRC (*l.h.s. diagrams*), magnitude of the displacement vector along the tunnel boundary for  $\sigma_a = 0$  (*middle diagrams*) and plastic zone (*r.h.s. diagrams*;  $a = 5$  m,  $\sigma_0 = 10$  MPa,  $c_h = 5$  MPa,  $E_w = 1$  GPa,  $c_w = 0.5$  MPa,  $v_h = v_w = 0.3$ ,  $\phi_h = \phi_w = 25^\circ$ ,  $\psi_h = \psi_w = 5^\circ$ ).

The displacement distribution may be even more non-uniform if the *in situ* stress field is non-hydrostatic; for example, according to Hefny and Lo [54], the crown displacement

increases, while the side wall displacement decreases with decreasing initial stress ratio  $K_0$ .

#### 4.2.4 Development of nomograms

This section develops dimensionless diagrams for the minimum, average and maximum magnitude of the displacement vector of the tunnel boundary.

The magnitude of the displacement vector in a specific location  $\beta$  of the tunnel boundary depends on all parameters of the problem under consideration:

$$u = f(x_h, E_h, \nu_h, \varphi_h, \sigma_{d,h}, \psi_h, x_w, E_w, \nu_w, \varphi_w, \sigma_{d,w}, \psi_w, \sigma_0, \sigma_a, a). \quad (4.17)$$

A dimensional analysis in combination with the findings of Section 3.2 and with the general property of elasto-plastic continua, according to which the displacements are inversely proportional to Young's modulus [60], suggests that the displacement  $u$  can be expressed as follows:

$$\frac{u}{u_{w,2D}} = f\left(\frac{x_h}{x_w}, \frac{E_h}{E_w}, \frac{\sigma_{d,h}}{\sigma_{d,w}}, \frac{\sigma_{d,w}}{\sigma_0}, \frac{\sigma_a}{\sigma_0}, \nu_h, \varphi_h, \psi_h, \nu_w, \varphi_w, \psi_w\right), \quad (4.18)$$

where  $u_{w,2D}$  is the radial displacement of a tunnel crossing only weak rock and can be computed using known closed-form equations (e.g., those of [60]). As the aforementioned property of elasto-plastic continua was proven only for an isotropic material, the correctness of the normalisation of Equation (4.18) was checked by performing a series of numerical calculations: As can be seen from Figure 4.10, the displacements  $u/u_{w,2D}$  obtained for different values of the initial stress  $\sigma_0$  and the Young's modulus of the weak layers  $E_w$  fall on one single curve.

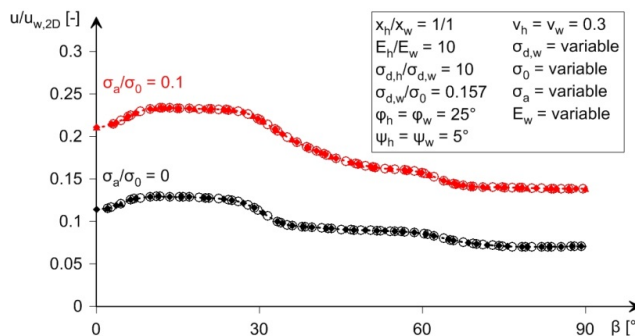


**Figure 4.10.** Normalised magnitude of the displacement vector along the tunnel boundary.

In order to reduce the computational effort, the numerical analyses were only carried out for specific ground parameters (according to Table 4.1). For the sake of simplicity, only Poisson's ratios of the hard and the weak layers amounting to 0.3 will be considered. Moreover, it can be assumed that the dilatancy angles  $\psi_h$  and  $\psi_w$  are interconnected with the friction angles. Furthermore, use will be made of the fact that weaker materials are generally also softer, exhibiting a Young's modulus in the order of 500 to 1000 times the uniaxial strength, which means that solely specific moduli ratio  $E_h/E_w$  have to be considered for given ratio  $\sigma_{d,h}/\sigma_{d,w}$  (cf. Section 3.3).

As the friction angle  $\varphi_h$  of the hard layers has a rather small influence on the tunnel displacements (cf. Section 4.2.3) and, for given cohesion of the hard layers, the assumption of a lower friction angle is on the safe side, the dimensionless diagrams were worked out only for  $\varphi_h = \varphi_w = \varphi = 20^\circ$  or  $30^\circ$  although  $\varphi_h$  is usually higher than  $\varphi_w$ .

In order to cover a wide range of parameters, but to reduce the computational effort anyway, only specific values of the thickness fraction  $x_h/x_w$ , of the strength ratio  $\sigma_{d,h}/\sigma_{d,w}$  and of the normalised support pressure  $\sigma_a/\sigma_0$  will be considered. The latter was chosen

such as to cover the practically important part of the GRC (at  $\sigma_{a1} = 0$ ,  $\sigma_{a2} = 0.1\sigma_0$  and  $\sigma_{a3} = 0.2\sigma_0$ ).

Bearing in mind that some of the parameters have been fixed, the maximum, minimum and averaged displacement along the tunnel boundary depend on the following parameters:

$$\frac{u_{max}}{u_{w,2D}}, \frac{u_{min}}{u_{w,2D}}, \frac{u_{average}}{u_{w,2D}} = f\left(\frac{\sigma_{d,w}}{\sigma_0}, \frac{x_h}{x_w}, \frac{E_h}{E_w}, \frac{\sigma_{d,h}}{\sigma_{d,w}}, \frac{\sigma_a}{\sigma_0}, \varphi\right). \quad (4.19)$$

The nomograms of Appendix I show these three normalised displacement values as a function of the normalised strength  $\sigma_{d,w}/\sigma_0$  of the weak layers in a series of figures. Each figure applies to a certain parameter set ( $\sigma_a/\sigma_0$ ,  $\sigma_{d,h}/\sigma_{d,w}$ ,  $x_h/x_w$ ) and contains a number of diagrams (each applying to another set ( $\varphi$ ,  $E_h/E_w$ )).

As the normalised displacements on the l.h.s. of Equation (4.19) are equal to 1 in the absence of hard layers, the nomograms of Appendix I show directly the stabilising effect of the hard layers.

For an unsupported tunnel, the ratio  $u/u_{w,2D}$  decreases (*i.e.*, the stabilising effect becomes more pronounced) with decreasing normalised strength  $\sigma_{d,w}/\sigma_0$  of the weak layers. Therefore, the nomograms are useful particularly for squeezing rocks. For large values of  $\sigma_{d,w}/\sigma_0$ , the weak and the hard layers behave elastically and the normalised displacements remain constant. In this case, the displacements can be calculated also after Hefny and Lo [54], but the nomograms can be used for a fast estimation of the tunnel displacements.

**Table 4.1.** Overview of the considered parameter ranges for the nomograms.

$x_h/x_w$ [-]	1/8 – 2		
$\sigma_{d,h}/\sigma_{d,w}$ [-]	2	6	10
$E_h/E_w$ [-]	1 - 4	3 - 12	5 - 20
$\nu_h = \nu_w$ [-]	0.3		
$\varphi = \varphi_h = \varphi_w$ [°]	20; 30		
$\psi_h = \psi_w$ [°]	1 for $\varphi_h = \varphi_w = 20^\circ$ 10 for $\varphi_h = \varphi_w = 30^\circ$ (according to [68])		
$\sigma_a/\sigma_0$ [-]	0; 0.1; 0.2		

## 4.2.5 Parameters of an equivalent isotropic material

### 4.2.5.1 Procedure

The response of a transversely isotropic material to tunnel excavation is very different from that of an isotropic material. It is thus obvious that an "equivalent" or "practically equivalent" isotropic material cannot exist. The notion of "equivalent material" is used here for simplicity and only in the following sense: It is equivalent in the sense that its (uniform) excavation-induced displacement is equal to the maximum, to the average or to the minimum displacement of the transversely isotropic rock. In spite of its obvious limitations, such an equivalent material model is valuable because it allows to determine an upper and a lower limit of the deformations of the profile.

The parameters of the equivalent isotropic elasto-plastic material can be determined analogously to Section 3.3, but using the nomograms of Appendix I. However, contrarily to Section 3.3, the displacements in a tunnel drive parallel to the bedding are very non-uniform along the tunnel boundary, which makes the determination of equivalent parameters more difficult. In the following, the procedure will be described based upon an example.

Section 4.2.3 showed that the bigger the contrast in the mechanical parameters of the weak and of the hard layers is, the less uniform the displacements of the tunnel profile will be.

Hence, an extreme case with  $E_h/E_w = 20$  and  $c_h/c_w = 10$  will be considered here, for which the non-uniformity of the displacement-distribution is considerable (Fig. 4.11a). For design purposes, usually the range of the displacements is assessed, considering therefore the maximum and the minimum displacement of the tunnel profile. (The consideration of the average values might make sense for dimensioning a stiff lining. Preliminary computational investigations show that the rock pressure distribution is approximately uniform even in a transversely isotropic rock; Fig. 4.11b.)

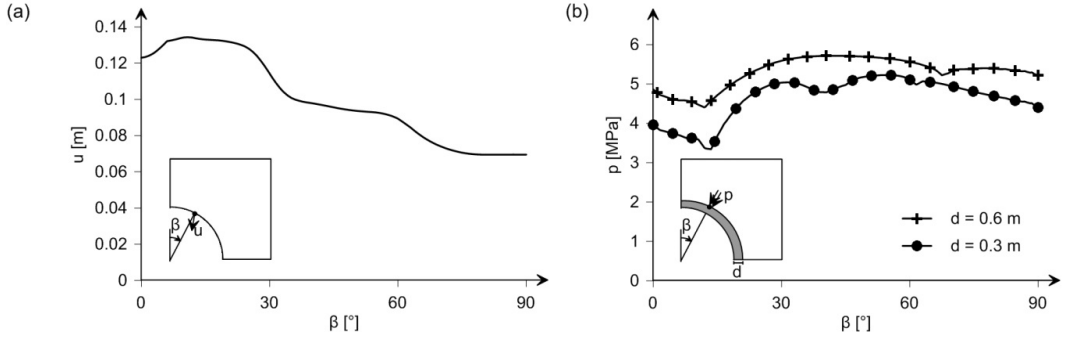


**Figure 4.11.** (a) Magnitude of the displacement vector along the tunnel boundary for  $\sigma_a=0$ ; (b) Radial pressure along a stiff lining ( $a = 5 \text{ m}$ ,  $\sigma_0 = 10 \text{ MPa}$ ,  $x_h/x_w = 0.25$ ,  $E_h = 20 \text{ GPa}$ ,  $c_h = 10 \text{ MPa}$ ,  $E_w = 1 \text{ GPa}$ ,  $c_w = 1 \text{ MPa}$ ,  $\nu_h = \nu_w = 0.3$ ,  $\varphi_h = \varphi_w = 20^\circ$ ,  $\psi_h = \psi_w = 1^\circ$ , lining thickness  $0.3 - 0.6 \text{ m}$ , Young's modulus of concrete =  $30 \text{ GPa}$ , frictionless rock-lining interface, 20% pre-deformation).

The GRC of the equivalent isotropic model can be written as follows:

$$u_a = \frac{\sigma_0 \cdot a}{E_{eq}} \cdot f_2 \left( \frac{\sigma_a}{\sigma_0}, \frac{\sigma_{d,eq}}{\sigma_0}, \nu_{eq}, \varphi_{eq}, \psi_{eq} \right), \quad (4.20)$$

where  $E_{eq}$ ,  $\nu_{eq}$ ,  $\sigma_{d,eq}$ ,  $\varphi_{eq}$  and  $\psi_{eq}$  denote the equivalent Young's modulus, Poisson's ratio, uniaxial compressive strength, friction angle and dilatancy angle. Parameters are sought that reproduce either the minimum or the maximum displacement of the transversely isotropic rock mass.

In the following, for the sake of simplicity, only the case of equal Poisson's ratios ( $\nu_{eq} = \nu_h = \nu_w$ ) will be considered. The equivalent Young's modulus  $E_{eq}$  can be calculated by setting the displacement of an elastic unsupported isotropic rock mass equal either to the maximum ( $u_{max}$ ; in order to estimate an upper limit of the displacements of the transversely isotropic material) or to the minimum ( $u_{min}$ ; in order to estimate a lower limit of the displacements) magnitude of the displacement vector in an elastic, transversely isotropic rock mass:

$$\left( \sqrt{u_{a,r}^2 + u_{a,t}^2} \right)_{max} = \frac{1 + \nu_{eq}}{E_{eq,max}} \cdot \sigma_0 \cdot a, \quad (4.21)$$

$$\left( \sqrt{u_{a,r}^2 + u_{a,t}^2} \right)_{min} = \frac{1 + \nu_{eq}}{E_{eq,min}} \cdot \sigma_0 \cdot a, \quad (4.22)$$

where the radial and tangential displacements of the transversely isotropic rock mass ( $u_{a,r}$ ,  $u_{a,t}$ ) can be calculated after Hefny and Lo [54]; Eqs. 4.10 and 4.11).

Setting the maximum displacement  $u_{max}$  (or the minimum displacement  $u_{min}$ ) of the transversely isotropic material ( $u_{max}$  and  $u_{min}$  can be obtained from the nomograms of Appendix I) equal to those of the equivalent isotropic model (Eq. 4.20) for three selected values of the support pressure ( $\sigma_{a1}$ ,  $\sigma_{a2}$ ,  $\sigma_{a3}$ ; preferably in the practical relevant range), provides a system of three nonlinear equations for the unknown plasticity parameters  $\sigma_{d,eq}/\sigma_0$ ,  $\varphi_{eq}$  and  $\psi_{eq}$ :

$$u_{max} = \frac{\sigma_0 \cdot a}{E_w} \cdot f \left( \frac{x_h}{x_w}, \frac{E_h}{E_w}, \frac{\sigma_{d,h}}{\sigma_{d,w}}, \frac{\sigma_{d,w}}{\sigma_0}, \frac{\sigma_{ak}}{\sigma_0}, \nu_h, \varphi_h, \psi_h, \nu_w, \varphi_w, \psi_w \right) \quad (\text{for } k = 1, 2, 3), \quad (4.23)$$

$$= \frac{\sigma_0 \cdot a}{E_{eq,max}} \cdot f_2 \left( \frac{\sigma_{ak}}{\sigma_0}, \frac{\sigma_{d,eq,max}}{\sigma_0}, \nu_{eq}, \varphi_{eq,max}, \psi_{eq,max} \right)$$

$$u_{min} = \frac{\sigma_0 \cdot a}{E_w} \cdot f \left( \frac{x_h}{x_w}, \frac{E_h}{E_w}, \frac{\sigma_{d,h}}{\sigma_{d,w}}, \frac{\sigma_{d,w}}{\sigma_0}, \frac{\sigma_{ak}}{\sigma_0}, \nu_h, \varphi_h, \psi_h, \nu_w, \varphi_w, \psi_w \right) \quad (\text{for } k = 1, 2, 3). \quad (4.24)$$

$$= \frac{\sigma_0 \cdot a}{E_{eq,min}} \cdot f_2 \left( \frac{\sigma_{ak}}{\sigma_0}, \frac{\sigma_{d,eq,min}}{\sigma_0}, \nu_{eq}, \varphi_{eq,min}, \psi_{eq,min} \right)$$

Applying this procedure to the parameters of the example of Figure 4.11 provides the equivalent parameters given in Table 4.2. Figure 4.12 compares the two GRCs of the isotropic rock mass (obtained with the two sets of equivalent parameters – one set based upon  $u_{min}$  and one set based upon  $u_{max}$ ) with the GRCs of the transversely isotropic material and shows that the equivalent isotropic model reproduces well the maximum or minimum displacement of the composite material and this even in the case of a big contrast in the mechanical parameters of the layers.

**Table 4.2.** Parameters of the hard and weak layers and corresponding parameters of the equivalent isotropic material.

	$x$ [-]	$E$ [GPa]	$\nu$ [-]	$c$ [MPa]	$\varphi$ [°]	$\psi$ [°]
hard layers	0.20	20	0.3	10	20	1
weak layers	0.80	1	0.3	1	20	1

Equivalent isotropic material fitted based upon:

$u_{max}$	-	1.26	0.3	2.12	20	1
$u_{min}$	-	2.95	0.3	3.45	1	1

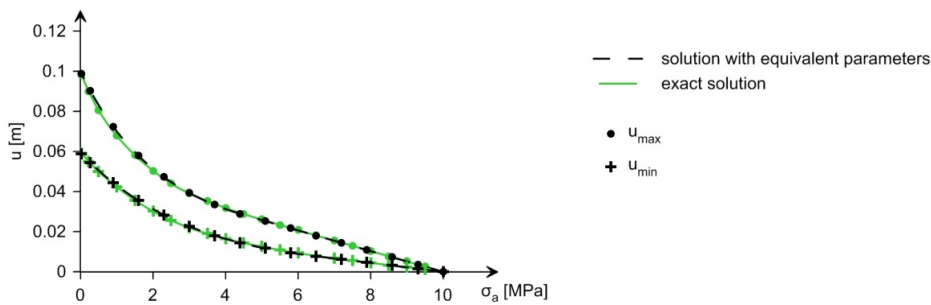


**Figure 4.12.** Maximum and minimum displacement at the tunnel boundary of a cylindrical tunnel as a function of the support pressure, obtained with the exact model and with the isotropic model considering equivalent parameters ( $a = 5$  m,  $\sigma_0 = 10$  MPa).

#### 4.2.5.2 Application examples

The value of using the proposed equivalent isotropic model will be illustrated by means of two tunnelling problems (considering an initial hydrostatic stress field of 10 MPa): (1) The longitudinal displacement profile of an unsupported tunnel (Fig. 4.13a); (2) The boundary displacements of an unsupported tunnel with a horseshoe profile assuming plane strain conditions (Fig. 4.13b).

These problems were solved numerically, either using the exact transversely isotropic material model of Section 4.2.2 (with the parameters given in the two first rows of Table 4.2) or considering an equivalent isotropic rock mass (with the parameters given in the last two rows of Table 4.2). (Numerical details for problem 1 can be found in Section 5.1.)

Figure 4.13 shows that the exact solution lies in-between the two solutions obtained considering an isotropic material. Using latter allows thus to bound satisfactorily the response of transversely anisotropic rock mass.

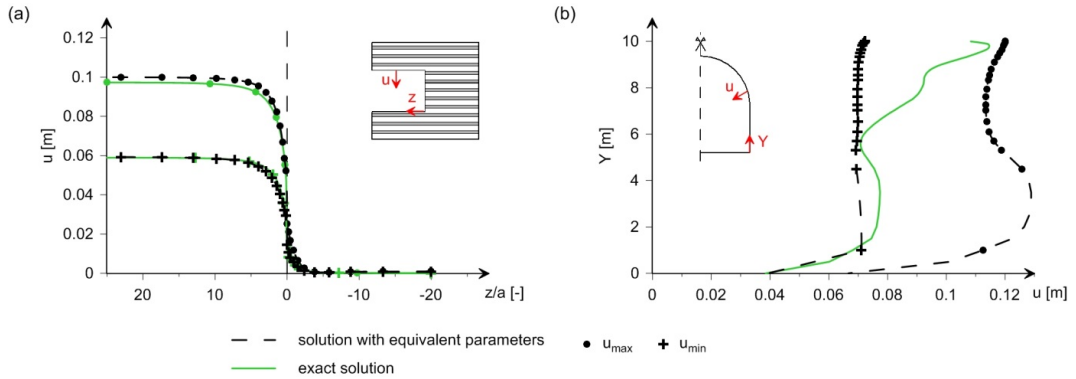


**Figure 4.13.** (a) Maximum and minimum longitudinal displacement profile of an unsupported tunnel. (b) Maximum and minimum magnitude of the displacement vector along the unsupported tunnel boundary of a horseshoe profile, obtained with the exact model and with the equivalent isotropic model (parameters after Table 4.2).

## 4.2.6 Conclusions

This chapter investigated the squeezing behaviour during tunnelling parallel to a sequence of thinly alternating weak and hard rocks, taking the rock mass as a homogeneous, transversely isotropic material. By means of application examples, the rock response to tunnelling was discussed, by specially focussing on the non-uniformity of the displacements in the tunnel profile, which may be considerable in certain cases. In order to facilitate the estimation of the displacements along the tunnel profile for given geotechnical conditions, design diagrams were developed that represent a valuable tool for engineering practice, as they enable to determine easily the maximum and minimum displacements in the tunnel profile (far behind the tunnel face) for a wide range of geotechnical conditions.

Furthermore, these diagrams allow determining the parameters of an equivalent isotropic rock mass based upon the maximum or the minimum displacement of the transversely isotropic material. Considering an isotropic material with these parameters makes it possible to estimate the range of deformations or pressures in problems that do not meet plane strain or rotationally symmetric conditions.

## 4.3 Influence of the heterogeneity scale on the distribution of the ground displacements in the profile

### 4.3.1 Introduction

Alternating weak and hard layers lying parallel to the tunnel axis may lead – depending on the heterogeneity scale (see Section 4.1) – to a considerable non-uniformity of the displacement distribution in the tunnel profile. The present section investigates: (i), under which conditions the homogenised model of Section 4.2 is adequate; (ii), in which cases the heterogeneity of the ground can be neglected in the design; and, (iii), whether the simple equation of Section 3.4.3 can be applied to the case of alternating layers that strike parallel to the tunnel axis.

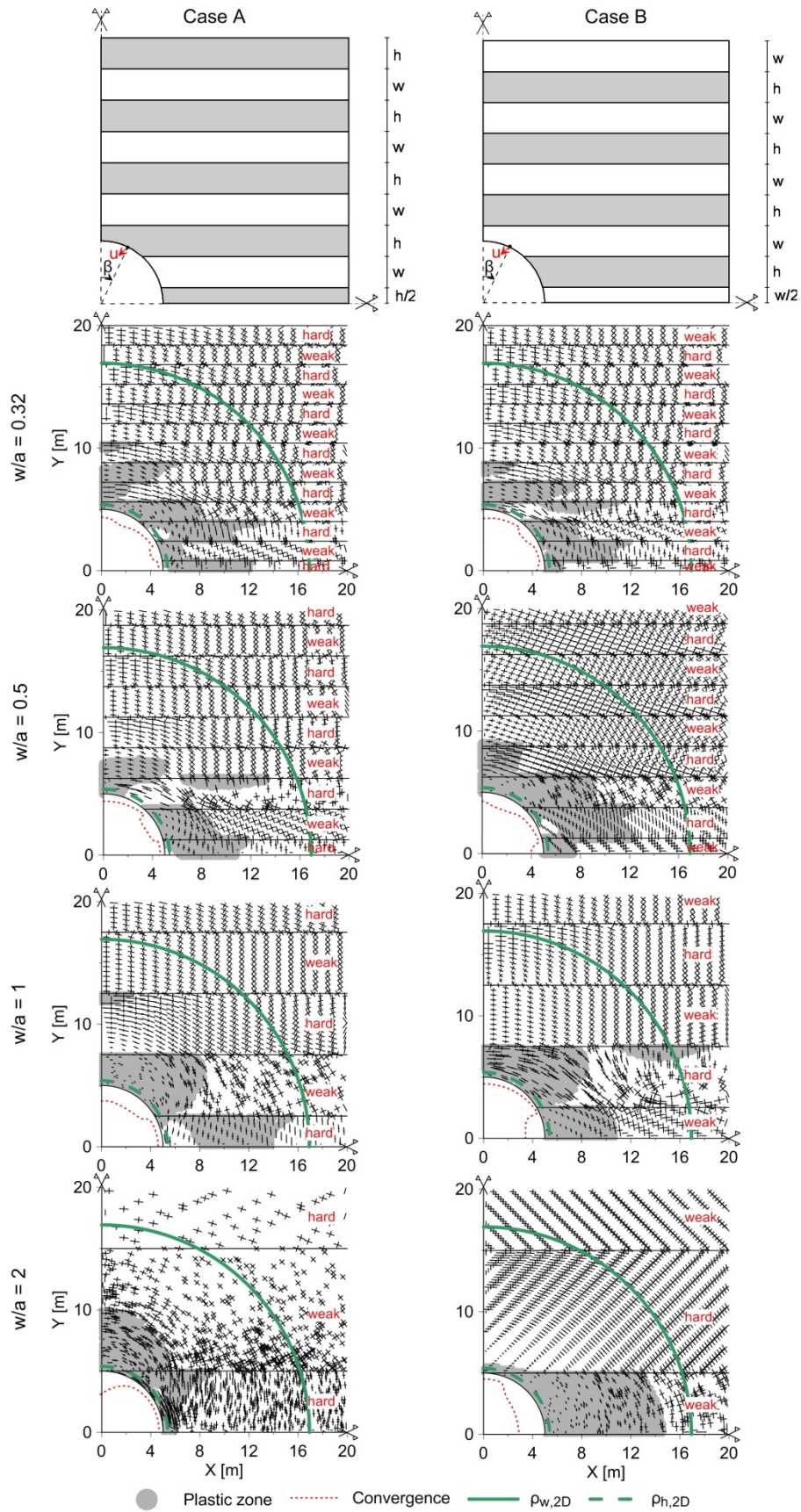
### 4.3.2 Adequacy of the homogenised model

Obviously, the homogenised model of a transversely isotropic rock mass is adequate if the layers are sufficiently thin relative to the tunnel radius. It is also obvious that if the contrast in the mechanical parameters of the layers is small, then homogenisation is adequate even for relatively thick layers. The bigger the contrast in the mechanical parameters, the thinner the layers must be in order to consider the rock mass as a homogeneous material in the scale of the tunnel cross-section.

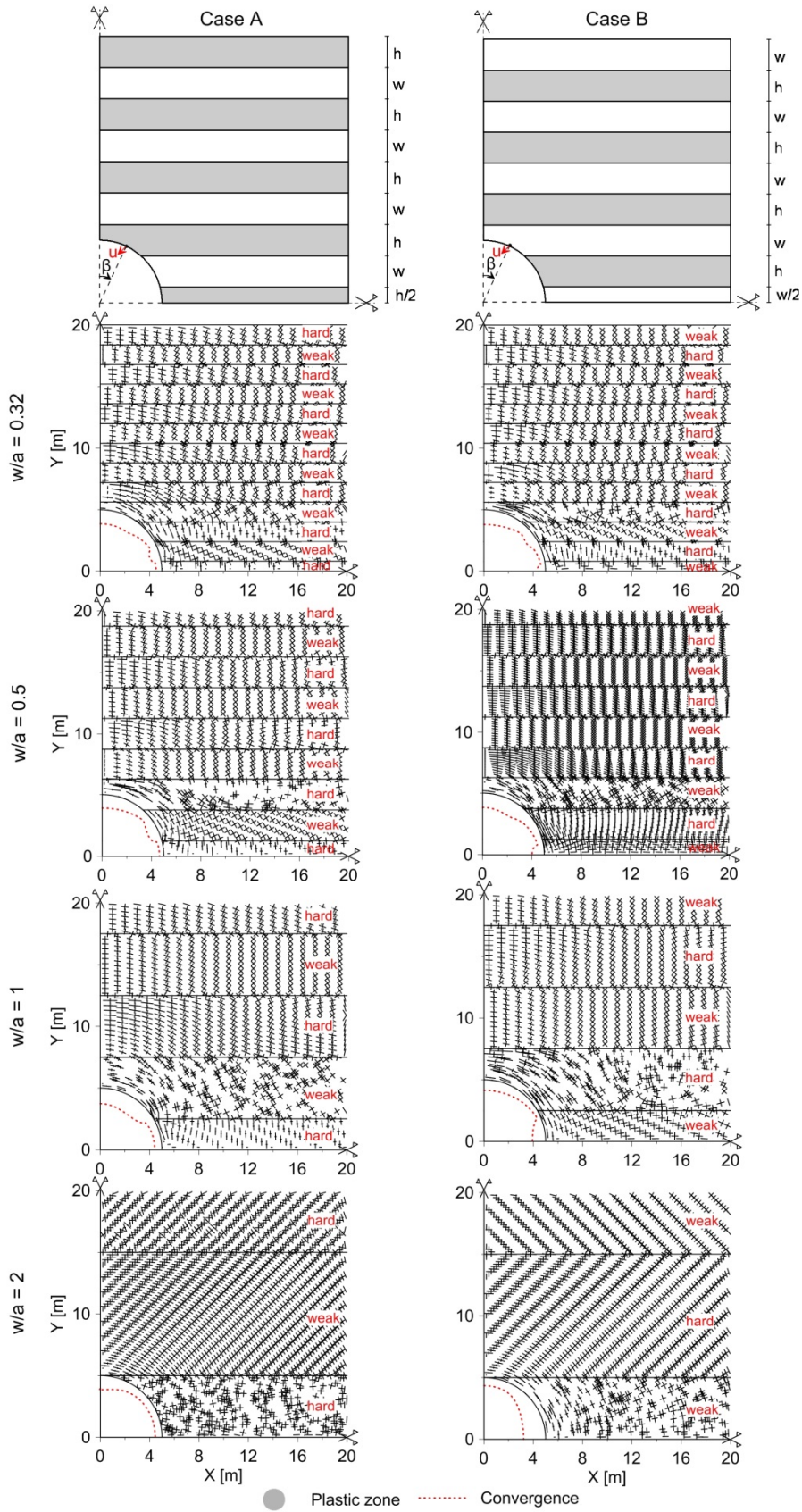
This will be illustrated by means of computational examples. The ground response to tunnel excavation is analysed by plane strain numerical calculations for a series of thicknesses of the hard  $h$  and the weak  $w$  layers as in Section 4.2.3. Besides an initial stress  $\sigma_0$  of 10 MPa (which in combination with the weak layer parameters results in severe squeezing conditions) also a low initial stress was considered (0.75 MPa) in order to check, whether the statements of this chapter also apply to slightly (or non-) squeezing conditions. (For the lower initial stress and the assumed strength parameters, both the hard and the weak layers behave elastically.) For simplicity, an unsupported tunnel crossing equally thick weak and hard layers will be considered first; the effect of the thickness ratio  $h/w$  will be discussed later.

Figure 4.14 shows the deformed tunnel boundary (red dotted line), the stress trajectories (crosses) and the plastic zone (grey) for a series of  $w/a$ -ratios, two only slightly different layer sequences ("case A/B"; see sketches at the top) and an initial stress of 10 MPa. For comparison, also the plastic radius of a homogeneous isotropic material (with the parameters either of the weak or of the hard layers) is presented (green lines). Figure 4.16 shows the distribution of the magnitude of the displacement vector along the tunnel boundary for the same  $w/a$ -ratios as Figure 4.14 and the mentioned cases A and B. Figures 4.15 and 4.17 present the same results for the lower initial stress of 0.75 MPa. The following conclusions can be drawn from these figures:

- The exact location of the layers in the tunnel profile can affect considerably the displacement distribution, particularly if the layers are not very thin; compare Case A (hard layer at the springline) with Case B (weak layer at the springline) in Figures 4.14 to 4.17.
- The principal stress axes deviate from the radial and tangential direction, indicating an arching in the weak layers against the hard layers, leading thus to an additional loading of the latter (Figs. 4.14 and 4.16).
- The stabilising effect (but also the overstressing) of the hard layers is particularly evident for thin layers under a high initial stress; the plastic zone would be considerably more extended in the absence of the hard layers and much more narrow in the absence of the weak layers.
- Due to arching, the maximum displacements for  $\sigma_0 = 10$  MPa amount to about 25% of those that would develop in the absence of the hard layers (Fig. 4.16). The stabilising effect of the latter is smaller for  $\sigma_0 = 0.75$  MPa ( $u_{max}/u_{w,2D} \approx 0.55$ ; Fig. 4.17).



**Figure 4.14.** Convergence  $u$  (magnified by factor 5), plastic zone (hatched area) and principal stress orientation for different thickness and location of the weak and of the hard layers ( $\sigma_0 = 10$  MPa,  $a = 5$  m,  $h/w = 1$ ,  $E_h = 10$  GPa,  $c_h = 5$  MPa,  $E_w = 0.5$  GPa,  $c_w = 0.5$  MPa,  $\nu_h = \nu_w = 0.3$ ,  $\phi_h = \phi_w = 25^\circ$ ,  $\psi_h = \psi_w = 5^\circ$ ).



**Figure 4.15.** Convergence  $u$  (magnified by factor 250), plastic zone (hatched area) and principal stress orientation for different thickness and location of the weak and of the hard layers ( $\sigma_0 = 0.75$  MPa,  $a = 5$  m,  $h/w = 1$ ,  $E_h = 10$  GPa,  $c_h = 5$  MPa,  $E_w = 0.5$  GPa,  $c_w = 0.5$  MPa,  $\nu_h = \nu_w = 0.3$ ,  $\varphi_h = \varphi_w = 25^\circ$ ,  $\psi_h = \psi_w = 5^\circ$ ).

- With decreasing layer thickness, the results of the discrete models converge to those of the homogenised models (Figs. 4.16 and 4.17). In these example, homogenisation is adequate if  $w/a = h/a < 0.16$ .
- Expectedly, the displacements along the tunnel profile are very non-uniform even for the homogenised model. This is such because the composite stiffness perpendicular to the layers is lower than parallel thereto (cf., e.g., [55], [73]).

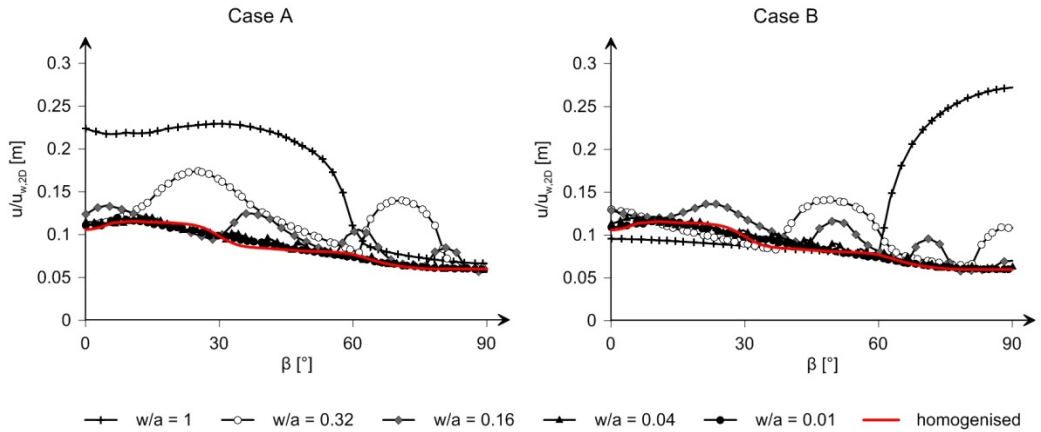


**Figure 4.16.** Magnitude of the displacement vector along the tunnel boundary according to the homogenised model (red line) as well as according to the discrete models (black lines; cf. inset of Fig. 4.14;  $\sigma_0 = 10$  MPa,  $a = 5$  m,  $h/w = 1$ ,  $E_h = 10$  GPa,  $c_h = 5$  MPa,  $E_w = 0.5$  GPa,  $c_w = 0.5$  MPa,  $\nu_h = \nu_w = 0.3$ ,  $\varphi_h = \varphi_w = 25^\circ$ ,  $\psi_h = \psi_w = 5^\circ$ ).

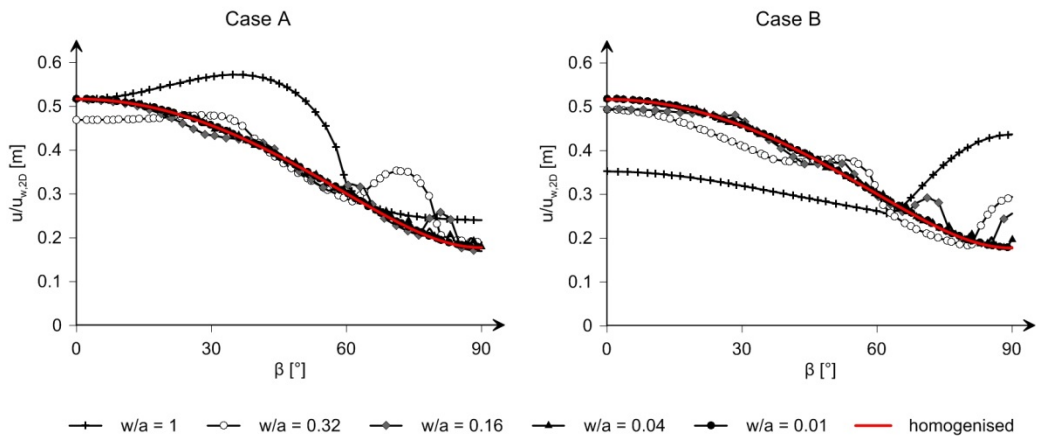


**Figure 4.17.** Magnitude of the displacement vector along the tunnel boundary according to the homogenised model (red line) as well as according to the discrete models (black lines; cf. inset of Fig. 4.15;  $\sigma_0 = 0.75$  MPa,  $a = 5$  m,  $h/w = 1$ ,  $E_h = 10$  GPa,  $c_h = 5$  MPa,  $E_w = 0.5$  GPa,  $c_w = 0.5$  MPa,  $\nu_h = \nu_w = 0.3$ ,  $\varphi_h = \varphi_w = 25^\circ$ ,  $\psi_h = \psi_w = 5^\circ$ ).

In order to estimate the applicability limit of the homogenisation, it is sufficient to consider the maximum and the minimum displacement at the tunnel boundary. The l.h.s. diagrams of Figures 4.18 and 4.19 show (for  $\sigma_0 = 10$  and 0.75 MPa, respectively) these displacements as a function of the weak layer thickness  $w/a$  and of the thickness-ratio  $h/w$ . The homogenised solution (which is strictly correct only for  $w/a \rightarrow 0$  or  $h/a \rightarrow 0$ ) is marked by the red symbols on the ordinate axis.

The middle and r.h.s. diagrams of the Figures 4.18 and 4.19 show the ratio  $u_{max}/u_{max,hom}$  as a function of the normalised layer thickness  $w/a$  and  $h/a$ , respectively, for a series of thickness ratios  $h/w$ . The error of the homogenised solution is zero if the ratio  $u_{max}/u_{max,hom} = 1$  and increases with the ratio  $u_{max}/u_{max,hom}$ .

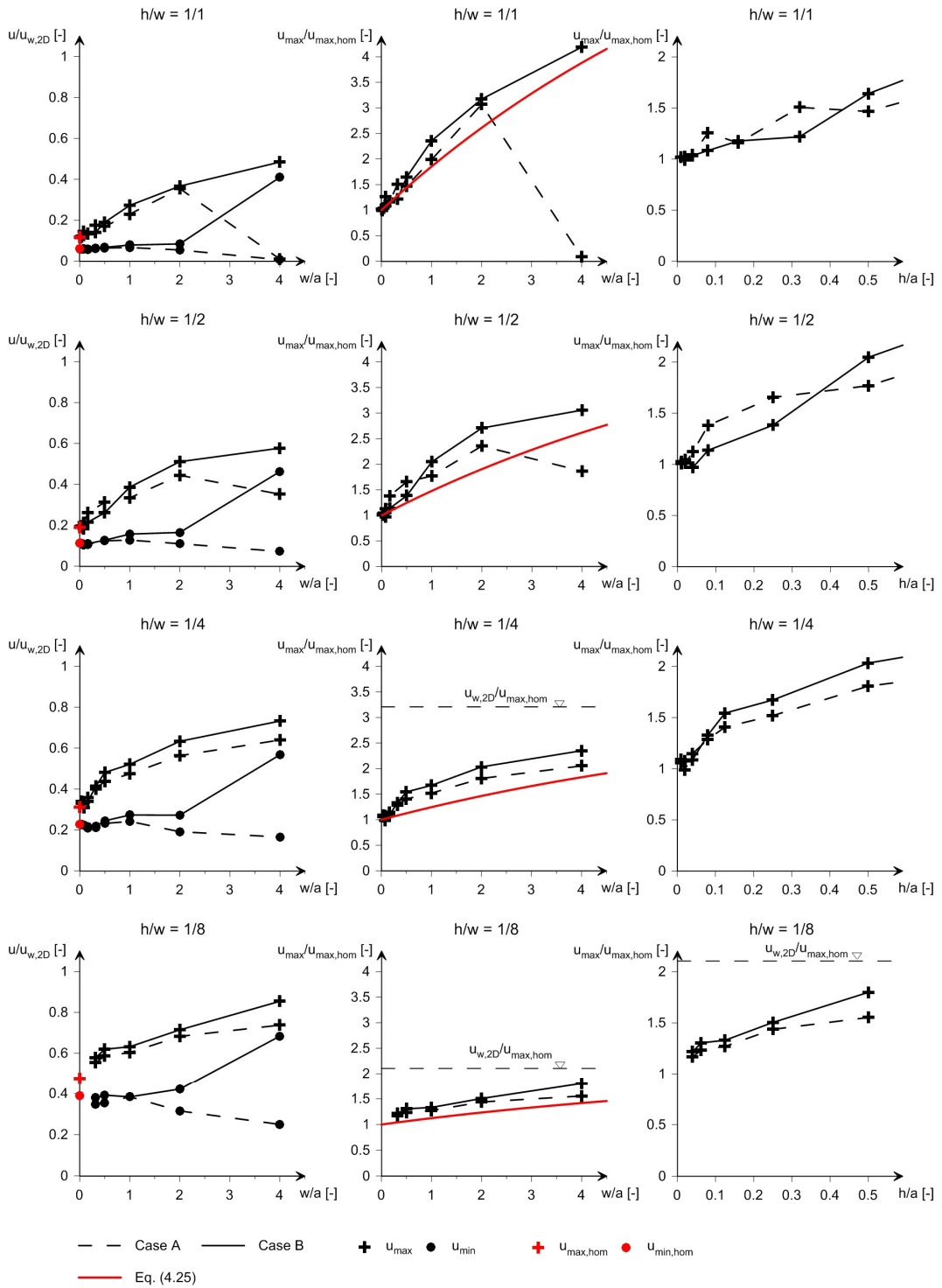


**Figure 4.18.** Maximum  $u_{max}$  and minimum  $u_{min}$  displacements (normalised by the displacements of a homogeneous weak ground  $u_{w,2D}$ ), compared with the displacements of the maximum  $u_{max,hom}$  and minimum  $u_{min,hom}$  displacements of the homogenised solution ( $\sigma_0 = 10$  MPa,  $a = 5$  m,  $E_h = 10$  GPa,  $c_h = 5$  MPa,  $E_w = 0.5$  GPa,  $c_w = 0.5$  MPa,  $\nu_h = \nu_w = 0.3$ ,  $\varphi_h = \varphi_w = 25^\circ$ ,  $\psi_h = \psi_w = 5^\circ$ ; cases A and B: see inset at the top of Fig. 4.14).

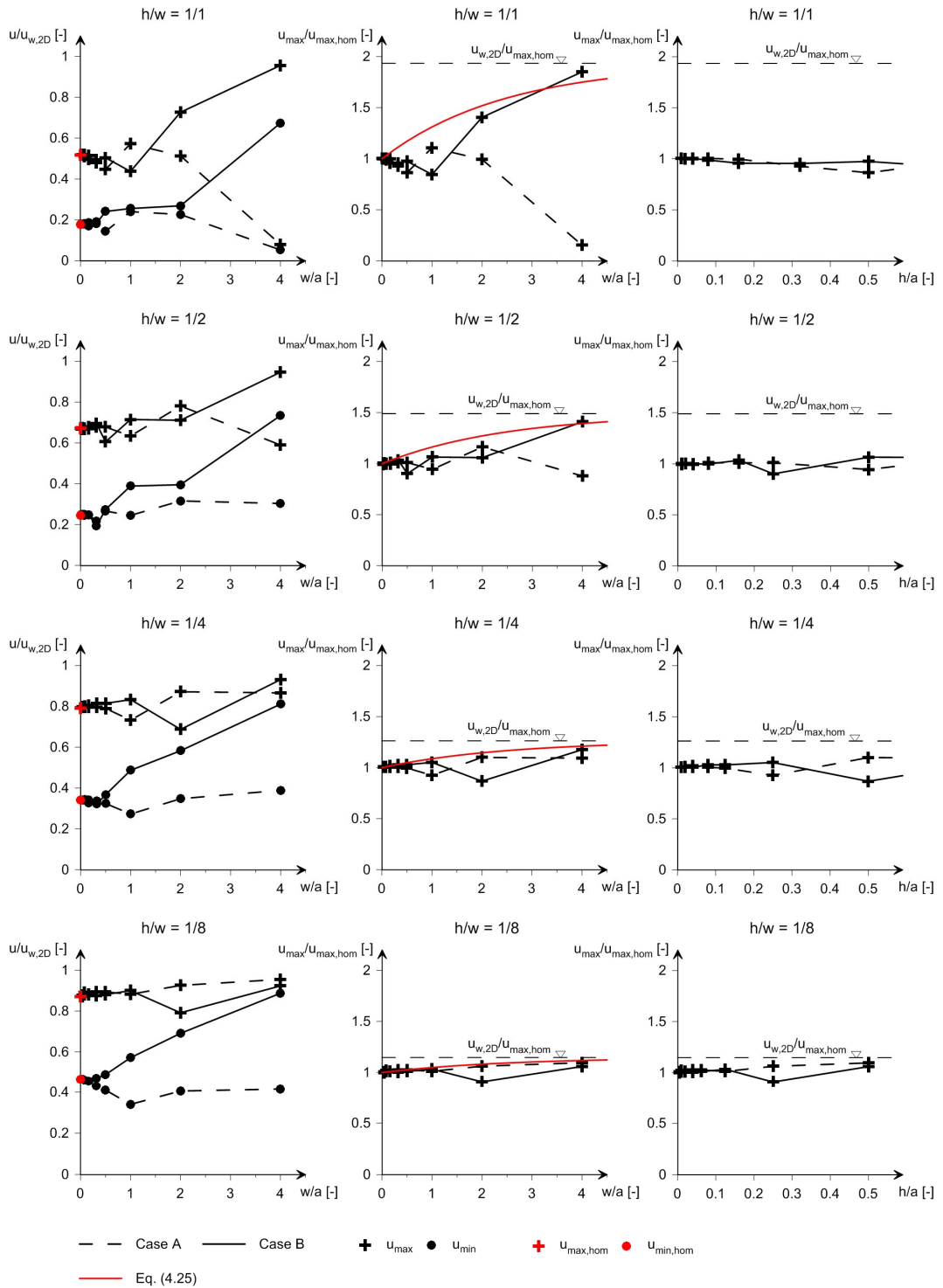


**Figure 4.19.** Maximum  $u_{max}$  and minimum  $u_{min}$  displacements (normalised by the displacements of a homogeneous weak ground  $u_{w,2D}$ ), compared with the displacements of the maximum  $u_{max,hom}$  and minimum  $u_{min,hom}$  displacements of the homogenised solution ( $\sigma_0 = 0.75$  MPa,  $a = 5$  m,  $E_h = 10$  GPa,  $c_h = 5$  MPa,  $E_w = 0.5$  GPa,  $c_w = 0.5$  MPa,  $\nu_h = \nu_w = 0.3$ ,  $\varphi_h = \varphi_w = 25^\circ$ ,  $\psi_h = \psi_w = 5^\circ$ ; cases A and B: see inset at the top of Fig. 4.15).

From these diagrams one may conclude that the error increases with  $h/w$ , particularly in the case of the high initial stress (Fig. 4.18); for the low initial stress of 0.75 MPa, the displacements  $u_{max,hom}$  are very close to  $u_{w,2D}$ . The homogenised solution  $u_{max,hom}$  becomes considerably smaller than  $u_{w,2D}$  only when the weak layers begin to yield. Consequently, the case of  $\sigma_0 = 10$  MPa is decisive for estimating the applicability limit of the homogenisation.

Analogous to Section 3.2.4, a general statement can be made based on the ratio  $h/a$  (r.h.s. diagrams of Fig. 4.18): For  $h/a < 0.05$ , the ratio  $u_{max}/u_{max,hom}$  is smaller than 1.25 (and consequently the error is less than 20%) for all  $h/w$ -values. Would the rock parameters, however, be less different than in the examined extreme case, the error when using the homogenised model would be smaller.

If the layers were oriented perpendicular to the tunnel axis, homogenisation would be adequate for  $h/a < ca. 0.10$  (see results of Section 3.2.4 for  $\sigma_0 = 10$  MPa). In the present case (strike parallel to the tunnel axis) the layers would have to be thinner. Homogenisation is thus easier in the case of tunnelling perpendicular to the layers, because the stabilising effect of the hard layers is more pronounced ( $u_{min}$  becomes considerably larger and  $u_{max}$  smaller, so that the values are closer to the homogenised solution).

Due to this smaller stabilising effect of the hard layers in the case of tunnelling parallel to the layers, the influence of the brittle behaviour of the hard layers is less pronounced than in Section 3.2 and was therefore not considered here.

### 4.3.3 Tunnelling parallel to the interface between a weak and a competent formation

In this section, the theoretical case of infinite layer thickness ( $w/a \rightarrow \infty$  and  $h/a \rightarrow \infty$ ) will be investigated. The distribution of the deformations in the tunnel profile depends on the distance of the formation interface from the tunnel: If the interface intersects (or is close to) the tunnel, then the displacements of the tunnel profile will be non-uniform (cf. Fig. 4.20).

This section investigates numerically, how far the formation interface has to be in order that the heterogeneity of the ground can be neglected (*i.e.*, in order to assume  $u_{w,2D}$  for the weak formation or  $u_{h,2D}$  for the hard formation, respectively). A weak formation overlain by a competent formation will be considered. The formation interface is located at a distance  $H$  above the tunnel axis (with  $H < 0$  meaning that the interface lies below the tunnel axis). Figure 4.20 shows the deformed profile (red dotted line), the stress trajectories and the plastic zone for a series of  $H$ -values. For the considered rock parameters and initial stress (10 MPa), the competent formation has a remarkable effect only if it crosses partially the tunnel.

The Figure 4.21 shows the results of a parametric study into the effect of the distance  $H$  of the hard formation to the tunnel axis. Specifically, the diagram shows the maximum ( $u_{max}$ ) and the minimum ( $u_{min}$ ) displacements of the tunnel cross-section, normalised by the convergence  $u_{w,2D}$  (upper diagrams) and  $u_{h,2D}$  (lower diagrams), which would develop in a homogeneous weak or competent ground, respectively. If  $H > 5a$ , the stabilising effect of the hard formation is negligible ( $u_{min}/u_{w,2D} \approx 0.8$ ; upper diagram of Fig. 4.21) and, vice versa, if  $H < -5a$ , then the unfavourable effect of the nearby weak formation can be neglected ( $u_{max}/u_{h,2D} \approx 1.2$ ; lower diagram of Fig. 4.21). These results can be regarded as generally valid, because they assume a big contrast in the mechanical parameters of the two zones and a high initial stress.

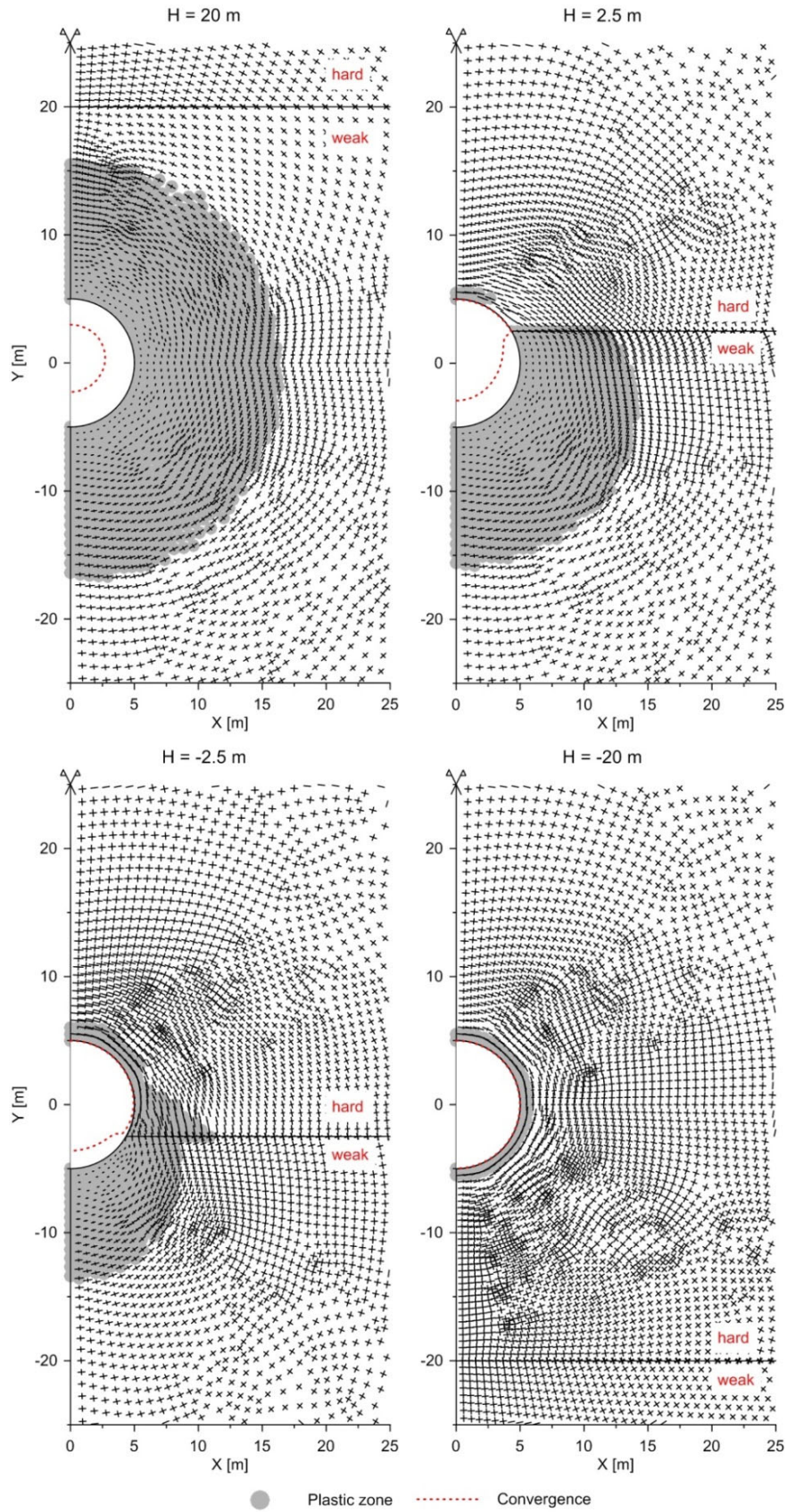


**Figure 4.20.** Convergence  $u$  (magnified by factor 2.5), plastic zone (hatched area) and principal stress orientation for different distances  $H$  of the hard formation to the tunnel axis ( $\sigma_0 = 10 \text{ MPa}$ ,  $a = 5 \text{ m}$ ,  $E_h = 10 \text{ GPa}$ ,  $c_h = 5 \text{ MPa}$ ,  $E_w = 0.5 \text{ GPa}$ ,  $c_w = 0.5 \text{ MPa}$ ,  $\nu_h = \nu_w = 0.3$ ,  $\phi_h = \phi_w = 25^\circ$ ,  $\psi_h = \psi_w = 5^\circ$ ).

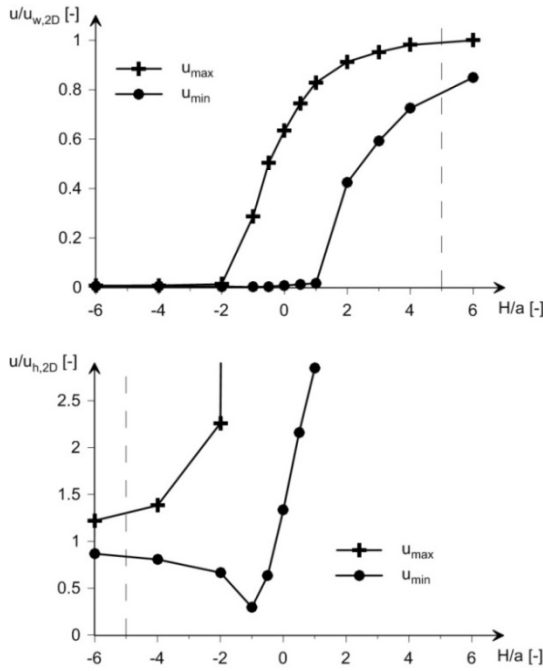


**Figure 4.21.** Maximum  $u_{max}$ , minimum  $u_{min}$  displacements of the tunnel profile (normalised by the convergence  $u_{w,2D}$  or  $u_{h,2D}$  which would develop in a homogeneous weak or hard ground, respectively) for different distances  $H$  of the hard formation to the tunnel axis (cf. Fig. 4.20;  $\sigma_0 = 10$  MPa,  $a = 5$  m,  $E_h = 10$  GPa,  $c_h = 5$  MPa,  $E_w = 0.5$  GPa,  $c_w = 0.5$  MPa,  $\nu_h = \nu_w = 0.3$ ,  $\varphi_h = \varphi_w = 25^\circ$ ,  $\psi_h = \psi_w = 5^\circ$ ).

### 4.3.4 Alternating weak and competent layers of medium thickness

In this section, it is investigated whether the equation

$$\frac{u_{max}}{u_{w,2D}} = \delta \cdot \left( 1 - \frac{u_{max,hom}}{u_{w,2D}} \right) + \frac{u_{max,hom}}{u_{w,2D}}, \tag{4.25}$$

where

$$\delta = 1 - e^{-0.4w / \rho_{w,2D}}, \tag{4.26}$$

which is practically identical with the one proposed in Section 3.4 for tunnelling perpendicularly to alternating weak and hard layers, can also be applied for estimating the maximum displacements in the case of tunnelling parallel to the layers. The red solid lines in the middle diagrams of Figures 4.14 and 4.15 show the displacements obtained with this equation. It is remarkable that this simple equation underestimates only slightly the maximum displacements for  $w/a$  smaller than a value of ca. 2 (by less than 25% for  $\sigma_0 = 10$  MPa, and even lesser for  $\sigma_0 = 0.75$  MPa). A better agreement could be achieved by selecting another constant (larger than 0.4) in the exponent of the last r.h.s. term of Equation (4.26). A definitive statement cannot be made, however, without checking Equation (4.25) for a wide parameter range, analogously to Section 3.4.

### 4.3.5 Conclusions

The homogenised model is adequate only if the hard layers are thinner than 5% of the tunnel radius. As this criterion is valid both for a tunnel parallel and a tunnel perpendicular to the layers, it seems that this criterion is applicable for any orientation of the layers to the tunnel axis.

For very thick formations, the influence of the adjacent hard or weak formation can be neglected, if the weak or the hard rock formation lies at a distance to the tunnel axis of at

least 5 times the tunnel radius. Otherwise, numerical calculations have to be performed in order to estimate the displacements of the tunnel profile.

For medium layer thicknesses, depending on the location of the layers in the tunnel profile, the tunnel displacements may vary considerably. Therefore, numerical calculations have to be performed that consider the exact location of the weak and the hard layers in the profile.

## 4.4 Response of a schistous rock mass striking parallel to the tunnel axis

### 4.4.1 Introduction

From the literature it is well known that planes of anisotropy may affect rock behaviour adversely, particularly if their strike direction forms a small angle with (or is parallel to) the tunnel axis ([9], [25]). This chapter will thus focus on the most adverse situation, which is tunnelling parallel to schistosity; the influence of the angle between schistosity plane and tunnel axis will be investigated in Section 5.1.

The influence of the planes of anisotropy, especially the schistosity planes, on the tunnel displacements was already described in a number of publications. On the one hand, the measured displacements occurring in some particular tunnel sections were examined empirically as well as numerically ([29], [74], [75], [76], [77], *etc.*; see also Section 2.1). On the other hand, the influence of the schistosity for the tunnel problem was investigated analytically [78] and numerically ([30], [45], [79], [80], [81], *etc.*). All investigations could show that the geometrical and mechanical properties of schistosity play an important role for the development of the displacements.

The influence of the discontinuities on the tunnel displacements is investigated in the literature either by continuum or by discontinuum models. In the discontinuum models, planes of anisotropy are explicitly represented in the numerical model, while in the continuum models, a homogenised rock mass is considered. As this chapter will focus on schistous rocks (*e.g.*, phyllites and schists) that are characterised by a large number of very closely spaced discontinuities, a continuum model is applied (*cf.* [82]). With the continuum models, an opening of discontinuities or a complete detachment of the elements cannot be simulated (*cf.* [83], [84], [85]). However, these mechanisms are relevant mostly for stability problems (*e.g.*, loosening or rock fall) and less for the analysis of squeezing (where large tangential stresses around the tunnel occur). For thinly layered rocks, a continuum model can adequately represent ground behaviour ([30], [86], [87]). Of course, with this kind of model, the influence of spacing cannot be investigated (*cf.* [30]). However, from Leitner *et al.* [30], it is known that the spacing may have an important influence on the tunnel displacements. This chapter will focus on schistous rocks characterised by very small spacing, which is the most critical case (*cf.* [30]).

In the current state of research a systematic, quantitative investigation of the influence of the properties of the schistosity planes on squeezing behaviour is missing. Furthermore, one misses practical guidelines on how this influence can be considered in the design.

From the mechanical point of view, schistosity can be conceived as the borderline case of a stratified rock mass with extremely thin weak layers. Therefore, the constitutive model of Section 4.2.2 could be used also in order to analyse the response of a schistous rock to tunnel excavation. This can be seen also in Figure 4.22, which presents the uniaxial compressive strength as a function of the angle  $\delta$  (defined as the angle between the direction of the maximum principal stress and the schistosity planes). For a tunnel drive parallel to the layers, the angle  $\delta$  varies along the tunnel boundary from  $0^\circ$  (at the crown for a horizontal stratification) to  $90^\circ$  (at the side wall). Therefore, for a tunnel drive parallel to the planes of anisotropy, the influence of the weak layers does not vanish with decreasing thickness fraction of the weak layers. If the latter is very small ( $x_w = 0.01$ ), the rock behaviour converges to the known behaviour of schistous rocks (which can be

obtained analytically according to [88]). With decreasing thickness fraction of the weak layers, the horizontal stiffness approaches the vertical stiffness of the composite, so that  $E_1 = E_2 = E_h$  (cf. Eqs. 4.4 and 4.5).

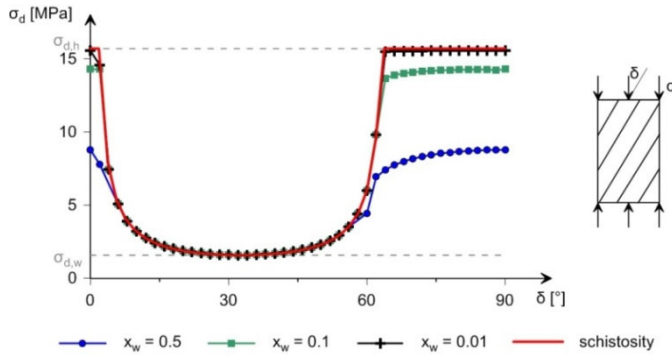


**Figure 4.22.** Uniaxial compressive strength  $\sigma_d$  of the stratified rock mass depending on the direction of loading for different thickness fractions  $x_w$  of the weak layers, obtained with Lydzba et al. [52] and compared to the analytical uniaxial compressive strength for the schistosity according to Jaeger and Cook [88] ( $E_h = 10 \text{ GPa}$ ,  $c_h = 5 \text{ MPa}$ ,  $E_w = 1 \text{ GPa}$ ,  $c_w = 0.5 \text{ MPa}$ ,  $\nu_h = \nu_w = 0.3$ ,  $\varphi_h = \varphi_w = 25^\circ$ ,  $\psi_h = \psi_w = 5^\circ$ ).

The displacements in a tunnel drive parallel to the layers can be obtained by numerical calculations, as in Section 4.2, with the constitutive model of the stratified rock mass. The results (Fig. 4.23) were compared to those obtained with constitutive models for the schistosity implemented in the commercially available software programs Plaxis ([89]; considering a Mohr-Coulomb failure criterion for the rock mass; more details concerning the implementation and verification: see [90] and [91]) and Abaqus ([64]; considering a Drucker-Prager failure criterion for the rock mass and determining the Drucker-Prager material parameters with a plane strain matching to the Mohr-Coulomb parameters). The results of all the constitutive models are in good agreement. However, if  $x_w$  approaches the value of zero, the constitutive model of Section 4.2.2 is extremely costly in terms of computer time.

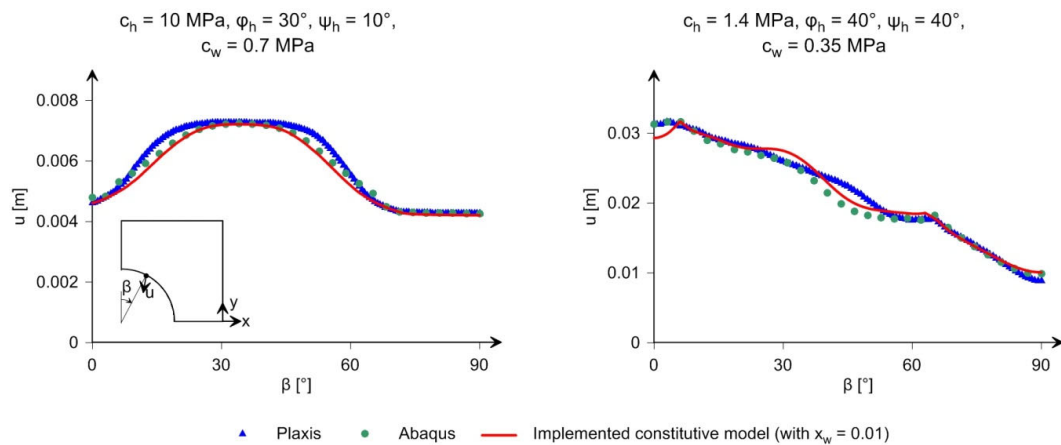


**Figure 4.23.** Magnitude of the displacement vector along the tunnel boundary obtained with the constitutive model of Section 4.2.2 and those implemented in Plaxis and Abaqus (unsupported tunnel,  $a = 5 \text{ m}$ ,  $\sigma_0 = 10 \text{ MPa}$ ,  $E_h = E_w = 20 \text{ GPa}$ ,  $\varphi_w = 20^\circ$ ,  $\psi_w = 20^\circ$ ,  $\nu_h = \nu_w = 0.3$ ).

Therefore, in Section 4.4.2, a constitutive model for the schistous rock mass is formulated. By means of this constitutive model, in Section 4.4.3, numerical calculations (assuming plane strain conditions) were carried out, in order to analyse the response of schistous rocks striking parallel to the tunnel axis. Based on these investigations, dimensionless diagrams are presented in Section 4.4.4 that allow a quick estimation of the displacements

(occurring far behind the tunnel face) to be made for a wide range of geotechnical conditions. Finally, Section 4.4.5 shows that considering an isotropic homogeneous model with appropriate parameters can be very valuable in spite of its inherent limitations and differences from a transversely isotropic rock mass.

## 4.4.2 Constitutive model

### 4.4.2.1 Formulation of the constitutive model

The mechanical behaviour of anisotropic rock mass was investigated over the last decades by many authors, particularly by means of laboratory tests. The main focus of these studies was the directional dependence of rock strength. An extensive review on this topic can be found in Pietruszczak *et al.* [92] or Duveau *et al.* [93].

Besides analysing the mechanical behaviour of anisotropic rock mass, various failure criteria have been proposed (*cf.* [93], [94]). Amongst these, the most representative model is the so-called “single plane of weakness theory” proposed by Jaeger [95]. Jaeger [95] considers a (Mohr-Coulomb) failure criterion for the rock matrix and one for the planes of weakness:

$$\tau = c_m + \sigma \tan(\varphi_m), \quad (4.27)$$

$$\tau = c_s + \sigma \tan(\varphi_s), \quad (4.28)$$

respectively. In order to model the schistous rocks realistically, elasto-plastic behaviour of the matrix should be considered (*cf.* [85]). Duveau *et al.* [93] could show that there is a good agreement between the model of Jaeger [95] and experiments. The model of Jaeger [95] was further developed by many authors (*e.g.*, [96], [97]), leading however to more complex failure criteria, which require more parameters than usually available, while the material model of Jaeger [95] can be described by means of a small number of easily interpretable material parameters, even in the case of anisotropy [98].

A schistous rock mass may be stiffer for loading parallel to the schistosity than perpendicular thereto ([99], [100], [101]). For the sake of simplicity, stiffness anisotropy is not considered here.

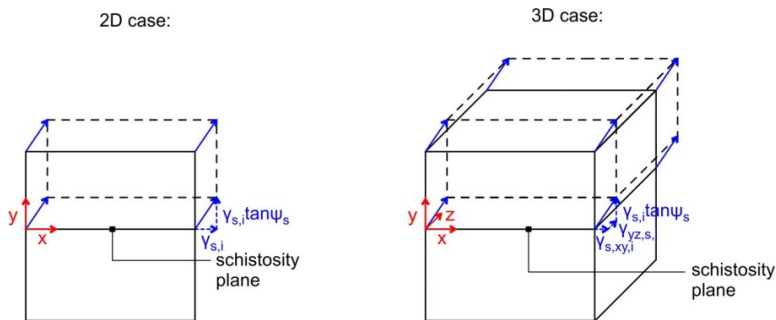


**Figure 4.24.** REV consisting of a single schistosity plane.

Constitutive models, which consider the failure of the rock mass and the planes of weakness according to the material model of Jaeger [95] have already been formulated (*e.g.*, [98], [102], [103], [104], [105], [106]) and implemented in the commercially available software programs Plaxis [89] and Abaqus [64]. However, in Chapter 5.2, the squeezing variability due to orientation changes of the anisotropy planes along the alignment will be investigated, which necessitates to formulate and implement the constitutive model of Jaeger [95] in Abaqus [64], based on the homogenisation technique (see Sections 3.2 and 4.2). This section will only show the most essential aspects of the formulation of the constitutive model. More details concerning the implementation and validation of the constitutive model can be found in Mezger [11].

For the derivation of the constitutive law, a representative elementary volume (REV) is considered, which consists of  $N$  schistosity planes and the surrounding matrix. The schistosity planes are perpendicular to the  $y$ -axis (cf. Fig. 4.24). At failure state, an irreversible shear strain  $\gamma_{s,i}$  occurs due to slip along the schistosity plane. This, in turn, leads to a normal strain perpendicular to schistosity plane, which amounts to  $\gamma_{s,i} \tan \psi_s$ , where  $\psi_s$  denotes the dilatancy angle of the schistosity (cf. Fig. 4.24). The shear strain of the REV due to failure in the schistosity planes is equal to

$$\gamma_s = N \cdot \gamma_{s,i}, \quad (4.29)$$

where  $N$  denotes the number of schistosity planes in the REV. Of course, slipping may only occur along the schistosity planes. This means that in the 2D case, the shearing strain increment occurs in  $xy$ -direction, while in the 3D case, it occurs in  $xy$ - and  $yz$ -direction (cf. Fig. 4.24). In general,

$$\gamma_s = \sqrt{\Delta\gamma_{xy,s}^2 + \Delta\gamma_{yz,s}^2}, \quad (4.30)$$

whereby the last r.h.s. term is equal to zero in the 2D case.

By definition, the variation of stresses and strains across the REV can be neglected, meaning that the resulting strains and stresses of the homogenised medium are the volumetric averages of the strain and stress components in the matrix and the schistosity planes. As the thickness fraction of the schistosity planes is small in comparison to the one of the surrounding matrix, the relations for the homogenised stress and strain increments can be simplified as follows:

$$\begin{aligned} \Delta\sigma_{xx} &= \Delta\sigma_{xx,m} & \Delta\epsilon_{xx} &= \Delta\epsilon_{xx,m} \\ \Delta\sigma_{yy} &= \Delta\sigma_{yy,m} = \Delta\sigma_{yy,s} & \Delta\epsilon_{yy} &= \Delta\epsilon_{yy,m} + \gamma_s \cdot \tan \psi_s \\ \Delta\sigma_{zz} &= \Delta\sigma_{zz,m} & \Delta\epsilon_{zz} &= \Delta\epsilon_{zz,m} \\ \Delta\tau_{xy} &= \Delta\tau_{xy,m} = \Delta\tau_{xy,s} & \Delta\gamma_{xy} &= \Delta\gamma_{xy,m} + \Delta\gamma_{xy,s} \\ \Delta\tau_{xz} &= \Delta\tau_{xz,m} & \Delta\gamma_{xz} &= \Delta\gamma_{xz,m} \\ \Delta\tau_{yz} &= \Delta\tau_{yz,m} = \Delta\tau_{yz,s} & \Delta\gamma_{yz} &= \Delta\gamma_{yz,m} + \Delta\gamma_{yz,s} \end{aligned} \quad \text{and} \quad (4.31)$$

where the subscript  $m$  denotes the strain and stress increments in the matrix and  $s$  those in the schistosity planes. As usual in design practice, the rock will be considered as linearly elastic and perfectly plastic, considering a Mohr-Coulomb failure criterion with a non-associated flow rule for the schistosity and the matrix. For the matrix the stress return algorithm after Clausen [65] will be used.

As mentioned before, in the constitutive model, a REV is considered whose schistosity planes lie perpendicular to the  $y$ -axis. By performing appropriate coordinate transformations, arbitrary orientations of the schistosity planes can be considered: the stresses and the strains are transformed from the global into the local coordinate system (where the  $y$ -axis is perpendicular to the planes of schistosity) and, after having performed all the computations in the local coordinate system, the resulting stresses are back-calculated into the global coordinate system. The only input needed for the coordinate transformation is the normal vector of the schistosity planes.

#### 4.4.2.2 Rock element behaviour

In order to illustrate the material behaviour, single element tests were performed considering plane strain conditions. According to the analytical solution of Jaeger and Cook [88], the uniaxial compressive strength of the schistous rock mass under a specific loading direction is the minimum between the one governed by the matrix and the schistosity and reads as follows:

$$\sigma_d = \min \left( \frac{2 \cdot c_s}{\sin 2\delta (1 - \tan \varphi_s \tan \delta)}, \frac{2 \cdot c_m \cdot \cos \varphi_m}{(1 - \sin \varphi_m)} \right). \quad (4.32)$$

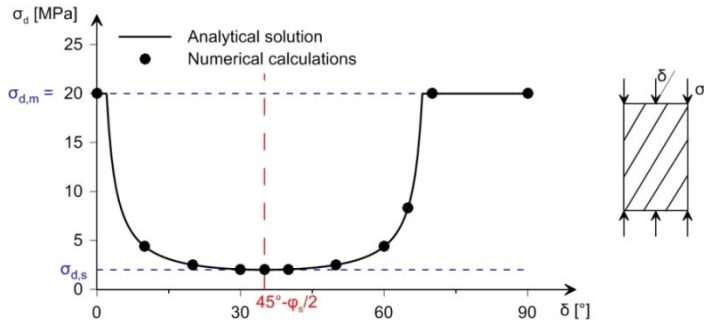


**Figure 4.25.** Uniaxial compressive strength  $\sigma_d$  of the REV depending on the direction of loading, obtained with numerical calculations and compared to the analytical solution of Jaeger and Cook [88] ( $E = 20 \text{ GPa}$ ,  $c_m = 5.77 \text{ MPa}$ ,  $\varphi_m = 30^\circ$ ,  $\psi_m = 10^\circ$ ,  $c_s = 0.7 \text{ MPa}$ ,  $\varphi_s = 20^\circ$ ,  $\psi_s = 20^\circ$ ,  $\nu = 0.3$ ).

The compressive strength reaches its minimum at an angle of  $\delta = 45 - \varphi_s/2 = 35^\circ$  between the schistosity planes and the loading direction and is given by the following equation:

$$\sigma_{d,s} = \frac{2 \cdot c_s \cdot \cos \varphi_s}{(1 - \sin \varphi_s)}. \quad (4.33)$$

If the angle  $\delta$  is greater than  $90^\circ - \varphi_s = 70^\circ$  or equals  $0^\circ$ , then failure in the schistosity planes cannot occur. The analytical uniaxial compressive strength is presented in Figure 4.25 and compared with the results obtained with numerical calculations; the schistous rock mass model (and thus the implemented elasto-plastic algorithm) behaves as expected.

#### 4.4.3 Basic aspects of the schistous rock response to excavation

In this section, some basic aspects of tunnelling through schistous rock mass will be analysed.

Considering the failure criterion of the schistosity (Eq. 4.28) and that, in the elastic state, the maximum principal stress (in tangential direction) amounts to  $2\sigma_0 - \sigma_a$  and the minimum principal stress (in radial direction) to  $\sigma_a$ , the support pressure at which failure in the planes of weakness occurs first amounts to

$$\sigma_a = \frac{2\sigma_0 - \sigma_{d,s}}{m_s - 1} = 5.9 \text{ MPa}, \text{ where } m_s = \frac{1 + \sin \varphi_s}{1 - \sin \varphi_s}, \quad (4.34)$$

and is located at  $\beta = 45^\circ - \varphi_s/2 = 35^\circ$  (Fig. 4.26; cf. [78]). The support pressure at which failure in the matrix would occur first amounts to (assuming elastic state and thus no failure in the schistosity):

$$\sigma_a = \frac{2\sigma_0 - \sigma_{d,m}}{m_m - 1} = -7.32 \text{ MPa}, \text{ where } m_m = \frac{1 + \sin \varphi_m}{1 - \sin \varphi_m}. \quad (4.35)$$

As this value is negative, it can be assumed that no failure in the matrix will occur, even for  $\sigma_a = 0 \text{ MPa}$ , as the largest deviatoric stresses occur in the elastic state. In reality, due to the failure in the planes of schistosity, the deviatoric stresses would be smaller than in the elastic state and thus the support pressure, at which failure in the matrix occurs, would be even smaller.

With a further decrease in support pressure, the plastic zone increases at the segment  $0^\circ < \beta < 90^\circ - \varphi_s$  (as failure at  $\beta = 0^\circ$  and  $\beta \geq 90^\circ - \varphi_s$  is not possible, cf. Section 0). Due to failure in these areas, stress redistribution occurs around the plastic zone, so that the

principal stress axes are not tangential and radial anymore (see results for  $\sigma_a = 3.5$  MPa in Fig. 4.26).

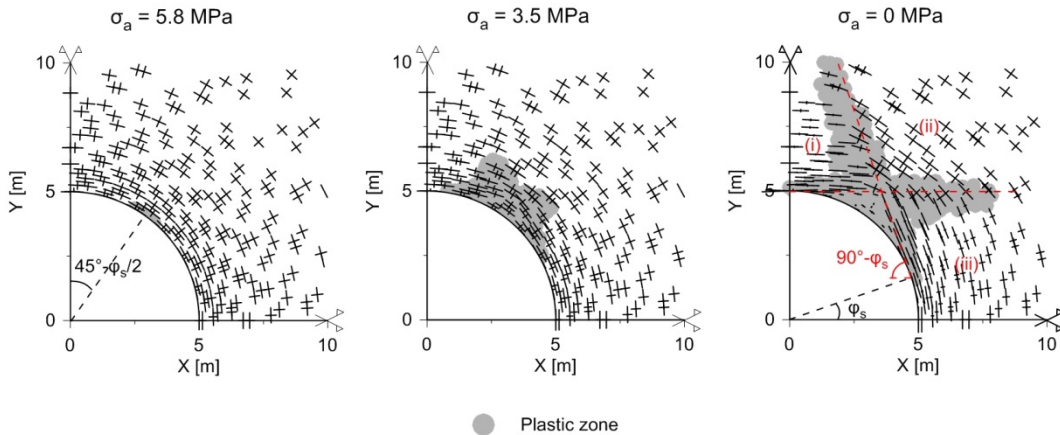


**Figure 4.26.** Principal stress orientation as well as plastic zone for different support pressures ( $a = 5$  m,  $\sigma_0 = 10$  MPa,  $E = 20$  GPa,  $c_m = 10$  MPa,  $\varphi_m = 30^\circ$ ,  $\psi_m = 10^\circ$ ,  $c_s = 0.7$  MPa,  $\varphi_s = 20^\circ$ ,  $\psi_s = 20^\circ$ ,  $\nu = 0.3$ ).

Due to this stress redistribution, three areas can be distinguished with respect to the direction of the principal axes (see results for  $\sigma_a = 0$  MPa in Fig. 4.26): (i) the area of the crown of the tunnel, where the maximum principal stress is horizontal; (ii) the area around  $\beta = 45^\circ - \varphi_s/2$ , where the maximum principal stress forms an angle of about  $45^\circ - \varphi_s/2$  with the horizontal; and, (iii), the area besides the tunnel, where the angle of the maximum principal stress to the horizontal is greater than  $90^\circ - \varphi_s$ . As in the area (ii), the minimum principal stress is nearly as large as the maximum principal stress, no failure can occur there. Furthermore, due to the fact that failure in the schistosity may only occur at an angle  $\beta$  between  $0^\circ$  and  $90^\circ - \varphi_s$ , the failure in the schistosity can solely propagate in the proximity of the two red lines drawn in Figure 4.26, which indicate the respective borders of the areas introduced before. The extent of the plastic zone along these two lines is approximately the same, so that the largest displacements occur exactly at  $\beta = 45^\circ - \varphi_s/2 = 35^\circ$  (cf. Fig. 4.27).

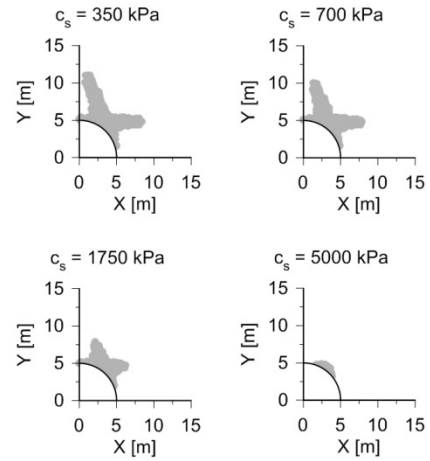
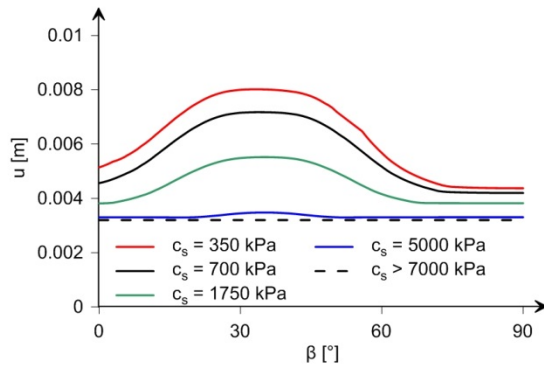
The influence of the rock parameters on the tunnel displacements will be discussed by the results of a parametric study (Figs. 4.27 and 4.28).

The upper diagrams of Figure 4.27 show the influence of the schistosity cohesion on the magnitude of the displacements along an unsupported tunnel boundary (l.h.s. diagram) and on the plastic zone (r.h.s. diagrams). A decrease in the cohesion of the schistosity leads to a larger extent of the plastic zone and consequently to larger deformations. According to Equation (4.32), failure in the schistosity plane only occurs, for an unsupported tunnel, if

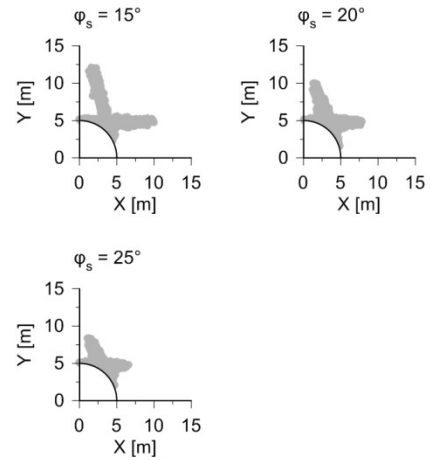
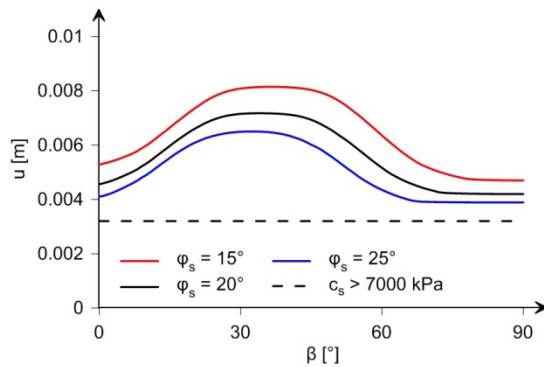
$$c_s \leq \sigma_0 \sin 2\beta (1 - \tan \varphi_s \tan \beta), \text{ where } \beta = 45^\circ - \varphi_s/2. \quad (4.36)$$

Therefore,  $c_s$  should be smaller than 7 MPa, in order that failure occurs in the schistosity plane. For  $c_s > 7$  MPa, the displacements are equal to those occurring in the absence of the schistosity. A decrease in  $c_s$  may lead to a considerable increase of the displacements. The maximum displacement along the unsupported tunnel, for  $c_s = 350$  kPa, may be about 2.5 times larger than those that would occur in the absence of the schistosity ( $u_{m,2D} = 0.0032$  m).

Influence of  $c_s$  (where  $\varphi_s = \psi_s = 20^\circ$ )



Influence of  $\varphi_s$  (where  $c_s = 0.7$  MPa,  $\psi_s = \varphi_s$ )



Influence of  $\psi_s$  (where  $c_s = 0.7$  MPa,  $\psi_s = 20^\circ$ )

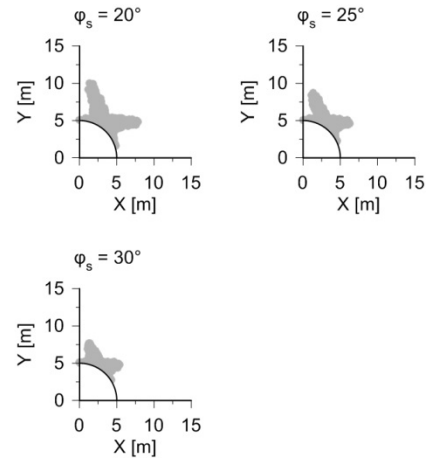
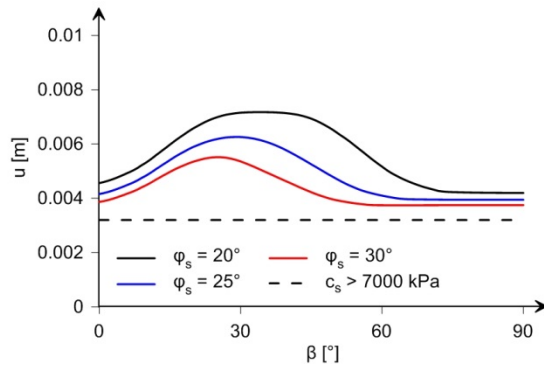


**Figure 4.27.** Magnitude of the displacement vector along the tunnel boundary (l.h.s.) as well as extent of the plastic zone (r.h.s.) for varying parameters (unsupported tunnel,  $a = 5$  m,  $\sigma_0 = 10$  MPa,  $E = 20$  GPa,  $c_m = 10$  MPa,  $\varphi_m = 30^\circ$ ,  $\psi_m = 10^\circ$ ,  $\nu = 0.3$ ).

The middle diagrams of Figure 4.27 show that larger friction angles in the schistosity plane lead generally to smaller plastic zones and consequently to smaller displacements. For  $\psi_s = \varphi_s$ , the largest displacements occur at  $\beta = 45^\circ - \varphi_s/2$ . An increase of  $\varphi_s$  leads therefore to moving of the location of maximum displacement towards the crown (i.e., towards smaller  $\beta$ ). Furthermore, for a high  $\varphi_s$ , the development of the almost vertical plastic zone is less steep, as the latter develops at an angle  $90^\circ - \varphi_s$  to the horizontal direction (cf. Fig. 4.26).

If the dilatancy angle remains constant and solely the friction angle of the schistosity plane increases (lowermost diagrams of Fig. 4.27), the displacements decrease and the

maximum displacements move towards the crown. This occurs also for decreasing dilatancy angles (see upper diagrams of Fig. 4.28) and can be explained as follows: As the extent of the plastic zones remains constant for decreasing dilatancy angles, the displacement occurring in vertical direction decreases (as it amounts to  $\gamma_s \tan \psi_s$ ) given the same portion of displacements in horizontal direction (*i.e.*,  $\gamma_s$ ). The displacement vectors at the tunnel boundary, therefore, experience larger horizontal than vertical displacements, which leads to moving of the deformation shape to the left (*i.e.*, towards smaller  $\beta$ ).

If the cohesion in the matrix decreases to less than 5.77 MPa (for an unsupported tunnel), failure occurs also in the matrix (see lower diagrams of Fig. 4.28). This happens in the areas, where the schistosity cannot fail (*i.e.*, in the areas (i) to (iii) of Fig. 4.26). With decreasing cohesion of the matrix, the displacements of the tunnel profile increase considerably (see Fig. 4.28). Furthermore, the largest displacements no longer occur at about  $\beta = 45^\circ - \varphi_s/2$ , but near the crown.

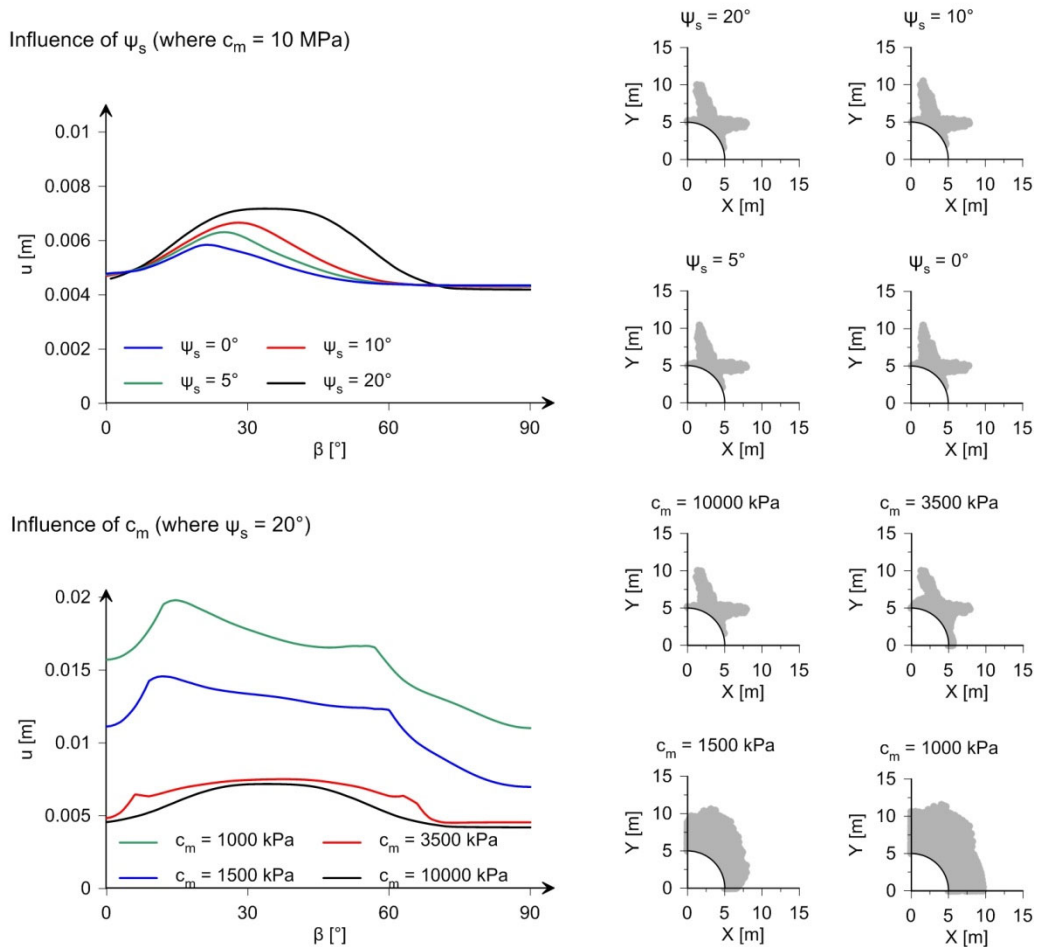


**Figure 4.28.** Magnitude of the displacement vector along the tunnel boundary (*l.h.s.*) as well as extent of the plastic zone (*r.h.s.*) for varying parameters (unsupported tunnel,  $a = 5$  m,  $\sigma_0 = 10$  MPa,  $E = 20$  GPa,  $\varphi_m = 30^\circ$ ,  $\psi_m = 10^\circ$ ,  $c_s = 0.7$  MPa,  $\varphi_s = 20^\circ$ ,  $\nu = 0.3$ ).

Figure 4.29 shows the displacements along the tunnel boundary as well as the extent of the plastic zone for three cases: (i), when solely the matrix reaches failure, (ii), when solely the schistosity reaches failure and, (iii), when both the matrix and the schistosity reach failure. (Of course, in reality, the cohesion of the schistosity is smaller than the one of the rock mass.) If solely the matrix or the schistosity reaches failure, the maximum displacements are smaller than 0.01 m, while for a failure of both, the displacements can be by a factor 4 larger.

In conclusion, it is the combined effect of failure in the schistosity planes and failure in the matrix which leads to very large deformations of the tunnel profile.

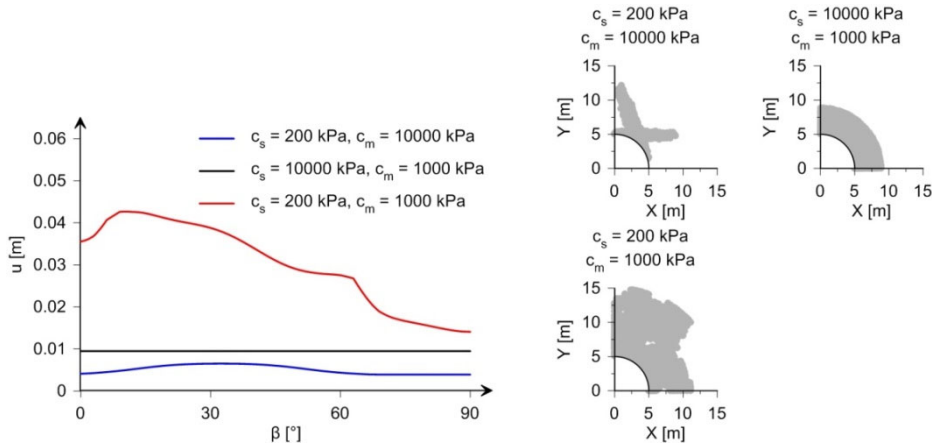


**Figure 4.29.** Magnitude of the displacement vector along the tunnel boundary (l.h.s.) as well as extent of the plastic zone (r.h.s.) for varying parameters (unsupported tunnel,  $a = 5$  m,  $\sigma_0 = 10$  MPa,  $E = 20$  GPa,  $\varphi_m = 30^\circ$ ,  $\psi_m = 10^\circ$ ,  $\varphi_s = 20^\circ$ ,  $\psi_s = 20^\circ$ ,  $\nu = 0.3$ ).

#### 4.4.4 Development of nomograms

The estimation of the displacements when tunnelling parallel to schistosity planes (see Section 4.4.3) shall be facilitated by dimensionless nomograms. The displacements at a specific location (*i.e.*, at a specific angle  $\beta$ ) of the tunnel boundary generally depend on all the parameters of the problem under consideration:

$$u = f(E, \nu, \varphi_m, \sigma_{d,m}, \psi_m, \varphi_s, \sigma_{d,s}, \psi_s, \sigma_0, \sigma_a, a), \quad (4.37)$$

where

$$\sigma_{d,s} = \frac{2 \cdot c_s \cdot \cos \varphi_s}{(1 - \sin \varphi_s)} \quad \text{and} \quad \sigma_{d,m} = \frac{2 \cdot c_m \cdot \cos \varphi_m}{(1 - \sin \varphi_m)}. \quad (4.38)$$

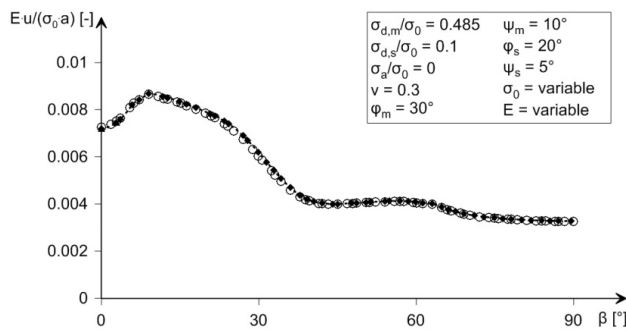


**Figure 4.30.** Magnitude of the displacement vector  $E u / (\sigma_0 a)$  along the unsupported tunnel boundary for various values of  $\sigma_0$  and  $E$ .

The number of parameters can be reduced by performing a dimensional analysis and by taking into account the findings of Chapter 4.2, considering that the schistosity represents from the mechanical point of view a special case of a stratified rock mass:

$$u = \frac{\sigma_0 \cdot a}{E} \cdot f\left(\frac{\sigma_{d,m}}{\sigma_0}, \frac{\sigma_{d,s}}{\sigma_0}, \frac{\sigma_a}{\sigma_0}, \nu, \varphi_m, \psi_m, \varphi_s, \psi_s\right). \quad (4.39)$$

This theoretical hypothesis was investigated for the problem under consideration by performing a series of numerical calculations. Figure 4.30 shows the considered parameter sets and the normalised magnitude of the displacement vector  $E u / (\sigma_0 a)$  along the tunnel

boundary. The results were obtained for different parameter sets but fall on one single curve.

As the displacements of the tunnel profile are very non-uniform, only the maximum ( $U_{max}$ ), the minimum ( $U_{min}$ ) as well as the averaged ( $U_{average}$ ) displacement at the tunnel boundary will be shown in the nomograms; these values are essential for design purposes.

In order to cover a wide range of parameters, but also to limit the computational effort, the numerical calculations (*cf.* Section 4.4.3) were only carried out for specific parameter sets (according to Table 4.3). The friction angles of the matrix  $\varphi_m$  were chosen to be larger than those of the schistosity  $\varphi_s$ . The support pressure was chosen such as to cover the practically important portion of the ground response curve (at  $\sigma_{a1} = 0$ ,  $\sigma_{a2} = 0.1\sigma_0$  and  $\sigma_{a3} = 0.2\sigma_0$ ). Moreover, it can be assumed that the dilatancy angle of the matrix  $\psi_m$  is interconnected with its friction angle  $\varphi_m$  [68]. The dilatancy angle of the schistosity is usually not constant during the shearing process, but decreases gradually until it approaches zero for large shear displacements [107]. In order to be on the safe side (see upper diagrams of Fig. 4.28), a rather high threshold value of  $5^\circ$  will be chosen.

For the sake of simplicity and considering that the effect of Poisson's ratio is subordinate, the Poisson's ratio was kept fixed to 0.3.

**Table 4.3.** Overview of the considered parameter ranges for the nomograms.

$\sigma_{d,s}/\sigma_0$ [-]	0.05; 0.1; 0.2; 0.3, $\infty$
$\nu$ [-]	0.3
$\varphi_m$ [°]	20; 25; 30
$\varphi_s$ [°]	10; 15; 20
$\psi_m$ [°]	1 for $\varphi_m = 20^\circ$ 5 for $\varphi_m = 25^\circ$ 10 for $\varphi_m = 30^\circ$ (according to [68])
$\psi_s$ [°]	$5^\circ$
$\sigma_a/\sigma_0$ [-]	0; 0.1; 0.2

Bearing in mind that some of the parameters have been fixed, the maximum, minimum and averaged displacement along the tunnel boundary depend on the following parameters:

$$\frac{u_{max} \cdot E}{\sigma_0 \cdot a}, \frac{u_{min} \cdot E}{\sigma_0 \cdot a}, \frac{u_{average} \cdot E}{\sigma_0 \cdot a} = f\left(\frac{\sigma_{d,m}}{\sigma_0}, \frac{\sigma_{d,s}}{\sigma_0}, \frac{\sigma_a}{\sigma_0}, \varphi_m, \varphi_s\right). \quad (4.40)$$

This equation is represented in form of nomograms in Appendix II. Each figure of Appendix II applies to a certain value of  $\varphi_s$ ,  $\varphi_m$  and  $\sigma_a/\sigma_0$ , while each diagram applies to a different value of  $\sigma_{d,s}/\sigma_0$  (where  $\sigma_{d,s}$  can be obtained with Eq. 4.38). Each curve shows the normalised maximum  $E_{max} u/(\sigma_0 a)$ , minimum  $E_{min} u/(\sigma_0 a)$  or averaged displacement  $E_{average} u/(\sigma_0 a)$  in function of the normalised strength  $\sigma_{d,w}/\sigma_0$ . Consequently, one can determine easily the maximum, minimum and averaged displacements for an unsupported as well as for a supported, cylindrical tunnel for given initial stress and mechanical parameters.

Furthermore, the nomograms allow assessing the influence of schistosity on the squeezing deformations easily, by comparing the displacements for the schistous rock mass (with the given rock parameters) with those in the absence of the schistosity planes (given by the lines for  $\sigma_{d,s}/\sigma_0 = \infty$  in the nomograms).

For the considered combinations of minimum uniaxial compressive strength and friction angle of the schistosity, it may happen in some cases that the schistosity cohesion is higher than the matrix cohesion. Nevertheless, for all the parameters of the nomograms, failure occurs first in the planes of weakness and not in the matrix (*cf.* Eqs. 4.34 and 4.35).

The displacements for other values than those considered in the nomograms can be estimated by interpolating between the respective curves of the nomograms. Generally, the error due to the interpolation is less than 20%. For example, the displacements for a friction angle  $\varphi_m$  of the matrix of  $22.5^\circ$  (and thus of a dilatancy angle  $\psi_m$  of  $3^\circ$ ) can be estimated by interpolating between the nomograms of  $\varphi_m = 20^\circ$  and  $25^\circ$ . (Of course, the estimated displacements for dilatancy angles smaller than  $3^\circ$  would be on the safe side.)

#### 4.4.5 Parameters of an equivalent isotropic material

Analogously to Section 4.2.5, the range of the (non-uniformly distributed) displacements of a schistous rock mass can be estimated by considering an isotropic elasto-plastic material with appropriately selected mechanical parameters. As the schistosity represents, from the mechanical point of view, a special case of the stratified rock mass, the parameters of the isotropic elasto-plastic model can be determined using the same procedure as in Section 4.2.5, the only difference being that the elasticity parameters of the equivalent material are equal to the actual ones and that the plasticity parameters are obtained (based upon the maximum or the minimum displacements of the anisotropic model) using the diagrams of Appendix II.

The goal of this section is to show, how equivalent parameters for an isotropic homogeneous rock mass can be determined for the case of a tunnel drive parallel to the layers, using the nomograms of Appendix II (introduced in Section 4.4.4). With these equivalent parameters, the assessment of the rock mass response to tunnelling can be facilitated, as the calculation methods commonly used in tunnelling can be applied for tunnels through schistous rocks, whose schistosity planes lie parallel to the tunnel axis. As the schistosity represents, from the mechanical point of view, a special case of the stratified rock mass, the same procedure as was already outlined in Section 4.2.5 can be used for determining the equivalent parameters for an isotropic homogeneous rock mass, by requesting that the maximum  $u_{max}$  or minimum  $u_{min}$  displacements of the exact model (obtained with the nomograms) are equal to those of the equivalent isotropic model for three selected values of the support pressure ( $\sigma_{a1}$ ,  $\sigma_{a2}$ ,  $\sigma_{a3}$ ).

Figure 4.31a compares the GRCs of the anisotropic model (obtained for the parameters in the first two rows of Table 4.4) with the GRCs obtained considering the two parameter sets of the equivalent isotropic material after Table 4.4 (last two rows). The equivalent isotropic material reproduces well the displacement range of the schistous material. Solely, the middle sections of the GRC cannot be fitted properly, no matter how well chosen the equivalent parameters are.

**Table 4.4.** Rock parameters.

	$E$ [GPa]	$\nu$ [-]	$c$ [MPa]	$\varphi$ [°]	$\psi$ [°]
Matrix	20	0.3	1.155	30	10
Schistosity	-	-	0.419	10	5
Equivalent isotropic material					
based upon $u_{max}$	20	0.3	0.518	20.0	1.0
based upon $u_{min}$	20	0.3	0.449	30.0	1.0

The usefulness of the proposed equivalent isotropic model will be illustrated by means of two further tunnelling problems assuming the parameters of Table 4.4 (considering an initial hydrostatic stress field of 10 MPa): (1) The longitudinal displacement profile of an unsupported tunnel (Fig. 4.31b); (2) The boundary displacements of an unsupported tunnel with a horseshoe profile assuming plane strain conditions (Fig. 4.31c). These problems were solved numerically, using the exact schistous material model and the equivalent isotropic model. (Numerical details for problem 1 can be found in Section 5.1.)

According to Figure 4.31, the results obtained with the equivalent isotropic model (fitted with the minimum and the maximum GRC) bound the exact solution. However, the pre-deformations obtained with equivalent isotropic model are larger than the exact ones. This is such because the middle section of the GRCs of the exact model does not fit perfectly with those obtained with equivalent parameters. However, the rock response to tunnelling obtained with equivalent parameters is accurate enough for practical purposes at least at the preliminary design stage.

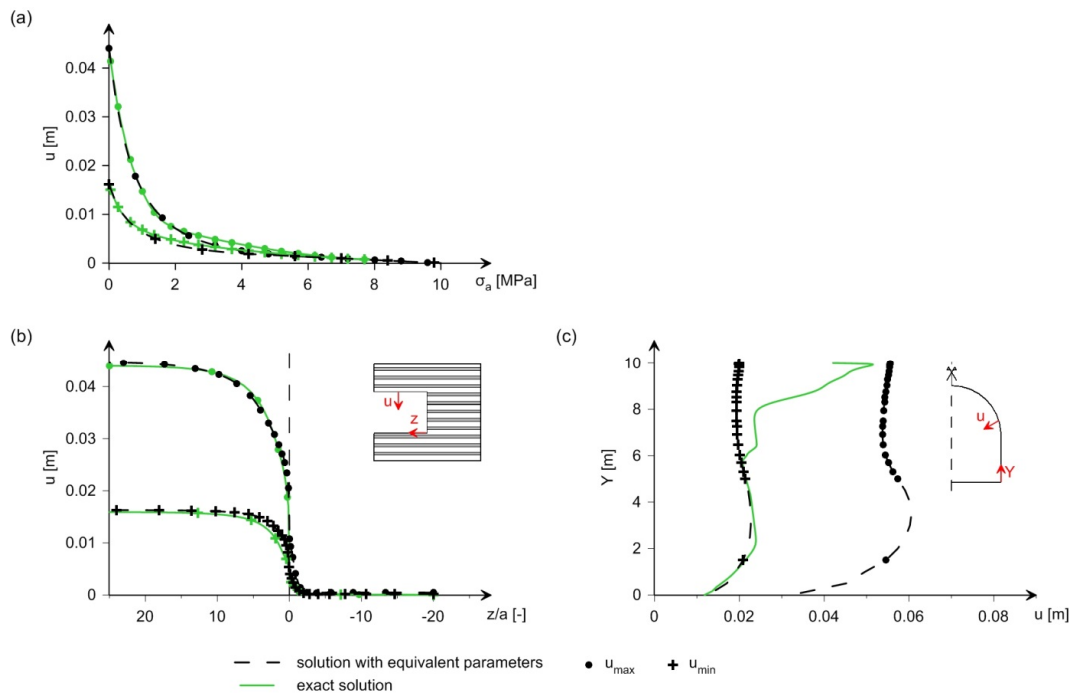


**Figure 4.31.** (a) Maximum and minimum displacement at the tunnel boundary of a cylindrical tunnel as a function of the support pressure (GRC). (b) Maximum and minimum longitudinal displacement profile of an unsupported tunnel. (c) Maximum and minimum magnitude of the displacement vector along the unsupported tunnel boundary of a horseshoe profile, obtained with the exact model and with the equivalent isotropic model (parameters after Table 4.4).

#### 4.4.6 Conclusions

This chapter investigated the response of schistous rock to tunnel excavation parallel to schistosity, considering a homogeneous rock mass with strength anisotropy.

In order to facilitate the assessment of squeezing in schistous rocks, dimensionless diagrams were worked out based upon the results of a parametric study. These diagrams serve to determine the parameters of an isotropic elasto-plastic model, which can be used for estimating an upper and a lower bound of the non-uniformly distributed deformations of the schistous rock.



## 5 Tunnelling with an arbitrary angle to the schistosity or bedding planes

### 5.1 Influence of the orientation of the anisotropy planes on the squeezing deformations

#### 5.1.1 Introduction

The orientation of planes of anisotropy, particularly of the bedding and schistosity planes, influences considerably the magnitude and distribution of the squeezing deformations ([9], [25], [45]). Particularly adverse are planes of anisotropy that strike parallel or with a small angle (less than  $25^\circ$ ) to the tunnel axis (*cf.* [108]). This was observed also in the case histories of Chapter 2.

In this chapter also the convergences are investigated, which are the displacements far behind the face minus the displacements that occur ahead of the face (hereafter referred to as “pre-deformation”). A review of pre-deformation estimation methods for homogeneous and isotropic materials can be found in Cantieni and Anagnostou [109]. There are only a few investigations concerning the pre-deformations in layered or schistous rocks. Carranza-Torres and Fairhurst [110] investigated the application of the convergence-confinement method for rock masses that satisfy the Hoek-Brown failure criterion. However, the failure of the planes of weakness was not considered explicitly. Tonon and Amadei [111] investigated numerically the effect of elastic anisotropy on the pre-deformations. They found out that the existing expressions (valid for isotropic rock masses under a uniform state of stress) are applicable only if the plane of transverse isotropy strikes parallel to the tunnel axis; otherwise three-dimensional analyses are necessary. Klopčič and Logar [112] and Madkour [113] showed that a large portion of displacements occurs ahead of the tunnel face especially when tunnelling with the dip, but did not consider failure of the rock matrix. Schubert and Mendez [114] also investigated the influence of the orientation of the schistosity on the tunnel behaviour using the example of the Galgenberg Tunnel. In the current state of research a systematic, quantitative investigation of the influence of the orientation of the planes of anisotropy on the convergences and easy-to-use, design-oriented methods of analysis are missing. This chapter shows that the tunnel convergences can be determined approximately based upon the solutions developed for the borderline cases of tunnelling parallel or perpendicularly to the anisotropy planes (Chapters 3 and 4) and the “schistosity influence factor” introduced in Section 2.1, which expresses the combined effect of the dip angle  $\omega_s$  and of the angle  $\theta_s$  between the strike direction of the planes of anisotropy and the tunnel axis.

The plane strain assumption is only valid, if the planes of anisotropy are parallel or perpendicular to the tunnel axis (*cf.* [115]): Plane strain calculations presuppose that (*cf.* [115], [116]) the normal strain  $\varepsilon_z$ , as well as the shear strains  $\gamma_{yz}$  and  $\gamma_{xz}$  are equal zero, *i.e.*, that one principal stress direction coincides with the tunnel axis. For a stratified or schistous rock mass with anisotropy planes, which are neither parallel nor perpendicular to the tunnel axis, the axial strain  $\varepsilon_z$  far behind the tunnel face equals zero, which is however not true for the shear strains  $\gamma_{yz}$  and  $\gamma_{xz}$ . According to Zienkiewicz *et al.* [116], the displacements in a cross-section far behind the tunnel face could be obtained by a so-called “complete plane strain analysis” (see, *e.g.*, [115], [117], [116]). In the present case, however, full 3D analyses are indispensable because the pre-deformations also have to be determined.

In order to determine the convergences, the ground response to tunnel excavation is analysed by 3D numerical calculations (using Abaqus; [64]), which consider the advancing tunnel face. An unsupported tunnel is considered and the excavation is simulated through a stepwise reduction of the tractions along the entire boundary and at the face from  $\sigma_0$  to zero (Fig. 5.1); a step-by-step simulation of tunnel advance is unnecessary for an unsupported tunnel.

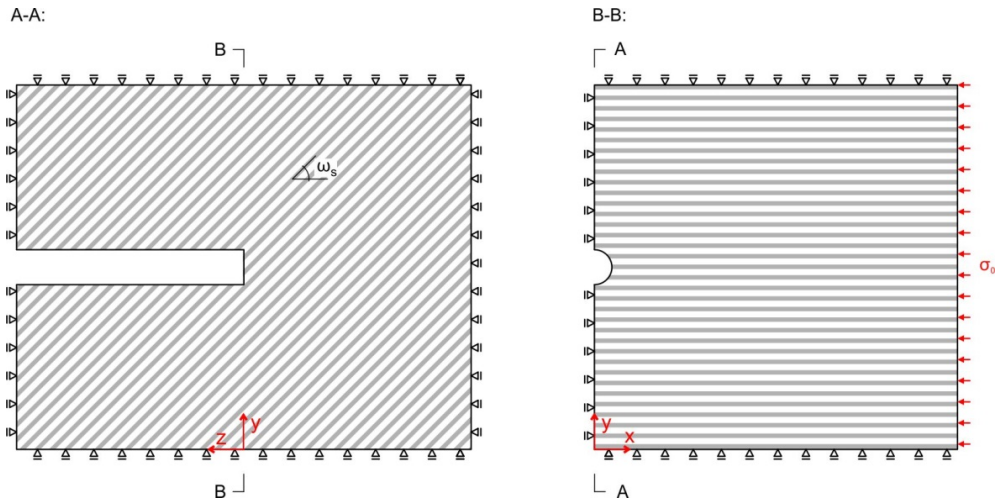


**Figure 5.1.** Problem layout with boundary conditions for the strike direction of the planes of anisotropy perpendicular to the tunnel axis.

Figure 5.1 shows the assumed boundary conditions. As the displacements and the shear stresses  $\tau_{yz}$  and  $\tau_{xz}$  at the left vertical boundary are fixed to zero (and this contradicts the actual behaviour, if the anisotropy planes are not parallel or perpendicular to the tunnel axis), boundary effects appear (see Fig. 5.2; cf. [116]). In order to eliminate the effect of the boundary condition, a sufficient long model is considered (50 times the tunnel radius).

The rock mass is taken as a homogeneous transversely isotropic material with the constitutive model after Section 4.2 (thinly stratified rock) or 4.4 (schistous rock). If the strike direction of the planes of anisotropy is perpendicular to the tunnel axis (as in Sections 5.1.2 and 5.1.3), only half of the system needs to be considered (Fig. 5.1). Otherwise (as in Section 5.1.4), symmetry is lost and the whole system has to be considered.

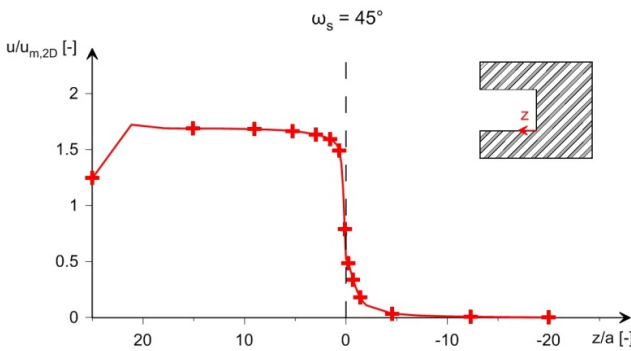


**Figure 5.2.** Normalised magnitude of the displacement vector  $u/u_{m,2D}$  at the crown along a tunnel through schistous rock ( $a = 5 \text{ m}$ ,  $\sigma_0 = 10 \text{ MPa}$ ,  $E = 1 \text{ GPa}$ ,  $c_m = 6 \text{ MPa}$ ,  $\varphi_m = 30^\circ$ ,  $\psi_m = 10^\circ$ ,  $c_s = 0.8 \text{ MPa}$ ,  $\varphi_s = 10^\circ$ ,  $\psi_s = 5^\circ$ ,  $\nu = 0.3$ ).

### 5.1.2 Tunnelling in schistous rock, perpendicular to the strike direction

In this section, the influence of the dip angle  $\omega_s$  (see inset of Fig. 5.4) on the displacements (Section 5.1.2.1), on the pre-deformations (Section 5.1.2.2) and on the convergences (Section 5.1.2.3) will be shown. The analyses were performed by considering a friction angle and cohesion of the schistosity, which are considerably smaller than those of the matrix. Two different values of the cohesion of the surrounding matrix  $c_m$  will be analysed: A rather small cohesion of  $c_m = 1 \text{ MPa}$  (where the matrix yields) and a larger value of  $c_m = 6 \text{ MPa}$ , where the matrix remains elastic. The latter was chosen, in order to investigate if the statements of this section are valid also for less severe squeezing conditions, where yielding occurs only along the schistosity plane.

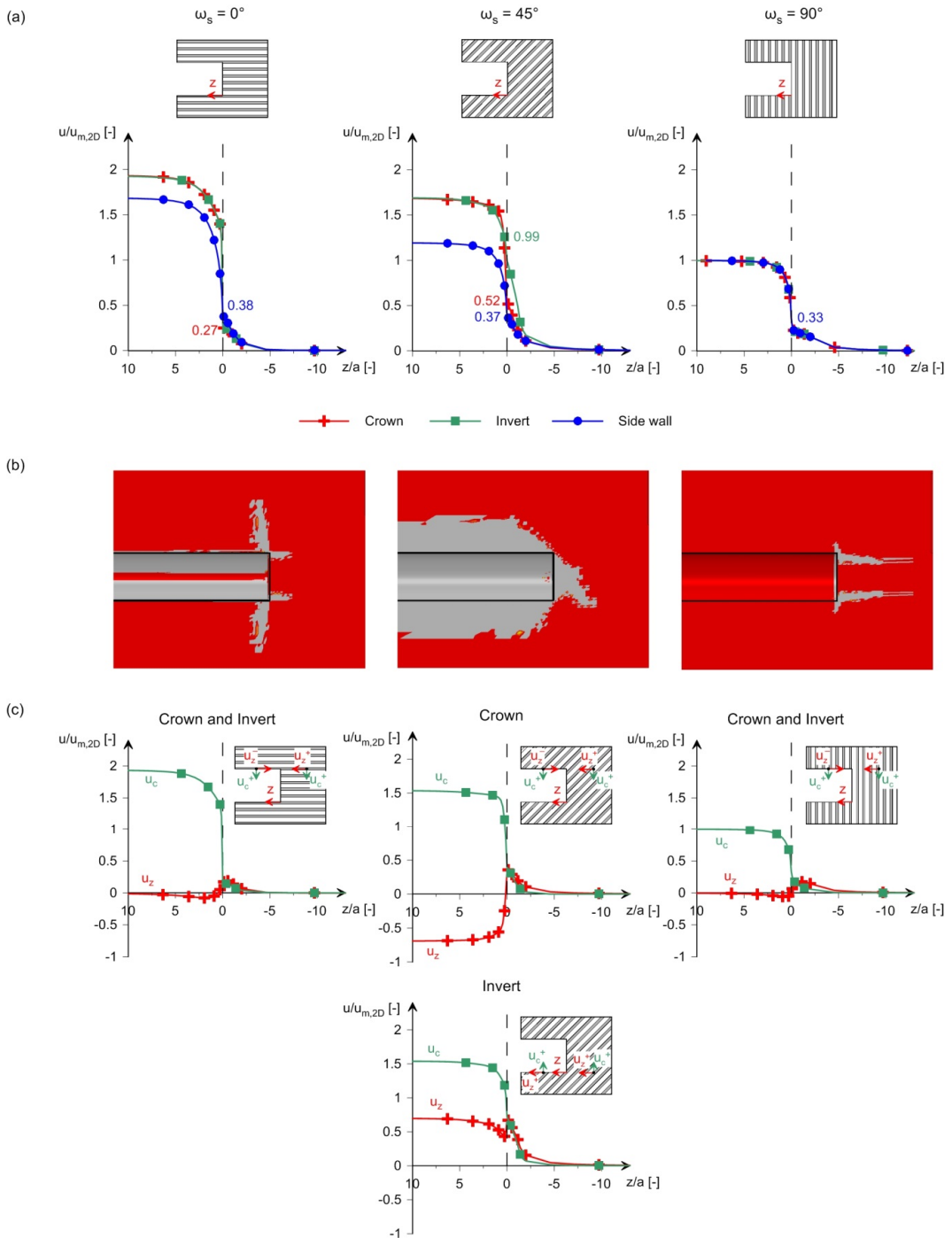


**Figure 5.3.** (a) Normalised displacement  $u/u_{m,2D}$  along the tunnel; (b) extent of the plastic zone; and, (c), normalised longitudinal displacement ( $u_z/u_{m,2D}$ ) and normalised cross-sectional displacement ( $u_c/u_{m,2D}$ ) along the tunnel ( $a = 5\text{ m}$ ,  $\sigma_0 = 10\text{ MPa}$ ,  $E = 1\text{ GPa}$ ,  $c_m = 6\text{ MPa}$ ,  $\varphi_m = 30^\circ$ ,  $\psi_m = 10^\circ$ ,  $c_s = 0.8\text{ MPa}$ ,  $\varphi_s = 10^\circ$ ,  $\psi_s = 5^\circ$ ,  $\nu = 0.3$ ).

### 5.1.2.1 Influence of the dip angle on the displacements

The Figure 5.3 shows, for a dip angle  $\omega_s$  of  $0^\circ$ ,  $45^\circ$  or  $90^\circ$ , (a), the longitudinal distribution of the magnitude of the displacement vector (hereafter referred as “the displacement”) at the crown, at the invert and at the side wall. The displacements are normalised by the displacement  $u_{m,2D}$ , which would occur in the absence of schistosity ( $u_{m,2D}$  can be determined analytically); (b) the plastic zone in the vertical symmetry plane of the tunnel; and, (c), the longitudinal distribution of the magnitude of the longitudinal component of the displacement vector as well as the magnitude of the projection of the displacement vector

in the plane of the tunnel cross-section (at the tunnel crown and invert; normalised by the displacement  $u_{m,2D}$ ).

For  $\omega_s = 90^\circ$ , schistosity is irrelevant for the displacements far behind the face, because failure in the schistosity plane cannot occur there. With decreasing dip angle the displacements increase and the profile deforms non-uniformly.

In the following, the maximum and minimum displacements of the profile will be considered rather than the displacements at specific points of the profile. (Note that the maximum displacements do not occur at the profile locations considered in Figure 5.3a and therefore the results of Figure 5.3a cannot be compared with those of the next figures.)

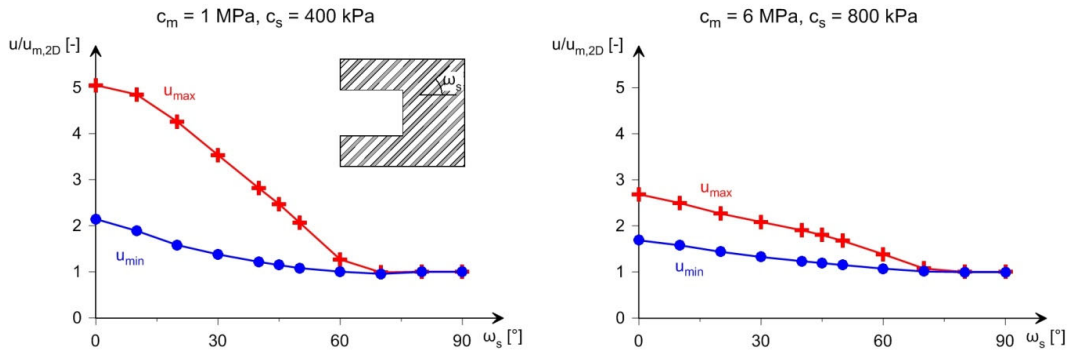


**Figure 5.4.** Normalised maximum and minimum displacements as a function of the dip angle  $\omega_s$  ( $a = 5$  m,  $\sigma_0 = 10$  MPa,  $E = 1$  GPa,  $\varphi_m = 30^\circ$ ,  $\psi_m = 10^\circ$ ,  $\varphi_s = 10^\circ$ ,  $\psi_s = 5^\circ$ ,  $\nu = 0.3$ ).

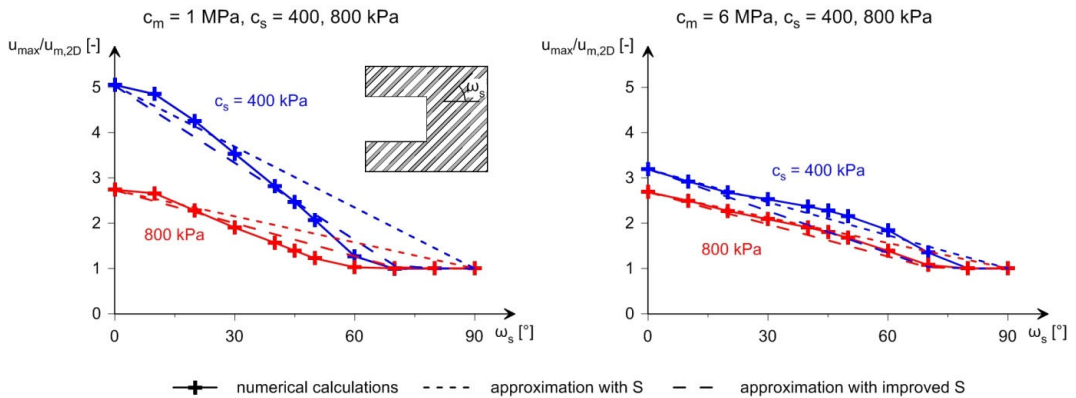


**Figure 5.5.** Effect of matrix and schistosity cohesion: Normalised maximum displacements as a function of the dip angle  $\omega_s$  ( $a = 5$  m,  $\sigma_0 = 10$  MPa,  $E = 1$  GPa,  $\varphi_m = 30^\circ$ ,  $\psi_m = 10^\circ$ ,  $\varphi_s = 10^\circ$ ,  $\psi_s = 5^\circ$ ,  $\nu = 0.3$ ).

Figures 5.4 and 5.5 show the normalised maximum and minimum displacements as a function of the dip angle for a matrix cohesion of 1 or 6 MPa and a schistosity cohesion of 400 or 800 kPa. The following conclusions can be drawn:

- The dip angle has a remarkable influence both on the maximum and on the minimum displacement (Fig. 5.4);
- The non-uniformity of the displacements in the tunnel profile is maximum at  $\omega_s = 0^\circ$  and decreases monotonously with increasing dip angle (Fig. 5.4);
- Schistosity does not play a role for the maximum and minimum displacements ( $u = u_{m,2D}$ ) if the dip angle is greater than ca.  $70^\circ$ ;
- The displacements in tunnelling parallel to schistosity plane can be considerably larger than in tunnelling perpendicular to the schistosity plane;
- The lower the schistosity cohesion, the bigger the effect of the dip angle will be (Fig. 5.5; l.h.s. diagram).

- It is the combination of a low schistosity cohesion with a low matrix cohesion which produces very large displacements: A by 50% lower cohesion in the schistosity planes results only in slightly larger displacements if the matrix is strong ( $c_m = 6$  MPa; r.h.s. diagram of Fig. 5.5), but to twice as big displacements if the matrix is weak ( $c_m = 1$  MPa; l.h.s. diagram of Fig. 5.5).

According to Figure 5.5, the maximum displacement can be approximated as a linear (or better bilinear) function of the dip angle. The linear function can be defined in terms of the schistosity influence factor  $S$  (Section 2.1), which combines the dip angle  $\omega_s$  and the angle  $\theta_s$  between the strike direction and the tunnel axis:

$$u_{max} = (u_{max,||} - u_{\perp}) \cdot S + u_{\perp}, \quad (5.1)$$

where

$$S = 1 - \frac{\omega_s}{90} \frac{\theta_s}{90} \in [0, 1], \quad (5.2)$$

( $\theta_s = 90^\circ$  in the present case) and  $u_{max,||}$  and  $u_{\perp}$  are the displacements in tunnelling parallel and perpendicular to the schistosity planes, respectively.  $u_{max,||}$  can be determined after Section 4.4, while  $u_{\perp}$  is equal to  $u_{m,2D}$ , which can be determined analytically.

The linear approximation (Eq. 5.1 with  $S$  after Eq. 5.2) is satisfactory for small dip angles, but overestimates the maximum displacement for steep schistosity planes, which – as mentioned before – do not play a role. The latter suggests a bilinear relationship, using an improved schistosity influence factor,

$$S = \max\left(1 - \frac{\omega_s}{90 - \varphi_s} \frac{\theta_s}{90 - \varphi_s}; 0\right) \in [0, 1], \quad (5.3)$$

which takes into account that failure is not possible for dip angles larger than  $90^\circ - \varphi_s$ . The  $S$  versus  $(\omega_s, \theta_s)$  plot is given in Figure 5.6.

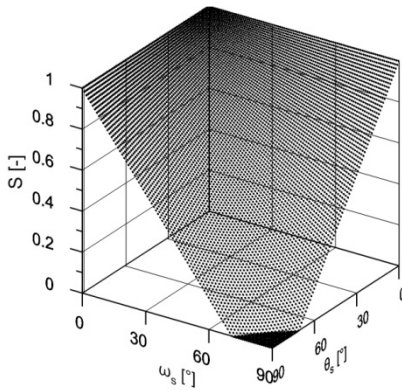


**Figure 5.6.** Improved schistosity influence factor  $S$  as a function of the schistosity dip angle  $\omega_s$  and the angle  $\theta_s$  between the strike direction of the schistosity and the tunnel axis ( $\varphi_s = 10^\circ$ ).

The accuracy of the improved schistosity influence factor for arbitrary strike directions will be demonstrated in Section 5.1.4.

The minimum displacements can be expressed analogously (see Fig. 5.4):

$$u_{min} = (u_{min,||} - u_{\perp}) \cdot S + u_{\perp}. \quad (5.4)$$

The relationships of this section provide a simple estimation of the displacements for different dip angles, which are satisfactory enough for practical purposes.

In Section 2.3, the so-called “schistosity angle”  $\beta$  (defined as the angle between the normal vector of the schistosity plane and the radial direction of the tunnel) was considered as a possible measure of the influence of the schistosity orientation on the displacement at a specific location of the tunnel profile. The underlying idea was that the largest displacements along the tunnel boundary occur at locations where the schistosity is almost parallel to the excavation boundary, while the smallest displacement occur at locations where the schistosity is almost perpendicular to the excavation boundary (provided that both, the schistosity and the matrix reach failure; see, e.g., [25], [45]). However, no clear correlation could be found in Section 2.3 between the displacements and the schistosity angle. This can be explained by means of numerical calculations. Figure 5.7 shows the displacements at the tunnel boundary as a function of the schistosity angle  $\beta$  and of the dip angle  $\omega_s$ . The displacements decrease with increasing schistosity angle, but only if the dip angle is fixed. The schistosity angle allows to estimate only the location of the tunnel boundary with the maximum displacement.

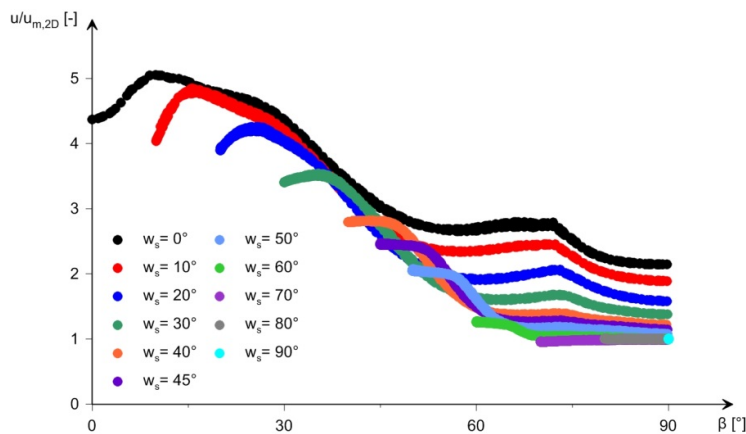


**Figure 5.7.** Normalised magnitude of the displacement vector  $u/u_{m,2D}$  as a function of the schistosity angle  $\beta$  for various dip angles  $\omega_s$  ( $a = 5$  m,  $\sigma_0 = 10$  MPa,  $E = 1$  GPa,  $c_m = 1$  MPa,  $\varphi_m = 30^\circ$ ,  $\psi_m = 10^\circ$ ,  $c_s = 0.4$  MPa,  $\varphi_s = 10^\circ$ ,  $\psi_s = 5^\circ$ ,  $\nu = 0.3$ ).

### 5.1.2.2 Influence of the dip angle on the pre-deformations

The numbers besides the  $z = 0$  line in Figure 5.3a give the normalised displacement at the face, i.e. the pre-deformation. The latter is considerably bigger for a dip angle  $\omega_s$  of  $45^\circ$  than for  $\omega_s = 0^\circ$  or  $90^\circ$  or for an isotropic material ( $0.27 \cdot u_{m,2D}$  in the example of Fig. 5.3). The existing pre-deformation estimation methods, which were developed for isotropic materials, underestimate the pre-deformation (and, consequently, overestimate the convergence) for schistous rocks with medium dip angles, but seem to be adequate for very steep or sub-horizontal schistosity planes.

The large pre-deformations occurring in the case of  $\omega_s = 45^\circ$  are caused by failure in the schistosity plane in an extended zone in the ground ahead of the face (over the entire face; Fig. 5.3b). The failure in the schistosity planes results also in bigger longitudinal displacements (Fig. 5.3c). For a tunnel drive perpendicular or parallel to the tunnel axis, the pre-deformations at the crown and the invert are the same (cf. Fig. 5.3) and lie almost in the cross-sectional plane of the tunnel. For  $\omega_s = 45^\circ$ , however, the longitudinal deformations are considerable at the face and along the entire tunnel; furthermore, the pre-deformations are considerably larger in the invert than in the crown (Fig. 5.3c), because the plastic zone ahead of the face is not symmetric with respect to tunnel axis (Fig. 5.3b). Klopčič and Logar [112] obtained similar results and therefore concluded that tunnel advance with the dip is advantageous because in this case the major part of the displacements occurs ahead of the face and, consequently, the convergences are smaller. This conclusion is correct concerning the crown displacement, but disregards that the convergence at the invert, which under squeezing conditions is equally important, will be considerably bigger.

Figure 5.8 presents additional computational results, for other values of the schistosity- and matrix-cohesion. The diagrams show the maximum of the “pre-deformation fraction” over the profile circumference as a function of the dip angle. (The “pre-deformation fraction” is defined as  $u/u(0)$ , where  $u$  is the displacement magnitude at a profile point far behind the face and  $u(0)$  denotes the displacement magnitude of the same profile point at the face.) The highest pre-deformation fractions occur at dip angles between  $20^\circ$  and  $70^\circ$ , irrespective of the cohesion of the schistosity and of the matrix.

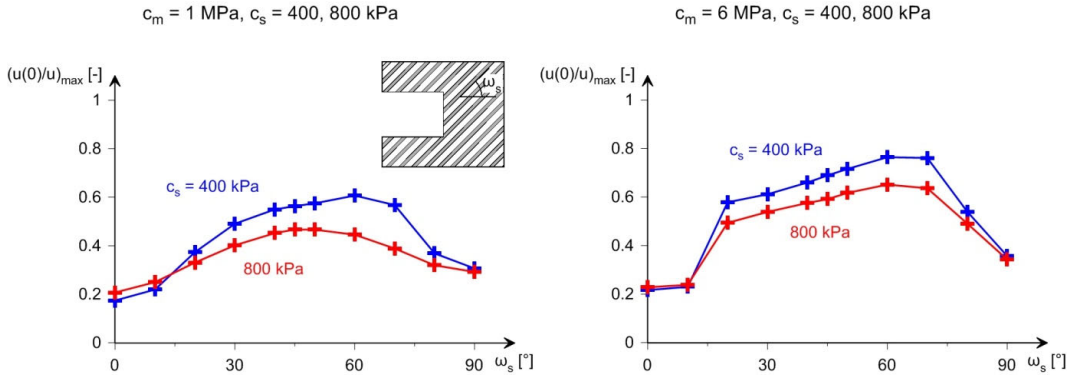


**Figure 5.8.** Maximum pre-deformation fraction as a function of the dip angle  $\omega_s$  ( $a = 5$  m,  $\sigma_0 = 10$  MPa,  $E = 1$  GPa,  $\varphi_m = 30^\circ$ ,  $\psi_m = 10^\circ$ ,  $\varphi_s = 10^\circ$ ,  $\psi_s = 5^\circ$ ,  $\nu = 0.3$ ).

### 5.1.2.3 Influence of the dip angle on the convergences

Figure 5.9 shows the maximum and minimum convergence as a function of the dip angle. One can recognise that:

- The dip angle influences considerably both the maximum and the minimum convergence;
- Schistosity does not play a role if the schistosity planes are steeper than about  $70^\circ$ ;
- The dip angle influences the convergences more than the displacements (for  $c_m = 1$  MPa and  $c_s = 0.4$  MPa, the maximum convergences for  $\omega_s = 0^\circ$  are by a factor of 6.5 higher than those for  $\omega_s = 90^\circ$ , while the maximum displacements for  $\omega_s = 0^\circ$  are by a factor of 5 higher than those for  $\omega_s = 90^\circ$ , see Fig. 5.4).

The relationship between the minimum or maximum convergence and dip angle can be approximated analogously to Section 5.1.2.1, *i.e.* by a linear or bilinear function (see Fig. 5.10):

$$\Delta u_{max} = (\Delta u_{max,||} - \Delta u_{\perp}) \cdot S + \Delta u_{\perp}, \quad (5.5)$$

$$\Delta u_{min} = (\Delta u_{min,||} - \Delta u_{\perp}) \cdot S + \Delta u_{\perp}. \quad (5.6)$$

where  $S$  denotes the schistosity influence factor after Eq. (5.2) or (5.3);  $\Delta u_{max,||}$  and  $\Delta u_{min,||}$  denote the maximum and minimum convergence, respectively, when tunnelling parallel to the schistosity planes and can be determined as usual for isotropic elasto-plastic materials (see [109]) with the parameters of the equivalent isotropic material after Section 4.4; and  $\Delta u_{\perp}$  is the convergence when tunnelling perpendicular to the schistosity planes and can be determined as usual for isotropic elasto-plastic materials with the parameters of the matrix. ( $\Delta u_{\perp}$  will be slightly overestimated, because the pre-deformations occurring in the absence of the schistosity are slightly smaller than those occurring in schistous rocks.)

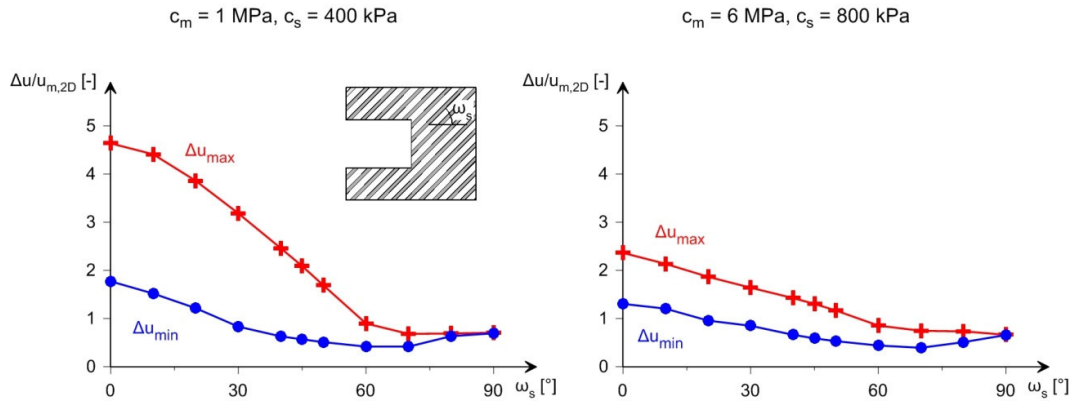


**Figure 5.9.** Normalised maximum and minimum convergences as a function of the dip angle  $\omega_s$  ( $a = 5\text{ m}$ ,  $\sigma_0 = 10\text{ MPa}$ ,  $E = 1\text{ GPa}$ ,  $\varphi_m = 30^\circ$ ,  $\psi_m = 10^\circ$ ,  $\varphi_s = 10^\circ$ ,  $\psi_s = 5^\circ$ ,  $\nu = 0.3$ ).

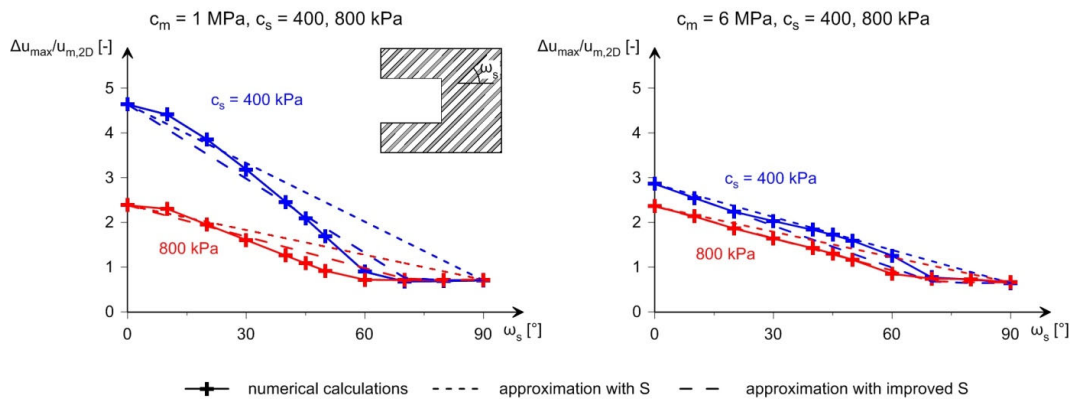


**Figure 5.10.** Effect of matrix and schistosity cohesion: Normalised maximum convergences as a function of the dip angle  $\omega_s$  ( $a = 5\text{ m}$ ,  $\sigma_0 = 10\text{ MPa}$ ,  $E = 1\text{ GPa}$ ,  $\varphi_m = 30^\circ$ ,  $\psi_m = 10^\circ$ ,  $\varphi_s = 10^\circ$ ,  $\psi_s = 5^\circ$ ,  $\nu = 0.3$ ).

### 5.1.3 Tunnelling in thinly stratified rock, perpendicular to the strike direction

This section discusses differences and similarities between schistous and stratified rocks with respect to the influence of the dip angle.

#### 5.1.3.1 Influence of the dip angle on the displacements

Figure 5.11 shows the displacement (the maximum one along the tunnel boundary in a cross-section far behind the tunnel face; normalised by the displacement that would occur in the absence of hard interlayers) as a function of the dip angle. As in the case of a schistous rock (Section 5.1.2), the dip angle has a remarkable influence on the displacements.

The dashed lines in Figure 5.11 represent the linear interpolation (Eqs. 5.1 and 5.2) between the displacements  $u^\perp$  and  $u_{max,||}$  occurring in the borderline cases of horizontal and vertical bedding, whereby  $u^\perp$  can be determined analytically after Section 3.2, while  $u_{max,||}$  can be estimated using the dimensionless diagrams introduced in Section 4.2.

Contrarily to a schistous rock mass, the bilinear approximation (S after Eq. 5.3) is not meaningful; due to the direction-dependent stiffness of the stratified rock mass, the displacements for dip angles larger than about  $90^\circ - \varphi_w = 65^\circ$  are not constant.

The linear approximation underestimates the displacements considerably for the low initial stress  $\sigma_0$  of 0.75 MPa (for which both the weak and the hard layers remain elastic) but provides satisfactory results for the practically relevant case of a high initial stress

( $\sigma_0 = 10$  MPa in the example of Fig. 5.11). Therefore, in the next sections, only the case of  $\sigma_0 = 10$  MPa will be analysed.

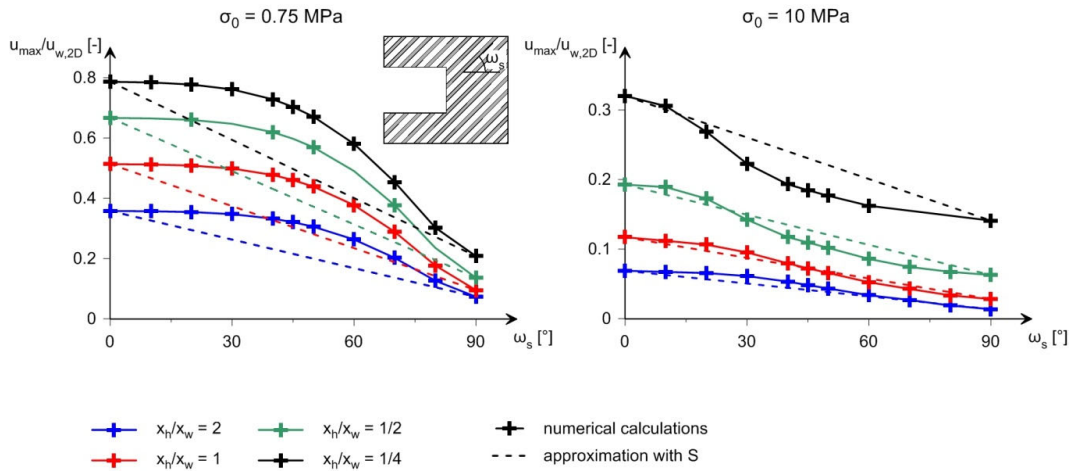


**Figure 5.11.** Normalised maximum displacement as a function of the dip angle  $\omega_s$  ( $a = 5$  m,  $E_h = 10$  GPa,  $c_h = 5$  MPa,  $E_w = 0.5$  GPa,  $c_w = 0.5$  MPa,  $\nu_h = \nu_w = 0.3$ ,  $\varphi_h = \varphi_w = 25^\circ$ ,  $\psi_h = \psi_w = 5^\circ$ ).

### 5.1.3.2 Influence of the dip angle on the pre-deformations

As for a schistous rock, the pre-deformation in the invert is large for  $\omega_s = 45^\circ$  (Fig. 5.12a). (For comparison, the pre-deformation for a tunnel drive in only hard rocks would amount to  $0.016 \cdot u_{w,2D}$  and those in only weak rocks to  $0.25 \cdot u_{w,2D}$ .) However, contrary to schistous rocks, considerable pre-deformation fractions occur also for a dip angle of  $90^\circ$ .

The large pre-deformations in tunnelling perpendicular to the layers are associated with the large longitudinal deformations (Fig. 5.12b), which occur due to the considerably lower stiffness perpendicular to the layers: As the ground deforms more ahead of the tunnel face, the rock behind the face experiences a longitudinal displacement towards the excavated part of the tunnel. The opposite happens in a tunnel drive parallel to the layers: As the ground deforms more behind the tunnel face, it experiences a longitudinal displacement towards the tunnel face.

As for schistous rocks, large longitudinal deformations ahead of the face take also place for a dip angle of  $\omega_s$  of  $45^\circ$  (Fig. 5.12b); they are considerably larger in the invert than in the crown. This aspect is more pronounced than for the schistous rock mass and was already observed by Tonon and Amadei [111]: A transversely isotropic rock mass is stiffer in direction parallel to the layers and more deformable in direction normal to them. When excavating against dip, the rock mass at the invert is more deformable towards the excavated part of the tunnel. On the contrary, the rock mass at the crown is more deformable towards the non-excavated part of the tunnel, leading thus to smaller pre-deformations at the crown (*cf.* [111]).

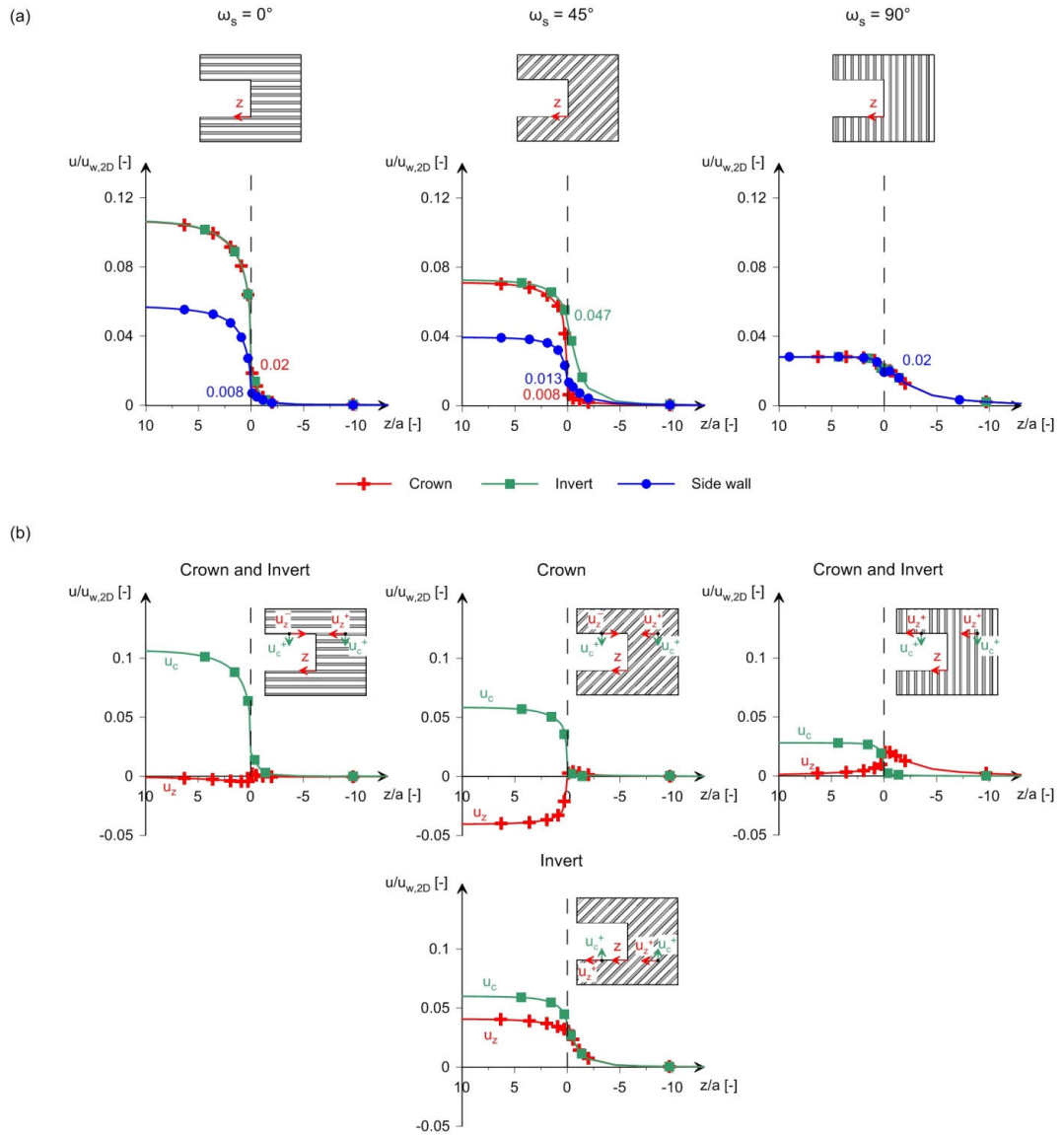


**Figure 5.12.** (a) Normalised displacement  $u/u_{w,2D}$  along the tunnel; and, (b), normalised longitudinal displacement ( $u_z/u_{w,2D}$ ) and normalised cross-sectional displacement ( $u_c/u_{w,2D}$ ) along the tunnel ( $a = 5 \text{ m}$ ,  $\sigma_0 = 10 \text{ MPa}$ ,  $x_h/x_w = 1$ ,  $E_h = 10 \text{ GPa}$ ;  $c_h = 5 \text{ MPa}$ ,  $E_w = 0.5 \text{ GPa}$ ,  $c_w = 0.5 \text{ MPa}$ ,  $\nu_h = \nu_w = 0.3$ ,  $\phi_h = \phi_w = 25^\circ$ ,  $\psi_h = \psi_w = 5^\circ$ ).

Therefore, according to Tonon and Amadei [111], larger tunnel convergences develop when tunnelling with dip (as when tunnelling against dip), as the pre-deformations occurring ahead of the tunnel are larger (while the total displacements are the same). Figure 5.13, however, shows that the tunnel convergences when tunnelling with or against dip are exactly the same, but do not develop at the same location in the tunnel (*i.e.*, mirroring the tunnel problem). Tonon and Amadei [111] only considered the pre-deformations in the crown and did not take into account that the pre-deformations in the invert (when advancing in dip direction) are considerably smaller. Of course, the excavation direction can be important in tunnelling – as for example tunnelling against dip is more critical in respect to the stability of the tunnel face (due to loosening) – but not in respect to squeezing.

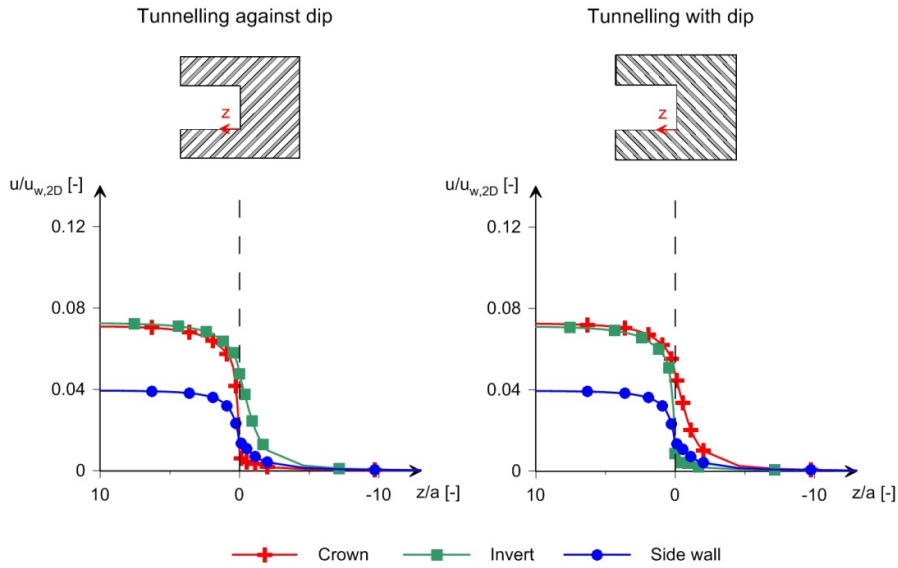


**Figure 5.13.** Normalised magnitude of the displacement vector  $u/u_{w,2D}$  along the tunnel for a dip angle  $\omega_s$  of  $45^\circ$  ( $a = 5\text{ m}$ ,  $\sigma_0 = 10\text{ MPa}$ ,  $x_h/x_w = 1$ ,  $E_h = 10\text{ GPa}$ ;  $c_h = 5\text{ MPa}$ ,  $E_w = 0.5\text{ GPa}$ ,  $c_w = 0.5\text{ MPa}$ ,  $\nu_h = \nu_w = 0.3$ ,  $\varphi_h = \varphi_w = 25^\circ$ ,  $\psi_h = \psi_w = 5^\circ$ ).

According to Figure 5.14, which shows the pre-deformation fraction as a function of the dip angle, the pre-deformation fraction reaches considerable values for dip angles between  $20^\circ$  and  $70^\circ$ . However in contrast to schistous rocks, for dip angles of about  $90^\circ$ , the pre-deformation fraction can also be large, because large longitudinal deformations occur ahead of the face due to the stiffness difference parallel and perpendicular to the layers.

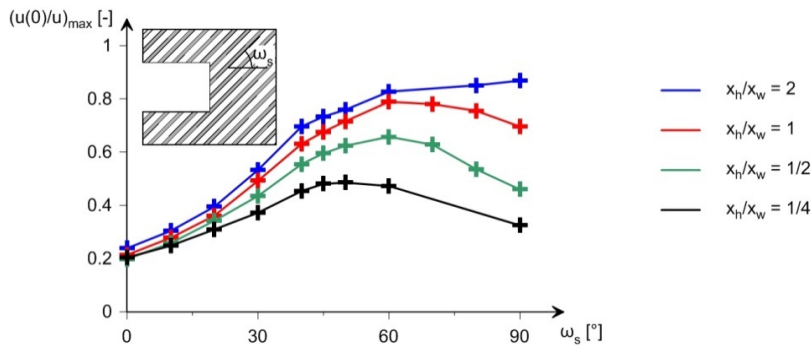


**Figure 5.14.** Maximum pre-deformation fraction as a function of the dip angle  $\omega_s$  ( $a = 5\text{ m}$ ,  $\sigma_0 = 10\text{ MPa}$ ,  $E_h = 10\text{ GPa}$ ,  $c_h = 5\text{ MPa}$ ,  $E_w = 0.5\text{ GPa}$ ,  $c_w = 0.5\text{ MPa}$ ,  $\nu_h = \nu_w = 0.3$ ,  $\varphi_h = \varphi_w = 25^\circ$ ,  $\psi_h = \psi_w = 5^\circ$ ).

### 5.1.3.3 Influence of the dip angle on the convergences

The linear approximation (Eq. 5.5) can also be applied for stratified rocks, whereby  $\Delta u_\perp$  and  $\Delta u_{max,II}$  can be determined as usual for isotropic elasto-plastic materials (see [109]) with the parameters of an equivalent isotropic material after Section 3.3 and 4.2, respectively. The linear approximation is satisfactory for stratified rocks (Fig. 5.15), although not so good as for schistous rocks.

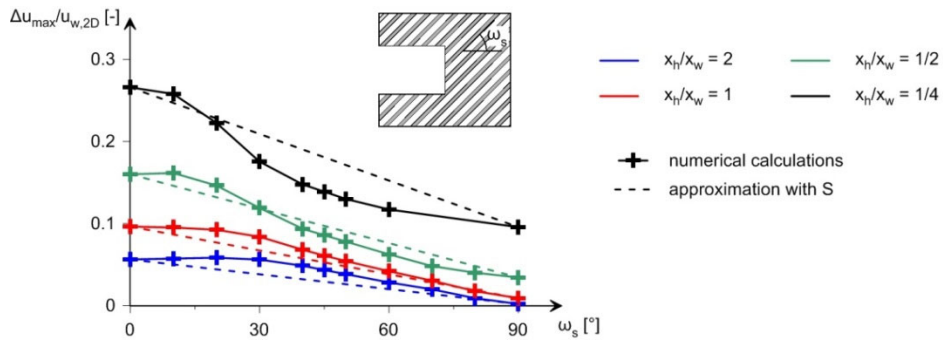


**Figure 5.15.** Normalised maximum tunnel convergences as a function of the dip angle  $\omega_s$  ( $a = 5\text{ m}$ ,  $\sigma_0 = 10\text{ MPa}$ ,  $E_h = 10\text{ GPa}$ ;  $c_h = 5\text{ MPa}$ ,  $E_w = 0.5\text{ GPa}$ ,  $c_w = 0.5\text{ MPa}$ ,  $\nu_h = \nu_w = 0.3$ ,  $\varphi_h = \varphi_w = 25^\circ$ ,  $\psi_h = \psi_w = 5^\circ$ ).

### 5.1.4 Arbitrary strike

The linear or bilinear approximations of Section 5.1.2 (Eqs. 5.1 to 5.6) are sufficiently accurate also for arbitrary dip angles  $\omega_s$  and strike directions  $\theta_s$ . This will be shown by the computational results of a parametric study considering schistous rock. (The behaviour of thinly stratified rocks is mostly the same in this respect; see Section 5.1.3.)

$$c_s = 800\text{ kPa}, c_m = 6000\text{ kPa}$$

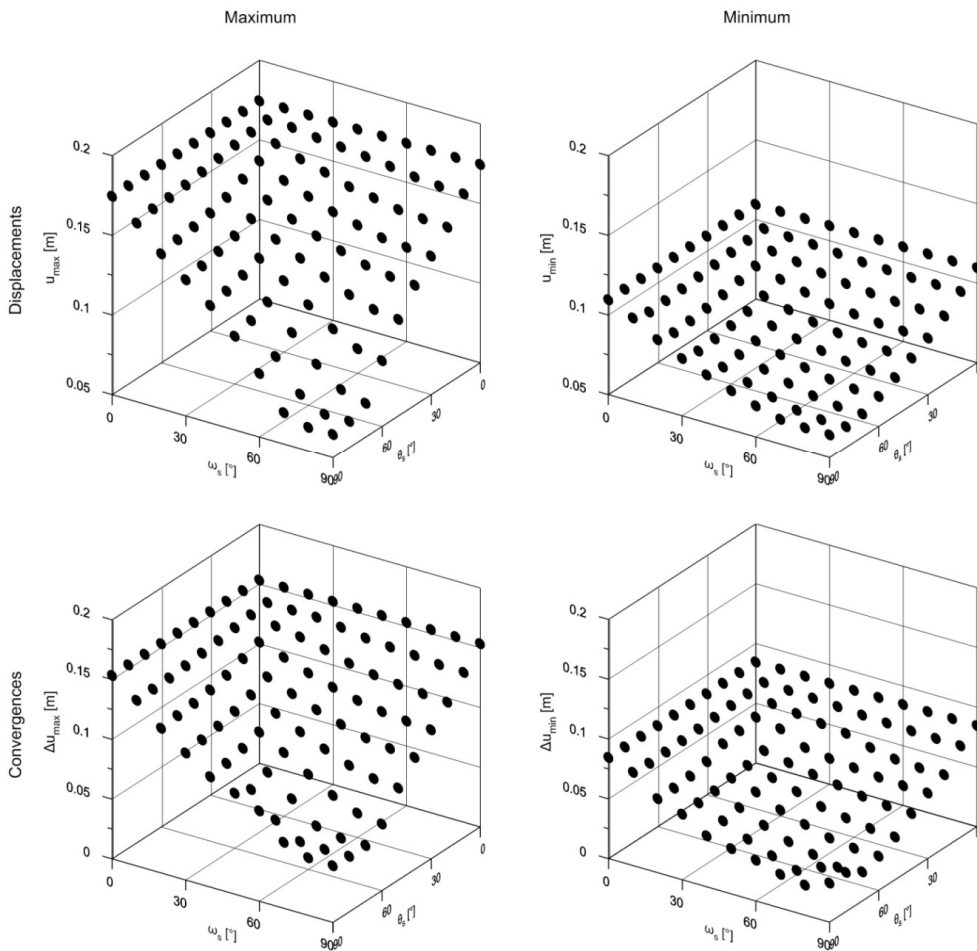


**Figure 5.16.** Maximum and minimum displacements and convergences as a function of the dip angle  $\omega_s$  and the angle  $\theta_s$  between the schistosity strike direction and tunnel axis ( $a = 5\text{ m}$ ,  $\sigma_0 = 10\text{ MPa}$ ,  $E = 1\text{ GPa}$ ,  $c_m = 6\text{ MPa}$ ,  $\varphi_m = 30^\circ$ ,  $\psi_m = 10^\circ$ ,  $c_s = 0.8\text{ MPa}$ ,  $\varphi_s = 10^\circ$ ,  $\psi_s = 5^\circ$ ,  $\nu = 0.3$ ).

Figures 5.16 and 5.17 show the numerically obtained displacement versus  $(\omega_s, \theta_s)$  and the convergence versus  $(\omega_s, \theta_s)$  diagrams for less and more severe squeezing conditions, respectively. (In the first case, yielding occurs only in the schistosity plane.)

The diagrams of Figures 5.16 and 5.17 are very similar to the  $S$  versus  $(\omega_s, \theta_s)$  diagram of Section 2.1 and, particularly, to the one of Figure 5.6 (improved schistosity influence factor  $S$ ), supporting thus the conclusion that the linear and, particularly, the bilinear approximation introduced in Section 5.1.2 are sufficiently accurate for practical purposes for any strike direction to the tunnel axis.

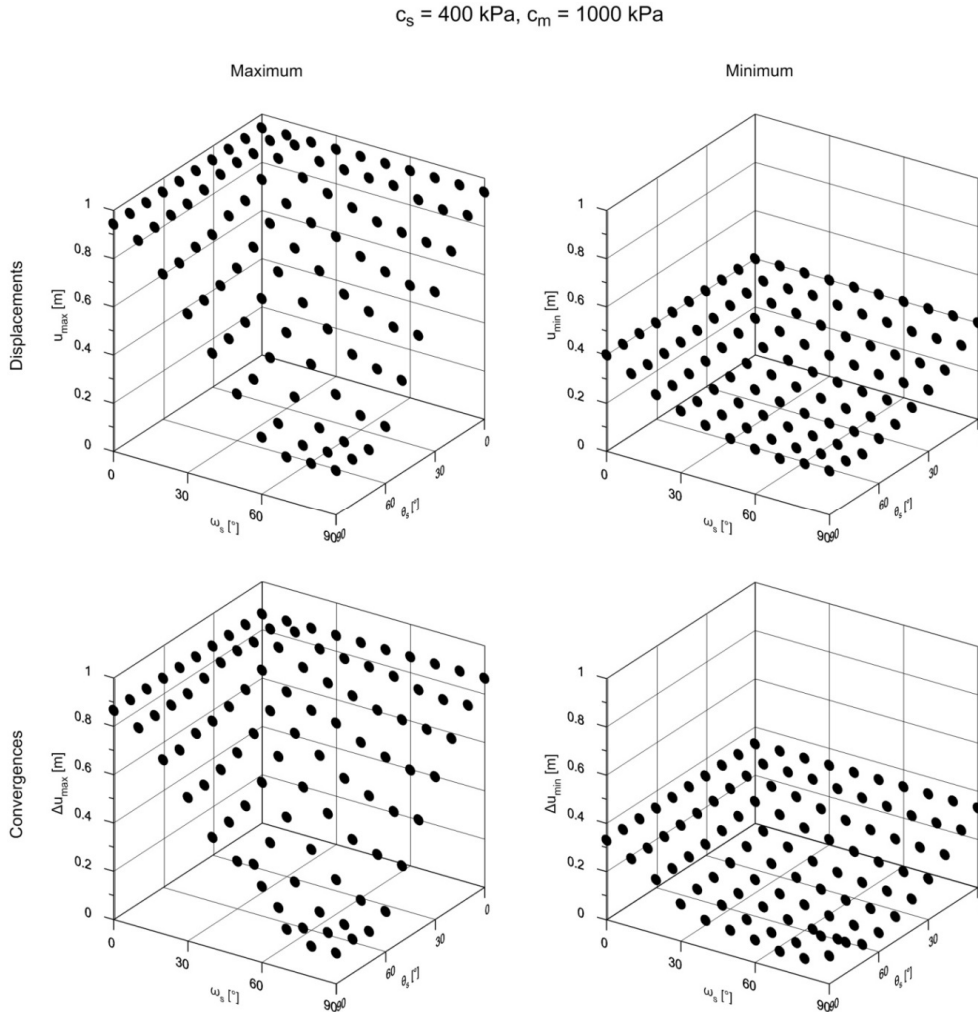


**Figure 5.17.** Maximum and minimum displacements and convergences as a function of the dip angle  $\omega_s$  and the angle  $\theta_s$  between the schistosity strike direction and tunnel axis ( $a = 5 \text{ m}$ ,  $\sigma_0 = 10 \text{ MPa}$ ,  $E = 1 \text{ GPa}$ ,  $c_m = 1 \text{ MPa}$ ,  $\varphi_m = 30^\circ$ ,  $\psi_m = 10^\circ$ ,  $c_s = 0.4 \text{ MPa}$ ,  $\varphi_s = 10^\circ$ ,  $\psi_s = 5^\circ$ ,  $\nu = 0.3$ ).

### 5.1.5 Conclusions

This chapter investigated the influence of bedding and schistosity planes using spatial calculation models with arbitrary orientation of the planes of anisotropy relative to the tunnel axis and showed that the orientation of the planes of anisotropy to the tunnel has a considerable influence on the convergences (considering the pre-deformation occurring ahead of the tunnel face), when tunnelling through thinly stratified and schistous rock masses.

Furthermore, this chapter could show that there are relevant differences to the well-known case of an isotropic rock mass and that the numerical calculations reproduce well the

empirically determined relationship between convergence and spatial orientation of the schistosity considering the so-called “schistosity influence factor”, which combines the dip  $\omega_s$  and the strike direction  $\theta_s$  of the planes of anisotropy to the tunnel axis and was developed based on the data from the Gotthard Base Tunnel (Section 2.1). This relationship allows to estimate the displacement for an arbitrary orientation of the anisotropy planes to the tunnel axis based upon the displacements for the borderline cases of vertical or horizontal anisotropy planes, rendering thus spatial numerical analyses unnecessary at least in the preliminary design stage.

## 5.2 Variability of squeezing deformations in folded rocks

### 5.2.1 Introduction

Section 5.1 showed that the orientation of bedding or schistosity plays a very important role for the magnitude and distribution of the deformations in the cross-section of the tunnel. Specifically, planes of anisotropy may affect rock behaviour adversely, particularly if their strike direction forms a small angle with (or is parallel to) the tunnel axis. The orientation of bedding or schistosity may change frequently along a tunnel through folded rocks and result in variable squeezing intensity.

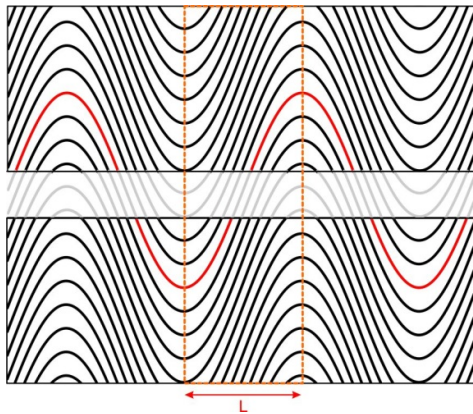


**Figure 5.18.** Tunnelling through a folded structure with strike direction of the planes of anisotropy perpendicular to the tunnel axis.

In this chapter, a folded rock mass is considered, whose strike direction is perpendicular to the tunnel, while the dip angle changes along the alignment. A folded structure is characterised by tunnel sections, where the schistosity planes lie parallel to the tunnel axis and tunnel sections with larger dip angles (see Fig. 5.18). From Section 5.1, it is known that the most adverse conditions occur, when the schistosity lies parallel to the tunnel axis and the most favourable conditions occur, when the dip angle of the schistosity becomes maximum. Due to the interaction between tunnel sections with more favourable anisotropy plane orientations and tunnel sections with adverse anisotropy plane orientations, the deformations may become more uniform along the tunnel, so that the squeezing variability may even disappear completely. This can be the case in an extremely folded rock mass, where the orientation of the anisotropy planes changes within few meters. The influence of frequent orientation changes of the planes of anisotropy in folded rocks on the squeezing behaviour has not been investigated so far.

Starting with the problem definition and the geometric modelling of a folded rock mass in Section 5.2.2, it will be shown that even small variations of the orientation of the planes of anisotropy may cause a significant variability of the intensity of the convergences, and this both for schistous (Section 5.2.3) and for thinly stratified rock masses (Section 5.2.4).

Finally, in Section 5.2.5, the influence of the variation of the orientation of the planes of anisotropy on the tunnel convergences will be shown by means of an application example concerning the Sedrun section of the Gotthard Base Tunnel, where heavily squeezing conditions were encountered during construction (Section 2.1), and the predictive capacity

of the so-called “schistosity influence factor”  $S$ , which was already introduced in Section 2.1, will be discussed.

### 5.2.2 Problem definition

Due to buckling of the formation, a folding may develop that has a symmetric, periodic, sinusoidal shape (cf., e.g., [118]). The geometry of the folding can be simplified as a sinusoidal function in the  $z$ -direction (Fig. 5.19):

$$y = A \cdot \sin\left(\frac{(z - L/2) \cdot \pi}{L}\right), \tag{5.7}$$

where  $L$  denotes half the period and  $A$  the amplitude of the folds.

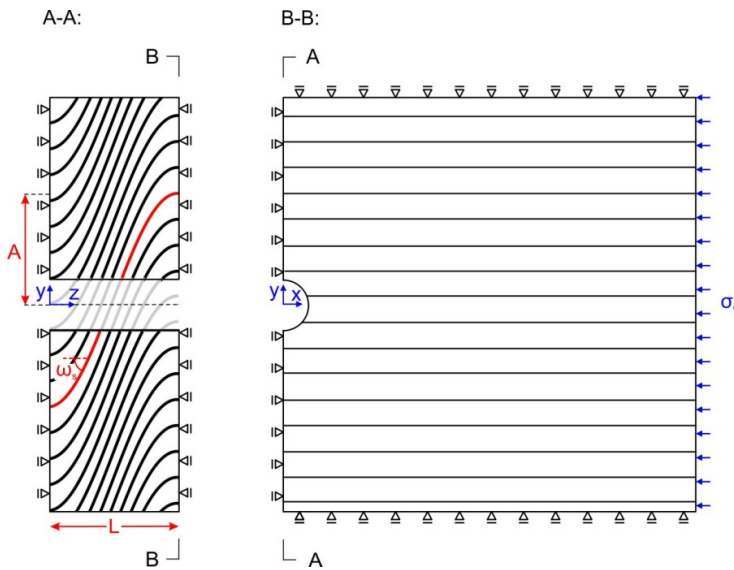


**Figure 5.19.** Problem layout with boundary conditions assuming that the strike direction of the planes of anisotropy is perpendicular to the tunnel axis.

The dip angle  $\omega_s$  varies then along the tunnel according to the equation:

$$\omega_s = \left| \arctan\left(A \cdot \frac{\pi}{L} \cos\left(\frac{(z - L/2) \cdot \pi}{L}\right)\right) \right| \in [0; 90], \tag{5.8}$$

while the maximum dip angle of the folds reads as follows:

$$\omega_{s,max} = \arctan\left(A \cdot \frac{\pi}{L}\right). \tag{5.9}$$

Folding is taken into account numerically on the level of the constitutive model, by considering a position-dependent normal vector to the anisotropy surface:

$$\vec{n} = \begin{pmatrix} 0 \\ 1 \\ -\frac{A \cdot \pi}{L} \cdot \cos\left(\frac{(z - L/2) \cdot \pi}{L}\right) \end{pmatrix}. \tag{5.10}$$

According to Equation (5.10), the geometry of the folded rock mass is defined solely by the maximum dip angle  $\omega_{s,max}$  (defined by  $A\pi/L$ ; Eq. 5.9) and the period  $2L$  of the sinuisodal folds.

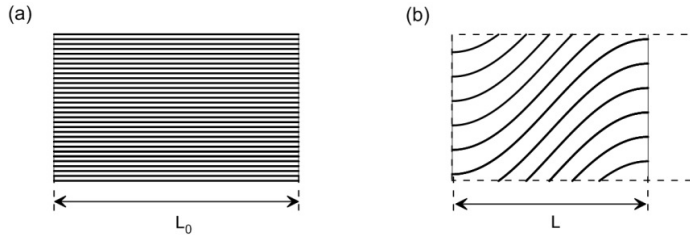


**Figure 5.20.** (a) Undeformed formation, (b), folding due to shortening of the formation by 20%.

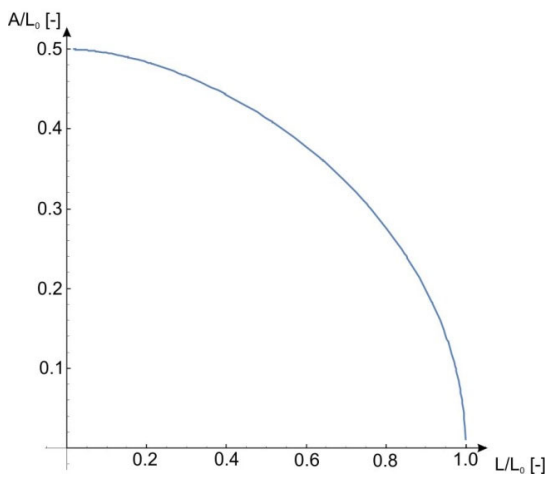


**Figure 5.21.** Amplitude of the folding  $A/L_0$  according to Equation (5.11) as a function of  $L/L_0$ .

Physically meaningful pairs of these two parameters could be chosen by considering an initially unfolded formation of length  $L_0$  (Fig. 5.20a), which buckles under the action of horizontal tectonic stresses and becomes compressed to a length  $L$  (Fig. 5.20b). The corresponding amplitude of the folding (cf. Eq. 5.7) can be calculated with the requirement that the arc length of the folding corresponds to the original length of the formation:

$$L_0 = \int_0^L \sqrt{1 + (y')^2} \cdot dz = \int_0^L \sqrt{1 + \left( \frac{A \cdot \pi}{L} \cos\left( \frac{\pi \cdot z}{L} \right) \right)^2} \cdot dz, \quad (5.11)$$

which can be solved with respect to  $A$  by using the elliptic integral of the function. The results are represented in Figure 5.21. The more the formation is compressed, the larger the amplitude and thus the maximum dip angle  $\omega_{s,max}$  of the folding will be (Eq. 5.9).

The numerical model is presented in Figure 5.19 and is delimited by the symmetry planes of the folding, having thus a length equal to half a period  $L$  (cf. Fig. 5.18). If the strike direction of the planes of anisotropy is perpendicular to the tunnel axis (due to symmetry), only half of the system has to be considered; otherwise the whole system has to be considered (as in Section 5.2.5).

An unsupported tunnel will be considered and the excavation will be simulated through a stepwise reduction of the tractions at the excavation boundary from  $\sigma_0$  to zero along the entire tunnel (Fig. 5.19). The displacements, that are calculated in this way, include the pre-deformations. Only the magnitude of the displacement vector will be considered

(hereafter referred to as “displacement”). (The longitudinal displacement is small, which means that the main component of the displacement vector is the cross-sectional one.) In order to reduce the sensitivity of the results to the mesh discretisation, sufficiently fine meshes were chosen (e.g., Fig. 5.22).

The rock structure is taken as a homogeneous, transversely isotropic material, which accounts either for the presence of schistosity planes, or for the mechanical parameters and thickness fractions of thinly alternating weak and hard layers. The constitutive models were already presented and validated in the Sections 4.2 and 4.4, respectively. The computations are carried out with Abaqus [64].

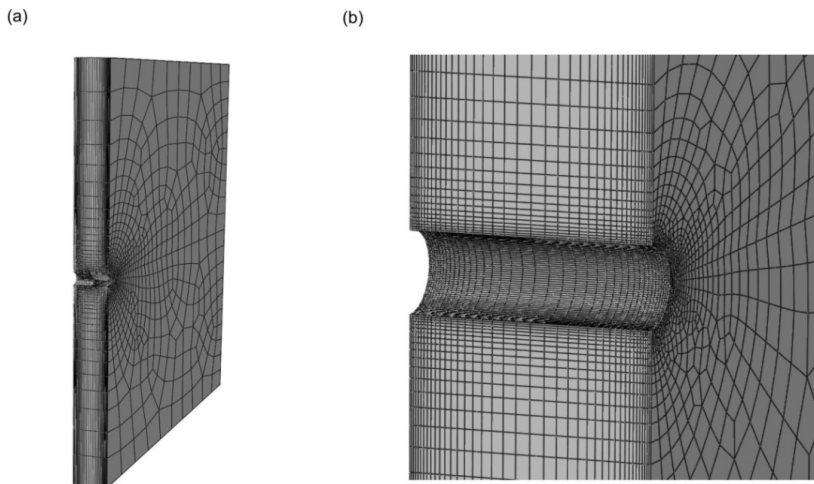


**Figure 5.22.** (a) Numerical model for  $L = 25$  m for the strike direction of the planes of anisotropy perpendicular to the tunnel axis, (b), Detail of the numerical model.

### 5.2.3 Schistous rocks

According to Section 5.1, the largest displacements develop when yielding occurs both in the schistosity planes and in the matrix. Therefore, low cohesion values will be chosen both for the matrix and the schistosity planes (see legend of Fig. 5.23).

The l.h.s. diagrams of Figure 5.23 show the longitudinal displacement distribution (maximum, minimum and averaged values, normalised by the tunnel radius) for an unfolded formation as well as for the folding resulting from a formation compression  $\varepsilon_f$  by 3.5%, 20% and 50%. The r.h.s. diagrams show the displacement distribution along the circumference of the tunnel cross-section at the fold peak ( $z = 0$ ; the most unfavourable cross-section) as well as at the location of the maximum dip angle ( $z = L/2$ ; the most favourable cross-section). In the following, the magnitude and distribution of the displacements will be discussed, considering the ratio of the maximum displacements at the two aforementioned cross-sections (at  $z = 0$  and  $L/2$ ) as a measure of the squeezing variability. (The minimum and averaged displacements remain nearly constant along the tunnel.) Studying the computational results of Figure 5.23 from top to down, one can readily recognise the effect of an increasing tectonic compression  $\varepsilon_f$  and folding of the formation:

- The maximum dip angle  $\omega_{s,max}$  increases and consequently (Section 5.1) the displacements at  $z = L/2$  decrease. For  $\varepsilon_f \geq 50\%$ , the anisotropy plane becomes so steep at the cross-section  $z = L/2$  ( $\omega_{s,max} > 68^\circ$ ), that the schistosity does not play a role anymore (cf. Section 5.1). The displacements at the cross-section  $z = L/2$  are approximately equal to the displacements that would occur if the dip angle were constant ( $= \omega_{s,max}$ ) along the tunnel. (This is, for example, recognisable for  $\varepsilon_f = 20\%$ , as  $u_{max}/a$  for the constant  $\omega_{s,max}$  amounts to ca. 0.1 and is the same as  $u_{max}(z = L/2)/a \approx 0.1$ .) This means that the tunnel section with steep anisotropy planes is not influenced by the nearby zones where the anisotropy planes are subhorizontal.

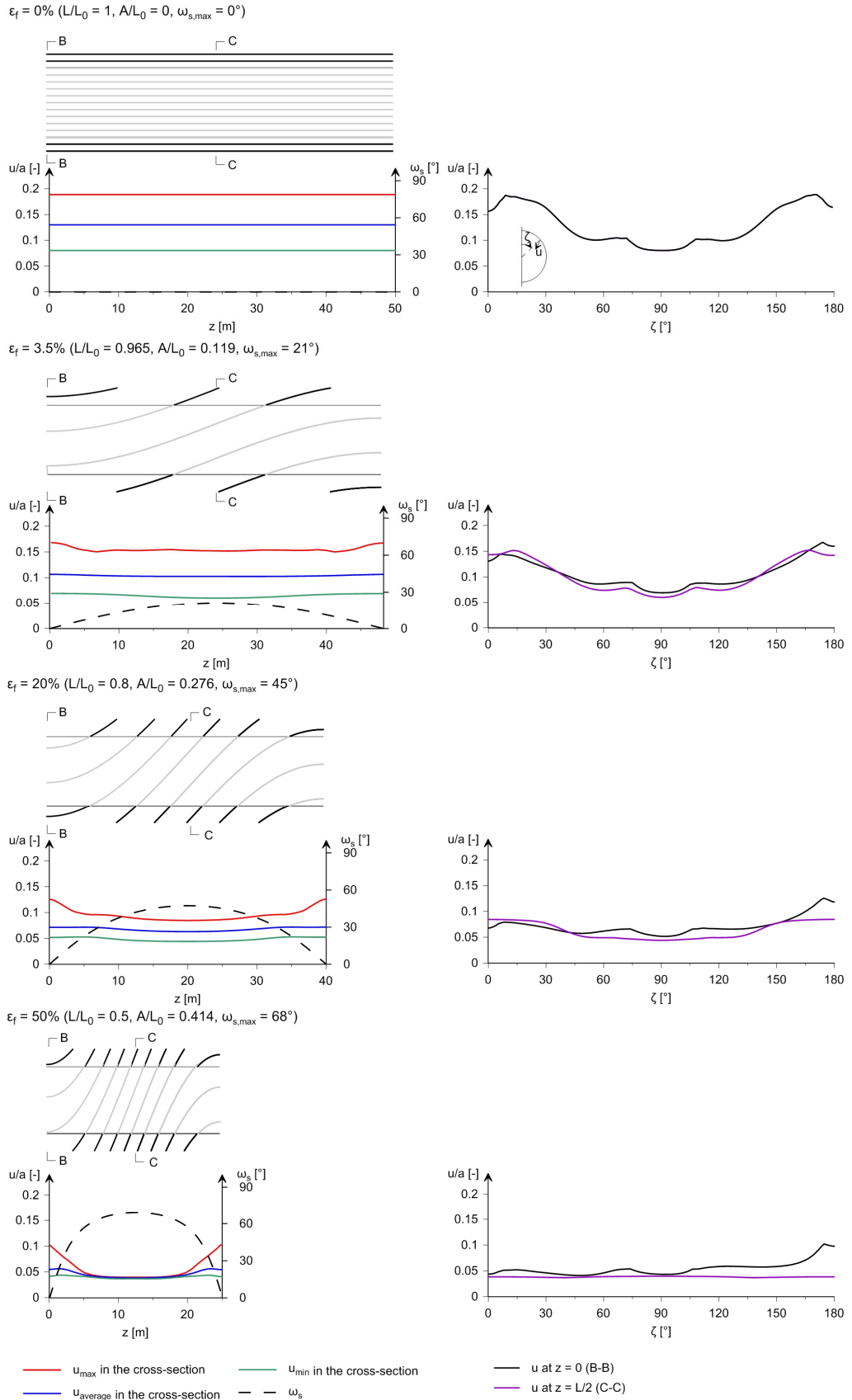


**Figure 5.23.** Influence of formation compression. Maximum, minimum and averaged tunnel displacements along the tunnel (l.h.s.) and displacements along the tunnel boundary at  $z = 0$  and at  $z = L/2$  (r.h.s.;  $a = 5$  m,  $\sigma_0 = 10$  MPa,  $E = 1$  GPa,  $c_m = 1$  MPa,  $\phi_m = 30^\circ$ ,  $\psi_m = 10^\circ$ ,  $c_s = 0.4$  MPa,  $\phi_s = 10^\circ$ ,  $\psi_s = 5^\circ$ ,  $\nu = 0.3$ ).

- The displacements at the fold peak ( $z = 0$ ) decrease (by a factor of two for a compression  $\varepsilon_f$  of 50%); the adjacent tunnel sections with steep anisotropy planes have a stabilising effect. Note that in the case of intensive folding ( $\varepsilon_f = 50\%$ ), particularly large displacements occur only very locally, in the very short tunnel sections with almost horizontal schistosity planes. The tunnel sections with steep schistosity planes are much more extended, which explains the observation made above that the displacements in these tunnel sections are not affected by the fold peaks.
- The displacement distribution becomes more uniform along the circumference of the tunnel cross-section (compare the r.h.s. diagrams for  $\varepsilon_f = 0\%$  with those for  $\varepsilon_f = 50\%$ ). In the case of intensive folding ( $\varepsilon_f = 50\%$ ), the displacements are non-uniformly distributed along the circumference of the tunnel cross-section only in the close vicinity of the fold peaks.
- The squeezing variability increases in the considered range of  $0\% < \varepsilon_f < 50\%$ . For  $\varepsilon_f = 50\%$ , the maximum displacement at the fold peak is by a factor 2.5 higher than the maximum displacement in the tunnel section with steep schistosity planes. It should be noted that the squeezing variability is maximum at  $\varepsilon_f = 50\%$ . If the formation were more intensively folded, then the displacements at  $z = L/2$  would remain constant (schistosity does not play a role for such big dip angles; cf. Section 5.1), but the displacements at  $z = 0$  (and consequently the variability, too) would decrease (due to the stabilising influence of the adjacent areas with steep schistosity planes). This will be shown later.

In the parametric study of Figure 5.23, the maximum dip angle  $\omega_{s,max}$  and the fold period are varied simultaneously. Next, the effect of these two parameters will be investigated separately. In Figure 5.24, the fold period is kept constant and the influence of the maximum dip angle  $\omega_{s,max}$  (or, equivalently, the fold amplitude; see Eq. 5.9) is investigated. The following conclusions can be drawn:

- The maximum displacements along the tunnel increase with decreasing  $\omega_{s,max}$ . (The influence of  $\omega_{s,max}$  on the averaged and minimum displacements is small.)
- A decrease in  $\omega_{s,max}$  from  $87.7^\circ$  to  $68^\circ$  results in a *larger* squeezing variability along the tunnel (the ratio of the maximum displacements at the cross-sections  $z = 0$  and  $z = L/2$  increases from 1.8 to 2.6). This is because the displacements at  $z = L/2$  remain constant (schistosity does not play a role, if the schistosity planes are so steep; cf. Section 5.1), but the maximum displacements at the fold peak ( $z = 0$ ) decrease due to the stabilising influence of the adjacent areas with steeply inclined schistosity planes.
- A further decrease in  $\omega_{s,max}$  from  $68^\circ$  to  $51^\circ$  leads to a *smaller* squeezing variability along the tunnel (the aforementioned ratio decreases from ca. 2.6 to 1.7), but to a bigger non-uniformity of the displacements in the tunnel profile, and this over the entire tunnel. (Note that, therefore, squeezing variability is maximum at  $\omega_{s,max} = 68^\circ$ .)
- The displacements in the long tunnel section with steep schistosity planes are not influenced by the adjacent tunnel sections with subhorizontal schistosity planes; they are almost equal to those that would occur if the dip angle were constant ( $= \omega_{s,max}$ ). As will be shown later, this is such due to the assumed, rather large, fold period (of  $L/a = 5$ ).

Next, the influence of the fold period is investigated, keeping the maximum dip angle  $\omega_{s,max}$  equal to almost  $90^\circ$  (Fig. 5.25). The following conclusions can be drawn:

- The displacements at the fold peaks increase with increasing fold period. The reason is that the tunnel sections with subhorizontal schistosity planes become longer. However, large displacements occur only locally (around the fold peaks), as the tunnel sections with steep schistosity planes become also very long.
- Squeezing variability along the tunnel also increases with increasing fold period, but is remarkable also for a relatively small fold period. (For  $L/a = 2.5$ , the maximum deformations  $u_{max}/a$  vary between 0.04 to 0.07).

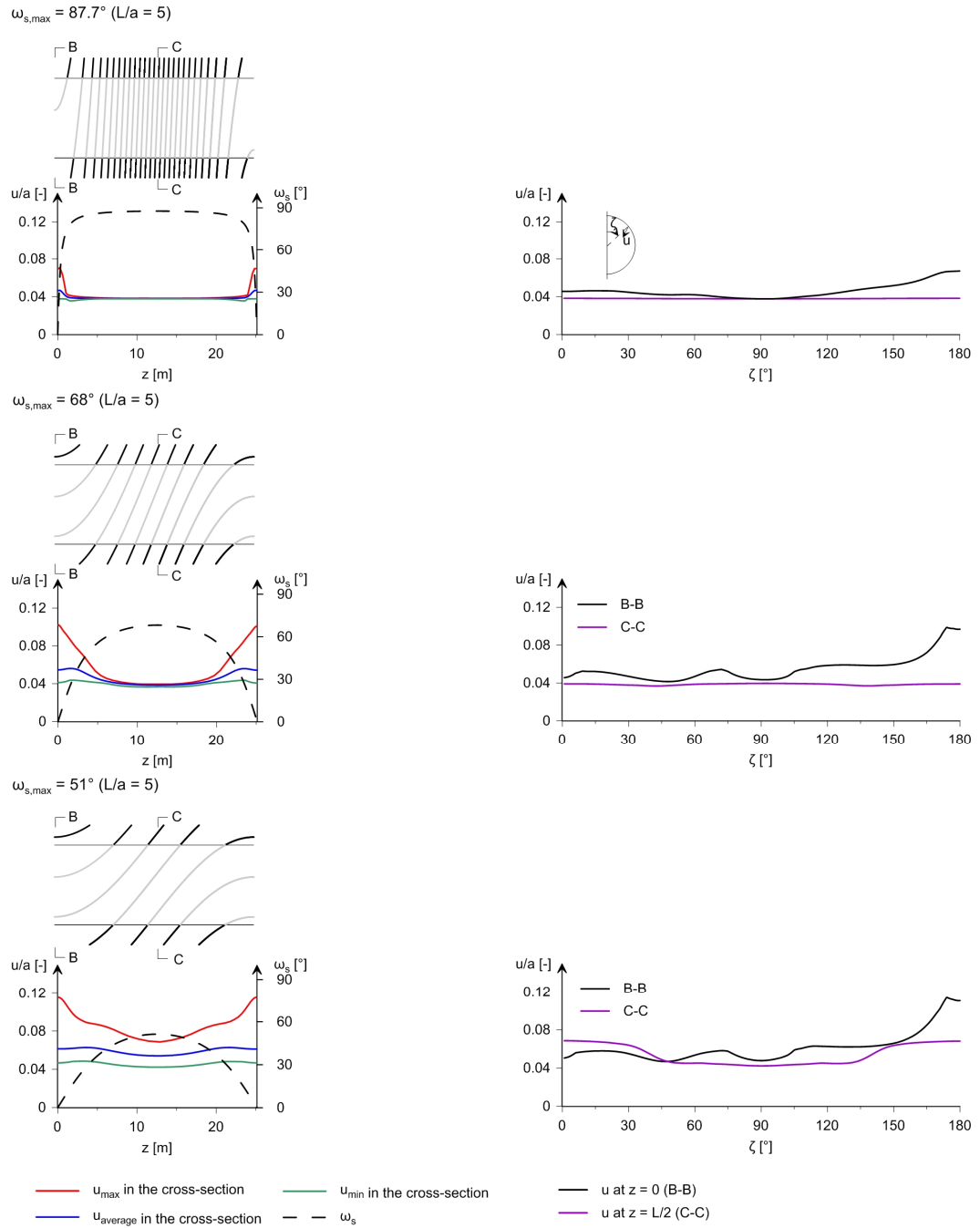


**Figure 5.24.** Influence of the maximum dip angle. Maximum, minimum and averaged tunnel displacements along the tunnel (l.h.s.) and displacements along the tunnel boundary at  $z = 0$  and at  $z = L/2$  (r.h.s.;  $a = 5$  m,  $\sigma_0 = 10$  MPa,  $E = 1$  GPa,  $c_m = 1$  MPa,  $\phi_m = 30^\circ$ ,  $\psi_m = 10^\circ$ ,  $c_s = 0.4$  MPa,  $\phi_s = 10^\circ$ ,  $\psi_s = 5^\circ$ ,  $\nu = 0.3$ ).

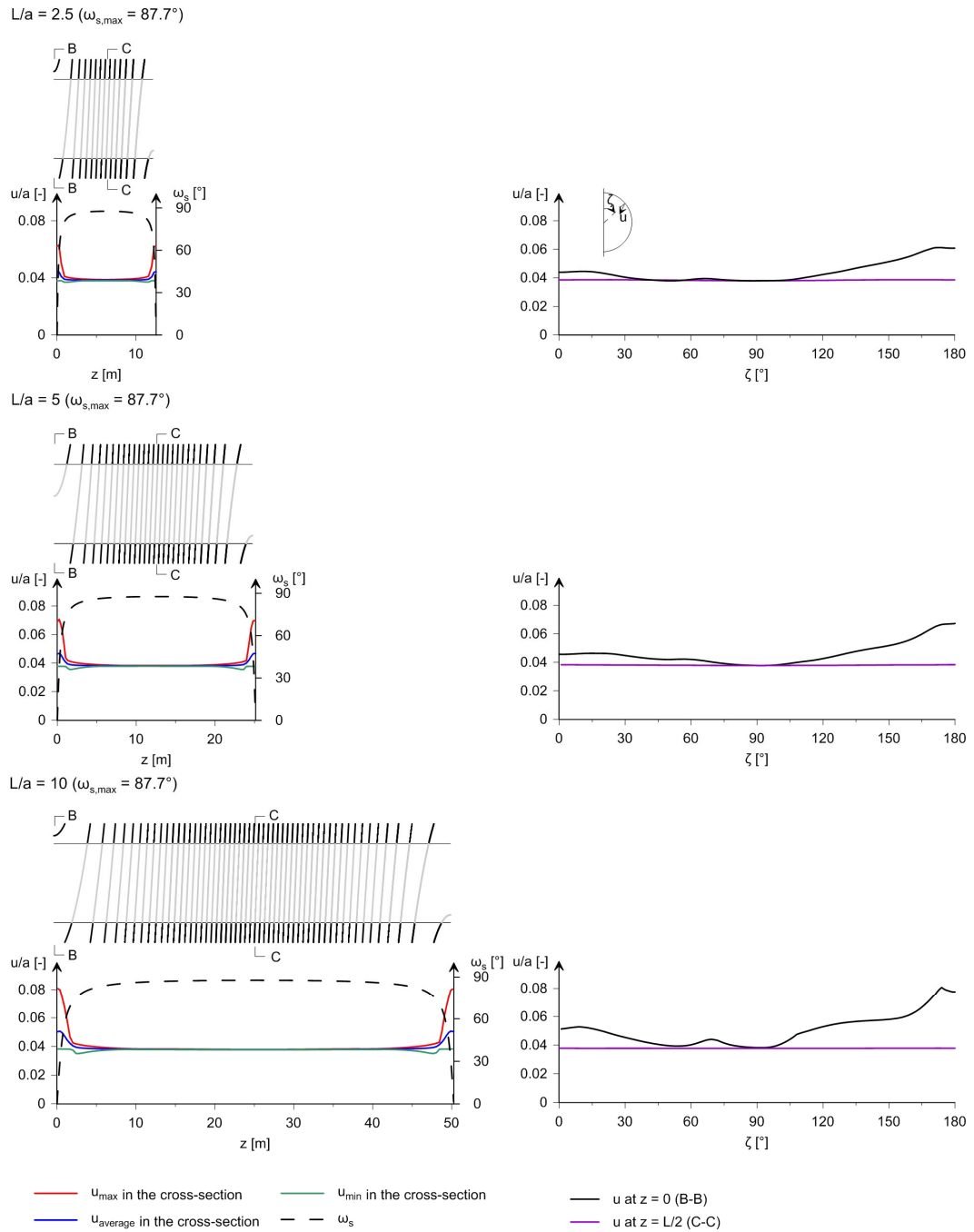


**Figure 5.25.** Influence of the fold period. Maximum, minimum and averaged tunnel displacements along the tunnel (l.h.s.) and the displacement distribution along the tunnel boundary at  $z = 0$  and at  $z = L/2$  (r.h.s.;  $a = 5$  m,  $\sigma_0 = 10$  MPa,  $E = 1$  GPa,  $c_m = 1$  MPa,  $\varphi_m = 30^\circ$ ,  $\psi_m = 10^\circ$ ,  $c_s = 0.4$  MPa,  $\varphi_s = 10^\circ$ ,  $\psi_s = 5^\circ$ ,  $\nu = 0.3$ ).

In order to identify the conditions under which folding can be neglected in design, a parametric study was performed. The maximum displacements  $u_{max}/a$  of the cross-sections at the fold peaks ( $z = 0$ ) and at the largest dip angle ( $z = L/2$ ) generally depend on the geometric parameters of the folding,

$$\frac{u_{max}}{a} \Big|_{z=0}, \frac{u_{max}}{a} \Big|_{z=L/2} = f\left(\frac{A}{L}, \frac{L}{a}\right) \text{ or } f\left(\omega_{s,max}, \frac{L}{a}\right), \quad (5.12)$$

and on the mechanical parameters of the schistous rock mass (see Chapter 4.4).

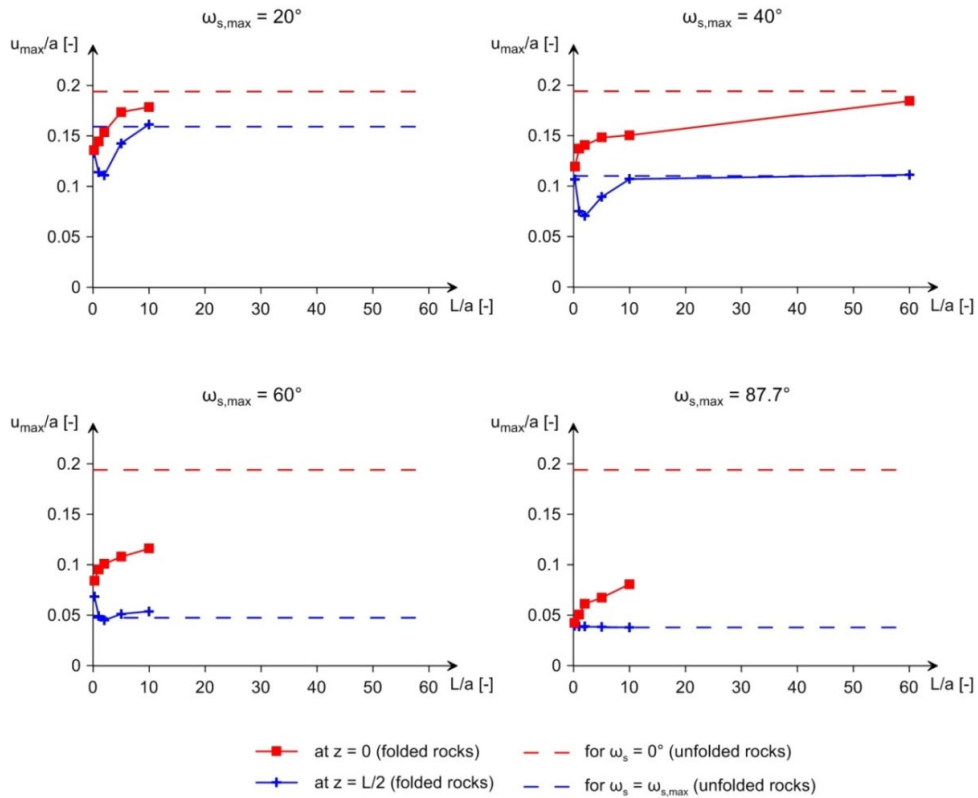


**Figure 5.26.** Influence of the period of the folding on the maximum tunnel displacements (normalised by the tunnel radius  $a$ ) at  $z = 0$  and at  $z = L/2$  ( $a = 5$  m,  $\sigma_o = 10$  MPa,  $E = 1$  GPa,  $c_m = 1$  MPa,  $\varphi_m = 30^\circ$ ,  $\psi_m = 10^\circ$ ,  $c_s = 0.4$  MPa,  $\varphi_s = 10^\circ$ ,  $\psi_s = 5^\circ$ ,  $\nu = 0.3$ ).

Figure 5.26 presents the maximum displacements at  $z = 0$  and  $z = L/2$  as a function of the fold period  $L/a$  for maximum dip angles of  $20^\circ$  to  $87.7^\circ$ . With increasing fold period, the displacements at the fold peaks ( $z = 0$ ) and at the locations with the steepest schistosity planes ( $z = L/2$ ) approach asymptotically the displacements that would occur if the schistosity planes had a constant dip angle (of  $0^\circ$  or  $\omega_{s,max}$ , respectively) along the entire tunnel. This happens relatively quickly in the locations with steep schistosity planes (cross-section  $z = L/2$ ), but very slowly (at much bigger fold periods) in the fold peaks (cross-section  $z = 0$ ). The reason is that the tunnel sections with steeply inclined planes are much longer than the peak zones. According to Figure 5.26, folding can be practically disregarded (the displacements at the fold peaks are by maximum 20% lower than in the case of uniformly horizontal schistosity planes), if the tunnel sections with subhorizontal schistosity planes (dip angle  $< 10^\circ$ ) have a length of minimum 4 times the tunnel radius. This leads to the following condition:

$$\frac{L}{a} = \frac{4}{1 - \frac{2}{\pi} \arccos\left(\frac{\tan(10^\circ)}{\tan(\omega_{s,max})}\right)} \quad (= 12.4 - 30 \text{ for } \omega_{s,max} = 20^\circ - 40^\circ). \quad (5.13)$$

The maximum displacements at the fold peaks ( $z = 0$ ) decrease monotonously with decreasing fold period, because the tunnel sections with subhorizontal schistosity planes become shorter and the stabilising effect of the adjacent sections with steeply inclined schistosity planes becomes more pronounced. The effect of the fold period on the maximum displacements at  $z = L/2$  is more complex (note the minima in the blue lines in Fig. 5.26), because of two opposite effects: With decreasing fold period,

- on the one hand, the adjacent tunnel sections with subhorizontal schistosity planes have an increasingly *unfavourable* effect, which tentatively increases the deformations at  $z = L/2$ ;
- on the other hand, the vertical symmetry planes at  $z = 0$  and  $z = L$  (where the axial displacements are equal zero) have an increasingly *favourable* effect (particularly for small  $\omega_{s,max}$  angles; cf. Section 5.1), which tentatively reduces the deformations at  $z = L/2$ .

For  $L/a$  of approximately 1, the maximum tunnel deformations are practically uniform along the tunnel, but considerably smaller than the displacements that would occur in a tunnel drive parallel to the schistosity. Therefore, it can be concluded, that even small scale folding may have a considerable influence on the tunnel displacements.

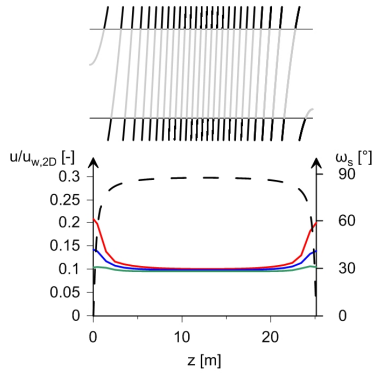
## 5.2.4 Stratified rocks

This section investigates similarities and differences of schistous and thinly stratified rocks with respect to the influence of folding. An extreme case is considered, for which the hard layers are considerably stronger and harder than the weak layers (see parameter values in the legend of Fig. 5.27). The thickness fractions of the layers are taken equal to 0.5. The initial stress  $\sigma_0$  amounts to 10 MPa or 0.75 MPa in order to check whether squeezing plays a role. (Under an initial stress of 0.75 MPa, the rock mass behaves elastically.)

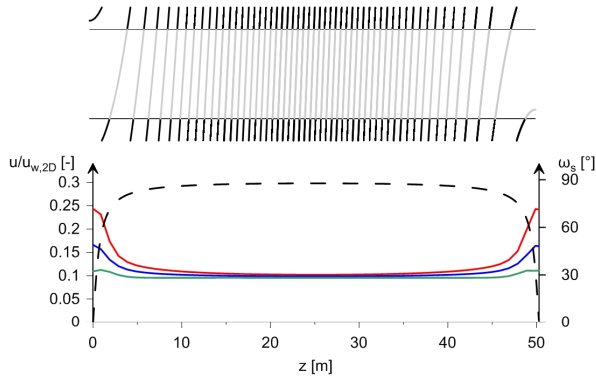
Figures 5.27 and 5.28 show the longitudinal distribution of the displacements (normalised by the displacement that would occur in the absence of hard interlayers) for  $\sigma_0 = 0.75$  MPa and 10 MPa, respectively, and various fold periods. One can recognise that:

- Folding results in considerable squeezing variability also in the case of thinly stratified rocks.
- The maximum deformations increase with the length of the tunnel sections with subhorizontal bedding.
- These tunnel sections are, nevertheless, much more extended than in the case of schistous rocks (compare Figs. 5.27 and 5.28 with Fig. 5.25). This was observed already in Section 5.1: In tunnelling through schistous rocks the displacements remain constant for dip angles of  $80^\circ$  to  $90^\circ$  (since no failure can occur in the schistosity), but in stratified rocks even small deviations from  $90^\circ$  lead to bigger displacements. This is particularly evident for  $\sigma_0 = 0.75$  MPa (due to the considerably larger deformability perpendicular to the layers than parallel thereto).

$L/a = 5$  ( $\omega_{s,max} = 87.7^\circ$ )



$L/a = 10$  ( $\omega_{s,max} = 87.7^\circ$ )



$L/a = 20$  ( $\omega_{s,max} = 87.7^\circ$ )

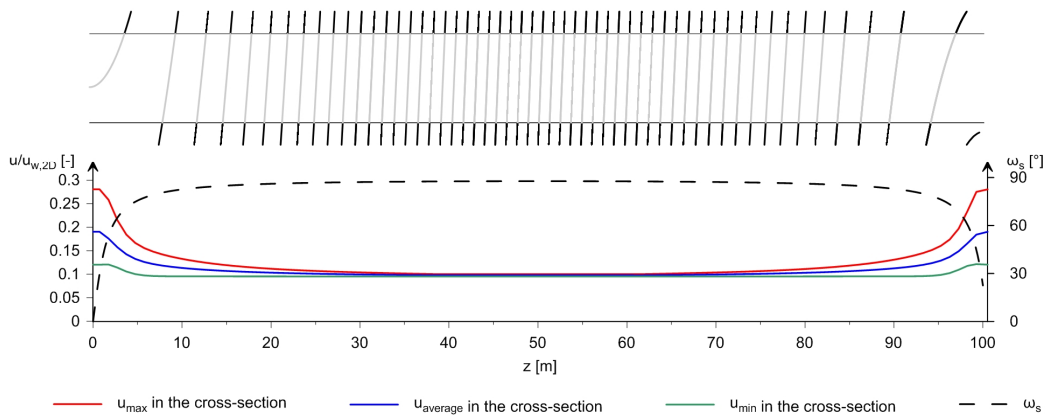
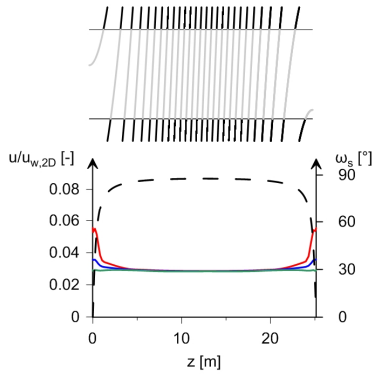
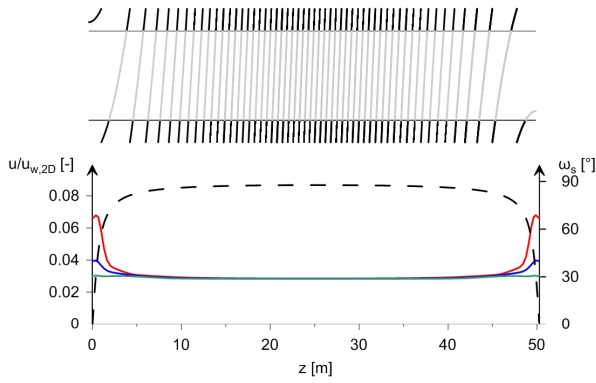


**Figure 5.27.** Influence of the fold period of stratified rocks ( $\sigma_0 = 0.75$  MPa). Maximum, minimum and averaged tunnel displacements along the tunnel ( $a = 5$  m,  $\sigma_0 = 0.75$  MPa,  $x_h = x_w = 0.5$ ,  $E_h = 10$  GPa,  $c_h = 5$  MPa,  $E_w = 0.5$  GPa,  $c_w = 0.5$  MPa,  $\nu_h = \nu_w = 0.3$ ,  $\phi_h = \phi_w = 25^\circ$ ,  $\psi_h = \psi_w = 5^\circ$ ).

$L/a = 5$  ( $\omega_{s,max} = 87.7^\circ$ )



$L/a = 10$  ( $\omega_{s,max} = 87.7^\circ$ )



$L/a = 20$  ( $\omega_{s,max} = 87.7^\circ$ )

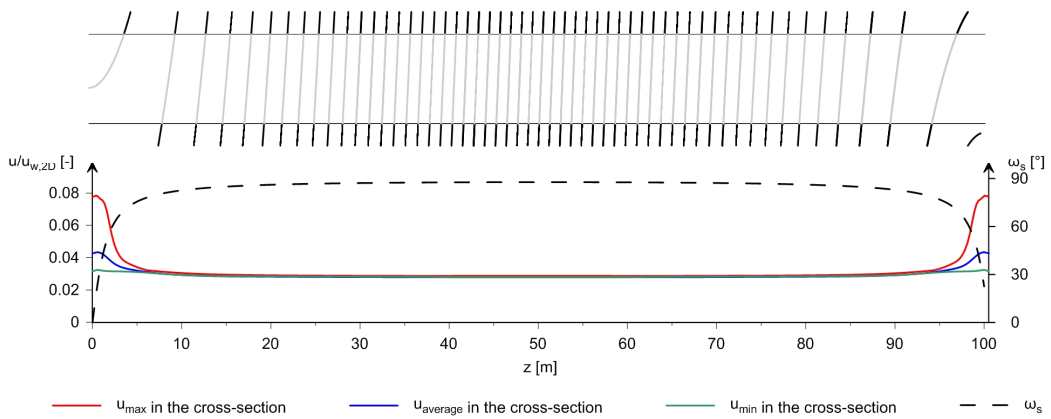


**Figure 5.28.** Influence of the fold period of stratified rocks ( $\sigma_0 = 10$  MPa). Maximum, minimum and averaged tunnel displacements in the cross-section along the tunnel ( $a = 5$  m,  $\sigma_0 = 10$  MPa,  $x_h = x_w = 0.5$ ,  $E_h = 10$  GPa,  $c_h = 5$  MPa,  $E_w = 0.5$  GPa,  $c_w = 0.5$  MPa,  $\nu_h = \nu_w = 0.3$ ,  $\varphi_h = \varphi_w = 25^\circ$ ,  $\psi_h = \psi_w = 5^\circ$ ).

### 5.2.5 Case history of the Sedrun section of the Gotthard Base Tunnel

According to Section 2.1, the “schistosity influence factor”  $S$ , which combines the dip angle and the strike direction of the planes of weakness to the tunnel axis, can be used as an indicator, in order to predict the tunnel convergences. This was particularly evident in Section 2.1 for a tunnel reach with constant degree of shearing of 4 (for the definition of the degree of shearing: see Section 2.1): The large variability of the averaged convergences (over all the measuring points) in this case was solely due to the change of the schistosity orientation (*cf.* Fig. 5.29a). Therefore, this section will analyse this tunnel reach (NE tube, chainage 1760 – 1900) and show, this time by means of numerical calculations, whether the schistosity influence factor  $S$  can adequately express the squeezing variability.

A comprehensive description of the Sedrun Section and the related experiences can be found in Section 2.1. The depth of cover amounts to about 800 m ( $\sigma_o = 20$  MPa). The rock parameters of Table 5.1 correspond to a rock with medium degree of kakiritization (as the shearing degree in this tunnel section amounts to 4 according to Section 2.1) and were chosen on the basis of the report of Ingenieurgemeinschaft Gotthard-Basistunnel Süd [119]. The computational model was already introduced in Section 5.2.2 (however, here the whole 3D model must be considered, as there are no planes of symmetry). The dip angle and the strike direction of the schistosity were implemented in the numerical model, considering the geological records made during tunnel advance (*cf.* [20]). Since the tectonic units are very disturbed, contrarily to Section 5.2.2, no equation for the folding of the schistosity can be defined and thus dip angle and strike direction of the schistosity were taken section-wise constant (see values in Fig. 5.29b). The resulting schistosity influence factors (obtained with Eq. 2.1) are also given in Figure 5.29b.

**Table 5.1.** Rock parameters (according to [119]).

$E$ [GPa]	$c_m$ [MPa]	$\varphi_m$ [°]	$\psi_m$ [°]	$c_s$ [kPa]	$\varphi_s$ [°]	$\psi_s$ [°]	$\nu$ [-]
4.4	1.3	30	10	600	20	5	0.3

Figure 5.29c shows the numerically determined maximum, minimum and averaged displacements along the tunnel, while Figure 5.29d compares them with the measured values. One can recognise that the deformations obtained with the numerical calculations are greater than the measured deformations. There are two main reasons for this: the computed displacements include the pre-deformations; the computations consider an unsupported tunnel. The pre-deformations and the installed support could be taken into account computationally by a step-by-step simulation of tunnel excavation, but this simulation would be very time-consuming without adding much value since the selection of appropriate parameters itself is a difficult task (due to the natural variability of the rock mass along the tunnel stretch). Hence, the calculated displacements can be compared only qualitatively with the measured tunnel convergences.

Figure 5.29d presents the measured as well as calculated displacements  $\bar{u}_c$  (according to Section 2.1). They correspond to the average values of the five to seven measuring points of each monitoring station. Depending on the position of the measuring points (which is not exactly known), these calculated average values may be subject of some uncertainty.

Nevertheless, one can readily recognise that the distribution of the calculated displacements along the tunnel is very similar to that of the measured ones, but the squeezing variability is less pronounced than actually observed. According to Section 5.1, the squeezing variability would be larger, had the tunnel convergences (rather than the total displacements) been considered in the numerical modelling. The deformations would then be on average 30% smaller (see Section 5.1) and thus the results of the numerical modelling would be in better agreement with the measured convergences. The squeezing variability would also be larger and thus more visible in the development of the displacements, if an even smaller value for  $c_s$  was chosen.

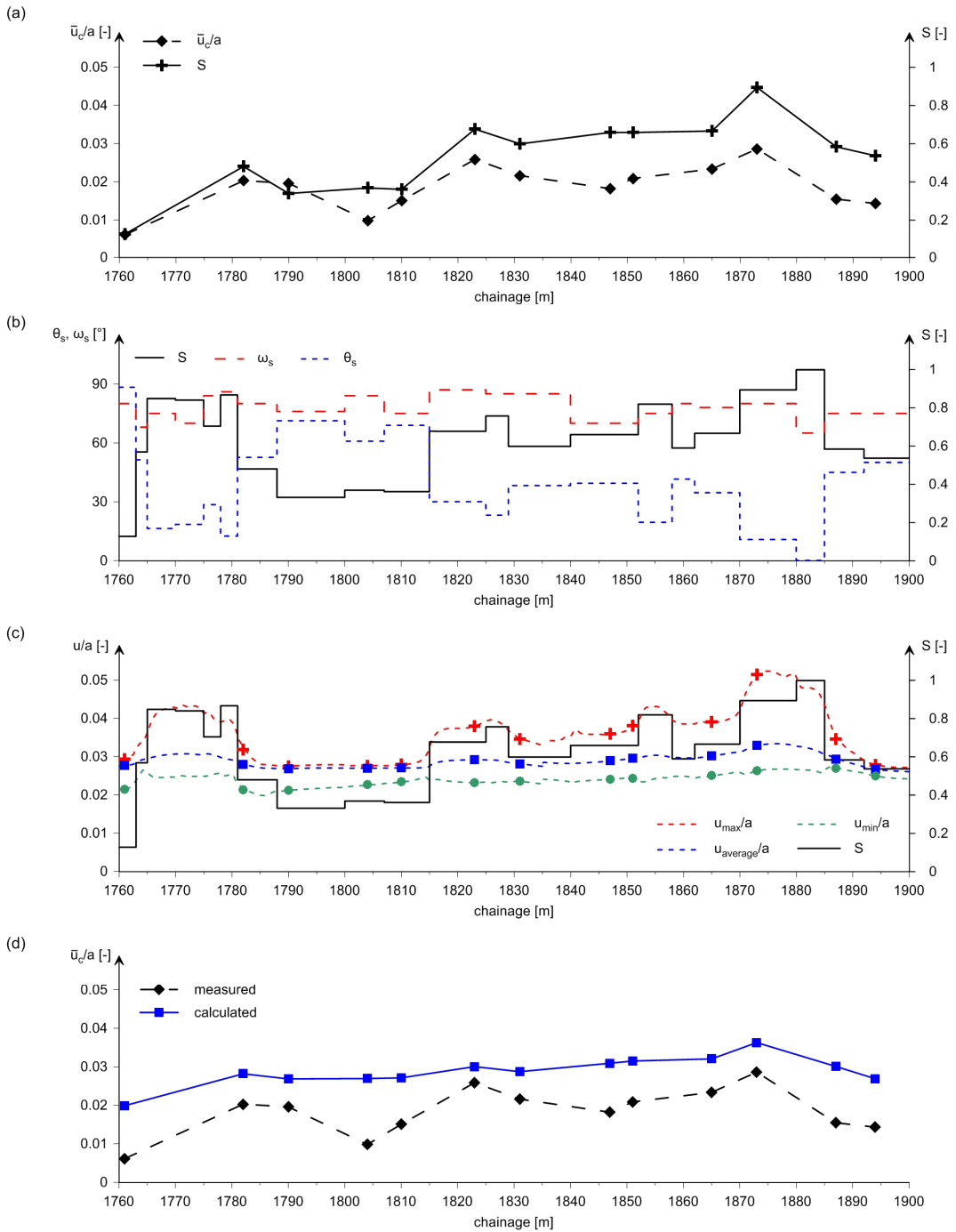


**Figure 5.29.** (a) Average magnitude of the projections of the displacement vectors in the cross-sectional plane of the tunnel normalised by the tunnel radius ( $\bar{u}_c/a$ ) along the tunnel as well as schistosity influence factor for chainage 1760-1900 of the NE tube, according to Section 2.1; (b) Implemented dip angle  $\omega_s$  and angle  $\theta_s$  between the tunnel axis and the strike direction of the planes of weakness, as well as resulting schistosity influence factor  $S$ ; (c) Maximum, minimum and averaged displacements of the tunnel boundary obtained with numerical calculations along the tunnel as well as schistosity influence factor  $S$ ; (d) Comparison between the measured convergences and the total displacements obtained from the numerical calculations.

Despite all the uncertainties mentioned before, the analysed case history shows that the schistosity influence factor is a reliable indicator, which enables to determine in which tunnel sections larger deformations have to be expected during tunnelling. Of course, this presupposes that the schistosity orientation can be identified in advance. This information can be obtained by means of advance probing (*cf.* Section 2.1).

## 5.2.6 Conclusions

The variation of the orientation of the planes of anisotropy is an important factor for the squeezing variability and this, when tunnelling through schistous or stratified rock mass. The results of numerical investigations indicate that, there is a mutual influence of the alternating areas of favourable and unfavourable inclination of the anisotropy planes along the tunnel. However, despite of this mutual influence, the folding leads to a considerable variability of the rock deformations along the tunnel.

Furthermore, this chapter could show that the squeezing variability observed in the Sedrun Section of the Gotthard Base Tunnel can be well understood with the help of numerical calculations taking into account the orientation of the schistosity to the tunnel axis. In order to predict the tunnel convergences, the “schistosity influence factor”  $S$ , which combines the dip angle and the strike direction of the planes of weakness to the tunnel axis, can be used as an indicator thus providing, in combination with advance core drilling, reliable indications of the squeezing intensity.

As was already illustrated in Section 5.2.3, depending on the length of the tunnel sections, which are parallel to the schistosity, and on the stabilising vicinity, the maximum displacement may vary considerably. Of course, this influence is not taken into account when predicting the convergences solely by means of the schistosity influence factor.

## 6 Concluding remarks

The case histories of the Gotthard, Ceneri and Lötschberg Base Tunnel (Chapter 2) could show that the squeezing deformations were mainly affected by the lithology, by the schistosity orientations and the effect of nearby weaker or stronger zones. Those variations – even if relatively small – may thus cause a significant variability of the squeezing intensities along the tunnel, which may additionally be accompanied by a pronounced non-uniformity of the displacements in the tunnel profile. Section 2.1 showed that the influence of the spatial orientation of the schistosity on the tunnel convergences can be determined by a simple, empirically proven (and later – in Chapter 5 – also theoretically justified) equation, which in combination with advance core drilling allows reliable predictions of the convergences. Therefore, the next chapters of this research report determined the influence of the factors mentioned above, in order to use them as indicators during construction for the timely identification and prediction of the squeezing behaviour. Furthermore, the carbon section of the Lötschberg Base Tunnel showed that considerable long-term deformations occurred, which could be, *inter alia*, traced back to creep. It was noticeable that with larger (short-term) tunnelling-induced deformations (occurring within a distance of about 50 m behind the tunnel face), larger long-term deformations due to creep occurred. Therefore, creep influences the squeezing intensity along the tunnel.

For a tunnel drive through heterogeneous rock mass consisting of alternating weak and competent rock layers lying perpendicular to the tunnel axis (Chapter 3), depending on the heterogeneity scale, a pronounced squeezing variability may occur (*cf.* Section 3.4). If the alternating weak and competent rocks are very thin, the displacements are almost uniform along the tunnel. For this special case, an analytical solution was derived which describes the relationship between rock deformation and support pressure under the assumption of rotational symmetry and plane strain conditions (Section 3.2). The derivation of this ground response curve was mathematically demanding, as a variety of cases regarding the failure state of the rock had to be considered (plastic and/or elastic behaviour of the weak and/or the hard layers considering a plastic flow either only in the tunnel cross-sectional plane or also perpendicular to it). This analytical solution is particularly important for practical reasons, as numerical modelling of a narrow sequence of hard and weak rocks is very time-consuming. Numerical calculations in Section 3.4, which consider the layers discretely, could show that the analytically derived solution mentioned before is sufficiently accurate for practical purposes if the thickness of the hard layers is less than about 5% of the tunnel radius. Based on the above-mentioned analytically derived ground response curve, the parameters of a mechanically equivalent homogeneous, isotropic and elasto-plastic material are determined and presented in Section 3.3. This is very useful for design purposes since it allows the use of common calculation methods and programs to solve problems that do not meet the conditions of rotational symmetry or plane strain and this even for thinly stratified rocks. For example, with the determined equivalent parameters, one can easily determine the effectiveness of a lining system in TBM tunnelling. Of course, the homogenised model provides only satisfactory results for small thicknesses of the layers and not for thickly alternating weak and competent layers. Therefore, in Section 3.4 a simple equation was developed, which allows to determine the squeezing intensities for all layer thicknesses in a quick and easy way, without making numerical modelling necessary (at least not in the preliminary stages of design). By a comprehensive parametric study, it could be shown that this equation is accurate enough for practical purposes.

Chapter 4 investigated the influence of the planes of anisotropy (schistosity, bedding) lying parallel to the tunnel axis. When tunnelling through a heterogeneous rock mass consisting of alternating weak and competent rock layers lying parallel to the tunnel axis, depending on the heterogeneity scale, considerable non-uniformity of the distribution of the deformations of the tunnel profile may occur. Even if the thicknesses of the alternating weak and hard layers are very small, a considerable non-uniformity of the displacements in the tunnel profile may occur. For this specific case, the rock mass can be perceived as a homogeneous, but transversely isotropic material. For the latter, in Section 4.2, a constitutive model was formulated and implemented in Abaqus, which describes the behaviour of a stratified rock mass (using the homogenisation technique). The elasto-

plastic parameters of this homogeneous and transversely isotropic medium depend on fraction, strength and stiffness properties of the alternating layers. With this, the ground response when tunnelling through thinly alternating weak and competent layers can be investigated computationally (assuming plane strain conditions). As the homogenised solution is particularly important for practical reasons (numerical modelling of a narrow sequence of hard and weak rocks is very time-consuming), the estimation of the displacements along the tunnel profile for given geotechnical condition is facilitated by dimensionless diagrams – presented in Section 4.2 – that represent a valuable tool for engineering practice, as they enable to determine the maximum and minimum displacements in the tunnel profile for a wide range of geotechnical conditions. Even if the response of the ground is anisotropic in this case, these design aids allow, analogously to Section 3.3, to determine the parameters for an isotropic homogeneous rock mass, which is equivalent to the isotropic rock mass in the sense that its tunnelling-induced displacements are equal either to the maximum or to the minimum displacements of the anisotropic model. As shown in Section 4.2.5, using this equivalent isotropic model makes it possible to find an upper and a lower bound of the displacements in more complex problems (that do not meet the condition of plane strain).

Numerical calculations in Section 4.3, which analyses the influence of the layer thickness by considering the individual layers discretely, could show that the homogenised model mentioned before is sufficiently accurate for practical purposes if the thickness of the hard layers is less than about 5% of the tunnel radius. As this criterion is also valid for a sequence of alternating layers lying perpendicular to the tunnel axis, this criterion is applicable for any orientation of the layers to the tunnel axis. Furthermore, Section 4.3 could show that, for very thick formations, the non-uniformity of displacements in the profile nearly disappears if the weak or the hard rock formation lies at a distance to the tunnel axis of at least 5 times the tunnel radius, so that, for design purpose, the weak or the hard formation can be neglected, respectively. Therefore, numerical calculations do not have to be performed (at least in the preliminary stages of design).

Finally, Section 4.4 investigated the squeezing behaviour in schistous rock mass – which is characterised by very thin weak discontinuities and thus represents, from the mechanical point of view, a special case of a stratified rock mass – when tunnelling parallel to the planes of schistosity. (The schistosity is irrelevant when tunnelling perpendicular to the planes of weakness.) As the implemented constitutive model for (thinly) stratified rocks is inefficient in computing terms for the borderline case of schistosity, in Section 4.4, a constitutive model was formulated and implemented specifically for schistous rock. With this, numerical calculations (assuming plane strain conditions) could be carried out in Section 4.4 that showed that the schistosity may affect rock deformations adversely, particularly if its cohesion and friction angle are small. If, in addition, the uniaxial compressive strength of the matrix is small, the squeezing deformations may be considerably larger than those occurring in non-schistous rocks. In order to better estimate the influence of the schistosity, dimensionless diagrams were developed and presented in Section 4.4, which make it possible to estimate the maximum and minimum displacements in the tunnel profile easily for given geotechnical conditions.

Chapter 5 investigated the influence of the orientation of the planes of anisotropy (bedding, schistosity) to the tunnel on the tunnel convergences. As the deformations determined under the assumption of plane strain conditions (as in the Chapters 3 and 4) include the deformations that occur ahead of the tunnel face (so-called “pre-deformations”) and are thus considerably larger than the convergences of the excavated tunnel profile, in Section 5.1, the influence of the planes of anisotropy on the convergences is investigated using spatial calculation models with arbitrary orientation of the planes of anisotropy relative to the tunnel axis. This section could show, first, that there are relevant differences to the well-known case of an isotropic rock mass and, second, that the numerical calculations reproduce well the empirically determined relationship between convergence and spatial orientation of the schistosity considering the so-called “schistosity influence factor” (which combines the dip  $\omega_s$  and the strike direction  $\theta_s$  of the planes of weakness to the tunnel axis), which was developed based on the data from the Gotthard Base Tunnel (*cf.* Section 2.1). Based on this relationship, a simple equation, which is accurate enough for most tunnelling problems, was developed which enable to calculate the convergence for all

orientation of the planes of anisotropy to the tunnel axis, taking into account the schistosity influence factor. With this equation, for a tunnel drive encountering schistous or stratified rock masses, costly spatial numerical analyses do not have to be carried out (at least not in the preliminary design stages) for estimating the tunnel convergences.

In fact, the variation of the orientation of the planes of anisotropy along the tunnel axis is an important factor for the squeezing variability and this, when tunnelling through schistous or stratified rock mass. This is clearly recognisable in Section 5.2, which investigated the influence of a folding on the distribution of the deformations along the tunnel numerically. The folding was implemented as a sinus function in the constitutive model, which is defined by its amplitude and its period. The results of the numerical investigations indicate that, there is a mutual influence of the alternating areas of favourable and unfavourable inclination of the anisotropy planes along the tunnel. However, despite of this mutual influence, the folding leads to a considerable variability of the rock deformations along the tunnel. Furthermore, the Section 5.2 could show, (i), that the squeezing variability observed in the Sedrun Section of the Gotthard Base Tunnel can be well understood with the help of numerical calculations taking into account the orientation of the schistosity to the tunnel axis and, (ii), that the “schistosity influence factor” can be used as a reliable indicator for the estimation of the squeezing intensities during advance, in combination with advance core drilling.

An overview of the design aids, which were developed in the context of this research project, is given in Table 1.1.

In this research project, the time-dependence of the rock behaviour due to consolidation was not considered. The existence of underground water or high pore water pressure favours the development of rock deformations ([1], [9], [17], etc.). In a saturated rock the permeability governs the rate of the deformations associated with the dissipation of excess pore pressures. Permeability variations may therefore lead to variable squeezing intensities. In particular, thin permeable interlayers can cause a substantial acceleration of the deformations as they lead to a shortening of the drainage paths (cf. Fig. 6.1). This hypothesis was put forward by Anagnostou and Kovári [120], but was not investigated quantitatively so far. Therefore, the influence of the heterogeneities of the ground with respect to its hydraulic characteristics on the squeezing variability should be subject of further research.

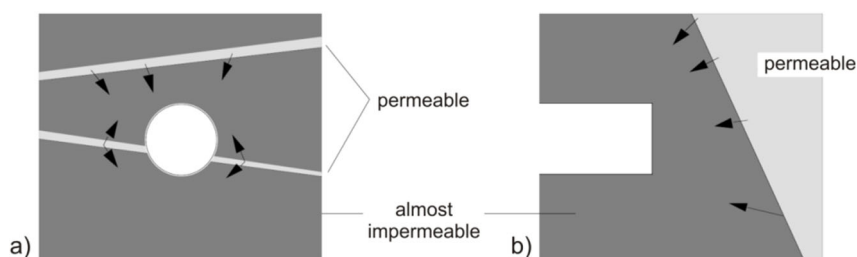


**Figure 6.1.** Shortening of the drainage paths due to, a) permeable layers, b) adjacent permeable formation [120].



## Appendices

<b>I</b>	<b>Tunnelling parallel to the bedding of a thinly stratified rock mass: Dimensionless diagrams for the displacements .....</b>	<b>155</b>
<b>II</b>	<b>Tunnelling parallel to the schistosity planes: Dimensionless diagrams for the displacements .....</b>	<b>165</b>



# I Tunnelling parallel to the bedding of a thinly stratified rock mass: Dimensionless diagrams for the displacements

This appendix presents the dimensionless diagrams introduced in Section 4.2. Table 1 gives an overview of the dimensionless diagrams.

**Table 1.** Overview of the dimensionless diagrams.

Figure	displacement	$\sigma_x/\sigma_0$
1	$U_{max}/U_{w,2D}$	0.0
2	$U_{average}/U_{w,2D}$	
3	$U_{min}/U_{w,2D}$	
4	$U_{max}/U_{w,2D}$	0.1
5	$U_{average}/U_{w,2D}$	
6	$U_{min}/U_{w,2D}$	
7	$U_{max}/U_{w,2D}$	0.2
8	$U_{average}/U_{w,2D}$	
9	$U_{min}/U_{w,2D}$	

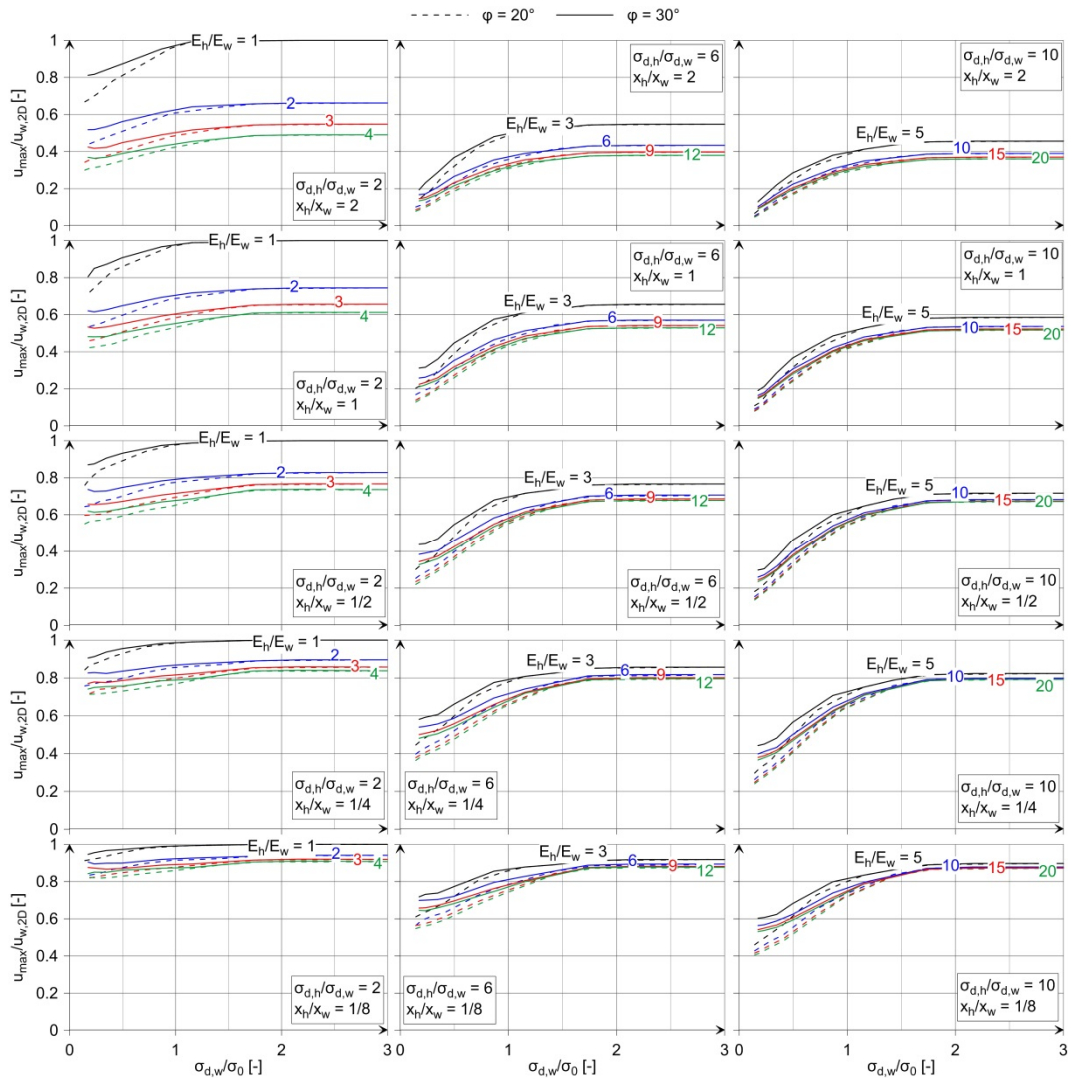


Figure 1. Nomograms for  $u_{max}/u_{w,2D}$  and  $\sigma_a/\sigma_0 = 0$ .

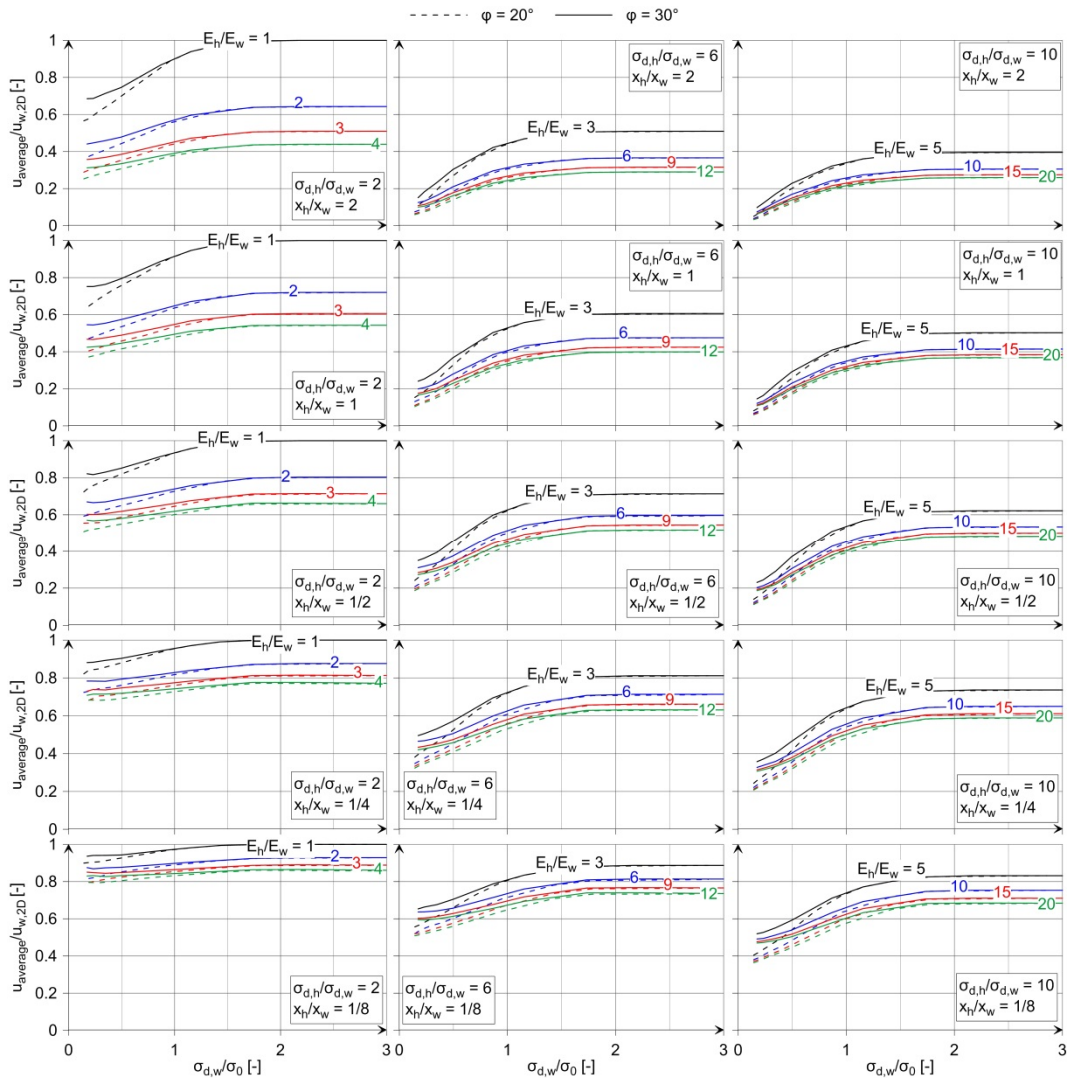


Figure 2. Nomograms for  $u_{average}/u_{w,2D}$  and  $\sigma_a/\sigma_0 = 0$ .

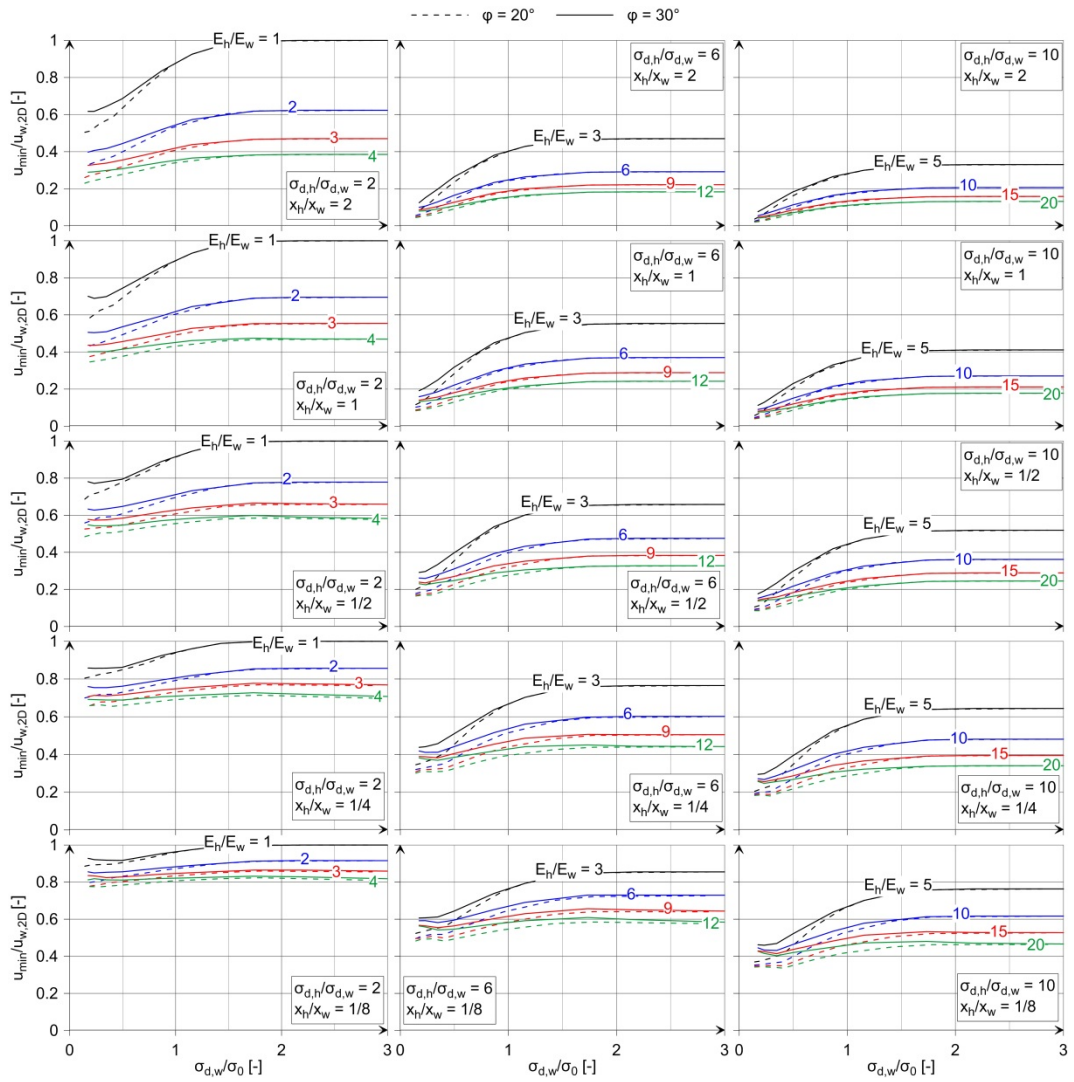


Figure 3. Nomograms for  $u_{min}/u_{w,2D}$  and  $\sigma_a/\sigma_0 = 0$ .

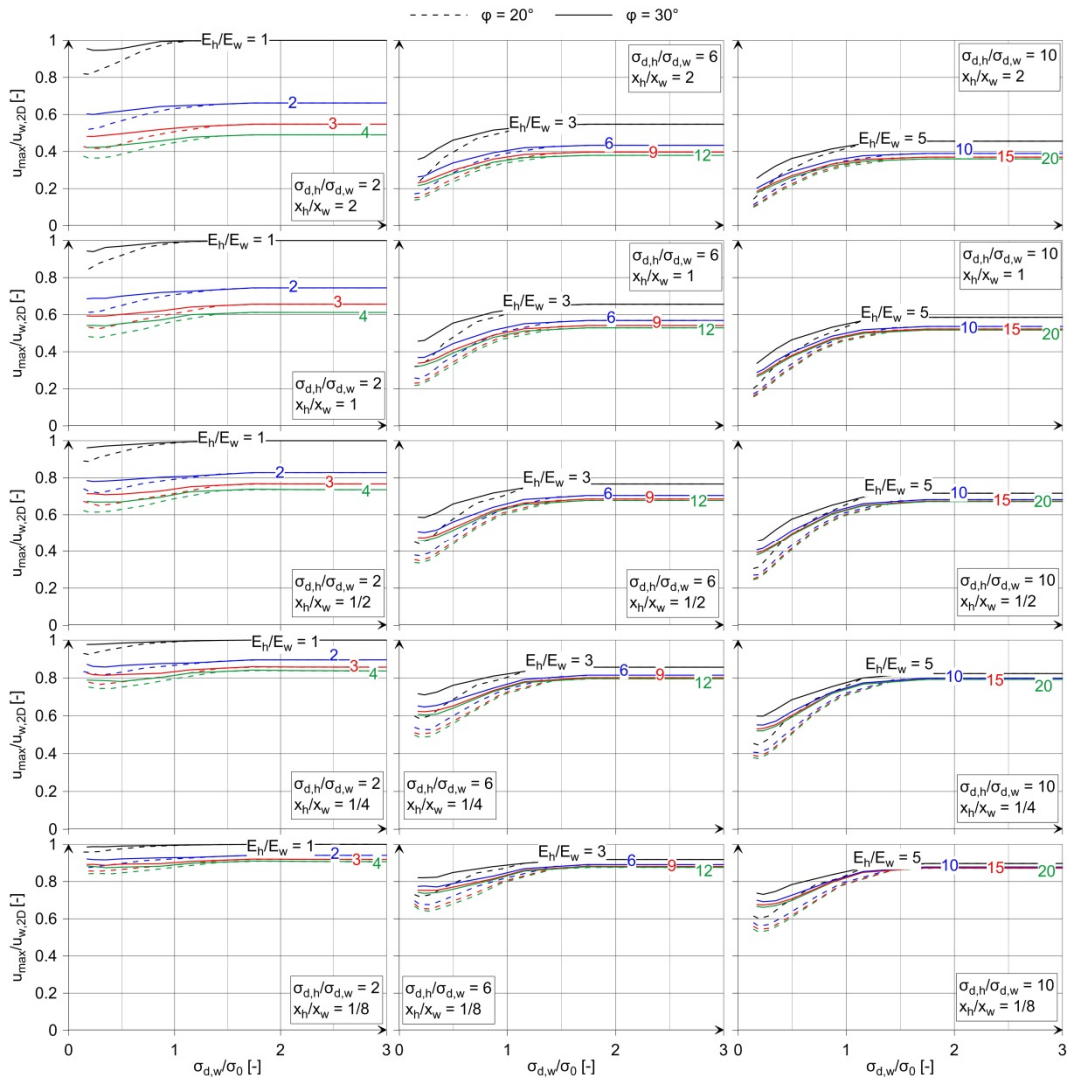


Figure 4. Nomograms for  $u_{max}/u_{w,2D}$  and  $\sigma_a/\sigma_0 = 0.1$ .

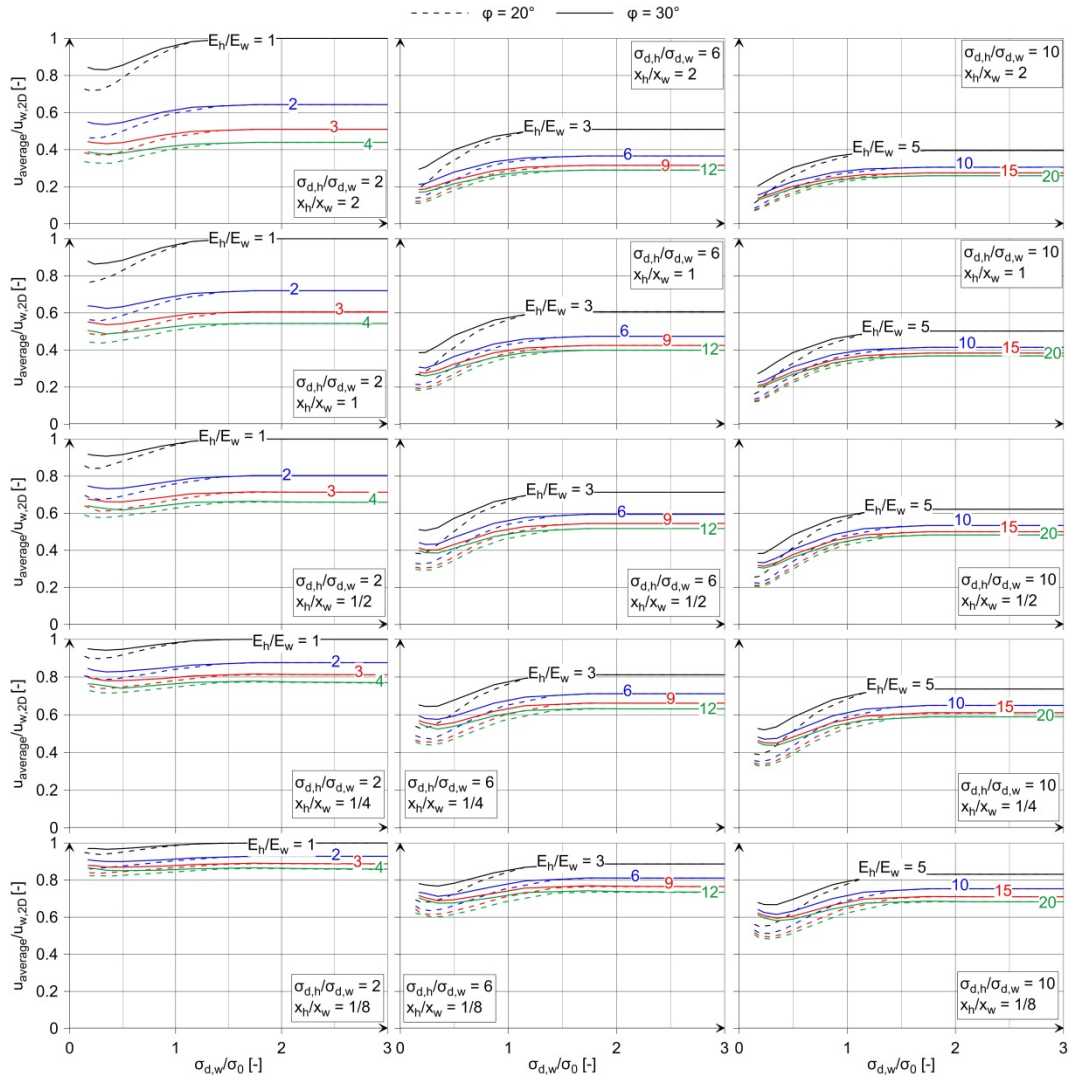


Figure 5. Nomograms for  $u_{average}/u_{w,2D}$  and  $\sigma_a/\sigma_0 = 0.1$ .

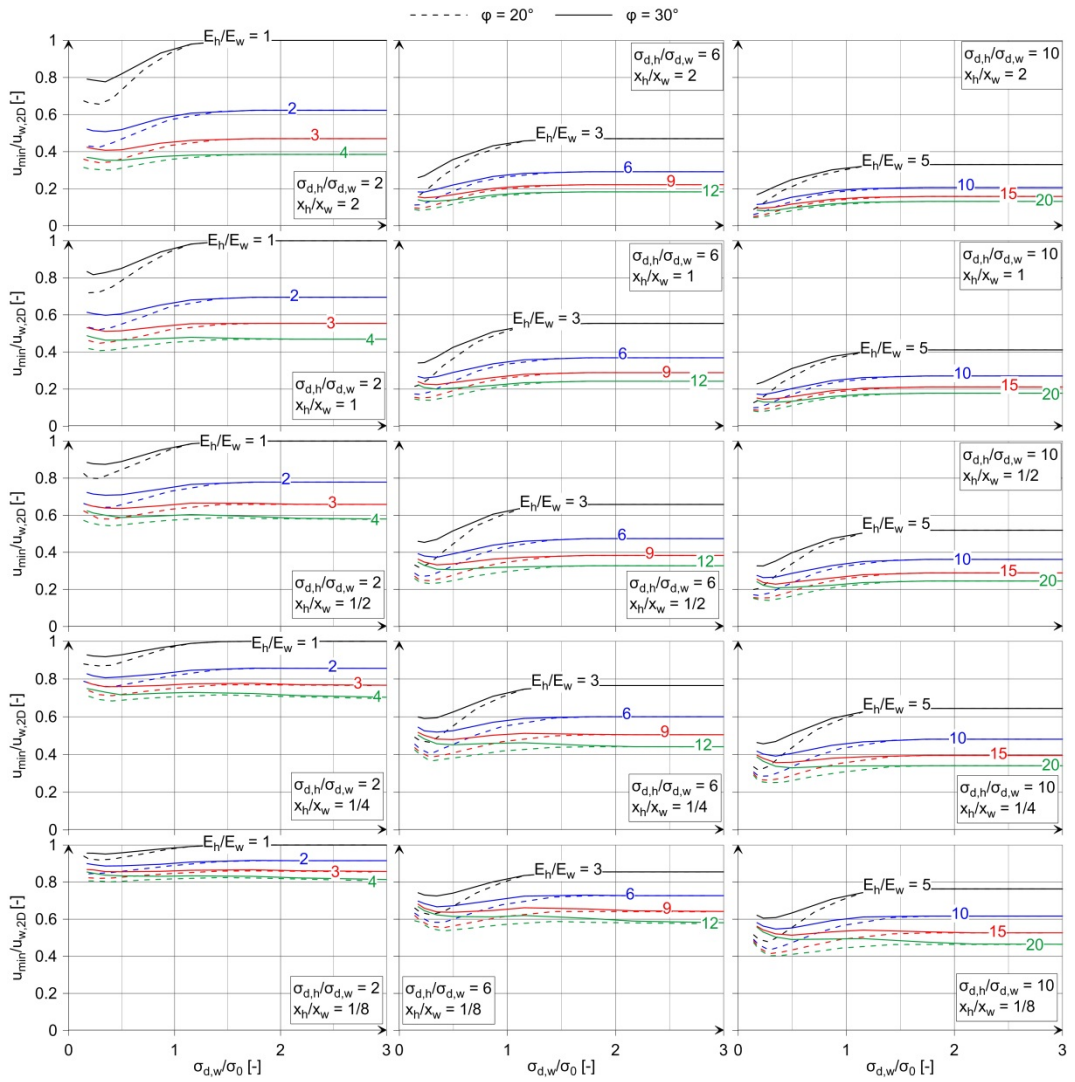


Figure 6. Nomograms for  $u_{min}/u_{w,2D}$  and  $\sigma_a/\sigma_0 = 0.1$ .

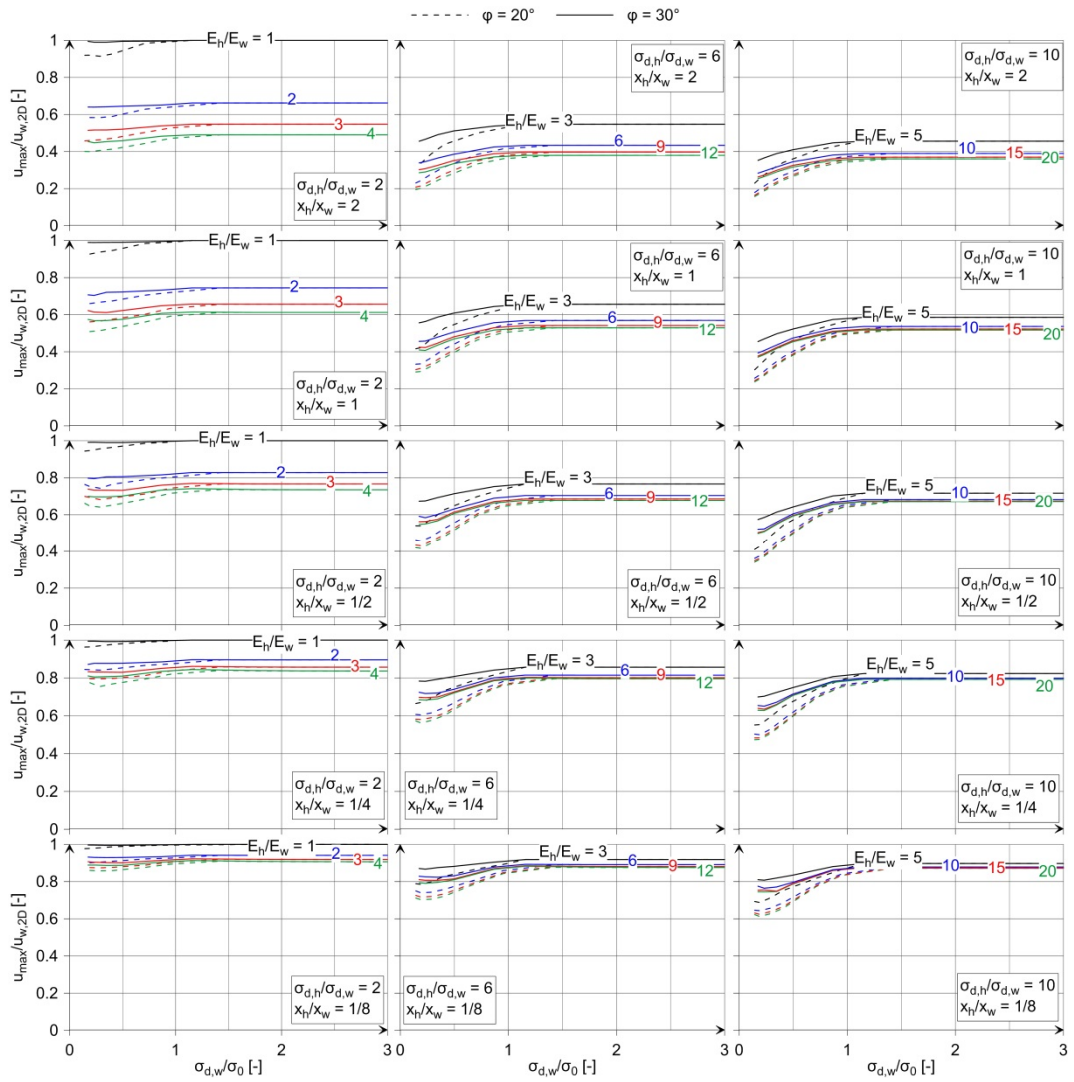


Figure 7. Nomograms for  $u_{max}/u_{w,2D}$  and  $\sigma_a/\sigma_0 = 0.2$ .

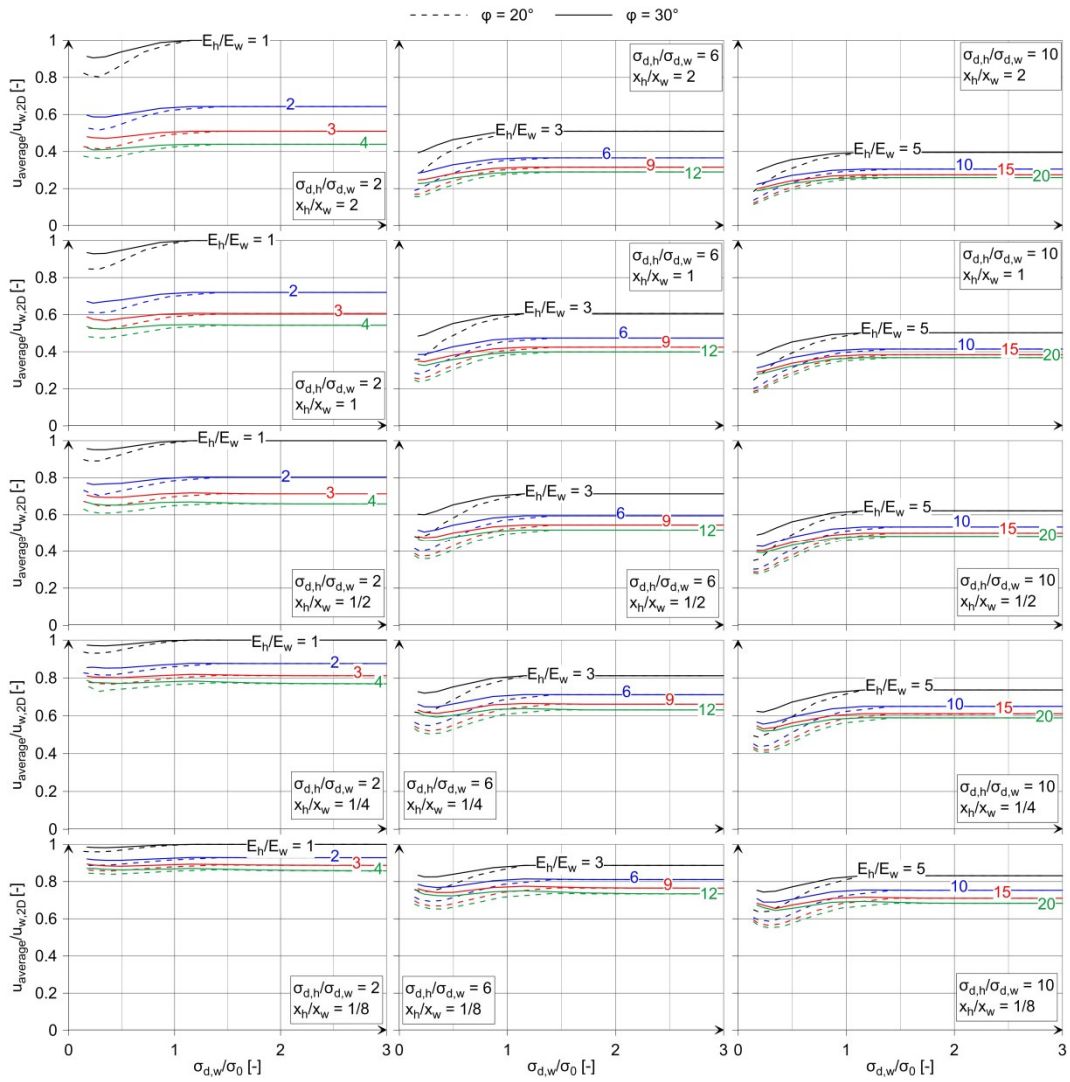


Figure 8. Nomograms for  $U_{average}/U_{w,2D}$  and  $\sigma_a/\sigma_0 = 0.2$ .

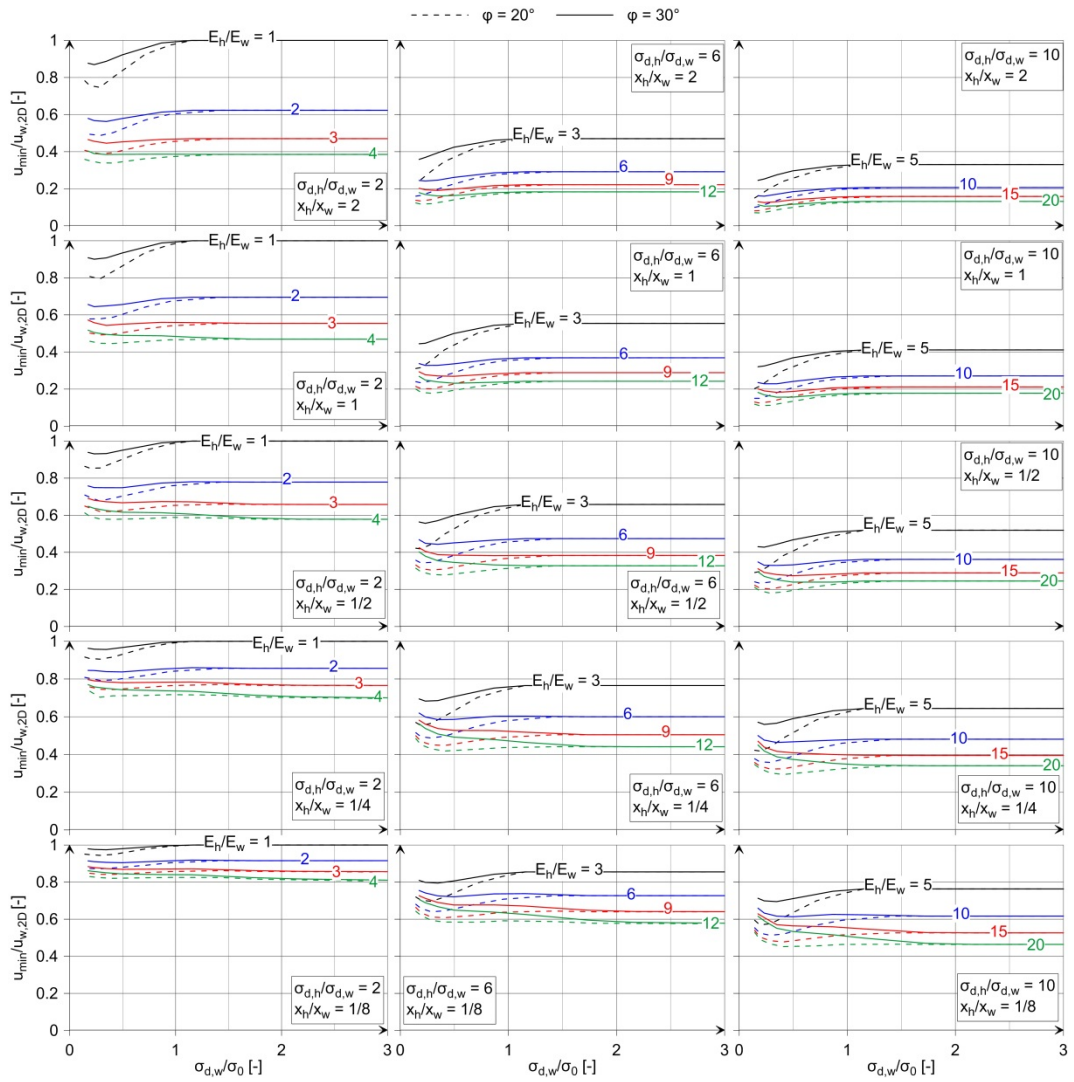


Figure 9. Nomograms for  $u_{min}/u_{w,2D}$  and  $\sigma_a/\sigma_0 = 0.2$ .

## II Tunnelling parallel to the schistosity planes: Dimensionless diagrams for the displacements

This appendix presents the dimensionless diagrams introduced in Section 4.4. Table 2 gives an overview of the dimensionless diagrams.

**Table 2.** Overview of the dimensionless diagrams.

Figure	$\varphi_m$	$\sigma_a/\sigma_0$
10	30°	0.0
11		0.1
12		0.2
13	25°	0.0
14		0.1
15		0.2
16	20°	0.0
17		0.1
18		0.2

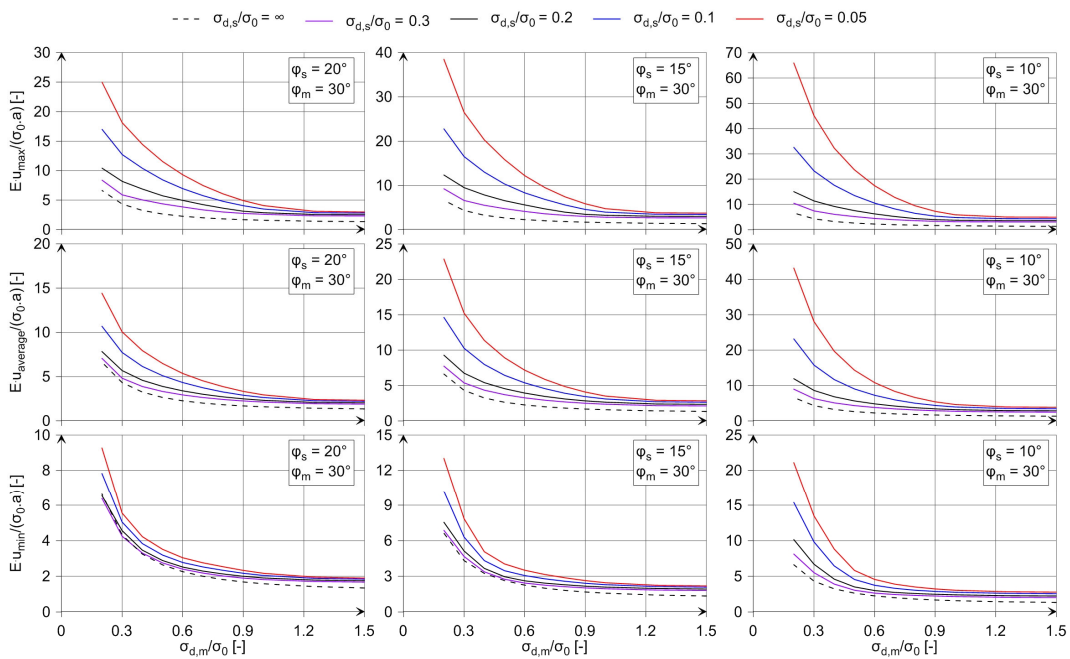


**Figure 10.** Nomograms for  $\varphi_m = 30^\circ$  and  $\sigma_a/\sigma_0 = 0$ .

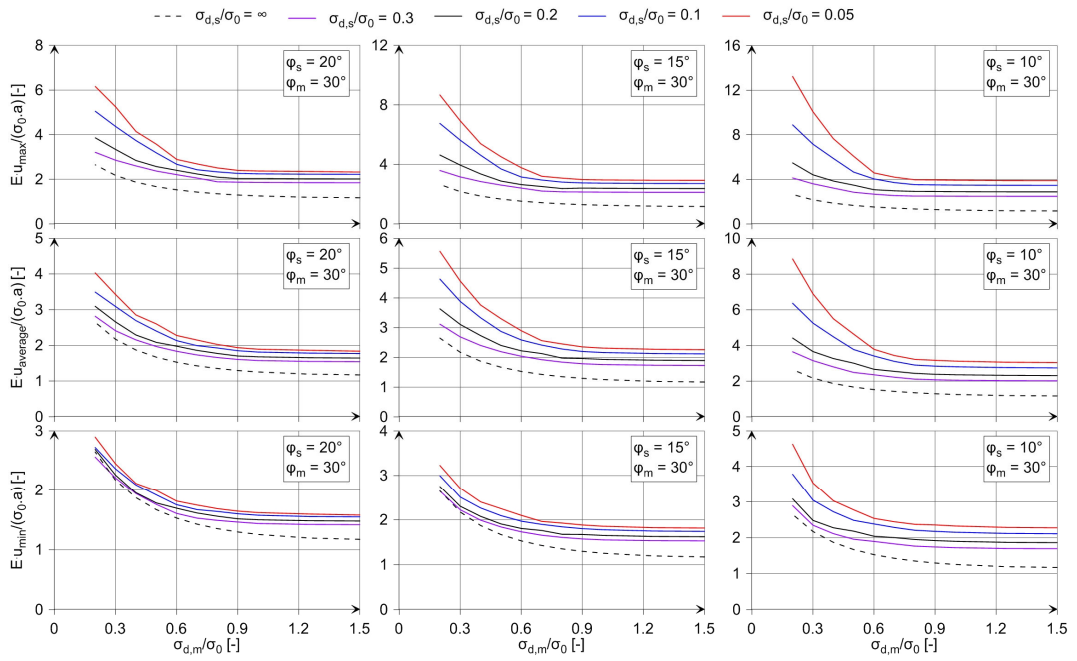


Figure 11. Nomograms for  $\phi_m = 30^\circ$  and  $\sigma_a/\sigma_0 = 0.1$ .

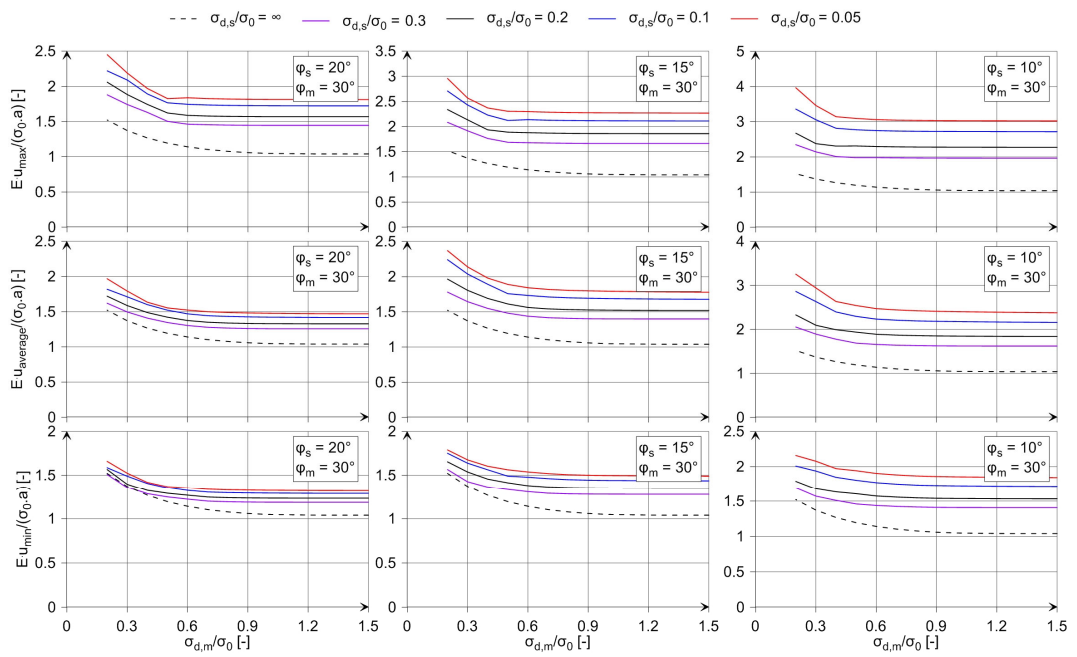


Figure 12. Nomograms for  $\phi_m = 30^\circ$  and  $\sigma_a/\sigma_0 = 0.2$ .

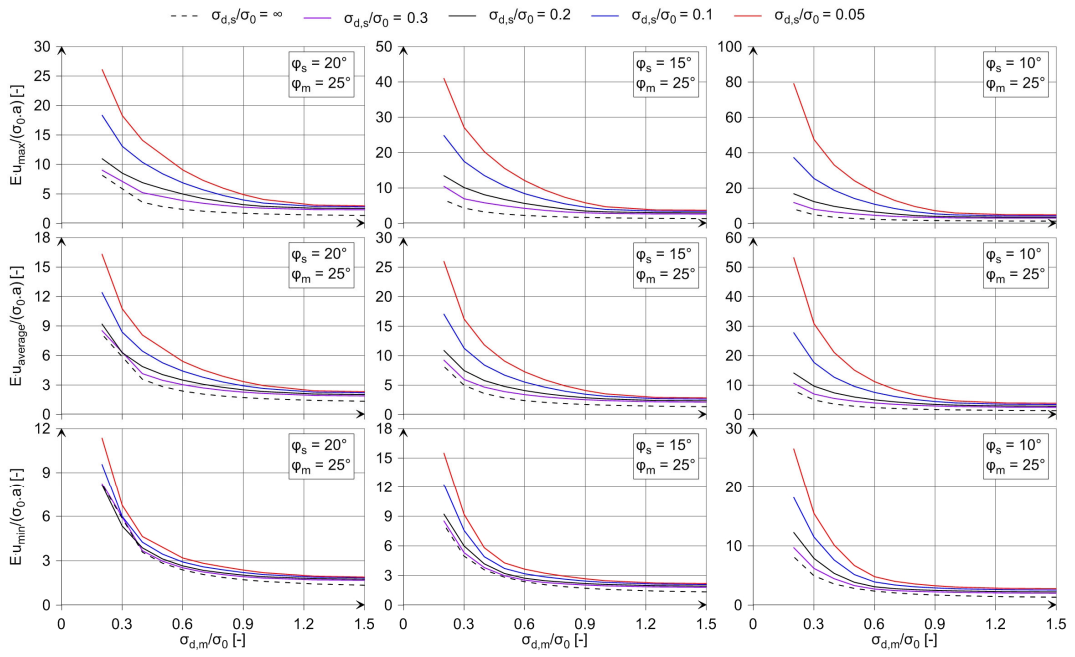


Figure 13. Nomograms for  $\phi_m = 25^\circ$  and  $\sigma_a/\sigma_0 = 0$ .

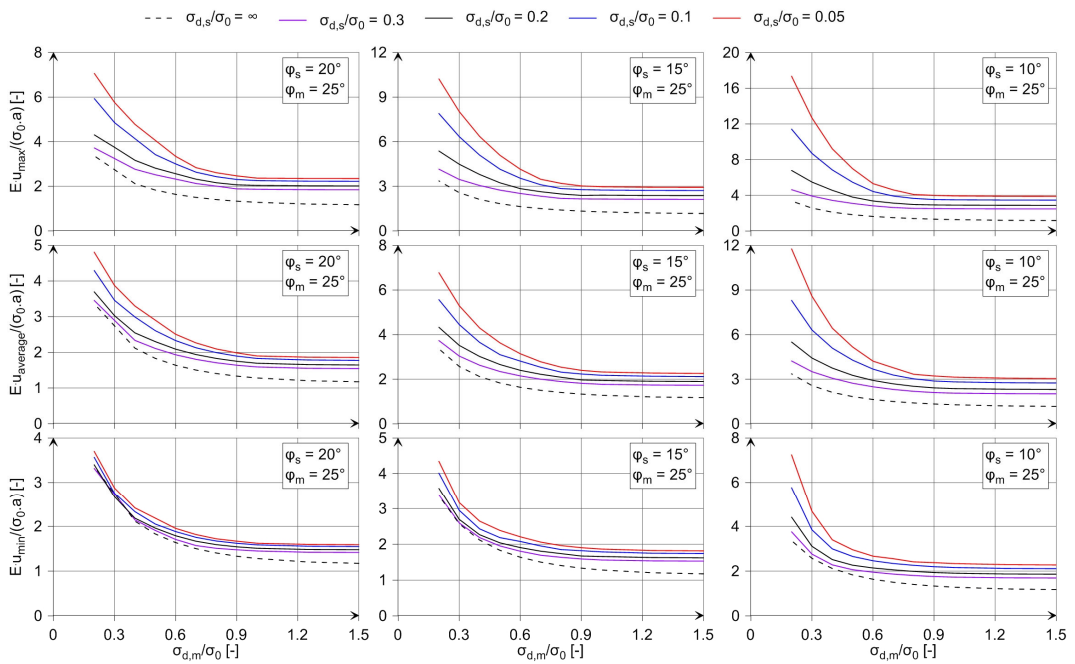


Figure 14. Nomograms for  $\phi_m = 25^\circ$  and  $\sigma_a/\sigma_0 = 0.1$ .

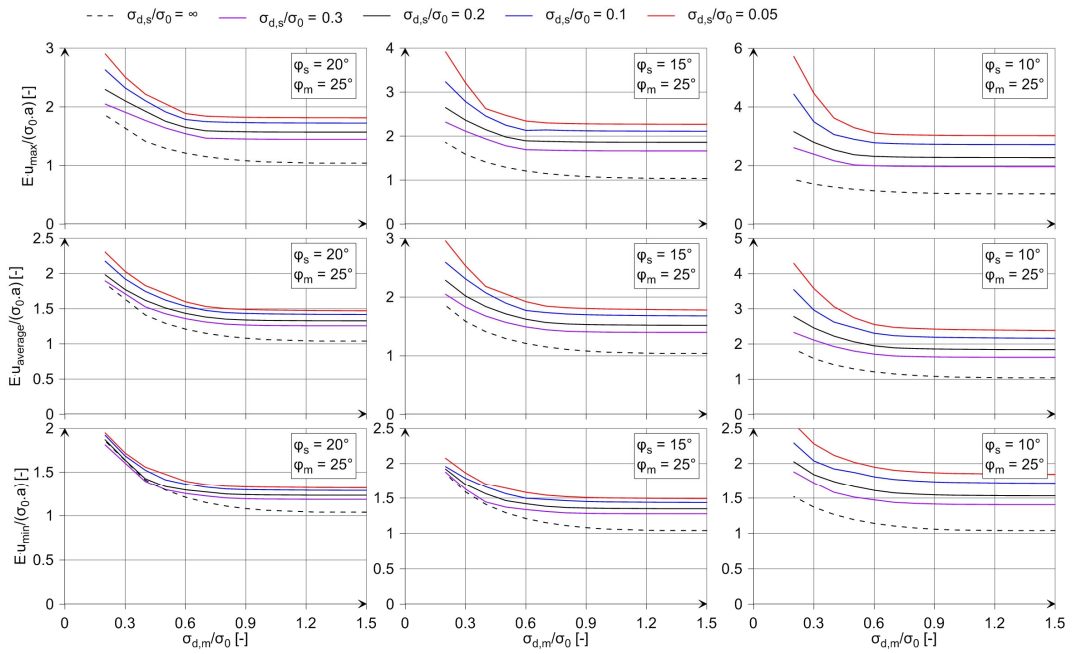


Figure 15. Nomograms for  $\varphi_m = 25^\circ$  and  $\sigma_a/\sigma_0 = 0.2$ .

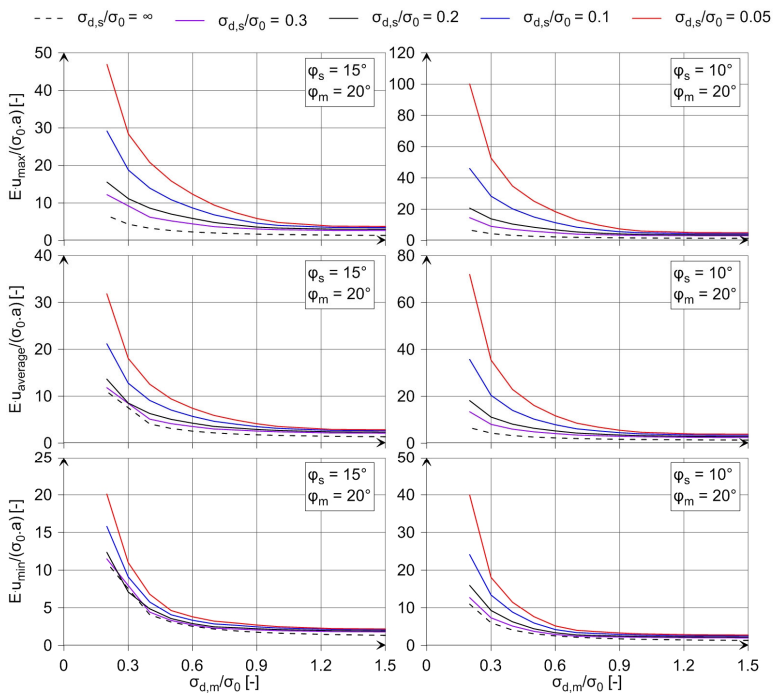


Figure 16. Nomograms for  $\varphi_m = 20^\circ$  and  $\sigma_a/\sigma_0 = 0$ .

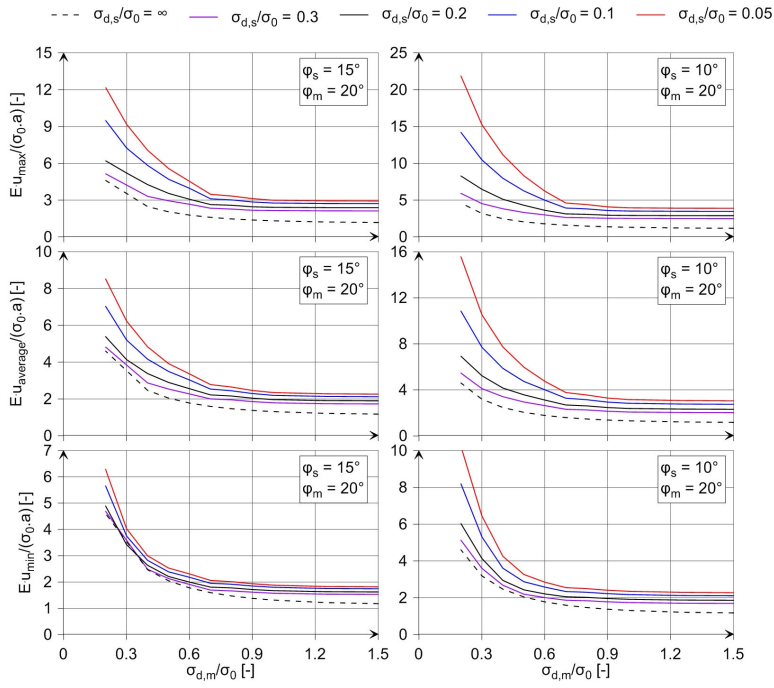


Figure 17. Nomograms for  $\phi_m = 20^\circ$  and  $\sigma_a/\sigma_0 = 0.1$ .

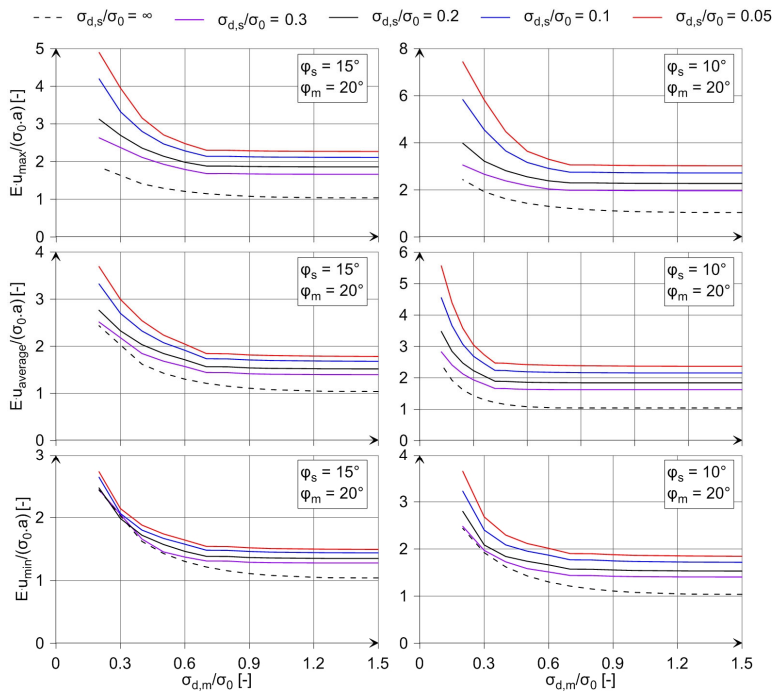


Figure 18. Nomograms for  $\phi_m = 20^\circ$  and  $\sigma_a/\sigma_0 = 0.2$ .



## Notation

### Latin symbols

$a$	tunnel radius
$A$	amplitude of the folding
$b$	width of the tunnel
$c$	cohesion of the ground
$c_{eq}$	equivalent cohesion of the simplified isotropic rock mass
$c_h, c_w$	cohesion of the hard and of the weak layers
$c_{h,H}, c_{h,R}$	peak and residual ( <i>i.e.</i> , post-peak) cohesion of the hard layers
$c_s, c_m$	cohesion of the schistosity and the surrounding matrix
$d$	thickness of the lining (in Section 4.2.5.1)
$d$	distance between the measuring point and the fault zone (except in Section 4.2.5.1)
$d_f$	distance between the tunnel face and the monitoring station
$d\varepsilon_r, d\varepsilon_t, d\varepsilon_z$	radial, tangential and axial strain increment of the equivalent continuum
$d\varepsilon_{r,h}, d\varepsilon_{t,h}, d\varepsilon_{z,h}$	radial, tangential and axial strain increment of the hard layers
$d\varepsilon_{r,w}, d\varepsilon_{t,w}, d\varepsilon_{z,w}$	radial, tangential and axial strain increment of the weak layers
$d\sigma_r, d\sigma_t, d\sigma_z$	radial, tangential and axial stress increment of the equivalent continuum
$d\sigma_{r,h}, d\sigma_{t,h}, d\sigma_{z,h}$	radial, tangential and axial stress increment of the hard layers
$d\sigma_{r,w}, d\sigma_{t,w}, d\sigma_{z,w}$	radial, tangential and axial stress increment of the weak layers
$E$	Young's modulus of the rock mass
$E_1, E_2$	Young's modulus of the composite parallel and perpendicular to the layers
$E_{eq}$	equivalent Young's modulus of the simplified isotropic rock mass
$E_{eq,max}, E_{eq,min}$	equivalent Young's modulus of the simplified isotropic rock mass fitted with the maximum or minimum GRC of the equivalent continuum
$E_h, E_w$	Young's modulus of the hard and of the weak layers
$E_{xx}, E_{yy}$	Young's modulus of the composite in <i>x</i> - and <i>y</i> -direction
$F$	degree of shearing of the rock mass in the monitoring station
$f(\dots)$	function of ...
$f_0(\dots)$	function of ...
$f_1(\dots)$	function of ...
$f_i(\dots)$	function of ...
$f_{n1}(\dots)$	function of ...
$F_1$	value for the determination of the equivalent parameters
$F_2$	value for the determination of the equivalent parameters
$F_V$	degree of shearing of the rock mass in the adjacent rock zone
$G_2$	shear modulus of the composite
$h$	thickness of the hard layers
$H$	distance of the hard formation to the tunnel axis
$I_R$	influence factor of the rock mass at the monitoring station
$I_s$	influence factor of the adjacent fault zone
$I_v$	influence factor of the adjacent rock zone
$K_0$	initial stress ratio
$K_l$	stiffness of the lining ( <i>cf.</i> [63])
$K_s$	stiffness of the shield ( <i>cf.</i> [63])
$L$	half of the period of the folding (in Section 5.2)
$L$	length of the shield (in Section 3.3.5)
$L_0$	initial length of the planes of anisotropy before folding
$L_V$	extent of the adjacent rock zone
$m_1$	value for the determination of the equivalent parameters
$m_2$	value for the determination of the equivalent parameters
$m_{eq}$	equivalent inclination of the failure surface of the simplified isotropic rock mass (function of the friction angle)
$m_h, m_w$	inclination of the failure surface of the hard and of the weak layers (function of the friction angle)
$m_m, m_s$	inclination of the failure surface of the schistosity and the surrounding matrix (function of the friction angle)
$m_{\varphi=20^\circ}$	inclination of the failure surface for $\varphi = 20^\circ$
$N$	number of schistosity planes in the REV
$n$	radial direction of the tunnel

$n_s$	normal vector of the schistosity planes
$p$	ground pressure acting upon the shield and the lining
$r$	radius, <i>i.e.</i> , distance to the tunnel axis
$R$	boring radius for TBM tunnelling
$S$	influence factor of the schistosity
$S_{11}, S_{12}, S_{13}$	constants for defining Hooke's law of the composite
$S_{22}, S_{33}, S_{44}$	constants for defining Hooke's law of the composite
$S_{11}, S_{12}, S_{21}$	constants for defining Hooke's law of the composite for plane strain conditions
$S_{22}, S_{33}$	constants for defining Hooke's law of the composite for plane strain conditions
$T$	lithological type at the monitoring station
$t$	thickness of the fault zone (in Section 2.2)
$t$	time after excavation (in Sections 2.1.6 and 2.3)
$u$	magnitude of the displacement vector at the tunnel boundary
$u(0)$	displacements occurring ahead of the tunnel face
$u_a$	radial displacements of the equivalent continuum at the tunnel boundary (for a tunnel drive perpendicular to the layers)
$u_{a,r}, u_{a,t}$	displacement at the tunnel boundary in radial and tangential direction
$u_{average}, u_{max}, u_{min}$	averaged, maximum and minimum magnitude of the displacement vector along the tunnel boundary
$u_{average,hom}, u_{max,hom}$	averaged and maximum magnitude of the displacement vector of the homogenised rock mass along the tunnel boundary
$u_{min,hom}$	minimum magnitude of the displacement vector of the homogenised rock mass along the tunnel boundary
$\bar{u}$	average magnitude of the displacement vectors
$u_c$	magnitude of the projection of the displacement vector in the cross-sectional plane of the tunnel
$\bar{u}_c$	average magnitude of the projections of the displacement vectors in the cross-sectional plane of the tunnel
$u_F$	displacement of the floor
$u_{h,2D}$	radial displacements that would occur in the absence of the weak layers
$u_K$	horizontal convergences
$u_{long}$	difference between the displacement that develops within 150 days (after reaching a face distance of 50 m to the monitoring station) and the displacement that develops after reaching a face distance of 5 m to the monitoring station
$u_{m,2D}$	radial displacements that would occur in the absence of the schistosity
$u_{max,ll}, u_{min,ll}$	maximum and minimum magnitude of the displacement vector along the tunnel boundary for a tunnel drive parallel to the planes of weakness
$u_{\perp}$	magnitude of the displacement vector along the tunnel boundary for a tunnel drive perpendicular to the planes of anisotropy
$\bar{u}_r$	average radial component of the displacement vectors
$u_{r,1}$	radial displacement of the tunnel crown
$u_{r,1,\infty}$	radial displacement of the tunnel crown far behind the face
$u_{short}$	magnitude of the displacement vector that develops as the face moves from a distance of 5 m to a distance of 50 m ahead of the monitoring station
$u_{tot}$	magnitude of the displacement vectors
$u_{w,2D}$	radial displacements that would occur in the absence of the hard layers or that would occur in a very long weak zone
$u_x, u_y$	displacement at the side wall (in <i>x</i> -direction) and at the crown (in <i>y</i> -direction)
$u_z$	longitudinal displacement
$u_{z,1}$	longitudinal displacement of the tunnel crown
$v$	deformation velocity
$w$	thickness of the weak layers
$x$	co-ordinate
$X$	co-ordinate
$x_h, x_w$	thickness fraction of the hard and of the weak layers in the REV
$y$	co-ordinate
$Y$	co-ordinate
$z$	co-ordinate
$Z$	shearing degree of the fault zone (in Section 2.2)
$Z$	constant (in Section 4.2)

**Greek symbols**

$\alpha$	angle between the cross-sectional plane of the tunnel and the displacement vector at the tunnel crown (in Section 2.1)
$\alpha$	ratio between $E_h/E_w$ and $\sigma_{d,h}/\sigma_{d,w}$ (in Section 3.3)
$\alpha_1, \alpha_2$	constants according to Hefny and Lo [54]
$\alpha_h$	ratio between the Young's modulus $E_h$ and the uniaxial compressive strength of the hard layers $\sigma_{d,h}$
$\alpha_w$	ratio between the Young's modulus $E_w$ and the uniaxial compressive strength of the hard layers $\sigma_{d,w}$
$\beta$	empirical curve-fitting parameter (in Section 2.1)
$\beta$	angle between the direction of the maximum principal stress and the planes of weakness (except in Section 2.1)
$\beta_1, \beta_2$	constants according to Hefny and Lo [54]
$\gamma_1, \gamma_2$	constants according to Hefny and Lo [54]
$\gamma_s$	shearing strain increment
$\gamma_{xy}$	shear strain of the composite
$\delta$	reduction factor (in Sections 3.1 and 4.2)
$\delta$	angle between the planes of weakness and the loading direction (in Sections 4.2 and 4.4)
$\delta_1, \delta_2$	constants according to Hefny and Lo [54]
$\Delta u$	horizontal convergences
$\Delta\gamma_{xy}, \Delta\gamma_{xz}, \Delta\gamma_{yz}$	homogenised shearing strain increment in the $xy$ -, $xz$ - and $yz$ -plane
$\Delta\gamma_{xy,m}, \Delta\gamma_{xz,m}, \Delta\gamma_{yz,m}$	shearing strain increment in the matrix in the $xy$ -, $xz$ - and $yz$ -plane
$\Delta\gamma_{xy,s}, \Delta\gamma_{xz,s}, \Delta\gamma_{yz,s}$	shearing strain increment along the schistosity in the $xy$ -, $xz$ - and $yz$ -plane
$\Delta\varepsilon_{xx}, \Delta\varepsilon_{yy}, \Delta\varepsilon_{zz}$	homogenised normal strain increment in $x$ -, $y$ - and $z$ -direction
$\Delta\varepsilon_{xx,m}, \Delta\varepsilon_{yy,m}, \Delta\varepsilon_{zz,m}$	normal strain increment in the matrix in $x$ -, $y$ - and $z$ -direction
$\Delta\varepsilon_{xx,s}, \Delta\varepsilon_{yy,s}, \Delta\varepsilon_{zz,s}$	normal strain increment in the schistosity in $x$ -, $y$ - and $z$ -direction
$\Delta\sigma_{xx}, \Delta\sigma_{yy}, \Delta\sigma_{zz}$	homogenised normal stress increment in $x$ -, $y$ - and $z$ -direction
$\Delta\sigma_{xx,m}, \Delta\sigma_{yy,m}, \Delta\sigma_{zz,m}$	normal stress increment in the matrix in $x$ -, $y$ - and $z$ -direction
$\Delta\sigma_{xx,s}, \Delta\sigma_{yy,s}, \Delta\sigma_{zz,s}$	normal stress increment in the schistosity in $x$ -, $y$ - and $z$ -direction
$\Delta\tau_{xy}, \Delta\tau_{xz}, \Delta\tau_{yz}$	homogenised shear stress increment in the $xy$ -, $xz$ - and $yz$ -plane
$\Delta\tau_{xy,m}, \Delta\tau_{xz,m}, \Delta\tau_{yz,m}$	shear stress increment in the matrix in the $xy$ -, $xz$ - and $yz$ -plane
$\Delta\tau_{xy,s}, \Delta\tau_{xz,s}, \Delta\tau_{yz,s}$	shear stress increment in the schistosity in $xy$ -, $xz$ - and $yz$ -plane
$\Delta u$	convergences, <i>i.e.</i> , displacements far behind the face minus pre-deformations (defined as $u-u(0)$ )
$\Delta u_{max,  }, \Delta u_{min,  }$	maximum and minimum convergence for a tunnel drive parallel to the planes of anisotropy
$\Delta u_{\perp}$	convergence for a tunnel drive perpendicular to the planes of anisotropy
$\varepsilon_1$	strain in direction of the maximum principal stress
$\varepsilon_r, \varepsilon_t$	radial and tangential strain of the equivalent continuum
$\varepsilon_{xx}, \varepsilon_{yy}, \varepsilon_{zz}$	strain of the equivalent continuum in $x$ -, $y$ - and $z$ -direction
$\varepsilon_{xy}, \varepsilon_{xz}, \varepsilon_{yz}$	shear strain of the equivalent continuum in the $xy$ -, $xz$ - and $yz$ -plane
$\varepsilon_f$	compression of the folding
$\zeta$	angle between the crown and the displacement in the cross-sectional plane of the tunnel (see inset of Fig. 5.23)
$\theta$	angle according to Hefny and Lo [54]
$\theta_s$	angle between the tunnel axis and the strike direction of the planes of weakness
$\lambda_{eq}$	Lamé constant of the equivalent continuum
$\lambda_h, \lambda_w$	Lamé constant of the hard and of the weak layers
$\mu_{eq}$	Lamé constant of the equivalent continuum
$\mu_h, \mu_w$	Lamé constant of the hard and of the weak layers
$\nu$	Poisson's ratio of the rock mass
$\nu_1, \nu_2$	Poisson's ratio of the composite parallel and perpendicular to the layers
$\nu_{eq}$	equivalent Poisson's ratio of the simplified isotropic rock mass
$\nu_h, \nu_w$	Poisson's ratio of the hard and of the weak layers
$\rho_1$	external radius of the plastic zone, where in-plane failure is reached in the hard or in the weak layers
$\rho_{1o}$	external radius of the plastic zone, where out-of-plane failure is reached in the hard or in the weak layers
$\rho_2$	external radius of the plastic zone, where in-plane failure is reached in both, in the hard and in the weak layers
$\rho_{2o}$	external radius of the plastic zone, where out-of-plane failure is reached in both, in the hard and in the weak layers
$\rho_{h,2D}$	radius of the plastic zone of the homogeneous competent ground
$\rho_{w,2D}$	radius of the plastic zone of the homogeneous weak ground

$\sigma$	normal stress
$\sigma_0$	initial stress
$\sigma_1, \sigma_3$	maximum and minimum principal stresses
$\sigma_a$	support pressure of the tunnel
$\sigma_d$	uniaxial compressive strength of the equivalent continuum
$\sigma_{d,eq}$	equivalent uniaxial compressive strength of the simplified isotropic rock mass
$\sigma_{d,eq,max}, \sigma_{d,eq,min}$	equivalent uniaxial compressive strength of the simplified isotropic rock mass fitted with the maximum or minimum GRC of the equivalent continuum
$\sigma_{d,h}, \sigma_{d,w}$	uniaxial compressive strength of the hard and of the weak layers
$\sigma_{d,s}, \sigma_{d,m}$	uniaxial compressive strength of the schistosity and the surrounding matrix
$(\sigma_{d,w}/\sigma_0)_{cor}$	characteristic value for the determination of the equivalent parameters
$(\sigma_{d,w}/\sigma_0)_{crit}$	characteristic value for the determination of the equivalent parameters
$\sigma_{max,h}, \sigma_{min,h}$	maximum and minimum stress of the hard layers
$\sigma_{max,w}, \sigma_{min,w}$	maximum and minimum stress of the weak layers
$\sigma_r, \sigma_t, \sigma_z$	radial, tangential and axial stress of the equivalent continuum
$\sigma_{r,h}, \sigma_{t,h}, \sigma_{z,h}$	radial, tangential and axial stress of the hard layers
$\sigma_{r,w}, \sigma_{t,w}, \sigma_{z,w}$	radial, tangential and axial stress of the weak layers
$\sigma_s$	value for the determination of the equivalent parameters
$\sigma_{xx}, \sigma_{yy}, \sigma_{zz}$	stress of the equivalent continuum in x-, y- and z-direction
$\sigma_{xx,h}, \sigma_{yy,h}, \sigma_{zz,h}$	stress of the hard layers in x-, y- and z-direction
$\sigma_{xx,w}, \sigma_{yy,w}, \sigma_{zz,w}$	stress of the weak layers in x-, y- and z-direction
$\sigma_p$	minimum support pressure for which the rock mass remains elastic
$\sigma_{r,p1}$	minimum support pressure for which the hard and the weak layers remain elastic
$\sigma_{r,p2}$	minimum support pressure for which the hard or the weak layers remain elastic
$\tau$	shear stress
$\tau_{xy}, \tau_{xz}, \tau_{yz}$	shear stress of the equivalent continuum in xy-, xz- and yz-direction
$\varphi$	friction angle of the ground
$\varphi_{eq}$	equivalent friction angle of the simplified isotropic rock mass
$\varphi_{eq,max}, \varphi_{eq,min}$	equivalent friction angle of the simplified isotropic rock mass fitted with the maximum or minimum GRC of the equivalent continuum
$\varphi_h, \varphi_w$	friction angle of the hard and of the weak layers
$\varphi_s, \varphi_m$	friction angle of the schistosity and of the surrounding matrix
$\psi_{eq}$	equivalent dilatancy angle of the simplified isotropic rock mass
$\psi_{eq,max}, \psi_{eq,min}$	equivalent dilatancy angle of the simplified isotropic rock mass fitted with the maximum or minimum GRC of the equivalent continuum
$\psi_h, \psi_w$	dilatancy angle of the hard and of the weak layers
$\psi_s, \psi_m$	dilatancy angle of the schistosity and of the surrounding matrix
$\omega_s$	dip angle of the planes of weakness
$\omega_{s,max}$	maximal dip angle of the planes of weakness

## References

- [1] Kovári, K. (1998). Tunnelling in squeezing rock. *Tunnel*, Vol. 5: 12-31.
- [2] Panet, M. and Guellec, P. (1974). Contribution à l'étude du soutènement derrière le front de taille. A.A. Balkema (Eds.), *Proceedings of the 3rd Congress ISRM, Denver*, pp. 1163-1168.
- [3] Salamon, M.D.G. (1968). Elastic moduli of a stratified rock mass. *International Journal of Rock Mechanics and Mining Sciences & Geomechanics Abstracts*, Vol. 5(6): 519-527.
- [4] Lourenço, P.B. (1995). The elastoplastic implementation of homogenisation Techniques with an extension to masonry structures. Delft University of Technology.
- [5] Mezger, F., Anagnostou, G., and Ziegler, H.J. (2013). The excavation-induced convergences in the Sedrun section of the Gotthard Base Tunnel. *Tunnelling and Underground Space Technology*, Vol. 38: 447-463.
- [6] Mezger, F., Anagnostou, G., and Ziegler, H.J. (2013). On some factors affecting squeezing intensity in tunnelling. G. Anagnostou and H. Ehrbar (Eds.), *ITA-AITES World Tunnel Congress, WTC 2013 - Underground : the way to the future*, Geneva, Switzerland, pp. 1990-1997.
- [7] Mezger, F. and Anagnostou, G. (2015). On the non-uniformity of squeezing deformations in the Ceneri Base Tunnel. W. Schubert and A. Kluckner (Eds.), *ISRM Regional Symposium EUROCK 2015 & 64th Geomechanics Colloquium, Salzburg, Oesterreich*, pp. 113-118.
- [8] Bachmann, T. and Vicenzi, I. (2008). Refurbishment in squeezing ground on large scale: lesson learned from the southern section of the Gotthard base tunnel. V.K. Kanjlia (Eds.), *AITES-ITA World Tunnel Congress, Agra, India*, pp. 1255-1262.
- [9] Barla, G. (2002). Tunnelling under squeezing rock conditions. *Tunnelling Mechanics - Advances in Geotechnical Engineering and Tunnelling*. D. Kolymbas. Logos Verlag, Innsbruck: 169-268.
- [10] Kovári, K., Amberg, F., and Ehrbar, H. (1999). Tunnelbau in druckhaftem Gebirge – Eine Herausforderung für die neuen Alpentransversalen. Lehrstuhl für Bauverfahrenstechnik, Tunnelbau und Baubetrieb (Eds.), *Kolloquium für Bauverfahrenstechnik, Bochum, Germany*, pp. 141-151.
- [11] Mezger, F. (2019). On the variability of squeezing behaviour in tunnelling. Dissertation ETH No. 25638.
- [12] Kovári, K. and Anagnostou, G. (1995). The ground response curve in tunnelling through short fault zones. T. Fujii (Eds.), *8th International Congress on Rock Mechanics, Tokyo*, pp. 611-614.
- [13] Cantieni, L. and Anagnostou, G. (2007). On the variability of squeezing in tunnelling. L. Ribeiro e Sousa, C. Olalla, and N.F. Grossmann (Eds.), *11th Congress of the International Society for Rock Mechanics (ISRM), Lisbon*, pp. 983-986.
- [14] Steindorfer, A. (1998). Short term prediction of rock mass behavior in tunneling by advanced analysis of displacement monitoring data. Graz, Techn. Univ. Graz.
- [15] Cantieni, L., Anagnostou, G., and Hug, R. (2011). Interpretation of core extrusion measurements when tunnelling through squeezing ground. *Rock Mechanics and Rock Engineering*, Vol. 44(6): 641-670.
- [16] Schneider, T.R. (1997). Treatment of the faults at the project of the Gotthard-basetunnel. *Felsbau*, Vol. 15(6): 489-495.
- [17] Vogelhuber, M. (2007). Der Einfluss des Porenwasserdrucks auf das mechanische Verhalten kakirtisierter Gesteine. Dissertation ETH No. 17079. ETH Zürich.
- [18] Anagnostou, G., Pimentel, E., and Cantieni, L. (2008). AlpTransit Gotthard Basistunnel – Teilabschnitt Sedrun – Felsmechanische Laborversuche Los 378. Schlussbericht Nr. 080109.
- [19] SISO (2012). "Site Information Software AlpTransit Gotthard." Retrieved March 2012, March 2012, from [www.sisonet.com](http://www.sisonet.com).
- [20] Guntli, P. and Weber, A. (2009). Einspurtunnel Ost km 118.835–120.039, Einspurtunnel West km 218.855–220.062 Tavetscher Zwischenmassiv Nord und Clavaniev-Zone, Geologischer Schlussbericht, Geologie, Geotechnik, Hydrogeologie. Bericht Nr.: GR 360B-2, Sieber Cassina + Handke AG.
- [21] Ehrbar, H. and Pfenninger, I. (1999). Umsetzung der Geologie in technische Massnahmen im Tavetscher Zwischenmassiv Nord. S. Löw and R. Wyss (Eds.), *Symposium Geologie Alptransit, Vorauserkundung und Prognose der Basistunnels am Gotthard und am Lötschberg Zürich*, pp. 381–394.
- [22] Kovári, K., Amberg, F., and Ehrbar, H. (2000). Mastering of Squeezing Rock in the Gotthard Base. *World Tunneling*, Vol. 13(5): 234-238.
- [23] Thut, A., et al. (2006). Tunneling in Squeezing Rock - Yielding Elements and Face Control. Society for underground and geotechnical constructions (Eds.), *8th International Conference on Tunnel Constructions and Underground Structures, Ljubljana, Slovenia*.
- [24] Kovári, K. and Ehrbar, H. (2008). Gotthard Basistunnel, Teilabschnitt Sedrun – Die druckhaften Strecken im TZM Nord – Projektierung und Realisierung. *Swiss Tunnelling Society (Eds.), Swiss Tunnel Congress Luzern*, pp. 39-47.
- [25] Goricki, A., et al. (2005). The influence of Discontinuity Orientation on the Behaviour of Tunnels. *Felsbau*, Vol. 23(5): 12-18.
- [26] Steiner, W. (1996). Tunnelling in Squeezing Rocks: Case Histories. *Rock Mechanics and Rock Engineering*, Vol. 29(4): 211-246.
- [27] Barla, G. and Barla, M. (2009). Innovative Tunnelling construction methods in squeezing rock. *Kolloquium der Professur für Untertagbau der ETH Zürich*.
- [28] Pini, O. and Skaanes, S. (2006). Ceneri Base Tunnel. *Tunnel* Vol. 4: 44-47.
- [29] Merlini, D. and Falanesca, M. (2013). Ceneri Base Tunnel advancement in difficult rock conditions: tunnel design and construction optimization through back-analysis of the geomechanical parameters. *ITA-AITES World Tunnel Congress, WTC 2013 - Underground: the way to the future*, Geneva, Switzerland
- [30] Leitner, R., Pötsch, M., and Schubert, W. (2006). Aspects on the Numerical Modeling of Rock Mass Anisotropy in Tunneling. *Felsbau* 24, Vol. 24(2): 59-65.
- [31] Stocker, D. (2006). Ceneri Basistunnel - Bautechnische Herausforderungen. *Der Bauingenieur*, Vol. 7: 14-16.

- [32] ITC (2014). Insight in the monthly reports, the geological journals and the execution plans. ITC ITECSA-TOSCANO Consorzio d'ingegneri, not published.
- [33] Fontana, A. (2012). Durchörterung «Linea Val Colla» Planungs- und Ausführungsaspekte. Kolloquium der Professur für Untertagbau der ETH Zürich, Bauhilfsmassnahmen im Tunnelbau, Zürich.
- [34] Keller, M. (2005). Die Beherrschung der Hohlraumverformungen in der Karbonzone. Fachgruppe für Untertagbau (Eds.), Swiss Tunnel Congress, Fachtagung für Untertagbau, Luzern, pp. 31-37.
- [35] Bonini, M. and Barla, G. (2012). The Saint La Porte access adit (Lyon-Turin Base Tunnel) revisited. *Tunnelling and Underground Space Technology*, Vol. 30: 38-54.
- [36] Geological Group of the Lötschberg Base Tunnel (2008). Geologischer Bericht, Vortrieb Mitholz Richtung Süden, Tunnelröhre Ost, BKm 22.043 - 31.828, Tunnelröhre West, BKm 22.043 - 31.647. Schlussdokumentation Lötschberg. BLS AlpTransit Lötschberg.
- [37] IG-LBT (2009). Schlussbericht Felsmechanik, Ausbruch, Sicherung. BLS AlpTransit Lötschberg.
- [38] Ziegler, H.J. and Isler, A. (2013). Lötschberg-Basistunnel - zusammenfassender geologischer Schlussbericht. Bericht der Landesgeologie 4.
- [39] Stech, H.-J., et al. (2005). Lötschberg-Basistunnel: Ausbrucharbeiten vollendet. *Tunnel*, Vol. 4: 16-39.
- [40] Kovári, K. (2005). Method and device for stabilizing a cavity excavated in underground construction. US Patent Appl. 20050191138.
- [41] Schubert, W. (1996). Dealing with squeezing conditions in Alpine tunnels. *Rock Mechanics and Rock Engineering*, Vol. 29(3): 145-153.
- [42] Anagnostou, G. (2007). The one-step solution of the advancing tunnel heading problem. J. Eberhardsteiner (Eds.), ECCOMAS Thematic Conference on Computational Methods in Tunnelling, Vienna, Austria, pp. 133.
- [43] Kaiser, P.-K. (1980). Effect of stress-history on the deformation behaviour of underground openings. H.R. Rice (Eds.), 13th Canadian Rock Mechanics Symposium, Toronto, pp. 133-140.
- [44] Schneider, A. (2002). Sicherheit gegen Niederbruch im Untertagbau. Dissertation ETH No. 14556. ETH Zürich.
- [45] Button, E.A., et al. (2006). Spatial Relationships Between Discontinuity Orientation and System Behavior in Underground Excavations. American rock mechanics association (Eds.), Golden Rocks 2006, Golden, Colorado
- [46] Anagnostou, G., Schuerch, R., and Ramoni, M. (2014). TBM tunnelling in complex rock formations. G. Barla (Eds.), MIR 2014, XV Ciclo di conferenze di meccanica e ingegneria delle rocce, Torino, Italy, pp. 307 - 331.
- [47] Suquet, P. (1987). Elements of Homogenization for Inelastic Solic Mechanics. E. Sanchez-Palancia and A. Zaoui (Eds.), Homogenization Techniques for Composite Media, New York, pp. 193-278.
- [48] Gerrard, C.M. (1982). Equivalent elastic moduli of a rock mass consisting of orthorhombic layers. *International Journal of Rock Mechanics and Mining Sciences & Geomechanics Abstracts*, Vol. 19(1): 9-14.
- [49] Taliercio, A. and Sacchi Landriani, G. (1988). A failure condition for layered rock. *International Journal of Rock Mechanics and Mining Sciences & Geomechanics Abstracts*, Vol. 25(5): 299-305.
- [50] Lai, Y.S., Wang, C.Y., and Tien, Y.M. (1999). Modified Mohr-Coulomb-type micromechanical failure criteria for layered rocks. *International Journal for Numerical and Analytical Methods in Geomechanics*, Vol. 23: 451-460.
- [51] Tien, Y.M. and Kuo, M.C. (2001). A failure criterion for transversely isotropic rocks. *International Journal of Rock Mechanics and Mining Sciences*, Vol. 38(3): 399-412.
- [52] Lydzba, D., Pietruszczak, S., and Shao, J.F. (2003). On anisotropy of stratified rocks: homogenization and fabric tensor approach. *Computers and Geotechnics*, Vol. 30(4): 289-302.
- [53] Triantafyllidis, T. and Gerolymatou, E. (2014). Estimation of the Strength of Stratified Rock Mass. *Rock mechanics and rock engineering*, Vol. 47(2): 535-547.
- [54] Hefny, A.M. and Lo, K.Y. (1999). Analytical solutions for stresses and displacements around tunnels driven in cross-anisotropic rocks. *Numerical and analytical methods in geomechanics*, Vol. 23(2): 161-177.
- [55] Bobet, A. (2011). Lined Circular Tunnels in Elastic Transversely Anisotropic Rock at Depth. *Rock Mechanics and Rock Engineering*, Vol. 44(2): 149-167.
- [56] Zhang, Z. and Sun, Y. (2011). Analytical solution for a deep tunnel with arbitrary cross section in a transversely isotropic rock mass. *International Journal of Rock Mechanics and Mining Sciences*, Vol. 48(8): 1359-1363.
- [57] Tran Manh, H., Sulem, J., and Subrin, D. (2015). A Closed-Form Solution for Tunnels with Arbitrary Cross Section Excavated in Elastic Anisotropic Ground. *Rock Mechanics and Rock Engineering*, Vol. 48: 277-288.
- [58] Park, P.H. and Kim, Y.J. (2006). Analytical solution for a circular opening in an elastic-brittle-plastic rock. *International Journal of Rock Mechanics and Mining Sciences*, Vol. 43(4): 616-622.
- [59] MathWorks (2017). Matlab®.
- [60] Anagnostou, G. and Kovári, K. (1993). Significant parameters in elasto-plastic analysis of underground openings. *Journal of Geotechnical Engineering*, Vol. 119(3): 401-419.
- [61] Cantieni, L. and Anagnostou, G. (2009). The interaction between yielding supports and squeezing ground. *Tunnelling and Underground Space Technology*, Vol. 24(3): 309-322.
- [62] Ramoni, M. and Anagnostou, G. (2011). Design aids for the planning of TBM drives in squeezing ground. Research project FGU 2007/005 of the Swiss Federal Roads Office (FEDRO), Report 1341. Swiss Association of Road and Transportation Experts (VSS). Zürich.
- [63] Ramoni, M. and Anagnostou, G. (2010). Thrust force requirements for TBMs in squeezing ground. *Tunnelling and Underground Space Technology* Vol. 25(4): 433-455.
- [64] Dassault Systèmes (2011). Abaqus 6.11 - Theory Manual and Analysis User's Manual.
- [65] Clausen, J. (2007). Efficient Non-Linear Finite Element Implementation of Elasto-Plasticity for Geotechnical Problems. Aalborg University Esbjerg.
- [66] Itasca Consulting Group (2001). FLAC: User's manual. Ver. 4.0.

- [67] Anagnostou, G. and Kovári, K. (2003). The stability of tunnels in grouted fault zones. *Mitteilungen des Institutes für Geotechnik (IGT)*, Vol. 220.
- [68] Vermeer, P.A. and de Borst, R. (1984). Non-associated plasticity for soils, concrete and rock. *HERON* Vol. 29(3): 1-64.
- [69] Elomri, A. and Sidoroff, F. (1991). Homogenization of a two-phase elastic-plastic layered composite. *Compte Rendu de l'Académie des Sciences*, Vol. 312(II): 425-30.
- [70] Pruchnicki, E. and Shahrour, I. (1994). A macroscopic elastoplastic constitutive law for multilayered media: Application to reinforced earth material. *Numerical and analytical methods in geomechanics*, Vol. 18(7): 507-518.
- [71] Nejad Ensan, M. and Shahrour, I. (2003). A macroscopic constitutive law for elasto-plastic multilayered materials with imperfect interfaces: application to reinforced soils. *Computers and Geotechnics*, Vol. 30(4): 339-345.
- [72] Bourne, S.J. (2003). Contrast of elastic properties between rock layers as a mechanism for the initiation and orientation of tensile failure under uniform remote compression. *Journal of Geophysical Research*, Vol. 108(B8).
- [73] Vu, T.M., et al. (2013). Semi-Analytical Solution for Stresses and Displacements in a Tunnel Excavated in Transversely Isotropic Formation with Non-Linear Behavior. *Rock mechanics and rock engineering*, Vol. 46(2): 213-229.
- [74] Panet, M. (1996). Two case histories of tunnels through squeezing rocks. *Rock mechanics and rock engineering*, Vol. 29(3): 155-164.
- [75] Thuro, K., Eberhardt, E., and Gasparini, M. (2004). Deep seated creep and its influence on a 1.5 GW hydroelectric power plant in the Himalayas. *Felsbau*, Vol. 22(2): 60-66.
- [76] Huber, G., Westermayr, H., and Alber, O. (2005). Einfluss der Gefügeorientierung am Strenger Tunnel. *Felsbau* Vol. 5(20-24).
- [77] Malaguti, A., Morandi, S., and Stocker, D. (2013). Anisotropic geomechanical behaviour of tunnelling Val Colla Line, Ceneri base Tunnel, Switzerland. G. Anagnostou and H. Ehrbar (Eds.), *ITA-AITES World Tunnel Congress, WTC 2013 - Underground: the way to the future*, Geneva, Switzerland, pp. 1730-1737.
- [78] Daemen, J.J.K. (1983). Slip zones for discontinuities parallel to circular tunnels or shafts. *International Journal of Rock Mechanics and Mining Sciences & Geomechanics Abstracts*, Vol. 20(3): 135-148.
- [79] Shen, B. and Barton, N. (1997). The Disturbed Zone Around Tunnels in Jointed Rock Masses. *International Journal of Rock Mechanics and Mining Sciences*, Vol. 34(1): 117-125.
- [80] Hsu, S.C., Chiang, S.S., and Lai, J.R. (2004). Failure mechanisms of tunnels in weak rock with interbedded structures. *International Journal of Rock Mechanics and Mining Sciences*, Vol. 41(3): 489.
- [81] Wang, T.T. and Huang, T.H. (2014). Anisotropic deformation of a circular tunnel excavated in a rock mass containing sets of ubiquitous joints: theory analysis and numerical modeling. *Rock mechanics and rock engineering*, Vol. 47: 643-657.
- [82] Sulem, J. and Mühlhaus, H.B. (1997). A continuum model for periodic two-dimensional block structures. *Mechanics of cohesive-frictional materials*, Vol. 2: 31-46.
- [83] Jing, L. (1998). Formulation of discontinuous deformation analysis (DDA) - an implicit discrete element model for block systems. *Engineering Geology*, Vol. 49(3-4): 371-381.
- [84] Barla, G. and Barla, M. (2000). Continuum and discontinuum modelling in tunnel engineering. *Rudarsko Geolosko Naftni Zbornik* Vol. 52(12): 45-57.
- [85] Lisjak, A., Grasselli, G., and Vietor, T. (2014). Continuum-discontinuum analysis of failure mechanisms around unsupported circular excavations in anisotropic clay shales. *International Journal of Rock Mechanics and Mining Sciences*, Vol. 65: 96-115.
- [86] Clark, I.H. (2006). Simulation of rock mass strength using ubiquitous joints. R. Hart and P. Varona (Eds.), *Fourth International FLAC Symposium on Numerical Modeling in Geomechanics*, Madrid.
- [87] Sainsbury, B., Pierce, M., and Mas Ivars, D. (2008). Simulation of rock mass strength anisotropy and scale effects using a Ubiquitous Joint Rock Mass (UJRM) model. D.H. Hart, C. Detournay, and P. Cundall (Eds.), *First International FLAC/DEM Symposium on Numerical Modeling*, (Continuum and Distinct Element Numerical Modeling in Geo-Engineering), Minneapolis, USA, pp. 1-10.
- [88] Jaeger, J.C. and Cook, N.G.W. (1976). *Fundamentals of Rock Mechanics*, Chapman and Hall, London.
- [89] Brinkgreve, R.B.J., Kumarswamy, S., and Swolfs, W.M. (2016). *Plaxis 2016*.
- [90] Azami, A., Yacoub, T., and Curran, J. (2012). Effects of strength anisotropy on the stability of slopes G. Robinson and K. Bannister (Eds.), *65th Canadian Geotechnical Conference, CSG Geo-Manitoba*, Winnipeg, Canada.
- [91] Azami, A., et al. (2013). A constitutive model for jointed rock mass. M. Kwasniewski and D. Lydzba (Eds.), *EUROCK 2013 - The ISRM International Symposium Wroclaw, Poland*.
- [92] Pietruszczak, S., Lydzba, D., and Shao, J.-F. (2002). Modelling of inherent anisotropy in sedimentary rocks. *International Journal of Solids and Structures*, Vol. 39(3): 637-648.
- [93] Duveau, G., Shao, J.F., and Henry, J.P. (1998). Assessment of some failure criteria for strongly anisotropic geomaterials. *Mechanics of cohesive-frictional materials*, Vol. 3(1): 1-26.
- [94] Ambrose, J. (2014). *Failure of Anisotropic Shales under Triaxial Stress Conditions*. Department of Earth Science and Engineering, Imperial College London.
- [95] Jaeger, J.C. (1960). Shear failure of anisotropic rocks. *Geological Magazine*, Vol. 97(1): 65-72.
- [96] Walsh, J.B. and Brace, W.F. (1964). A fracture criterion for brittle anisotropic rock. *Journal of Geophysical Research*, Vol. 69(16): 3449-3456.
- [97] Hoek, E. and Brown, E.T. (1980). Empirical strength criterion for rock masses. *Journal of the Geotechnical Engineering Division* Vol. 106(15715): 1013-1035.
- [98] Kovári, K. (1977). The elasto-plastic analysis in the design practice of underground openings. *Finite Elements in Geomechanics*. G. Gudehus: 377 - 412.
- [99] Amadei, B. (1996). Importance of Anisotropy When Estimating and Measuring In Situ Stresses in Rock. *International Journal of Rock Mechanics and Mining Sciences*, Vol. 33(3): 293-325.
- [100] Park, B. and Min, K.B. (2015). Bonded-particle discrete element modeling of mechanical behavior of transversely isotropic rock. *International Journal of Rock Mechanics & Mining Sciences*, Vol. 76: 243-255.

- [101] Ismael, M. and Konietzky, H. (2017). Integration of Elastic Stiffness Anisotropy into Ubiquitous Joint Model. *Procedia Engineering*, Vol. 191: 1032-1039.
- [102] Chen, E.P. (1986). Two-dimensional continuum model for jointed media with orthogonal sets of joints. *Proceedings - Symposium on Rock Mechanics*.
- [103] Cai, M. and Horii, H. (1993). A constitutive model and FEM analysis of jointed rock masses. *International Journal of Rock Mechanics and Mining Sciences & Geomechanics Abstracts*, Vol. 30(4): 351-359.
- [104] Itasca Consulting Group (2007). *Fast Lagrangian Analysis of Continua, Constitutive Models*.
- [105] Xu, L., et al. (2010). An Anisotropic Elastoplastic Constitutive Model for Layered Rock Masses and Its Implementation in ABAQUS. *ASCE (Eds.), Earth and Space 2010: Engineering, Science, Construction, and Operations in Challenging Environments*, pp. 305-318.
- [106] Zhao, Q. and He, Z.M. (2011). The ubiquitous-joint model and its application in predicting the strength of stratified rock. *GeoHunan International Conference*, Hunan, China.
- [107] Nguyen, V.M. and Konietzky, H. (2016). *Behaviour of joints*. Institut für Geotechnik TU Bergakademie Freiberg.
- [108] Cording, E.J. and Mahar, J.W. (1974). The effect of natural geologic discontinuities on behavior of rock in tunnels. *H. Pattison and E. D'Appolonia (Eds.), RETC Conference*, San Francisco, pp. 107-138.
- [109] Cantieni, L. and Anagnostou, G. (2009). The Effect of the Stress Path on Squeezing Behavior in Tunneling. *Rock Mechanics and Rock Engineering*, Vol. 42(2): 289–318.
- [110] Carranza-Torres, C. and Fairhurst, C. (2000). Application of the Convergence-Confinement method of tunnel design to rock masses that satisfy the Hoek-Brown failure criterion. *Tunnelling and Underground Space Technology*, Vol. 15(2): 187-213.
- [111] Tonon, F. and Amadei, B. (2002). Effect of Elastic Anisotropy on Tunnel Wall Displacements Behind a Tunnel Face. *Rock Mechanics and Rock Engineering*, Vol. 35(3): 141–160.
- [112] Klopčič, J. and Logar, J. (2014). Effect of relative orientation of anisotropy planes to tunnel axis on the magnitude of tunnelling displacements. *International Journal of Rock Mechanics & Mining Sciences*, Vol. 71: 235-248.
- [113] Madkour, H. (2012). Parametric analysis of tunnel behavior in jointed rock. *Ain Shams Engineering Journal*, Vol. 3: 79-103.
- [114] Schubert, W. and Mendez, J.M.D. (2017). Influence of Foliation Orientation on Tunnel Behavior. *Procedia Engineering*, Vol. 191: 880-885.
- [115] Amadei, B. and Goodman, R.E. (1981). Formulation of complete plane strain problems for regularly jointed rocks. *American Rock Mechanics Association (Eds.), The 22nd US Symposium on Rock Mechanics (USRMS)*, Cambridge, Massachusetts, pp. 245-251.
- [116] Zienkiewicz, O.C., Pande, G.N., and Taylor, R.L. (2015). Quasi-plane strain in the analysis of geological problems. *Computer Methods in Tunnel Design*: 19-40.
- [117] Rencis, J.J. and Huang, T.H. (1992). Boundary element formulation for generalized plane strain. *Engineering Analysis with Boundary Elements* Vol. 9 263-271(3): 263-271.
- [118] Burg, J.-P. (2018). *Script to Structural Geology*. Educational Material, ETH Zurich.
- [119] Ingenieurgesellschaft Gotthard-Basistunnel Süd (2009). *Einspurtunnel Nord, Bautechnischer Schlussbericht*. AlpTransit Gotthard AG.
- [120] Anagnostou, G. and Kovári, K. (1999). Tunnelbau in Störzonen. *S. Löw and R. Wyss (Eds.), Symposium Geologie Alptransit, Vorauserkundung und Prognose der Basistunnels am Gotthard und am Lötschberg Zürich, Switzerland*.



# Projektabschluss



Schweizerische Eidgenossenschaft  
Confédération suisse  
Confederazione Svizzera  
Confederaziun svizra

Eidgenössisches Departement für  
Umwelt, Verkehr, Energie und Kommunikation UVEK  
Bundesamt für Strassen ASTRA

## FORSCHUNG IM STRASSENWESEN DES UVEK

Version vom 09.10.2013

### Formular Nr. 3: Projektabschluss

erstellt / geändert am: 31. Juli 2019

#### Grunddaten

Projekt-Nr.: FGU 2014/003  
 Projekttitel: Zur Variabilität des Gebirgsverhaltens beim Tunnelbau im druckhaften Gebirge  
 Enddatum: 31. Juli 2019

#### Texte

Zusammenfassung der Projektergebnisse:

Die Intensität der Gebirgsverformung in einer druckhaften Strecke ist in der Regel stark veränderlich. Trotz gleichbleibender Ausbruchsicherung, Überlagerungshöhe und lithologischer Zusammensetzung lassen sich häufig auf kurzer Distanz beträchtliche Änderungen der Konvergenzen feststellen. So lange die Gründe für diese Variabilität nicht bekannt sind, sind zuverlässige Voraussagen des Gebirgsverhaltens beim Vortrieb schwierig. Letztere sind aber wichtig, um die Sicherungsmittel und den Ausbruchsquerschnitt zu bestimmen und damit kostspielige und aufwändige Nachprofilierungsarbeiten zu vermeiden.

Die Analyse von ausgewählten Vortrieben des AlpTransit Projektes zeigt, dass die Variabilität der Druckhaftigkeit auf die Heterogenität des Gebirges in verschiedenen Massstäben sowie auf die variierende Raumstellung der Trennflächen (Schieferung, Schichtung) in Bezug zur Tunnelachse zurückgeführt werden kann. Um die Sicherheit und Wirtschaftlichkeit beim Tunnelbau in druckhaftem Gebirge zu erhöhen, wurde der Einfluss dieser Faktoren auf die Konvergenzen quantitativ (mittels analytischer Lösungen oder numerischer Berechnungen) untersucht, so dass diese als Indikatoren für die rechtzeitige Identifikation und Vorhersage des druckhaften Verhalten genutzt werden können. Besondere Beachtung wurde Faktoren geschenkt, deren kleine Veränderungen einen starken Einfluss auf die Intensität der Konvergenzen haben. Basierend auf diesen quantitativen Untersuchungen wurden Entscheidungshilfen entwickelt, welche dem projektierenden Ingenieur helfen sollen, die Variabilität der Druckhaftigkeit zu beurteilen und besser zu erfassen.

Zielerreichung:

Die Projektziele wurden indem erreicht, dass die Gründe der oft beobachteten Variabilität d er Druckhaftigkeit analysiert und Hilfsmittel für die Projektierung erarbeitet wurden.

Folgerungen und Empfehlungen:

Die Variabilität der Druckhaftigkeit kann auf die Heterogenität des Gebirges sowie auf Änderungen der Raumstellung der Trennflächen (Schichtung, Schieferung) zurückgeführt werden. Der Einfluss dieser Faktoren kann im Rahmen der Vorprojektierung durch die in diesem Forschungsprojekt erarbeiteten Methoden rechnerisch erfasst werden.

Publikationen:

Mezger, F., Anagnostou, G., and Ziegler, H.J. (2013). The excavation induced convergences inthe Sedrun section of the Gotthard Base Tunnel. Tunnelling and Underground Space Technology, Vol. 38: pp. 447-463.

Mezger, F., Anagnostou, G., and Ziegler, H.J. (2013). On some factors affecting squeezing intensity in tunnelling. G. Anagnostou and H. Ehrbar (Eds.), ITA-AITES World Tunnel Congress,

WTC 2013 - Underground : the way to the future, Geneva, Switzerland, pp. 1990-1997.

Mezger, F. and Anagnostou, G. (2015). On the nonuniformity of squeezing deformations in

Der Projektleiter/die Projektleiterin:

Name: Anagnostou

Vorname: Georgios

Amt, Firma, Institut: Institut für Geotechnik, ETH Zürich

Unterschrift des Projektleiters/der Projektleiterin:

 26/8/2019

## FORSCHUNG IM STRASSENWESEN DES UVEK

### Formular Nr. 3: Projektabschluss

#### Beurteilung der Begleitkommission:

##### Beurteilung:

Das Forschungsprojekt ist umfassend und weist ein hohes wissenschaftliches Niveau sowie einen wertvollen praktischen Nutzen auf. Die Analysen zu ausgewählten Fallbeispielen sind gründlich durchgeführt und schlüssig interpretiert. Der Einfluss der Heterogenität des Gebirges auf seiner Druckhaftigkeit ist plausibel und detailliert dargelegt. Die durchgeführten numerischen Berechnungen sowie die damit erarbeiteten Hilfsmittel lassen eine Prognose der Deformationen zu, was sehr wertvoll ist und konkreten Einfluss auf die Arbeitssicherheit und die Wirtschaftlichkeit haben kann, wenn die Überlegungen zeitgerecht umgesetzt werden. Die durchgeführten Vergleichsrechnungen untermauern die Schlussfolgerungen.

##### Umsetzung:

Insbesondere die im Rahmen des Forschungsprojekts erarbeiteten Hilfsmittel für die Projektierung werden Eingang in die Praxis finden und den projektierenden Ingenieur in der Entscheidungsfindung respektive in seiner Planungsarbeit unterstützen. Die aus der Analyse von mehreren Fallbeispielen (CH-Basistunnel, welche in den letzten Jahren gebaut wurden) gewonnenen Erkenntnisse stützen die Aussagen im Forschungsbericht ab und bestätigen deren Umsetzbarkeit in der Praxis.

##### weitergehender Forschungsbedarf:

Die mögliche Zeitabhängigkeit des Gebirgsverhaltens infolge Konsolidation wird hier nicht berücksichtigt. Der Einfluss der Heterogenität der hydraulischen Eigenschaften des Gebirges auf seiner Druckhaftigkeit soll in zukünftigen Forschungsprojekten untersucht werden.

##### Einfluss auf Normenwerk:

---

#### Der Präsident/die Präsidentin der Begleitkommission:

Name: Ramoni

Vorname: Marco

Amt, Firma, Institut: Basler & Hofmann AG

#### Unterschrift des Präsidenten/der Präsidentin der Begleitkommission:

31.07.2019 

## Verzeichnis der Berichte der Forschung im Strassenwesen

Das Verzeichnis der in der letzten Zeit publizierten Schlussberichte kann unter [www.astra.admin.ch](http://www.astra.admin.ch) (*Forschung im Strassenwesen --> Downloads --> Formulare*) heruntergeladen werden.